

# **Investigations on Design and Development of Copper Based Shape Memory Alloy Bimorph and Their Application towards Micro- Robotics and Energy Systems**

Ph.D. Thesis

By

Akash K



**DISCIPLINE OF MECHANICAL ENGINEERING  
INDIAN INSTITUTE OF TECHNOLOGY  
INDORE  
JULY, 2018**

# Investigations on Design and Development of Copper Based Shape Memory Alloy Bimorph and Their Application towards Micro- Robotics and Energy Systems

**A THESIS**

*Submitted in partial fulfillment of the  
requirements for the award of the degree  
of*  
**DOCTOR OF PHILOSOPHY**

*by*

**AKASH K**



**DISCIPLINE OF MECHANICAL ENGINEERING  
INDIAN INSTITUTE OF TECHNOLOGY  
INDORE  
JULY, 2018**



# INDIAN INSTITUTE OF TECHNOLOGY INDORE

## CANDIDATE'S DECLARATION

I hereby certify that the work which is being presented in the thesis entitled **INVESTIGATIONS ON DESIGN AND DEVELOPMENT OF COPPER BASED SHAPE MEMORY ALLOY BIMORPH AND THEIR APPLICATION TOWARDS MICRO-ROBOTICS AND ENERGY SYSTEMS** in the partial fulfillment of the requirements for the award of the degree of **DOCTOR OF PHILOSOPHY** and submitted in the **DISCIPLINE OF MECHANICAL ENGINEERING, INDIAN INSTITUTE OF TECHNOLOGY INDORE**, is an authentic record of my own work carried out during the time period from January, 2014 to March, 2018 under the supervision of **Dr.I.A.Palani**, Associate Professor, Department of Mechanical Engineering, Indian Institute of Technology Indore.

The matter presented in this thesis has not been submitted by me for the award of any other degree of this or any other institute.

**Signature of the student with date  
(Akash K)**

-----  
This is to certify that the above statement made by the candidate is correct to the best of my/our knowledge.

Signature of Thesis Supervisor #1 with date

**Dr. I. A. Palani**

-----  
**Akash K** has successfully given his/her Ph.D. Oral Examination held on \_\_\_\_\_.

Signature of Chairperson (OEB)    Signature of External Examiner    Signature(s) of Thesis Supervisor(s)

Date:

Date:

Date:

Signature of PSPC Member #1  
DPGC

Signature of PSPC Member #2

Signature of Convener,

Date:

Date:

Date:

Signature of Head of Discipline

Date:

-----  
-----

## ACKNOWLEDGEMENTS

First, I would like to acknowledge and express my sincere gratitude to my research guide **Dr. I. A. Palani**, for providing me the opportunity to work under his supervision at IIT Indore. His research methodology towards developing practical applications was inspiring. His multitasking and man management skills are something I would like to learn and carry on in the future. I learnt a lot of new things, both in career as well as life, during the time I spent with him. He has been a mentor who was true to his position.

I would like to thank to **Prof. P. Mathur**, Director, IIT Indore, **Dr. D. Deshmukh** Head of the Department, Mechanical Engineering for supporting me with sophisticated facilities to conduct my research. I wish to thank the doctoral committee members **Dr. Vipul Singh** and, **Dr. Bupesh Lad**, for their valuable suggestions right from the beginning of the research work. I thank **Dr. Shailesh Kundalwal**, DPGC Convener and **Dr. Jayaprakash Murugasen**, OEB Chairman their sincere support.

I also express my sincere thanks to Sophisticated Instrumentation Centre (SIC), **Dr. Kinny Panday** and **Mr. Nitin Upadhyay** at IIT Indore for providing me the necessary characterization facility. I would like to thank **Dr. Anbarasu** for supporting me with characterization facility and timely discussions. I would also like to thank the Central work shop, IIT Indore for supporting me. I would like to thank **Prof. N. J. Vasa** for allowing me utilize the facilities from his lab at IIT Madras. My Sincere thanks are also due to **Simon Pauly** for providing his valuable comments. I also express my deep gratitude to **Dr. S. Kanmani Subbu** of Mechanical Engineering, NIT Warangal for his timely support.

I would like to thank my colleagues, **Shiva Sekar**, **Tameshwar Nath Tiwari**, **Ashish Shukla**, **Rajagopalan**, **Mani Prabhu**, **Nandini Patra**, **Manikanadan**, **Jayachandran**,

**Narayane Dhiraj, Sachin Bhirodkar, Anand Kumar, Vijay Choyal, Murali, Rohit Gagrani, Reena Disawal, Shivaani, Akash Jain, Hari Vasanth, Mithun, Deepesh, Brolin, Sai Pranesh, Anirudh, and Agnel** for their support in the past four years. I came alone to Indore, but now I have a family. I would like to thank **Anubha Bilgayan, Kshitij Bhargav, Mayoorika Shukla** from MNRG lab for their valuable support. They carried my research problems as their own and I am grateful for that. I would like to thank my colleagues at PCM lab, **Shivendre Panday and Krishna Dayal Shukla** for their characterization and analytical support.

I would like to convey my special thanks to **Srikanth Aditya, Moghul Mansoor, Farhan Ahmed, and Suresh Kumar**, for making my abroad trips memorable. I would like to thank my friends **Mohammed Waseem, Praveen Kumar, Dilip Ramani, Vinod, Balaji, V S Balaji, Anuj, Narendran and Rishi**, for their encouragement and moral support.

I would like to thank **Mayank Modak, Mukta Parihar, Rakesh Sharma, Harish Kotapally, and Gautamaraju** for making my stay at IIT Indore fruitful and memorable experience.

.I would like to thank **my parents** for their support to achieve this. Their unbelievable hope and trust on me made me the person who I am today. They thought me to work hard and take life positively in every instance. I would like to thank my sister and in-laws for their timely support.

I would like to thank my wife **Surya** for helping and encouraging me in every stage of my research work. She has changed her role from being a friend to a professional during these four years. With her beside me I could achieve any heights with ease.

*Dedicated to My Family and  
Friends*

# Abstract

The research work focuses on developing CuAlNi shape memory alloys thin films on pre-strained Kapton polyimide substrates through physical vapour deposition. Flexible substrate such as polyimide, is suitable for achieving two-way shape memory effect without any post processing and training. Investigations on the influence of substrate thickness and deposition temperature of polyimide were probed in detail. A substrate thickness of 75  $\mu\text{m}$  was found to be suitable for potential applications, exhibiting large recovery ratio and stable life for 500 cycles. Growth substrate temperature of 150  $^{\circ}\text{C}$  and 100  $^{\circ}\text{C}$  was appropriate for developing the bimorphs, as martensitic textures were large in number with low anisotropic ratio. Further, the samples developed at 150  $^{\circ}\text{C}$  displayed larger displacement than rest of the bimorphs. A custom-made thermomechanical setup using Joule heating was utilized to analyse the thermomechanical and life cycle behaviour of the developed bimorphs. Various actuation properties such as voltage, frequency and load were varied to realize the bimorph for potential applications. Further, enhancement of life cycle from 14,000 cycles to 25,000 cycles was observed when manganese was added as the quaternary element. Improvement in ductility with suppression of precipitates, displayed excellent shape memory properties by displacing up to 8 mm with 1 V. However, Mn addition led to loss in load bearing capacity, as the bimorphs failed to actuate beyond 60 mg loads. Further investigations with improving the force generated beyond 1.5 mN at varying frequencies were performed. The experimental results were compared with theoretical simulation on the structural and thermal behaviour of the bimorphs using COMSOL Multiphysics software. The developed bimorphs were implemented in MEMS applications such as micro-flapper for aerial robots at frequencies beyond 5 Hz. The utilization of bimorph as temperature sensor in transformer oils was

probed, and a sensitivity of  $0.2\text{ }^{\circ}\text{C}/\text{min}$  was observed. Further, a bimorph belt was developed using customized flash evaporation system for developing SMA Johnson's heat engine for energy harvesting applications.

# List of Publications

## Journal Publications

- ❖ **K. Akash**, S.S.M. Prabu, T. Gustmann, S. Jayachandran, S. Pauly, I.A. Palani, “**Enhancing the life cycle behaviour of Cu-Al-Ni shape memory alloy bimorph by Mn addition**”, *Mater. Lett.* 226 (2018) 55–58. doi:10.1016/j.matlet.2018.05.008 (I.F – 2.6)
- ❖ **Akash K**, Akash K Jain, Gaurav Karmarkar, Aniket Jadhav, Palani I A. “**Investigations on Actuation Characteristics and Life Cycle behaviour of Shape Memory Alloy/Polyimide Composite Bimorph towards Developing Micro Aerial Robots**” Accepted - <https://doi.org/10.1016/j.matdes.2018.02.013> *Materials & Design* 2018 – (I.F – 4.5).
- ❖ **K. Akash**, A. K. Shukla, S. S. Mani Prabu, D. C. Narayane, S. Kanmanisubbu, and I. A. Palani, “**Parametric investigations to enhance the thermomechanical properties of CuAlNi shape memory alloy Bi-morph,**” *J. Alloys Compd.*, vol. 720, pp. 264–271, Oct. 2017 - <https://doi.org/10.1016/j.sna.2016.12.008> (I.F – 3.7)
- ❖ **K, Akash**, Mani Prabu SS, Ashish K. Shukla, Tameshwer Nath, Karthick S, and I.A. Palani. “**Investigations on the Life Cycle Behavior of Cu-Al-Ni/polyimide Shape Memory Alloy Bi-Morph at Varying Substrate Thickness and Actuation Conditions.**” *Sensors and Actuators A: Physical* 254. Elsevier B.V.: 28–35., 2017. doi:10.1016/j.sna.2016.12.008. (I.F – 2.3)
- ❖ **K. Akash**, Rajat Chourasia, S. Karthick, Dheeraj Kumar Meena, and Palani I A. 2016. “**Investigations on the Influence of Substrate Temperature in Synthesizing CuZnAl Alloy Thin Films Using Spray Pyrolysis.**” *Advanced Science, Engineering and Medicine* 8 (1): 1–8, 2016. doi:10.1007/s13398-014-0173-7.2. (I.F – 1)
- ❖ **Akash K**, Shivaani A S, Narayane Dhiraj Chindhuji1, Mani Prabu SS, Palani I A. “**Control of Shape Memory Alloy/Polyimide bimorph for MEMS Applications**” (Under review – *Thin Solid Films*)

## Patents

- ❖ Design and Development of Universal Testing Machine for flexible Thin Films (*Indian Patent Filed 2017 - 201721035555*)
- ❖ Design and Development of self-energized solar tracking system using textured shape memory bimorph substrate based thin film solar panel (*Indian Patent Application No: 201721026063*)

### **Journal – Published (Other than Thesis)**

- ❖ Nandini P, **Akash K**, Rohit G, Vipul S, Palani IA. "Investigations on the Influence of Liquid-Assisted Laser Ablation of NiTi Rotating Target to Improve the Formation Efficiency of Spherical Alloyed NiTi Nanoparticles". *J Mater Eng Perform* 2017;1–11. doi:10.1007/s11665-017-2886-1. (I.F - 1.09)
- ❖ Patra N, **Akash K**, Shiva S, Gagrani R, Rao HSP, Anirudh VR, et al. Parametric investigations on the influence of nano-second Nd<sup>3+</sup>:YAG laser wavelength and fluence in synthesizing NiTi nano-particles using liquid assisted laser ablation technique. *Appl Surf Sci* 2016;366:104–11. doi:10.1016/j.apsusc.2016.01.072. (I.F - 3.38)
- ❖ Mani Prabu SS, Madhu HC, Perugu CS, **Akash K**, Ajay Kumar P, Kailas S V., et al. Microstructure, mechanical properties and shape memory behaviour of friction stir welded nitinol. *Mater Sci Eng A* 2017;693:233–6. doi:10.1016/j.msea.2017.03.101. (I.F - 3.09)
- ❖ Shukla AK, **Akash K**, Palani IA, Manivannan A. Materials Science & Engineering B Laser assisted wet texturing of flexible polyethylene terephthalate substrate using Nd<sup>3+</sup>: YAG laser for photovoltaics devices. *Mater Sci Eng B Solid-State Mater Adv Technol* 2017;226:78–85. doi:10.1016/j.mseb.2017.08.028. (I.F - 2.55)
- ❖ Ashish K S, Vinayak M Y, **Akash K**, Palani IA, Manivannan A. Investigations on Effect of Laser Induced Self-assembled Patterning on Optical Properties of Flexible Polyimide Substrates for Solar Cell Applications *J Phys D Appl Phys* 2017:0–20. (I.F - 2.58)
- ❖ Nath T, **Akash K**, Chouhan P, Lad BK, Palani IA. Investigation on thermo-mechanical behavior of SMA spring under the influence of different actuation medium. *Microsyst Technol* 2018. doi:10.1007/s00542-017-3695-z. (I.F - 1.19)

### **Conference Papers**

- ❖ **Akash.K**, Rajat Chourasia, Dheeraj Kumar Meena, and Palani.I.A. “Development of Cu-Zn-Al Shape Memory Alloy and Investigation on Pulsed Laser Annealing to Induce Shape Memory Properties”. *International Symposium for Research Scholars 2014*.
- ❖ **Akash K**, Mani Prabu S S, S Karthick, and I A Palani. “Investigations on the Influence of Growth Substrate Temperature on the Development of CuZnAl / Polyimide Composite.” *6<sup>th</sup> International & 27<sup>th</sup> ‘All India Manufacturing Technology, Design and Research’ Conference (AIMTDR-2016), 1590–93, 2016*.
- ❖ **Akash.K**, Chandan.K, Parikshit.G, Reena Disawal, Palani.I.A. “Transformer Oil Temperature Measurement by CuAlNi/Polyimide Shape Memory Alloy Composite film”. *Advances in Smart and Functional Materials, Bhopal Chapter 2017*.

- ❖ **Akash.K**, Chandan.K, Parikshit.G, Narayane Dhiraj.C, Reena Disawal, Lad.B.K, Vipul Singh, Palani.I.A: “Investigations on Transformer Oil Temperature Sensing using CuAlNi/Polyimide Shape Memory Alloy composite film”. *SPIE –Smart Structures NDE 2017*
- ❖ **Akash K**, Shivaani AS, Dhiraj Narayane, Manoraj R, Patturaj, I.A.Palani “Investigations on control of CuAlNi/polyimide Bi-morphs by using PID controller”. *10th International Conference on Precision, Micro, Miso and Nano Engineering 2017.*

# TABLE OF CONTENTS

	<b>Page no.</b>
<b>LIST OF FIGURES</b>	<b>XVIII</b>
<b>LIST OF TABLES</b>	<b>XXV</b>
<b>NOMENCLATURE</b>	<b>XXVI</b>
<b>ABBREVIATIONS</b>	<b>XXVII</b>

## **CHAPTER 1** **Introduction**

1.1	Introduction to Shape Memory Alloy	1
1.2	Shape Memory effect	1
1.3	Pseudoelastic Behaviour	4
1.4	Two-way Shape memory Effect with Training	5
1.5	Thin Film Shape Memory Alloys	6
1.6	Shape Memory Alloy Composites	7
1.7	Copper Based Shape Memory Alloys	9
1.8	Motivation for the Study	9
1.9	Research Objectives	10
1.10	Outline of the Thesis	10

## **CHAPTER 2**

### **Literature Review on Copper Based Shape Memory Alloys**

2.1	Martensitic Transformation in SMA	13
2.2	Shape Memory Effect in Copper Based Shape Memory Alloys	14
2.2.1	CuZnAl SMA	15
2.2.2	CuAlNi SMA	15
2.2.3	Effect of Composition on the Cu-based SMA	16
2.3	Theory of SME in Cu-based Alloys	18

2.4	Cu- based Quaternary SMAs	21
2.4.1	Influence of Quaternary Element	21
2.5	Influence of Thin Film Deposition Parameters on Developing Cu-based SMA	21
2.5.1	Influence of Substrate Thickness	22
2.5.2	Influence of Substrate Temperature	23
2.6	Thermomechanical Behaviour of Cu-based Alloys	24
2.7	Status of Thin Film Shape Memory Materials	26
2.8	Preliminary Experiments with CuZnAl SMA	26
2.8.1	Chemical Deposition of CuZnAl	27
2.8.2	Outcomes of Chemical Deposition Techniques	34
2.8.3	Physical Vapour Deposition of CuZnAl	35
2.8.4	Outcomes of Physical Vapour Deposition of CuZnAl SMA	38
2.9	Approach for Developing CuAlNi Thin Films	38
2.10	Summary	40

## **CHAPTER 3**

### **Experimental Specifications and Theory of SMA Bimorphs**

3.1	Thermal Physical Vapour Deposition System	41
3.1.1	Deposition Parameters and Pellet Preparation	42
3.2	Theory of SMA Bimorph	43
3.3	Characterization Utilized for the Analysis	45
3.4	Thermomechanical Analysis Setup	47
3.4.1	Joule Heating Setup	47
3.4.2	Substrate Heating Setup	47
3.5	Micro Universal Testing Machine	49
3.6	Summary	52

## **CHAPTER 4**

### **Parametric Investigation on Development of SMA Bimorph**

4.1	Introduction	53
4.2	Influence of Different Substrates	53
4.3	Influence of Substrate Thickness	57
4.3.1	Surface Morphological Analysis	57
4.3.2	Adhesion and Roughness Analysis	59
4.3.3	Structural Analysis	61
4.3.4	Thermal Analysis	62
4.3.5	Shape Recovery Ratio Analysis	65
4.3.6	Thermomechanical and Life Cycle Analysis	68
4.4	Influence of Substrate Temperature	72
4.4.1	Surface Morphological Analysis	73
4.4.2	Adhesion and Compositional Analysis	75
4.4.3	Structural Analysis	76
4.4.4	Thermal Analysis	77
4.4.5	Shape Recovery Ratio	81
4.4.6	Life Cycle Analysis	82
4.5	Summary	85

## **CHAPTER 5**

### **Theoretical Simulations on Structural and Thermal Behaviour of SMA Composite**

5.1	Introduction	87
5.2	Structural Analysis	88
5.2.1	Case of the transverse loading	88

5.2.2	The equation for the elastic curve	89
5.2.3	Equation related to Solutions	89
5.2.4	Von Mises Stress	89
5.3	Joule Heating Equations	91
5.4	Material Properties and Global Definition	92
5.5	Boundary Conditions	93
5.6	Meshing Properties	95
5.7	Effect of Von Mises Stress	96
5.8	Effect of Emissivity	97
5.8.1	Temperature profile at Varying Emissivity	98
5.8.2	Temperature Profile at varying current	99
5.8.3	Temperature Profile at various spots during Actuation	101
5.9	Summary	101

## **CHAPTER 6**

### **Investigations on Inclusion of Mn in CuAlNi SMA Bimorph**

6.1	Introduction	103
6.2	Surface Morphological Analysis	104
6.3	Thickness, Composition and Roughness	105
6.4	Structural Analysis	107
6.5	Thermal Analysis	107
6.6	Thermomechanical Analysis	111
6.6.1	Maximum Displacement Analysis	111
6.6.2	Frequency Actuation with 30 mg Load	114
6.6.3	Frequency Actuation with 45 mg Load	116

6.6.4	Frequency Actuation with 60 mg Load	116
6.7	Life Cycle Analysis	119
6.8	Discussion	120
6.9	Summary	122

## **CHAPTER 7**

### **Suitability of CuAlNiMn Bimorph towards Micro-Robotic and Energy systems**

7.1	Introduction	125
7.2	Microflapper with Bimorphs	125
7.2.1	Force Generated by Bimorphs during Actuation	127
7.2.2	Controller System Design	129
7.2.3	Controller Selection	130
7.2.4	PID Tuning	130
7.2.5	PID Controller	131
7.2.6	Design of the Control System	131
7.2.7	Ziegler Nichol's PID Controller	132
7.2.8	Experimental Setup	133
7.2.9	Results and Discussion	133
7.3	Micro Circuit Breaker	134
7.3.1	Oil test Rig	135
7.3.2	Displacement Measurement	135
7.3.3	Contamination Tests	137
7.4	Shape memory alloy Belt for Energy Harvesting	139
7.4.1	Bonding of Polyimide	140
7.4.2	Metallic Belt Deposition System	141

7.4.3	Proposed Methodology	142
7.5	Summary	143

## **CHAPTER 8**

### **Conclusion and Future Work**

8.1	Conclusions	145
8.2	Scope and Future Work	147
	References	149

# List of Figures

Figure No.	Title	Page No.
Figure 1.1	(a) Pictorial representation of shape memory effect with phase transformation (b) application in clamp (c) & (d) shows the shape change during actuation [1].	1
Figure 1.2	Block diagram of phase transformation with the various transformation stages	2
Figure 1.3	Stress-strain-temperature data exhibiting the shape memory effect for a typical NiTi SMA [3]	3
Figure 1.4	Stress-strain behaviour of (a) shape memory effect (b) superelasticity	4
Figure 1.5	Training process utilized in SMA NiTi wires	5
Figure 1.6	Various alloys that exhibit shape memory effect	6
Figure 1.7	(a) Polymer matrix reinforced with smart SMA (b) Bio inspired turtle robot embedded with SMA composite as actuators.	7
Figure 1.8	(a) Dragon fly with NiTi bimorph as wings (b) NiTi bimorph with copper contacts for micro flappers	8
Figure 1.9	Major Research Objectives	10
Figure 2.1	Phase diagram of CuAlNi shape memory alloy. Vertical cross-section with 3 mass% Ni	16
Figure 2.2	Phase diagram of CuZnAl Shape memory alloy. Vertical cross section with 6 mass % Al	17
Figure 2.3	DO <sub>3</sub> unit cell showing the arrangement of atoms	19
Figure 2.4	Long period stacking of 2H and 18R martensite	20
Figure 2.5	Relation between M, temperature and alloy composition in CuZnAl SMAs.	20
Figure 2.6	Spray Pyrolysis block diagram	21
Figure 2.7	Surface morphological analysis through SEM at different temperatures (a) 250 °C (b) 300 °C (c) 350 °C (d) 400 °C (e) 450 °C	30
Figure 2.8	XRD plots at different substrate temperatures (a) 250 °C (b) 300 °C (c) 350 °C (d) 400 °C (e) 450 °C	32

Figure 2.9	DSC thermogram of sample deposited at 350 °C	34
Figure 2.10	SEM analysis: (a) & (b) SEM and EDS of sample deposited without substrate heating (c) & (d) EDS of samples developed at 100 °C	35
Figure 2.11	XRD plots showing the results of samples developed at different substrate temperatures.	37
Figure 2.12	Approach and design of experiments for developing CuAlNi bimorphs	39
Figure 2.13	Flow chart displaying the various characterization techniques and various thermomechanical parameters used for analysis.	40
Figure 3.1	Images showing (a) deposition unit (b) chamber with the crucible and substrate holder (c) block diagram of the thermal evaporation system	42
Figure 3.2	Pictures of (a) CuAlNi targets of various composition (b) Plasma etching used for cleaning the substrates	43
Figure 3.3	Graph showing the different transformation temperatures, phase change and shape memory effect exhibited by sample developed at 150 °C without any post-processing	44
Figure 3.4	Images showing (a) bare polyimide substrate (b) pre-straining (c) bimorph after deposition and (d) bimorph on actuation	45
Figure 3.5	Characterization techniques used for analysing the bimorphs	46
Figure 3.6	Initial setup with silver paste and copper contacts.	47
Figure 3.7	Images showing the pictures of (a) the bimorph cut into small samples for electrical actuation (b) block diagram of the electrical actuation setup	48
Figure 3.8	(a) Bimorph heated with plate heater (b) the measurement used for recovery ratio analysis	48
Figure 3.9	Image shows the clamping design utilized for uniform tension	49
Figure 3.10	(a) Block diagram of the micro tensile testing equipment (b) Image of the clamp utilised for the testing process.	50
Figure 3.11	Illustrates the flow chart for the testing process using the UTM	51
Figure 4.1	Images of the SMA film deposited on (a) Glass (b) Silicon and (c) Polyimide substrates.	53

Figure 4.2	SEM images showing the surface morphology of (b) Glass (b) Silicon and (c) Polyimide substrates. Inset shows the picture of the substrate after deposition.	54
Figure 4.3	Plots showing the (a) XRD pattern obtained with three different substrates before annealing (b) XRD after annealing at 400 °C for 1 hr.	55
Figure 4.4	DSC analysis showing the phase transformation temperatures of a) silicon substrate (b) polyimide substrate a) silicon substrate (b) polyimide substrate	56
Figure 4.5	Images showing SMA film deposited on polyimide of varying substrate thickness	57
Figure 4.6	Images showing the (a) morphology of SMA film deposited on 25 μm polyimide (b) morphology of SMA film deposited on 25 μm polyimide (c) morphology of SMA film deposited on 25 μm polyimide (d) EDS analysis showing the composition of samples deposition on polyimide of varying thickness	58
Figure 4.7	Figure 4.7: Images showing the scotch tape analysis performed on varying polyimide thickness (i) sample before testing (ii) scotch tape after testing (iii) sample after testing	59
Figure 4.8	Roughness profile of SMA bimorph with varying polyimide thickness	60
Figure 4.9	XRD pattern of SMA bimorph with varying polyimide thickness (a) 50 μm (b) 75 μm	62
Figure 4.10	Thermogravimetric analysis showing the decomposition of different polyimide samples	63
Figure 4.11	Temperature vs Resistance plot showing the transformation temperatures of SMA bimorph of varying thickness	64
Figure 4.12	Images showing the actuation of the bimorph at different temperature obtained through plate heating	65
Figure 4.13	(a) shows the recovery ratio of both the bimorph, (b) cycling heating and cooling to find the maximum displacement of the bimorph	66
Figure 4.14	(a) hysteresis curve showing the time lag which was high at initial stages, (b) Hysteresis plot after attaining maximum displacement	67
Figure 4.15	(a) Time vs displacement plot at varying voltages (b) Variation in displacement of all the three bimorphs at varying voltage	68

Figure 4.16	(a) Maximum displacement obtained through electrical actuation for 50 $\mu\text{m}$ bimorph, (b) Maximum displacement obtained through electrical actuation for 75 $\mu\text{m}$ bimorph	70
Figure 4.17	(a) Life cycle analysis of 50 $\mu\text{m}$ bimorph, (b) Life cycle analysis of 75 $\mu\text{m}$ bimorph	71
Figure 4.18	Scanning Electron Microscope images showing the morphology of the developed films (a) Without substrate heating (b) at 100°C (b) at 150 °C (c) 200°C	74
Figure 4.19	X-ray diffractogram showing the different phases observed from the film.	77
Figure 4.20	Resistance vs temperature plots of samples developed at (a) without growth substrate temperature (b) @ 100 °C (c) @ 150 °C and (d) 200 °C.	78
Figure 4.21	Differential Scanning Calorimetry graphs showing the phase transition of the composite films. (a) Endothermic plot, (b) Exothermic plot	80
Figure 4.22	Recovery ratio calculation during heating	82
Figure 4.23	Life Cycle Analysis graphs showing the change in displacement for 500 cycles. (a) Joule heating with 2 V (b) Joule heating with 2.5 V (c) Joule heating with 3 V	83
Figure 5.1	Single beam cantilever	88
Figure 5.2	Flow chart of the structural analysis	90
Figure 5.3	Flow chart of the thermal analysis	91
Figure 5.4	Global definition and part modelling of bimorph	92
Figure 5.5	Boundary conditions and the constraints implemented in bimorph simulation	93
Figure 5.6	Tetragonal meshing used in simulation	95
Figure 5.7	(a) Von misses stress variation across length as the load is increased (b) Variation in displacement with reversed arc length under varying loads at the tip of the bimorph.	96
Figure 5.8	(a) Single beam cantilever model of bimorph for thermal analysis (b) copper contact for Joule heating (c) Tetragonal meshing of bimorph and (d) heat transfer profile during Joule heating.	98
Figure 5.9	Results displaying the temperature vs Emissivity at varying current	99
Figure 5.10	Results displaying the temperature vs current at varying emissivity	99

Figure 5.11	(a) Temperature profile obtained by Joule heating and the various set points taken (b) Temperature vs emissivity at varying set points	100
Figure 6.1	Images showing the (a) SEM image of CuAlNi at 25 KX and 1 KX and (b) CuAlNiMn bimorph at 25 KX and 1 KX	104
Figure 6.2	Results of (a) Thickness measurement, (b) Composition analysis from EDS (c) Roughness profile after scratching (d) Roughness plot of CuAlNiMn	106
Figure 6.3	X-ray diffraction displaying the martensitic phase present in CuAlNiMn bimorph	107
Figure 6.4	Images showing the results of transformation temperature of the samples as measured from DSC	108
Figure 6.5	Graphical plot displaying the results of TGA analysis	109
Figure 6.6	Images showing the (a) Thermal image of CuAlNiMn bimorph during actuation and various set points (b) variation in temperature with change in emissivity	110
Figure 6.7	Results of thermal images showing the temperature vs time plots at various set points of (a) CuAlNi bimorph (b) CuAlNi	111
Figure 6.8	Images showing the results of Maximum Displacement of (a) CuAlNiMn/polyimide at 1 V and three different loads (b) CuAlNiMn/polyimide at 1.5 V and three different loads (c) CuAlNiMn/polyimide at 2 V and three different loads.	113
Figure 6.9	Electrical actuation results with 30 mg load at different voltages of 1 V, 1.5 V and 2 V (a) CuAlNi/Polyimide at 0.5 Hz (b) CuAlNiMn/polyimide at 0.5 Hz (c) CuAlNi/Polyimide at 0.33 Hz (d) CuAlNiMn/polyimide at 0.33 Hz (e) CuAlNi/Polyimide at 0.25 Hz (f) CuAlNiMn/polyimide at 0.25 Hz	115
Figure 6.10	Electrical actuation results with 45 mg load at different voltages of 1 V, 1.5 V and 2 V (a) CuAlNi/Polyimide at 0.5 Hz (b) CuAlNiMn/polyimide at 0.5 Hz (c) CuAlNi/Polyimide at 0.33 Hz (d) CuAlNiMn/polyimide at 0.33 Hz (e) CuAlNi/Polyimide at 0.25 Hz (f) CuAlNiMn/polyimide at 0.25 Hz	117
Figure 6.11	Electrical actuation results with 60 mg load at different voltages of 1 V, 1.5 V and 2 V (a) CuAlNi/Polyimide at 0.5 Hz (b) CuAlNiMn/polyimide at 0.5 Hz (c) CuAlNi/Polyimide at 0.33 Hz (d) CuAlNiMn/polyimide at 0.33 Hz (e) CuAlNi/Polyimide at 0.25 Hz (f) CuAlNiMn/polyimide at 0.25 Hz	118

Figure 6.12	Life cycle behaviour of the developed samples tested with eight samples, exhibiting life more than 20, 000 cycles	119
Figure 7.1	Figure 7.1: (a) Picture of the analysis setup with flapper (b) CAD model of the proposed microflapper setup with bimorph (c) Result showing the displacement at high frequency	126
Figure 7.2	(a) Force vs Displacement plot (b) Battery operated flapper setup	129
Figure 7.3	Block diagram of process control	129
Figure 7.4	Block diagram of types of controller	130
Figure 7.5	Block diagram of the control system	131
Figure 7.6	Block diagram of the feedback control system	132
Figure 7.7	Screenshot of the LabVIEW program used for control	133
Figure 7.8	Plots showing the (a) Control achieved with $K_p - 5.88$ , $T_i - 2$ and $T_d - 0.5$ (b) Error plot showing minimum fluctuation during control	134
Figure 7.9	(a) Setup with bimorph for transformer oil temperature sensing (b) Setup with NiTi Spring	135
Figure 7.10	Results indicating the (a) temperature profile of CuAlNi bimorph (b) the displacement of CuAlNi bimorph	136
Figure 7.11	Pictures showing the contamination test results with water and acid	138
Figure 7.12	Drivers of Industrial waste heat sources	139
Figure 7.13	First Shape memory alloy heat engine developed by Bank's (a) actual photograph (b) top view of the engine with SMA wires.	140
Figure 7.14	Pictures showing the (a) Pressure bonding setup (b) Polyimide in 3d printed pulley setup	141
Figure 7.15	Pictures showing the (a) Metallic Deposition Unit (b) Pulley arrangement for belt deposition	141
Figure 7.16	Images of (a) developed belt with $75 \mu\text{m}$ thickness and (b) SEM image of the bimorph belt.	142

Figure 7.17	Developed belt with aluminium pulleys for exhaust gas test (b) Proposed block diagram of hybrid energy harvesting system with NiTi springs and CuAlNi bimorphs	142
Figure 8.1	Samples developed with selective laser melting on Kapton polyimide sheets.	147
Figure 8.2	Schematic layout of hybrid SMA/solar tracker self-energized device	147
Figure 8.3	Schematic layout of the interferometry technique proposed for measuring micron deflections	148

# List of Tables

<b>Table No.</b>	<b>Title</b>	<b>Page No.</b>
Table 1.1	Various actuation principles	7
Table 2.1	Experimental parameters used for Spray Pyrolysis	27
Table 2.2	Details the of the chemicals used	28
Table 2.3	EDS analysis showing the composition of the developed film at different substrate temperature	30
Table 2.4	Adhesion test results after Scotch tape analysis	35
Table 2.5	Composition analysis from EDS of CuZnAl	35
Table 3.1	Parameters used for the deposition process	43
Table 4.1	Results of Scotch Tape analysis	59
Table 4.2	The results of Roughness analysis	61
Table 4.3	EDS analysis displaying the composition of the developed samples	75
Table 4.4	Scotch tape analysis showing the adhesion results	76
Table 4.5	Transformation temperatures from DSC and Van der Pauw method	79
Table 5.1	Material properties of CuAlNi and polyimide	92
Table 5.2	Meshing properties and the elements present after meshing	95
Table 6.1	Results of the scotch tape analysis	106
Table 6.2	Maximum displacement results at different loads and different voltages	112
Table 6.3	Results of the life cycle analysis of CuAlNi and CuAlNiMn bimorphs	120
Table 7.1	Parameters of PID Controller	132
Table 7.2	Preliminary sensor properties	136
Table 7.3	Contamination test results	137

# Nomenclature

Symbol	Unit	Description
$\xi$		Martensitic fraction
$\beta$		Twinned Martensite
$\beta_1$		DO <sub>3</sub> ordered phase
$\gamma$		Martensitic structure
T	°C/K	Temperature
k/k <sub>m</sub>	W/m K	Thermal Conductivity
$\rho$	Kg/m <sup>3</sup>	Density
k <sub>o</sub>	W/m K	Thermal conductivity of the material
C <sub>p</sub>	J /kg K	Specific heat capacity of the material
$\sigma$		Stefan-Boltzmann constant
$\varepsilon$		Emissivity
k <sub>n</sub>	W/m K	Thermal conductivity normal to the surface
$\tau$		stress tensor
D <sub>temp</sub>	°C/K	Curvature at particular temperature
D <sub>R</sub>	°C/K	Curvature at room temperature
D <sub>RT</sub>		Recovery ratio
d <sub>s</sub>	cm	Horizontal length of curvature
d <sub>l</sub>	cm	Vertical length of curvature
d	nm	Grain size
$\lambda$	nm	wavelength
Q	J/m <sup>3</sup>	Heat source
<b>u</b>		Translational velocity
$\Delta u$		Temperature at given location
J	A/m <sup>2</sup>	Current density
$\kappa$	Ω/m <sup>2</sup>	Electrical conductivity
E'	Gpa	Elastic modulus

# Acronyms

S.No	Acronym	Expansion
1.	SMA	Shape Memory Alloys
2.	PI	Polyimide
3.	SME	Shape Memory Effect
4.	TWSME	Two Way Shape Memory Effect
5.	PE	Pseudo Elasticity
6.	$M_s$	Martensitic start
7.	$M_f$	Martensitic finish
8.	$A_s$	Austenite Start
9.	$A_f$	Austenite Finish
10.	$T_A$	Austenite transformation temperature
11.	$T_M$	Martensitic transformation temperature
12.	MEMS	Micro Electro Mechanical Systems
13.	$M_d$	Martensitic Deformation
14.	PVD	Physical vapor deposition
15.	SMA_rho	Density
16.	SMA_Cp	Heat capacity at constant pressure
17.	SMA_K	Thermal Conductivity
18.	SMA_sigma	Electrical Conductivity
19.	SMA_epsilonr	Relative Permittivity
20.	SMA_res	Resistivity
21.	SMA_E	Young's Modulus
22.	SMA_alpha	Coefficient of thermal expansion
23.	SMA_sigmae	Endurance limit
24.	P_nu	Poisson's Ratio of polyimide
25.	SMA_emissivity	Emissivity
26.	I	Initial Current

27.	V	Initial voltage
28.	E	Young's Modulus of Elasticity for the given sheet
29.	I	Second moment of Inertia
30.	d	Displacement of the free edge
31.	t	Thickness of the substrate
32.	b	Width of the cantilever
33.	L	Length of the cantilever
34.	PID	Proportional, integral and derivative

# Chapter 1

## Introduction

### 1.1 Introduction to Shape Memory Alloy

Shape memory alloys are a group of smart materials that exhibit exceptional mechanical and thermal responses. Shape Memory Alloys (SMA) can recover previously applied strains on the application of heat, as shown in Fig. 1(a). The alloys can recover their original geometry from the deformed shape, which has led to the development of substantial applications [1], such as clamping as shown in Fig. 1(b), 1(c) and 1(d). Diffusionless phase transformation that occurs between the austenite phase and the martensite phase is primarily responsible for functional properties of the SMA, such as shape memory effect (SME), pseudoelasticity or superelasticity and the two-way shape memory effect (TWSME) [2,3]. The SME can be used to produce motion or force, while super elasticity supports energy storage and both properties have found many applications in different fields of engineering and science [4].

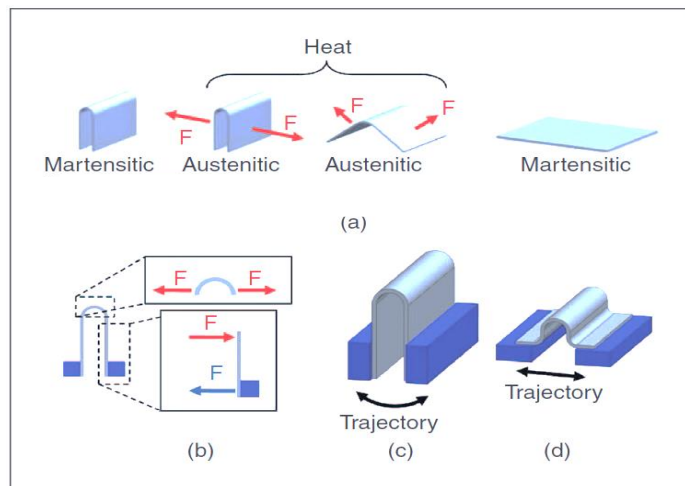


**Figure 1.1: (a) Pictorial representation of shape memory effect with phase transformation (b) application in clamp (c) & (d) shows the shape change during actuation [1].**

### 1.2 Shape memory effect

The two phases of SMA are: a high-temperature phase called austenite (A), and the other is a low-temperature phase called martensite (M). Each phase has a different crystal structure and hence, exhibits different properties. Primarily, austenite has

cubic crystal structures whereas martensite has tetragonal, orthorhombic or monoclinic structures. The transformation from austenite to martensite occurs due to lattice distortion rather than by diffusion of atoms. This phenomenon of crystalline phase change is termed as martensitic transformation or diffusionless transformation. Each crystal formed due to martensitic transformation have different orientation direction, called a variant. The martensitic variants occur in two forms: twinned martensite ( $M_t$ ), that occurs at a temperature below the transformation temperature and is developed by a combination of “self-accommodated” martensitic variants, and another form is the detwinned or reoriented martensite that has a specific dominant variant ( $M_d$ ). When the alloys are heated above the transformation temperature the original shape of the material is restored and converts the material to its high strength, austenitic, condition. The forward transformation from austenite (parent phase) to martensite (product phase) and vice versa forms have fascinated researchers to study these unique behaviour of SMA [5–7].

In the absence of an applied load, forward transformation occurs upon cooling and formation of several martensitic variants form, as the crystal structure changes from austenite to martensite. The assembly of variants ensues such that the formed twinned martensitic phase has negligible average macroscopic shape change. The reverse transformation occurs during heating as the phase changes from low-temperature martensite to high-temperature austenite [8,9].

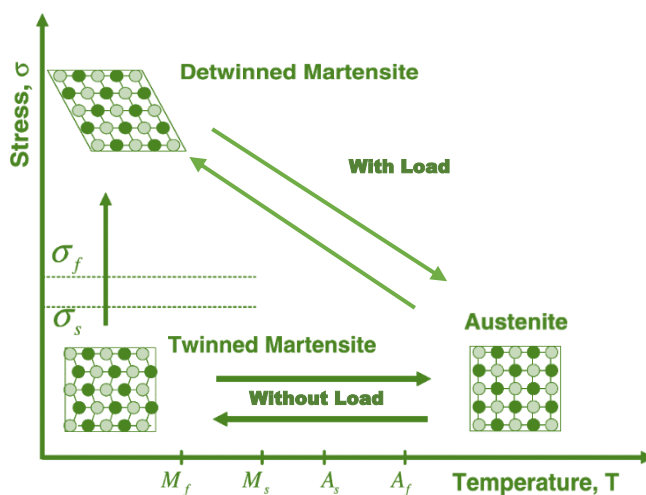
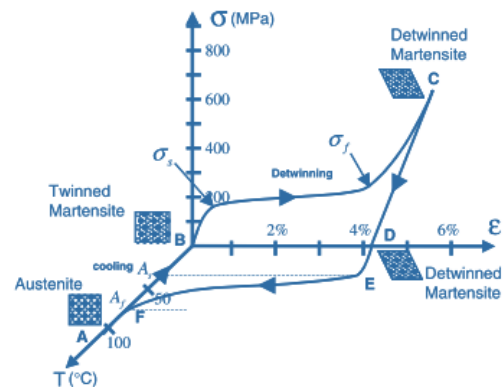


Figure 1.2: Block diagram of phase transformation with the various transformation stages [1]

Four characteristic temperatures are associated with the phase transformation. The forward transformation from austenite, under zero load, begins

to transform to twinned martensite at the martensitic start temperature ( $M_s$ ) and completes transformation to martensite at the martensitic finish temperature ( $M_f$ ). The transformation is complete once the material reaches  $M_f$ , as the material is completely in the twinned martensitic state. Similarly, during heating, the reverse transformation originates at the austenitic start temperature ( $A_s$ ), and the transformation is completed at the austenitic finish temperature ( $A_f$ ). Fig. 1.2 shows the phase transformation behaviour along with the various transformations.

The mechanical load applied to the material, at low temperature twinned martensitic phase, paves the way to detwin the martensite by reorienting a specific number of variants. When an external load is applied, there is macroscopic shape change at detwinned martensite, and the deformed configuration has the ability to return back to normal position when a load is released. On



**Figure 1.3: Stress-strain-temperature data exhibiting the shape memory effect for a typical NiTi SMA [1]**

subsequent heating of the alloy to a temperature beyond  $A_f$  will lead to a reverse phase transformation (from detwinned martensite to austenite) and completes the shape recovery[10,11] . Cooling back to a temperature below  $M_f$  (forward transformation) originated the formation of twinned martensite once more with no associated shape change. The process described above is referred to as the Shape Memory Effect (SME). The load applied must be adequately large to begin the detwinning process. The minimum stress essential for detwinning commencement is termed the detwinning start stress ( $\sigma_s$ ). Fig. 1.3 shows the relation between stress-strain and temperature in shape memory alloys. Appropriately, high loads will result in complete detwinning of martensite and the analogues stress level are called the detwinning finish stress ( $\sigma_f$ ). As the material is cooled with a mechanical load larger than  $\sigma_s$  applied to the austenitic phase, the phase transformation will result in the direct formation of detwinned martensite, yielding a shape change. As the load in applied condition, reheating the material will result in shape recovery. Identifying that the forward and reverse transformations follow a range of

temperatures ( $M_s$  to  $M_f$ ,  $A_s$  to  $A_f$ ) for a particular alloy composition, transformation regions in the stress-temperature space can be deduced. [12,13].

### 1.3 Pseudoelastic Behaviour

SMA pseudoelastic behaviour is related to the transformation strain recovery at the time of unloading where the temperatures are above  $A_f$ . At an exceptionally high temperature a pseudoelastic thermomechanical loading path mostly begins, where the austenite is stable, then grows under an applied load to a state at which detwinned martensite is stable, and lastly returns to the austenitic phase upon unloading. In general, a pseudoelastic test is measured where the temperature is steadily above  $A_f$ . In general, pseudoelasticity encompasses both superelastic behaviour and the rubber-like behaviour. Superelastic behaviour in SMA is more common compared to that of rubber-like effect and is associated with reversible phase transformation induced due to the thermomechanical loading path. Due to loading and unloading, there is an occurrence of detwinning and twinning of martensitic variants, provided the material is in the martensitic state, this phenomenon is the rubber-like effect it occurs mainly due to the reversible reorientation of martensite. In some cases, ageing the martensitic phase can enable the reversal of the martensitic detwinning process upon unloading at temperatures below  $M_f$  [7]. The resulting stress-strain curve is similar to the superelastic curve, and this phenomenon is called the rubber-like effect to emphasise the similarities with the nonlinear elastic behaviour of rubber as shown in Fig. 1.4. In SMA

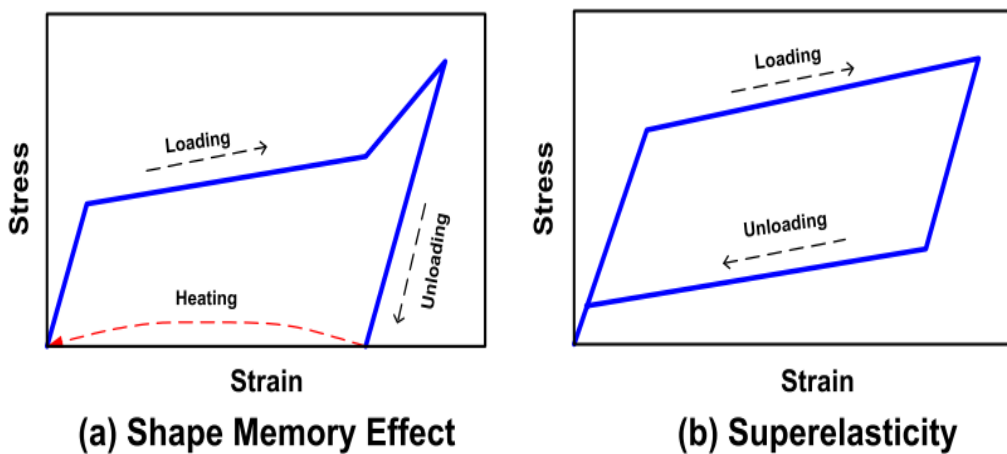


Figure 1.4: Stress-strain behaviour of (a) shape memory effect (b) superelasticity

exhibiting the rubber-like effect, the stress required to detwin martensite is minimal compared to  $\sigma^{Ms}$  (stress levels at which the martensite transformation initiates).

#### 1.4 Two-way Shape Memory Effect with Training

SMA when subjected to thermal cycling yields a reversible and spontaneous change in materials. Such behaviour is termed Two-Way Shape Memory Effect (TWSME). TWSME is not an inherent characteristic of SMA but can be exhibited after undergoing repeated thermomechanical treatments along a specific loading path known as training procedures. TWSME is a result of defects introduced during training. This procedure develops a residual internal stress state, thereby facilitating the growth of preferred martensitic variants when the SMA is stress-free cooled. The mechanisms involved in this TWSME phenomenon are highly correlated to the martensitic transformation, between the parent phase at high temperatures and the martensite phase at low temperatures. A large number of repeated cycles along a loading path would induce changes in the microstructure of the material, which in turn causes permanent changes in the material behaviour[14,15] Thermal loading cycles of an SMA sample under constant applied stress follows a partial recovery of the strain generated during the first cooling cycle [16,17]. After the completion of each thermal cycle a small but permanent strain remains, and with the onset of the consecutive cycle, the permanent strain begins to decrease gradually until further accumulation ceases to

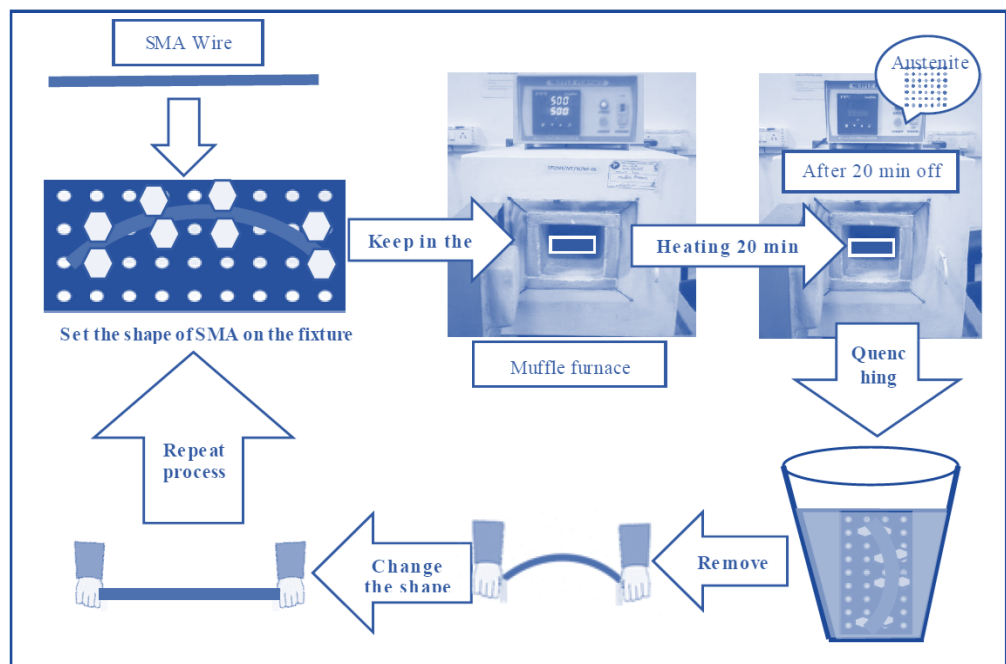
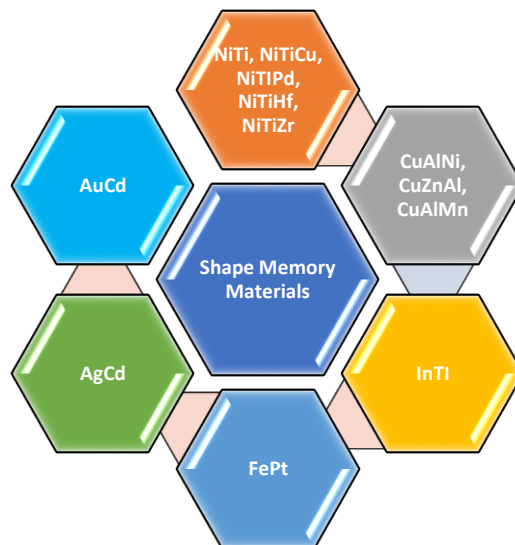


Figure 1.5: Training process utilized in SMA NiTi wires.

exist. Different training procedures exist in literature in order to achieve the TWSME behaviour such as shape memory cycling, pseudoelastic cycling, combined shape memory cycling/pseudoelastic cycling and constrained cycling of deformed martensite. Ageing the material under stress in the martensitic state is one such recent method to develop TWSME behaviours [18,19]. However, the training process as shown in Fig. 1.5 is unfeasible with a thin film and requires other means to obtain TWSME.

### 1.5 Thin Film Shape Memory Alloys

Thin film shape memory alloys are used in several micro-electro-mechanical system (MEMS) actuators due to their high surface to volume ratio. There are reports on utilization of SMA thin films in various application such as diaphragms, gripper, switch, platform etc. Fig. 1.6 shows the various alloy that exhibits shape memory effect. Most of them employ Nickel – Titanium as the primary alloy for actuation due to its superior properties. Further, these alloys are easier to fabricate due to the equiatomic composition. Moreover, the martensitic phase required for phase transformation is stable for long cycles making them reliable. For (MEMS) applications, a thin film based shape memory alloys (SMA) possess many desirable properties, such as high power density (up to  $10 \text{ J/cm}^3$ ), the ability to recover large transformation stress and strain upon heating and cooling, pseudoelasticity (or superelasticity) and biocompatibility. The large surface to volume ratio of the NiTi thin films results in higher frequency response than that of bulk SMA. The work output per volume of thin film SMA exceeds those of other



**Figure 1.6: Various alloys that exhibit shape memory effect**

micro-actuation mechanisms as shown in Table 1.1. The phase transformation in SMA thin film is also accompanied by significant changes in the mechanical, physical, chemical, electrical and optical properties. These changes can be fully made use in design and fabrication of microsensors and microactuators.

**Table 1.1: Various actuation principles**

<b>Principle of Actuator</b>	<b>Maximum Energy density (J/m<sup>3</sup>)</b>	<b>Maximum Frequency (Hz)</b>	<b>Voltage (V)</b>
Piezoelectric	$1.2 \times 10^5$	<5000	5-100
Electrostatic	$1.8 \times 10^5$	<10000	5-500
Thermo pneumatic	$5 \times 10^5$	<100	10
Electromagnetic	$4 \times 10^5$	<1000	20
Conductive polymer	$3.4 \times 10^6$	<1000	5
Bimetallic	$4 \times 10^5$	<100	5
Shape memory Effect	$2.5 \times 10^7$	<100	2-5

### 1.6 Shape Memory Alloy Composites

Researchers are working on expanding their potential applications by exploring ways to improve their unique performance-related characteristics. In order to achieve this, researchers have taken two paths: (i) the development of new alloys and material systems or (ii) the creation of hybrid materials that combine the characteristics of existing materials [20–22]. The former approach led to the development of high-temperature SMA, shape memory polymers and magnetic

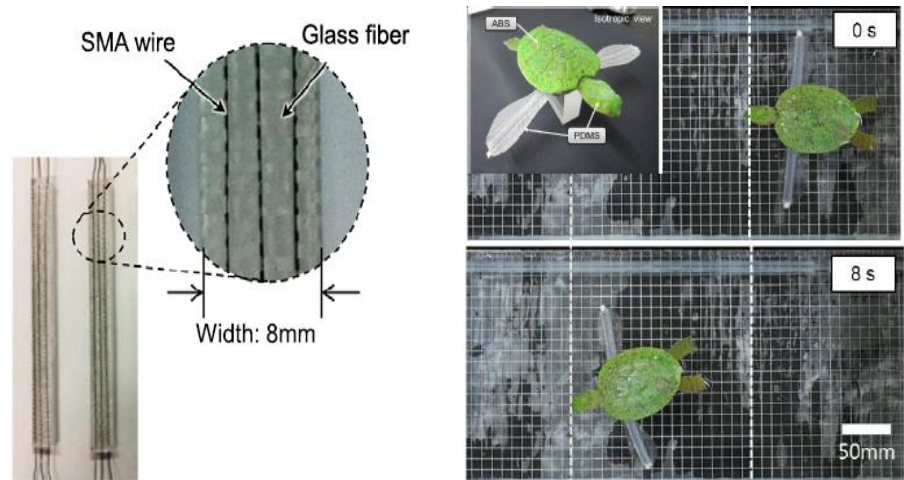


**Figure 1.7: (a) Polymer matrix reinforced with smart SMA (b) Bio inspired turtle robot embedded with SMA composite as actuators.**

shape memory alloys. Composite SMA Structures were first developed by *Rogers (1991)* [23] where they embedded NiTi wires in a laminated polymer matrix composite (PMC) [14]. Recent developments in composites are utilized in many damping and mimicking applications as shown in Fig. 1.7 However, with thin film SMA, unimorph or monomorph having one active layer and one passive layer has been developed for majorly for semiconductor applications. Reports on thin films with a smart material such as SMA representing the active medium has been less. Bimorphs are smart structures which, has two active medium which contributes effectively during the functioning. SMA bimorphs with flexible substrates have gained attention due to the role of flexible substrate in two-way shape memory effect. SMA thin film composites led to the latest development by *Ishida.A (2014)*, in which he has developed a NiTi/Polyimide bimorph and explored its potential application as micro-flapper [24–27], shown in Fig. 1.8. Further *Kotnur(2014)* has studied the influence of different parameters while developing NiTi/Polyimide composites through sputtering at low temperatures [28,29]. The technology of integrating SMA structures in the form of composites has opened new applications, towards the development of macro and microdevices. One such technology is of using a flexible polyimide substrate to act along with the SMA is a novel and cutting-edge phenomenon [12,30,31]. The flexible substrate can act as a bias force during the cooling cycle. Further, the flexible substrates can be pre-strained in different shapes according to the requirement of the device [14,22,32]. Such bimorphs can be extensively used in MEMS devices to overcome the difficulties in development and training process. However, the thermomechanical behaviour of such films has not been studied in detail.

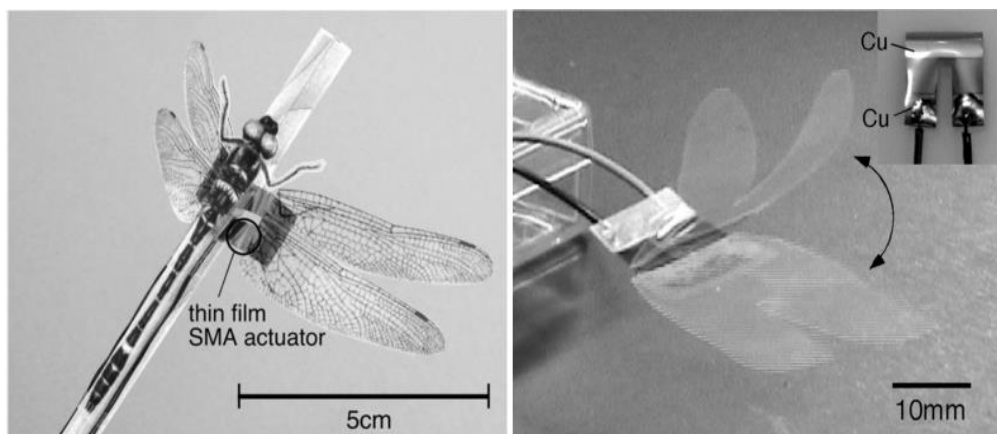


**Figure 1.8: (a) Dragon fly with NiTi bimorph as wings (b) NiTi bimorph with copper contacts for micro flappers.**

## 1.7 Copper Based Shape Memory Alloys

Cu-based SMA can be an attractive and cost-effective solution for actuator applications, and it has the potential to replace the conventionally used NiTi [1,33]. Primary alloys include CuZnAl and CuAlNi which exhibit exceptional SME. Cu-Al-Ni shape memory alloys have been particularly interesting due to the large recoverable strain of 18 % which is much higher when compared to conventionally utilized Ni-Ti [34,35]. The transformation temperatures of the alloy are extremely sensitive to composition, as adding Al or Ni of 5 – 10 wt% can tune the transformation temperature from -100 °C to 300 °C. Their properties such as excellent machinability, ease in the forming process, high thermal stability, rapid heating and cooling rate, less hysteresis and higher Young's modulus acts as a significant advantage [36,37]. However, CuAlNi alloys are difficult to fabricate due to high sensitivity to the composition. Further conventional techniques for thin film deposition often fail to acquire a stable phase due to precipitate formation. However, with thin film deposition techniques, the cooling rate can be controlled to some extent, which can be utilized in developing efficient CuAlNi SMA.

## 1.8 Motivation for the Study

The present literature report the development of SMA thin film through sputtering on flexible substrates [29,38,39]. Further, theoretical simulation on force generated during actuation and the effect of the composition were found [25,26,40]. However, reports on significant issues such as post-processing, thermomechanical and life cycle behaviour of such bimorph are less. The limitations of the present techniques and research gaps are

- Need for post-processing to obtain stable martensite structure
- Need for the training of SMA thin films for TWSME
- Lack of thermomechanical analysis for MEMS applications
- Lack of life cycle analysis with thin film SMA.
- Need for implementation in functional devices of Cu-based SMA.

The above points indicated the need for a straightforward method in developing thin SMA, which can be readily utilized in applications. Further, an approach that can be industrialized will be beneficial in developing low-cost devices. As copper-

based SMA are commercially unavailable, present actuators mostly employ Ni-Ti alloy, which is approximately ten times costlier [7]. The copper-based SMA bimorphs have a potential application towards the development of high-temperature actuators [41–44].

### 1.9 Research Objective

The objective of the work is to employ a straightforward technique suitable for industries to develop two-shape memory alloy thin film bimorphs. The investigations on the material properties thermomechanical and lifecycle behaviour of such bimorphs are investigated in detail. The objective can be split into three major sections as shown in Fig. 1.9.

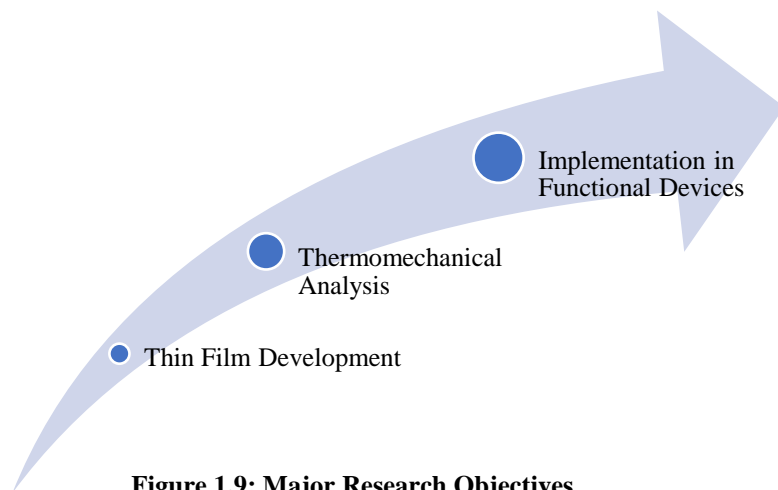


**Figure 1.9: Major Research Objectives**

### 1.10 Outline of the Thesis

The thesis is divided into eight chapters, and the brief description is given below.

- Chapter 1: Introduction to shape memory alloys, composites and the technologies used in developing bimorphs
- Chapter 2: Discussion on copper-based SMA and the challenges involved in developing their thin film.
- Chapter 3: Experimental approach employed in synthesizing copper based bimorphs and the theory behind their actuation.
- Chapter 4: Influence of substrate thickness and substrate temperature in developing efficient bimorphs.

- Chapter 5: Theoretical studies on thin film SMA bimorph with structural and thermal analysis.
- Chapter 6: Investigation on manganese addition on improving the thermomechanical and lifecycle property of the bimorphs.
- Chapter 7: Implementation of the developed bimorphs in robotic and energy systems as actuator and sensor.
- Chapter 8: Conclusions obtained from the experimental and theoretical investigations along with the scope for future work.



## Chapter 2

---

# Literature Review on Copper Based Shape Memory Alloys

### 2.1 Martensitic Transformation in SMA

The shape memory effect of SMA has triggered a number of potential applications spanning in the range from fundamental phenomena via modelling aspects to structural applications. SMA enduring thermoelastic martensitic transformations displays remarkable properties due to the crystallographic reversibility. Martensitic transformations can be produced in two ways (i) undercooling and (ii) by application of stress. A deformation applied to the material at martensitic phase producing plastic strains will recover by increasing the temperature leading to external shape returning to original shape. Complete SME occurs under certain conditions of thermoelastic nature in the martensitic phase. The principal motive for such reversibility of thermoelastic martensites is due to the characteristically low elastic strains related to the crystal structure. The elastic limit of the parent phase is not surpassed in order to avoid irreversible plastic deformation. Additionally, the strains, failing to build up as the martensite plates propagate, are negated efficiently out by forming groups of commonly complimenting plates. In addition, the individual plates are internally twinned to accommodate the transformation strains. Thermoelastic martensites are soft and ductile as they deform by movement of twin or variant boundaries, which are not stabilized due to low shape strains. The accommodation elastic strain fields are not influenced by the boundaries to make it unfeasible. Additionally, twin boundaries have low energy and are highly mobile interfaces. Overall energy change in low hysteresis thermoelastic martensitic transformations can be characterized by the Gibbs free energy which influences the transformation and hinders the elastic strain energy. The growth velocity is proportional to the cooling rate, once martensite crystals are nucleated below  $M_s$  temperature. However, after reaching a certain size, there is a decrease in Gibbs energy and the elastic strain energy increases due to growing plate, leading to obstruction of growth. The martensite crystals will be disrupted after attaining the thermal equilibrium and begin to grow or shrink only

when subjected to heating, cooling or external force after. Besides, the reversibility criterion, the other essential requirement for a comprehensive SME are (i) the lattice invariant deformation occurs by twinning rather than by slip and (ii) the martensite formation from an ordered parent phase. Both conditions provide high resistance to slip yielding and assist the underlying reversibility condition of thermoelastic martensitic transformation, which has a significant advantage in the absence of plastic yielding during such accommodations [45–48].

Assuming the parent phase to be a single crystal, a number of martensitic structures with different but crystallographically equivalent habit plane indices called as variants emerge throughout the specimen. The basal plane of long period stacking order martensite initiates from one of the  $\{110\}$  planes of the parent phase and the inhomogeneous shear during transformation occurs on the same plane. There are six  $\{110\}$  planes in the ordered parent phase and has two possible shear directions for each  $\{110\}$  plane. Thus, there are 12 possible combinations of stacking planes and shear directions, each combination leading to two possible crystallographically equivalent habit planes. Therefore, 24 martensite variants can result from a single parent phase. During cooling below  $M_s$ , the single parent crystal transforms in a self-accommodating manner. Further, six groups of four variants form from the parent phase, and the four variants have habit plane normals clustered about one of the six  $\{110\}$  poles of the parent. There are specific twin relations among these four self-accommodating variants[4,49,50]. The 24 martensite variants will individually be subjected to shape deformations, even if all of the parent phases is transformed into martensite, as the specimen is cooled below  $M_f$ . The specimen as a whole will experience no shape change, due to the formation of martensite crystals as the self-accommodation principle plays a vital role. A parent phase with an orientation identical before deformation is created from the similar variants in accordance with the lattice correspondences between the original parent phase and each variant. This phenomenon causes the specimen to revert completely to the shape it had before the deformation.

## **2.2 Shape Memory Effect in Copper based Shape Memory Alloys**

NiTi alloys are the most popular of shape memory alloys with their excellent shape memory characteristics. However, they are very costly to be

employed in various applications leading. Cost-effective and efficient to some extent Cu- based SMA such as CuZn and CuAl have been developed as an alternative to NiTi SMA. Although CuZnAl alloys with superior mechanical properties are the most popular among the copper-based SMA, they suffer from lack of adequate thermal stability, while CuAlNi shape memory alloys, despite their enhanced thermal stability, have found only limited application because of insufficient formability due to the brittle  $\gamma_2$  precipitates. CuAlNi alloys are also less prone to martensite stabilisation than CuZnAl alloys. NiTi and CuZnAl alloys cannot be used practically over 100°C. Therefore, in recent years Cu-Al-Ni-Mn-Ti (CANTIM) series alloys have been developed [51–53] as potential candidates for high-temperature SMA applications.

### **2.2.1 CuZnAl SMA**

The martensitic transformation starts temperature,  $M_s$  of the  $\beta$  phase Cu-Zn binary alloys around 40 at % Zn is far below room temperature, and in the alloys with Zn contents lower than about 38 at %, a massive transformation occurs, which is a composition invariant but diffusional phase change. Ternary elements such as Al, Ga, Si and Sn are added to raise transformation temperature, and to stabilise the  $\beta$  phase. Among them, CuZnAl ternary SMA are the most excellent with excellent ductility and resistance to grain boundary fracture.

### **2.2.2 CuAlNi SMA**

CuAlNi is not susceptible to stabilisation and ageing phenomena. Similar to CuZnAl, the transformation temperatures of CuAlNi can be varied by changing the aluminium or nickel content. Varying the aluminium composition from 11 at.% and 14 at.% can change the  $M_s$  temperature from -100 °C - 200 °C. Since this alloy is harder to produce, manganese and titanium are often added to improve its ductility and to refine its grains. However, the primary limitation of the CuAlNi system is the poor ductility due to intergranular cracking [54,55]. This phenomenon also affects the mechanical behaviour such that the material typically fractures at a stress level less than 300 MPa.

### 2.2.3 Effect of Composition on the Cu-based SMA

Martensitic transformation temperature,  $M_s$  of Cu-based SMA is strongly dependent on composition. In CuZnAl alloys, increasing the zinc or aluminium contents causes a decrease in  $M_s$  temperature and Cu-Al-4%Ni SMA, transformation temperatures decrease steeply with slight increases in Al content, (approximately 100°C per 1%Al) [56–58]. Although they also decrease with increasing Ni content, the dependence of  $M_s$  temperature upon Ni content is much weaker than that on Al content. In CuAl binary systems with high concentrations of Al, precipitation of  $\gamma_2$  phase cannot be prevented even with extremely rapid quenching; There are several reports indicating the effect of adding Ni to suppresses the diffusion of Cu and Al and to stabilise the  $\beta$  phase effectively. If vertical cross-sections of a ternary CuAlNi system for varying Nickel contents have been compared, the boundary between the  $\beta$  and the  $\beta+\gamma_2$  phases is observed to be a shift towards higher aluminium concentrations on increasing nickel content. The range of composition at which CuAlNi and CuZnAl alloys can be used as an SMA is the region allowing  $\beta$  phase to exist alone at high temperatures and is limited, approximately to, Cu-(12-14) wt% Al - (3-4) wt% Ni and Cu- (10-30) wt% Zn-(5-

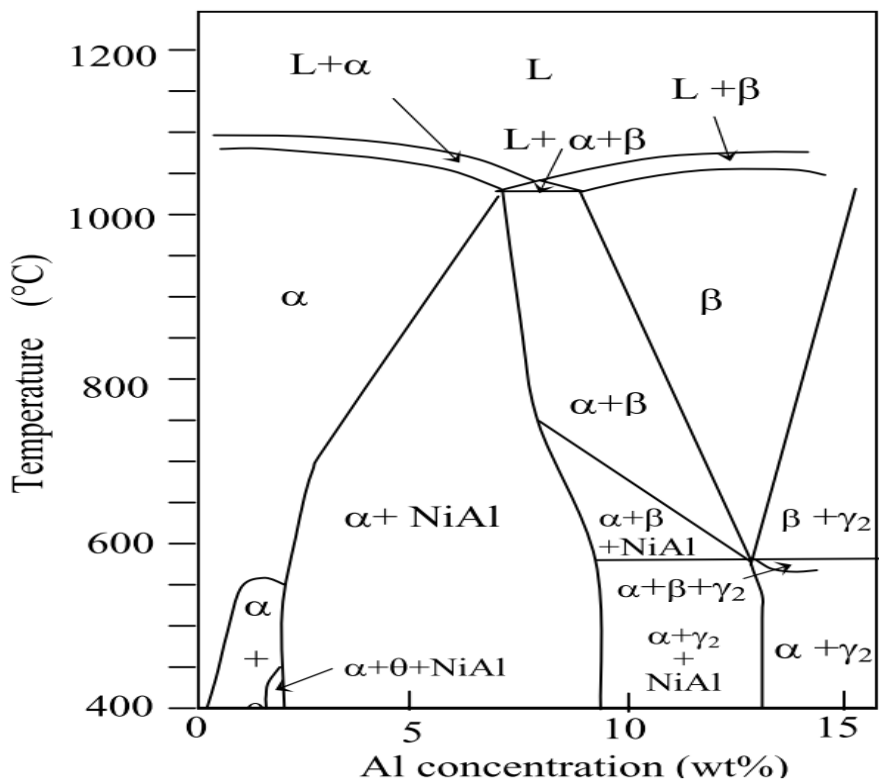
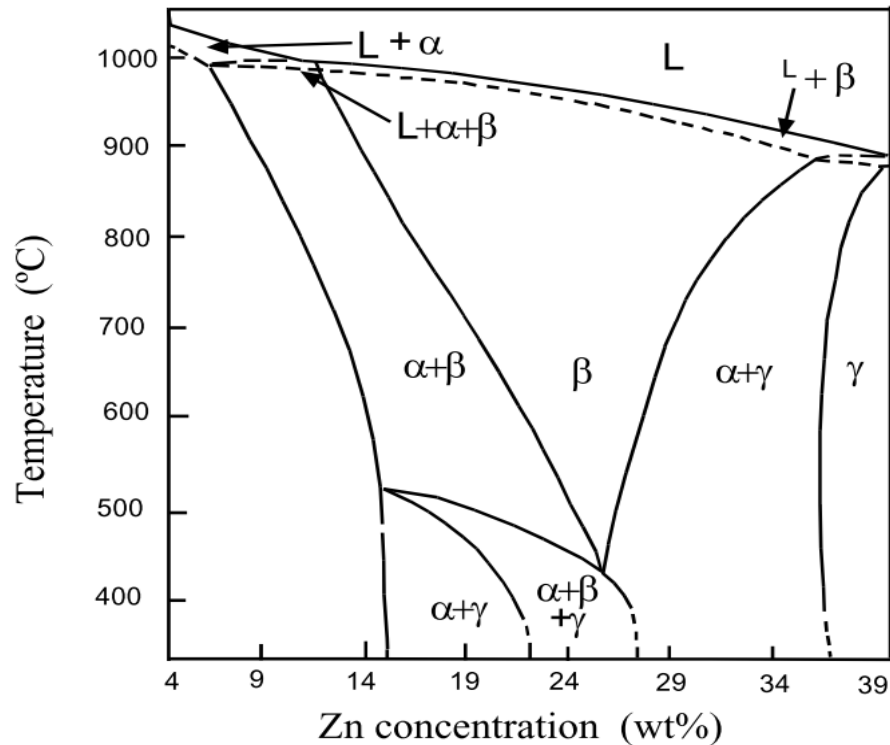


Figure 2.1: Phase diagram of CuAlNi shape memory alloy. Vertical cross-section with 3 mass% Ni

10) wt% Al as seen from the phase diagrams given in Fig. 2.1 and Fig. 2.2, respectively.



**Figure 2.2: Phase diagram of CuZnAl Shape memory alloy. Vertical cross section with 6 mass % Al**

The investigation on the dependence of  $M_s$  transformation temperature on the amount of Ni and Al content was analysed, and the influence of concentration on the variety of martensite phases formed in CuAlNi single crystals has been reported [48,53,59]. It was found that aluminium content increases, holding the nickel concentration constant and the transformation evolves from  $L2_1 \rightarrow 18R$  to  $L2_1 \rightarrow 2H$ , displaying an intermediate concentration range where both martensitic structures coexist, at  $L2_1 \rightarrow 18R+2H$ . Conversely, an increase in nickel concentration for constant aluminium content results in an evolution from the diverse  $L2_1 \rightarrow 18R + 2H$  transformation to the  $L2_1 \rightarrow 18R$  transformation.

The difference in transformation temperature between experimental and calculated values was found to be around  $\pm 8^\circ\text{C}$  [60]. It was concluded that the transformation temperature depends strongly on the on the aluminium content. Variation in martensite from 18R into 2H type with increasing aluminium content in CuAlNi alloys has also been reported by C.M. Friend [49]. It is well known that the transformation temperatures of shape memory alloys decrease as the grain size

is reduced [60,61]. However, they are independent of grain size for grains larger than 100  $\mu\text{m}$  [62]. The effect of grain size on transformation temperature was suggested to be due to a grain constraint effect where grain boundaries retard the martensite transformation and lower the  $M_s$  temperature [63]

### 2.3 Theory of SME in Cu-based SMA

Cu-based shape memory alloys have a disordered  $\beta$  phase at high temperatures, and upon cooling  $\beta \rightarrow \text{B2}$  ordering, the transition takes place, and rapid quenching fails to prevent the ordering. Further lowering of temperature leads to  $\text{B2} \rightarrow \text{DO}_3$  ordering, depending on the alloy composition and cooling rate. B2 ordering is a first order transformation, whereas the  $\text{DO}_3$  ordering is a second order transformation. In nucleation and growth controlled first order transformations, a substantial change takes place intermittently at critical ordering temperature (TC). Further the thermodynamically first derivative of Gibbs free energy changes discontinuously characterised by discontinuous changes in entropy,  $S$ . On the other hand, for second order transformations, which are rather a similar type phase transformations, there is no abrupt change in TC. The second derivative of Gibbs free energy is discontinuous, exhibiting a continuous change in entropy [50,61,62,64]. Cu-based shape memory alloys with ordered B2 or  $\text{DO}_3$  phases transform into one of the long period stacking order martensites (LPSO) structures such as 2H, 3R, 9R, and  $18\text{R}_1$  using thermoelastic martensite transformation. Crystal structures of  $\text{DO}_3$  parent phase, 2H and  $18\text{R}_1$  LPSO martensites are schematically drawn in Fig. 2.3, and Fig. 2.4, respectively. LPSO martensite structures are formed by shearing of  $\{110\}$  parent phase planes, becomes the basal planes of long period stacking order martensites, along with  $\langle 110 \rangle$  directions by an amount  $1/6 \text{DO}_3$ . The low symmetry of martensite structure provides formation of 24 crystallographic variants from the high symmetry parent phase. During cooling below  $M_s$  temperature, the parent phase transforms in a self-accommodating manner, in which the martensite variants are created side by side forming diamond-like morphologies, to minimise the total shape change [65–67]. Due to the displacive shear nature of martensitic transformation the crystal structure, atomic ordering and microstructural defects of parent phase are inherited by the product martensite phase

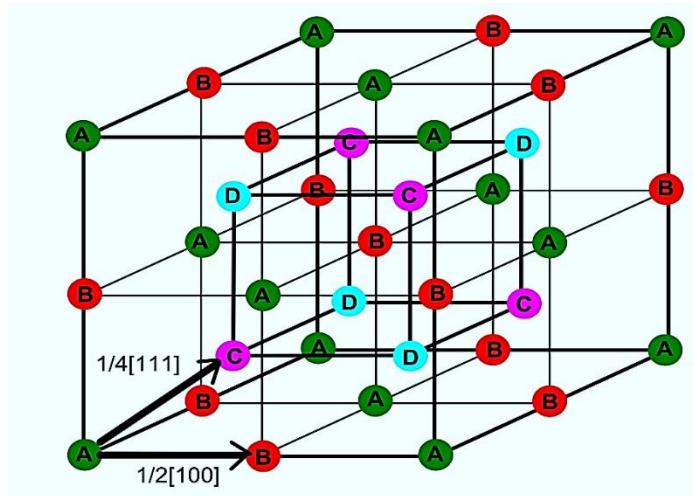


Figure 2.3: DO<sub>3</sub> unit cell showing the arrangement of atoms

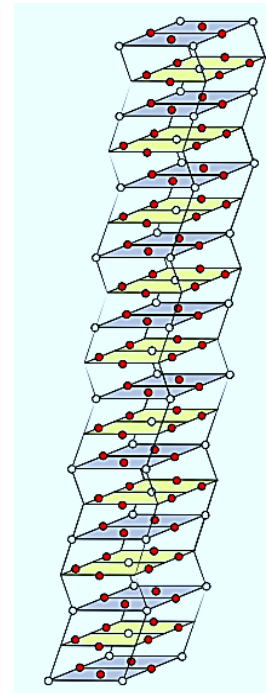
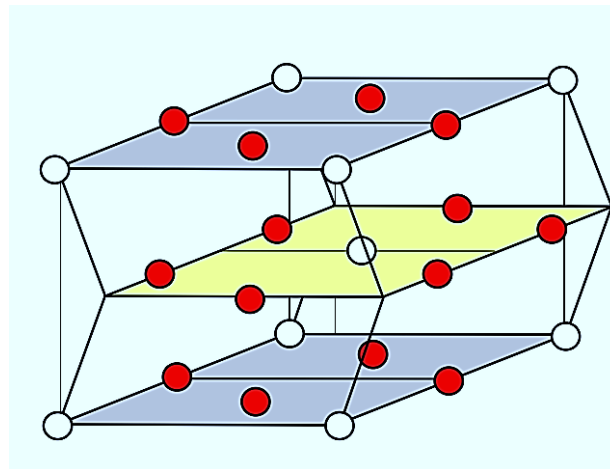


Figure 2.4: Long period stacking of 2H and 18R<sub>1</sub> martensite

It should be noted here that although the main factor controlling the transformation temperatures is alloy composition, the transformation temperature is significantly affected by other factors such as heat-treatment, quenching rate, grain size and the number of transformation cycles. For example, in general, the smaller the grain size, the lower the martensite temperature. Single-crystalline Cu-based SMA exhibit unusual mechanical behaviour. Mechanical behaviour of the polycrystalline Cu-based SMA, however, is different from that of the single-



## **2.4 Cu- based Quaternary SMA**

Various attempts have been made to improve the thermal and mechanical stability of the SME characteristics, especially for the most promising CuZnAl and CuAlNi SMA. Pre-ageing or step-quenching is effective for retardation of ageing effects due to the excess quenched-in vacancies are annealed out to some extent. However, one of the most noteworthy improvements to be made for Cu-based SMA is in their fatigue and fracture characteristics as they are fatal defects of the SMA. As mentioned above, the ease of fracture and fatigue is due to the difficulty of relaxation of stress concentrations at grain boundaries. Hence it becomes essentially important to refine the grain size of these SMA for their improvement.

### **2.4.1 Influence of Quaternary Element**

Grain refining by little increments of alloying components has generally been endeavoured conscientiously [41,46,68]. The impacts of different components, such as Ti, Zr, V, Pb, and B have been examined with CuAlNi and CuZnAl SMA. Among them, the impact of Ti, to reduce the grain size to 15  $\mu\text{m}$  from 1 mm was particularly significant. The component of grain refinement was once represented by the nearness of finely scattered Ti-rich particles that obstructs to grain boundary movement. However, the mechanism was not straightforward as two kinds of precipitates were found with Ti-doped SMA. The precipitates, typically in nanometre order were observed of having L2<sub>1</sub>, type (Cu, Ni), TiAl structures, but with different proportions of the constituent atoms. Later it was proposed that grain refinement is the combined result of two effects (i) the presence of Ti atoms brings about lowered diffusion rates of constituent atoms, resulting in grain refinement and (ii) the pinning effects of the precipitates particles to suppress the growth of grains, resulting in the ultimate refinement. By grain refining, the fracture strength, the strain to fracture and the fatigue life were all improved to a great extent. For example, when the grain size is refined to less than 20  $\mu\text{m}$ , the number of cycles to failure for Ti-doped CuAlNi SMA increases two orders.

## **2.5 Influence of Thin film Deposition Parameters on Developing Cu- based SMA**

Since 1990, various physical vapour deposition (PVD) techniques have been used to fabricate thin NiTi films. After the first reports on the deposition of

NiTi by Magnetron Sputtering [69,70] other processes like Ion Beam Sputtering [71–73] ECR Sputtering [21], Laser Ablation, Pulsed Laser Deposition [74,75], Flash Evaporation [24], Electron Beam Deposition [25] and Vacuum Plasma Spraying [26] have been used. The most common PVD process is the Magnetron Sputtering technique since it allows to deposit with different rates of about 10 m/h combined with the relatively simple process. The major challenge remains in depositing SMA films with definite stoichiometry and high purity. It was found that in general, in the deposited films, the content of titanium is considerably smaller than in the used sputtering targets [27]. In order to control the stoichiometry, different approaches have been realized. Ishida et al. fixed Ti-plates on stoichiometric NiTi-targets [3], Chang et al. used a multilayer structure of Ti and NiTi layers which were dissolved after a subsequent annealing treatment [28] and Holleck et al. used NiTi-targets with slightly enhanced Ti content [1]. Ho and Carman adjusted the Ti-content of the sputtered films by controlling the target temperature [29]. There are very few reports on utilising thermal evaporation system for developing CuAlNi thin films. Even though sputtering is widely used, thermal evaporation is a simple and cost-effective technique. It is one technique which will be suitable for large-scale production. In order to obtain thin films of high purity, targets manufactured by vacuum cast melting are preferable in comparison to targets made by powder metallurgy. The influencing parameters in thermal evaporation deposition are (i) distance from the crucible to substrate (ii) time after deposition (iii) temperature near the substrate (iv) vacuum conditions (v) weight of material used for deposition.

### **2.5.1 Influence of Substrate Thickness**

There are very few reports on the utilisation of flexible substrates for the development of SMA thin films. *Ishida et. Al* [25,26,71,76,77] have investigated the force generated by NiTi SMA deposited on polyimide substrates of varying thickness. Composite-film actuators consisting of a Ti<sub>49</sub>-Ni<sub>33</sub>-Cu<sub>18</sub> film and a polyimide film (Kapton H or EN) with thickness ranges of 0.8–13 and 25–175  $\mu\text{m}$ , respectively, were successfully fabricated by sputtering an alloy target. The composite films could be utilized as one-way or two-way actuators. The report suggested the two-way actuation was caused by a thermal strain due to cooling from the deposition temperature. The motion (the direction and displacement) was

found to be mainly controlled by the thickness of the Ti–Ni–Cu film and Young’s modulus of the polyimide film. Further, it was reported that the thickness of the polyimide film reduced the two-way shape memory actuation and increased the one-way shape memory effect under external loads. A simulation tool based on a simple deformation model for a Ti–Ni–Cu film was developed to investigate the effects of thickness, length, width and material parameters such as Young’s modulus, elastic strain limit, and transformation strain on the actuation force and stroke. The simulation results revealed that various combinations of force and stroke, which could not have been realized by other types of thin-film SMA actuators, could be obtained by using composite-film actuators. Optimized polyimide/Ti–Ni–Cu film actuators exhibited a long stroke, a high response speed of 3 Hz, and a large force of 0.4 N. Further, other reports on SMA/polyimide focuses on the development process film through sputtering with high stoichiometry.

### **2.5.2 Influence of Substrate Temperature**

There are reports on the influence of deposition temperature on the structural properties of the film. Recently *Kotnur et al.* demonstrated the development of NiTi films through sputtering at low temperature. Thin films of NiTi are usually grown on silicon wafers by physical vapour deposition technique, and magnetron sputtering was utilized. The study was aimed at developing NiTi thin films at elevated and room temperature (RT). NiTi thin films sputter-deposited at room temperature was found to be amorphous in some cases [78–80]. To crystallise the amorphous NiTi, post-sputter annealing was required in order to obtain reversible martensitic phase transformation. The crystallisation temperature needed during annealing for the amorphous films was found to be above 500 °C [50,51]. Reports are suggesting the crystalline nature of as-deposited films at elevated temperatures above 450 °C [47,28]. It was found that growing a crystalline film is easier than crystallising an amorphous film, due to the higher diffusivity of surface atoms compared to bulk atoms. In both cases temperatures above the glass transition temperature of polyimide (360 – 410 °C) were needed to obtain crystalline NiTi films. Further, studies on the SMA thin films deposited on polyimide substrates fail to investigate the thermomechanical and life cycle behaviour of such composite structures.

## 2.6 Thermomechanical Behaviour of Cu-based alloys

Thermal cycling effects in copper-based SMA, are mostly devoted to predict the life and to enhance the properties to actuate for a large number of cycles. There is an insufficient study on early stages of thermal cycling, fatigue and the thermomechanical behaviour of copper-based alloys. It has been shown many times that thermal cycling introduces dislocations, which establish favoured nucleation sites for thermoelastic martensite through repeated thermal cycling. Changes in transformation temperatures have been reported, and those changes reach saturation after a certain number of cycles, and thereby thermal cycling may be used in inhibition of stabilisation to a certain extent. In CuZnAl alloys,  $M_s$  and  $A_f$  temperatures increase while  $M_f$  and  $A_s$  temperatures remain constant with increasing number of thermal cycles. Hundreds of cycles, as opposed to controversial results in CuAlNi alloys where a decrease in  $M_s$  and  $A_f$  temperatures [67], increase in all temperatures [68], increase in  $M_s$  and  $A_s$  temperatures [69] by thermal cycling are some of the contradictory examples from CuAlNi alloys. Briefly, whatsoever the sense of transformation temperature change in alloys due to thermal cycling, it has been mostly attributed to the enhancement of martensite nucleation due to dislocations introduced by thermal cycling.

The transformation temperatures and thermal hysteresis behaviour of a Cu-29 wt% Zn - 3wt% Al alloy have been determined by electrical resistance measurement [73]. Specimens were cyclically transformed between 38 °C and -20°C for 400 cycles. It was evident that transformation temperature characteristics of  $M_s$  and  $A_f$  temperatures increased while  $M_f$  and  $A_s$  temperatures remained constant. Additionally, the area of the hysteresis loop decreased with cycling. Finally, with increasing number of cycles, the electrical resistance of  $\beta$  phase increased whereas electrical resistance of martensite remained constant. The resistance change has been explained as the martensite to beta reversion being incomplete, and some martensite retaining above the  $A_f$  temperature. Martensite retained with cycling reduces the total extent of thermoelastic transformation. The unrelaxed elastic strain accompanying the transformation could act to stabilise the martensite. It was clear from that the changes resulted from cycling after approximately 300 cycles.

Nakata *et al.* [81] have examined the thermal cycling effects in a Cu-13.7 wt% Al- 4 wt% Ni alloy having  $M_s = 24^\circ\text{C}$ . Both  $M_s$  and  $A_f$  temperatures decreased gradually on increasing number of cycles and a decrease of  $40^\circ\text{C}$  after 10,000 cycles were observed. The rate of decrease in transformation temperatures has slowed down after about 4000 cycles. TEM investigation resulted in increased dislocation density with cycling. At the end of 10,000 cycles, there was no unique structure other than dislocations. Moreover, martensite plates tend to become smaller with increasing number of cycles. They found that the degree of  $\text{DO}_3$  order decreases with thermal cycling and it leads to decrease of transformation temperatures. In order to determine the change in the degree of order by cycling, intensity ratios of four superlattice reflections to the one fundamental reflection have been measured as a function of a number of cycles. Further, the degree of  $\text{DO}_3$  order decreased after thermal cycling. Decreasing rate of change in transformation temperatures after about 4000 cycles has been explained as a disordering of the  $\text{DO}_3$  structure. Gao *et al.* [82] have investigated the effect of thermal cycling on transformation temperatures of a C- 15 wt% Al- 7wt% Ni- 0.5 wt% Mn-0.5 wt% V alloy. All transformation temperatures increased about  $20^\circ\text{C}$  after 50 thermal cycles. Observed Vanadium –rich precipitates in the as-quenched samples were held responsible for the increase of the transformation temperatures due to cycling. Morris and Gunter [70] have studied the effect of heat treatment and thermal cycling on transformation temperatures of a Cu-12 wt%, Al-4 wt%, Ni-3 wt%, Mn-0.1 wt%, alloy. Alloy samples were either betatized at  $820^\circ\text{C}$  for 30 minutes and directly quenched into water. This treatment is followed by additional annealing at  $300^\circ\text{C}$  for 30 minutes and air cooling, and they were thermally cycled 8-10 times. At the end of eight thermal cycles, they have observed  $10\text{-}20^\circ\text{C}$  increase in  $M_s$  and  $A_s$  temperatures in the directly quenched alloys on the other hand in the annealed and air-cooled samples the increase was only  $5\text{-}7^\circ\text{C}$ . The increased stability of transformation temperatures observed in the annealed specimens has been attributed to the increase of order obtained by annealing treatment. The incomplete order obtained by the direct quenching leads to a fast change in transformation temperatures during cycling of quenched samples. The post-quench increase in transformation temperatures in CuZnAl alloys has also been attributed to incomplete  $\text{L2}_1$  ordering resulted from direct quenching [78]. However, there are

very fewer reports on the life of actuation and thermomechanical behaviour during actuation of such shape change alloys.

## **2.7 Status of Thin Film Shape Memory Materials**

With the recent advents in MEMS, NiTi-based thin films are potentially desirable for microscale devices such as accelerometers, gyroscopes, microvalves, microphones, micro pressure sensors, micro scanners, optical switches for their potential applications in the field of automotive, aerospace, biomedical, industrial process control, electronic instrumentation, telecommunications, and military applications [30,33,77,83–85]. NiTi thin films are a promising material for these applications as the work output per unit volume of NiTi exceeds that of other micro-actuation mechanisms, and it can be patterned with standard lithography techniques in the batch process [20–23]. A large number of micro-sensors and micro-actuators such as microswitches, micro relays, micropumps, microvalves, micro-grippers, and micropositioners can be made using NiTi thin films [24–26]. In addition, a high damping capacity makes NiTi SMA an attractive, functional material for vibration damping applications at microscale [27]. However, there are some potential problems associated with NiTi thin films including low energy efficiency, low dynamic response speed, large hysteresis, and fatigue problems [28, 29]. Nickel-Titanium (Nitinol, NiTi) is the alloy primary used in applications. It exhibits strong SME, TWSME, and pseudoelastic behaviour under the right conditions, which makes this material ideal for a variety of applications. It also exhibits resistance to corrosion and is biocompatible, making it suitable for use in biomedical applications. Compared to the less widely used alloys, the crystallography and thermomechanical response of NiTi are well understood, as the effects of heat treatment and the variation of transformation temperatures with changes in composition [78,86–89]. There are no reports on the functional application of Cu-based alloys.

## **2.8 Preliminary Experiments with CuZnAl SMA**

Cu-Zn-Al shape memory alloy has excellent properties such as high damping capacity, low-temperature actuation, high energy efficiency and low cost which makes it suitable for MEMS devices [90]. The composition of the film drastically affects the transformation temperatures. The binary Cu-Zn alloy has a

transformation temperature 200 K. However the addition of Al in the alloys allows extending the Martensite ( $M_s$ ,  $M_f$ ) temperature range from 0 K to 700 K [91]. However poor ductility and workability, due to intergranular cracking acts as significant limitations, which leads to reduced cyclic behaviour [1]. The experiments on developing CuZnAl SMA was carried out with both chemical and physical deposition techniques.

The effect of composition in the film drastically affects the transformation temperatures. The binary Cu-Zn alloy has a transformation temperature 200 K, which makes it unsuitable for practical usage. However, the addition of Al in the alloys allows extending the Martensite ( $M_s$ ,  $M_f$ ) transformation temperature from 0 to 700 K, thereby making it possible for device application. Moreover, the transformation temperatures can also be varied according to the application.

### 2.8.1 Chemical Deposition of CuZnAl

Spray Pyrolysis technique is used to prepare a wide variety film on a large scale. Furthermore, it can be used for depositing material on any substrates. Spray Pyrolysis works on the principle of the thermochemical decomposition process, where a chemical solution is sprayed onto to heated substrate using air blast technique. Although ultrasonic atomiser has been widely used, air blast technique

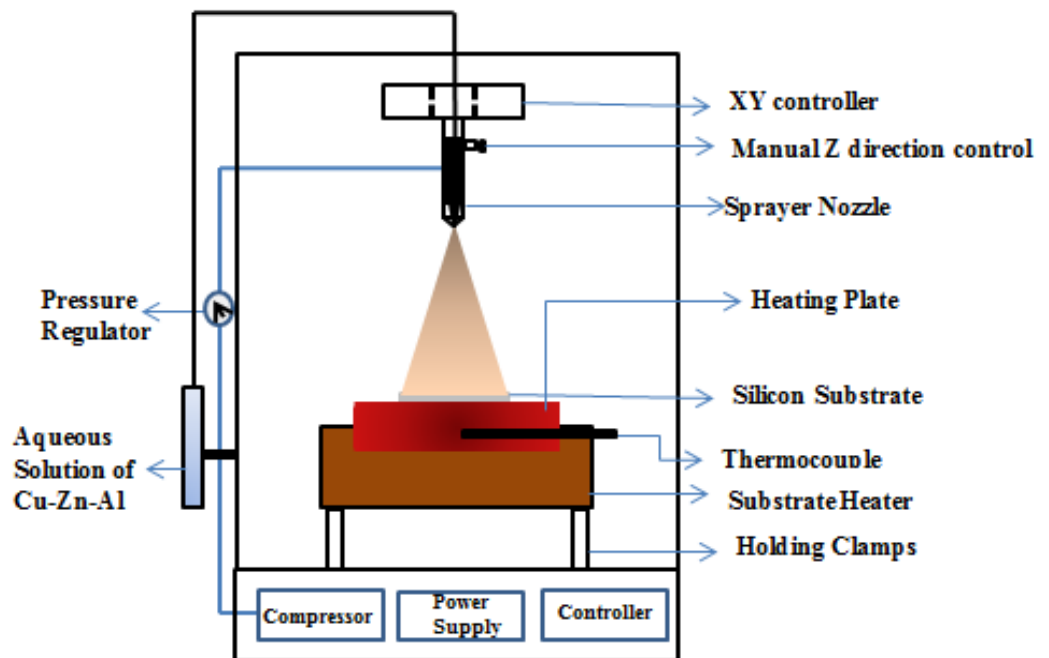


Figure 2.6: Spray Pyrolysis block diagram

is a cheap and an effective method, where the air pressure can be controlled to vary the properties of the film. So far, spray pyrolysis has been used in the preparation of CZTS, Sb<sub>2</sub>S<sub>3</sub>, SnO<sub>2</sub>, MgO, Co<sub>3</sub>O<sub>4</sub> and ZnO to name a few. It is the most prominent technique used in the glass industry and solar cell gas sensors, anti-reflection coatings. Electrodeposition of Cu-Zn shape memory alloy has so far been the only chemical process for fabricating SMA.

Fig. 2.6 shows the block diagram of the spray pyrolysis setup (HOLMARC thin film Spray Pyrolysis equipment Model No HO-TH-04), which was used in the process. A constant pressure of 1.2 bar was used for the deposition process. The distance between the nozzle and substrate was kept constant at 15 cm. The atomiser is connected to linear X-Y motorised stage controlled by a stepper motor, where the dispensing rate of the solution and speed of spray head movement are controlled by PC based automation. The sprayer can travel up to 20 cm on X and Y direction with a maximum speed of 800 mm/sec and 12 mm/sec respectively. The maximum substrate temperature that can be obtained from the heater was 650°C, and the maximum area that can be sprayed was 324 cm<sup>2</sup>. Glass sample of 2×2 cm<sup>2</sup> was used for deposition of CuZnAl. Table 2.1 shows the various parameters used for the experiments.

**Table 2.1: Experimental parameters used for Spray Pyrolysis**

<i>Element</i>	<i>Copper Acetate</i>	<i>Zinc Acetate</i>	<i>Aluminium Chloride</i>
Wt (mg)	1126.33	379.13	166.83
Molar Mass (g/mol)	181.63	183.48	133.34
Density (g/cm <sup>3</sup> )	1.882	1.735	2.48
Melting Point (°C)	115	Decomposes 237	192.4
Purity	99.999%	99.99%	99.999%

An aqueous solution of Copper (II) Acetate, Zinc Acetate and Aluminum Chloride, trace metal basis powders (99.99% purity) procured from Sigma Aldrich was mixed in weight proportions (Cu 70.1%, Al 24.3%, and Zn 5.6%) was mixed with deionized water to make a precursor solution. The percentage of the elements in the chemicals was calculated and precisely weighed using electronic balance (Shimadzu, Model-ATX224). The solution was prepared by dissolving Cu(CH<sub>3</sub>COO)<sub>2</sub>-1126.33 mg, Zn(CH<sub>3</sub>COO)<sub>2</sub>-379.13 mg and AlCl<sub>3</sub>-166.83 mg in 50 ml of deionised water. Diluted NaOH of 5 ml was added to the aqueous solution

to react with the acetate. The details of the chemicals are given in Table 2.2. The solution was stirred using a magnetic stirrer for 30 min before deposition. The flow rate was kept constant at 5 ml/cm and spray duration of 15 seconds was maintained constant for all the substrate temperatures. The motion of XY controller was set to travel 5 mm on each side during the spray. Following the spraying process, the samples were left on the heater for 5-20 seconds before removing.

The decomposition of the chemicals mainly depends on the substrate temperature. The spray droplets will form a uniform and a continuous film only when (i) evaporation of the solvent (ii) spreading of the salt (iii) decomposition of the salt, happens homogeneously. If the substrate temperature is too low, the droplet will hit the substrate and splash and thereby create voids in the films, and if it is too high, it might lead to vaporising of the chemical before reaching the substrate. Optimizing the deposition temperature will affect the material properties drastically. Hence experiments were performed with different substrate temperatures ranging from 250 – 450 °C with 50 °C intervals and the optimum substrate temperature to obtain thin film without defects was found.

**Table 2.2: Details the of the chemicals used**

<i>Parameter</i>	<i>Value</i>
Substrate Temperatures (°C)	250, 300, 350, 400, 450
The distance between nozzle and substrate (cm)	15
Carrier gas Pressure	Air at 1.2 bar
Flow Rate (ml/min)	5 ml/min
Flow Duration (sec)	15 sec
Composition (wt%)	Cu 70.1%, Al 24.3%, and Zn 5.6%

The grain size and the evolution of phases were studied using field emission scanning electron microscopy (FE-SEM). Fig. 2.7 (a) - (d) shows the field electron scanning electron microscopic images of the thin films. The grain size measured from SEM images is approximately 700 nm. It was observed that at lower temperature-250 °C, there is a discontinuous film as shown in Fig. 2.7 (b). At 300 °C and 350 °C, the film was brownish in colour with continuous structures when compared to higher temperatures. There were few isolated peaks at 300 °C, but the film at 350 °C appeared to have a more homogeneous structure with firmly packed grains without any peaks or valleys. Moreover, the film was without any

hollows or distortions, which was noticeably present in samples deposited at higher temperatures. Fig 2.7 (e) and 2.7 (f) show that the film deposited at 400 °C and 450 °C which had hollows and large cavities in between.

The morphology of the film is affected by two important factors (I) substrate temperature (II) air pressure. As a result, evaporation rate influenced the morphology [[92,93]]. At lower temperature, the substrate was not having enough nucleation sites for the formation of the continuous film as it was confirmed with XRD plots which showed amorphous nature of the film. At higher temperature, the rate of evaporation is higher, and it leads to an incomplete thermochemical decomposition, which results in discontinues and hollow films. It was observed by the charring of the films at higher temperatures. The effect of thermophoretic force will increase at higher temperatures [[94]], which can be related to the charring of the chemicals. The hollow and discontinuous structures obtained at higher temperatures can be used to prepare low-density films, but they will lack in mechanical and electrical properties.

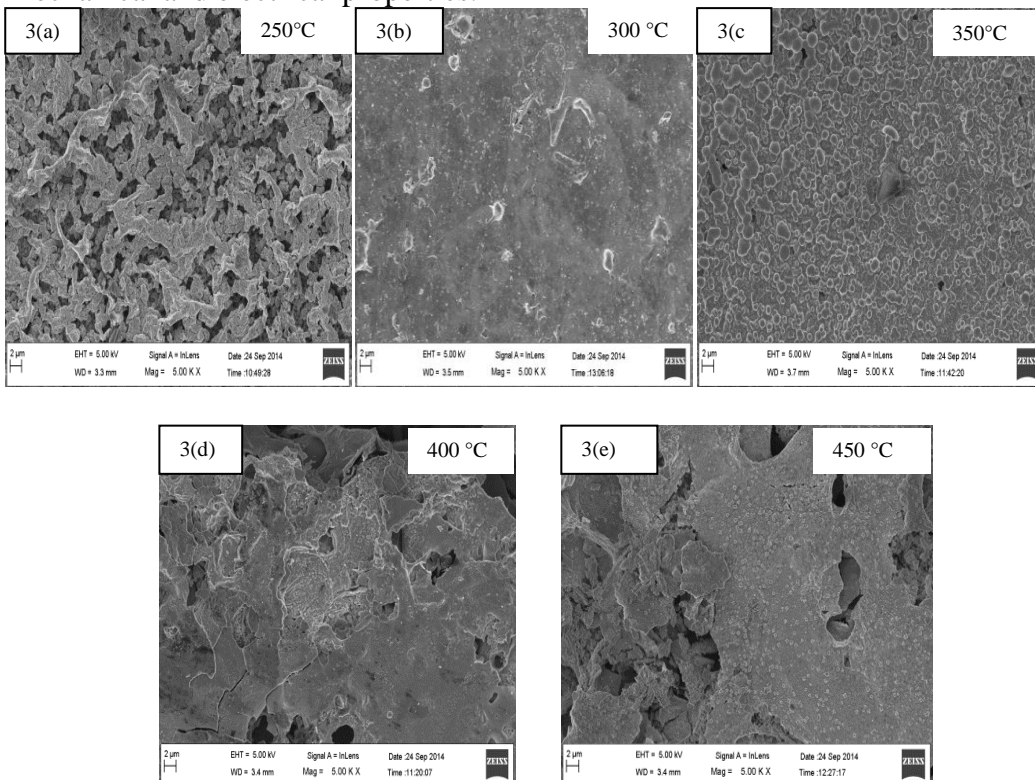


**Figure 2.7: Surface morphological analysis through SEM at different temperatures (a) 250 °C (b) 300 °C (c) 350 °C (d) 400 °C (e) 450 °C**

The composition of the developed samples was found out by taking an average value obtained from five different places in the samples. Table 2.3, shows

the compositions of the deposited samples which was obtained from EDS analysis. There were traces of by products such as C, Cl and Ca and there was variation in the composition of the substrates. The wt % of Al was less as there was difficulty in reducing AlCl<sub>3</sub> to Al which requires a reducing agent [[95,96]]. It requires further understanding of the chemical reaction taking place to improve the composition of the films. The substrate temperatures 300 °C and 350 °C showed a composition close to the initial values.

**Table 2.3: EDS analysis showing the composition of the developed film at different substrate temperature**

<i>Element</i>	<i>250 °C</i>	<i>300 °C</i>	<i>350 °C</i>	<i>400 °C</i>	<i>450 °C</i>
Cu	63.36	64.85	70.20	59.10	56.32
Zn	15.64	14.20	8.83	19.83	22.42
Al	0.67	0.61	0.60	0.71	0.91

The adhesion tests were conducted by scotch tape analysis and the results showed that the adhesion was excellent, with the substrates deposited from 300 °C to 450 °C and there was approximately 0.4 mg, 0.5 mg, 0.5 mg and 0.8 mg of material adhered with the tape after adhesion test. There was a significant amount of material which got adhered to the tape. This shows that the temperature was less for the nucleation and grain growth to happen and thereby to result in a jelly layer which did not adhere to the substrate.

The diffraction pattern of the spray pyrolysis deposited thin film is shown in Fig. 2.8. It showed the presence of at least two different phases of the CuZnAl alloy at different substrate temperature. Along with this, a binary alloy such as CuZn was observed, which agrees with XRD patterns of samples prepared using other synthesis techniques [97–99]. The deformed martensite phase M18R (0018) was present in 300 °C, 350 °C and 400 °C substrate temperature along with secondary peaks (320) were also observed. At 250 °C and 450 °C, the film was amorphous, and there was no structural information corresponding to the alloy, and the erroneous signal was high due to the defects in the developed thin film and was not chosen for further studies. Crystallite size calculated using FWHM from XRD graphs was 16.3 nm. The intensity of the predominant alloy

peak was less, indicating very less alloy formation. The chemical reaction had by-products such as CuOH, CuCl which will hinder the formation of an alloy. There can be few acids which will form during the reaction such as acetic acid and formic acid, which was expected to evaporate at high temperatures, but it can affect the alloy formation by forming oxides and hydroxides. The effect of the aqueous solution, the activation energy required for the chemical reaction and the influence of the other experimental process parameters must be further studied.

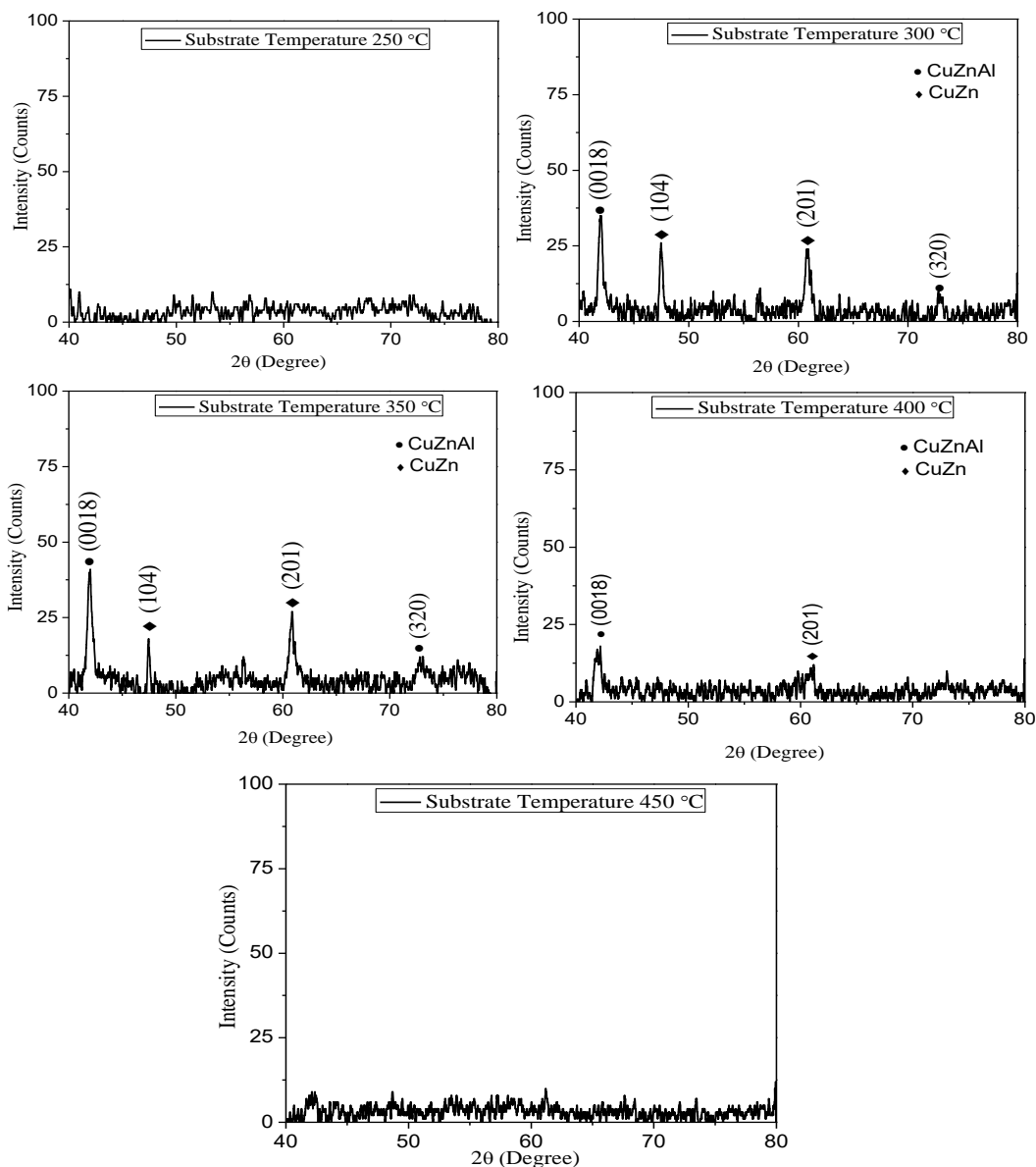


**Figure 2.8: XRD plots at different substrate temperatures (a) 250 °C (b) 300 °C (c) 350 °C (d) 400 °C (e) 450 °C**

Cu based shape memory alloys exhibit shape memory effect in metastable  $\beta$ - phase region based on the  $\{110\}$  basal plane. The parent phase or the high-temperature austenite phase of CuZnAl shape memory alloy has two variants of the

ordered cubic structure; B2 and DO<sub>3</sub> superlattice. The parent phase depends on the type of heat treatment of the alloys during the fabrication. In spray pyrolysis, the thin film undergoes a rapid chemical decomposition results in a disordered martensitic monoclinic structure M18R. In the case of disordered M18R structure [100,101], the ratio of a/b lattice parameters should be less than  $\sqrt{3}/2$  or equal to it. The obtained ratio was 0.82 which is less, confirming the ordered structure from the ordered parent phase.

The M18R peaks (0018) and (320) are obtained while quenching the alloys from high temperature in different conditions. In spray pyrolysis, the deposited film undergoes rapid heating of the deposited solution within a few milliseconds. This can affect the microstructure of the alloy, as the thermal effects play a vital role in obtaining the desired martensitic transformation. This can be overcome by post-thermal treatment of the alloy thin, as reported earlier for bulk materials. The binary alloy CuZn (104), (201) is a metastable state, which also shows shape memory effect. This metastable state is a result of the higher concentrations of the binary elements which might bond with each other during the nucleation process. The probability of Al bonding with Cu or Zn is lesser because of the difficulty in reducing Al. Since the oxidation state of Al is 3, during heating alumina (Al<sub>2</sub>O<sub>3</sub>) will be formed due to its high affinity towards O. Therefore, the formation of a binary alloy of CuZn is more probable.

As the results for samples developed at a substrate temperature of 350 °C was significant, a Differential Scanning Calorimetry (DSC) analysis was conducted. 10 mg powder samples scratched from the glass substrate was used for the analysis, and the results are given in Fig. 2.9. Heating and cooling rate was controlled at 5 °C/min. The transformation temperature for most of the CuZnAl alloys ranges in-between -100 °C – 100 °C [10,44]. The predominant structure M18R plays a vital role in the phase transformation and the initial composition used had austenite temperatures of  $A_s = 30$  °C and  $A_f = 61$  °C [27]. There was an endothermic reaction indicating the transformation temperature of the spray deposited a thin film, which was observed to be  $A_s = 70$  °C  $A_f = 90$  °C. During cooling the martensite transformation was observed at  $M_s = 65$  °C and  $M_f = 55$  °C. For alloys having similar composition, the DSC graph showed a transformation temperature [44]. As the EDS results showed, there is variation in the final composition of the obtained thin films which affects the transformation

temperature. It has also been reported that small change in the Al concentration will affect the transformation temperatures drastically [12]. Thus, the obtained thin film showed some traces of shape memory effect.

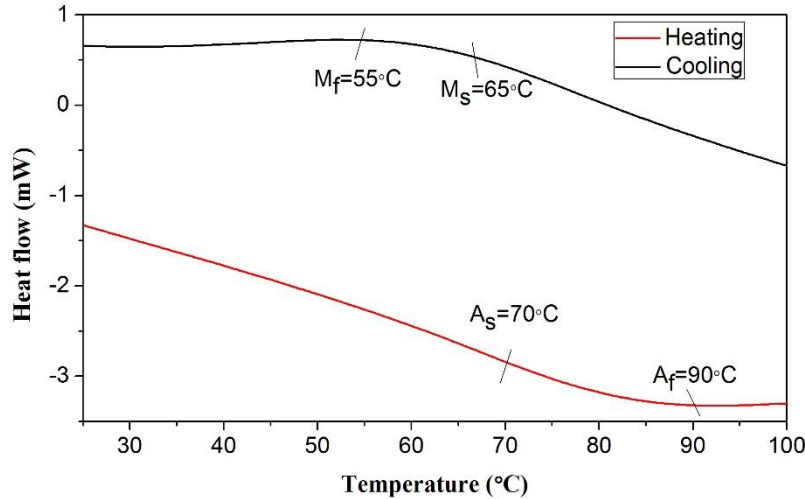


Figure 2.9: DSC thermogram of sample deposited at 350 °C

### 2.8.2 Outcomes of Chemical Deposition of CuZnAl SMA

Suitability of using Spray Pyrolysis in the development of CuZnAl shape memory alloy thin film has been investigated for the first time. The property such as thickness, roughness and adhesion were in good agreement with requirements of a MEMS device. The effect of the deposition at different substrate temperature was investigated, and it was concluded that a substrate temperature of 350 °C was suitable for the development of CuZnAl shape memory alloy thin films. SEM images showed a uniform, and homogeneous film at 350 °C and the measured thickness was 6  $\mu\text{m}$ . the roughness of the deposited samples was high due to the periodic crest and trough formation during deposition. The XRD results exhibited the presence of ternary CuZnAl alloy. DSC thermogram showed a trivial signal which can be due to the shape memory effect, and the transformation temperature was observed to in the region of  $A_s = 70^\circ\text{C}$  and  $A_f = 90^\circ\text{C}$ , and  $M_s = 55^\circ\text{C}$  and  $M_f = 65^\circ\text{C}$ . However further work is required in studying the shape memory properties and their different phase transformation temperatures so that it can test in practical applications.

### 2.8.3 Physical Vapour Deposition of CuZnAl

Cu-Zn-Al/Polyimide bimorph has been developed by a direct thermal evaporation method on pre-strained polyimide. An alloy composition of Cu-Zn 33.1 %-Al 1.3 % (wt %), was used for the deposition process. The deposition was carried without substrate heating and with substrate heating of 100 °C. Figure 2.10 (a) – (d) shows the SEM images of the samples deposited at different substrate temperatures. In Fig. 2.10 (a) the surface morphology of CuZnAl/polyimide deposited without substrate heating is shown, and it is a smooth surface with a few random peaks of buried particles and no pores. Fig. 2.10 (c) shows the surface morphology of CuZnAl/Polyimide bimorph deposited at 100 °C, which has cracks all over the film.

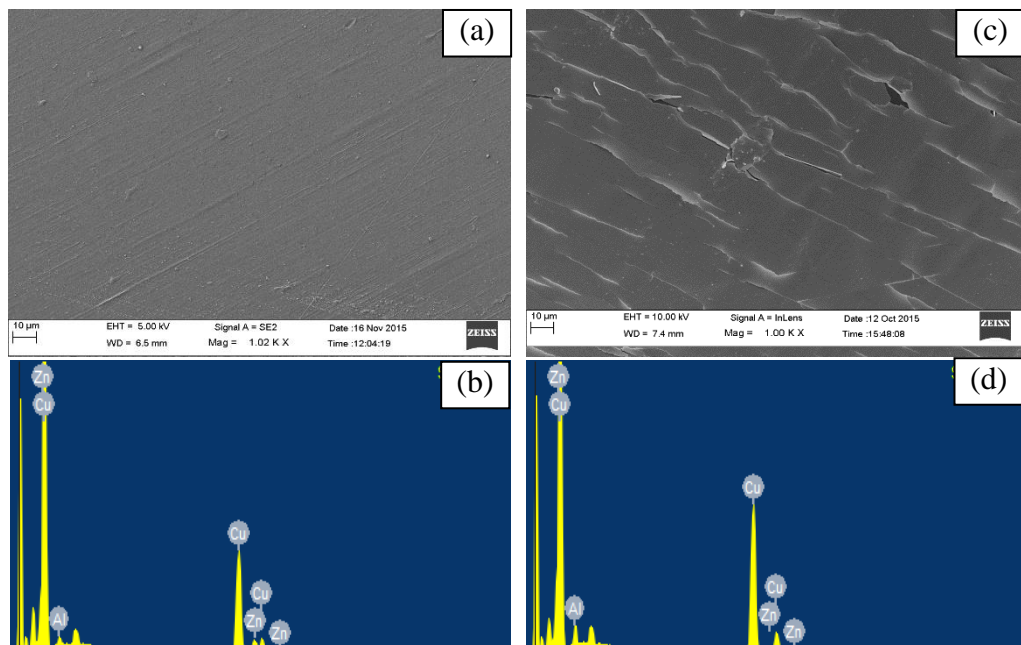


**Figure 2.10: SEM analysis: (a) & (b) SEM and EDS of sample deposited without substrate heating (c) & (d) EDS of samples developed at 100 °C**

It can be observed that the samples developed without heating had less than 100 nm grains, whereas the samples prepared with substrate heating had grains larger than 300 nm. Further, there were precipitates which might belong to Zn due to its low melting point. There have been reports suggesting the loss of Zn. From the microscopic images, it can be concluded that the samples deposited without substrate heating might be more suitable for MEMS devices as their bonding and morphology seem to be uniform. However, the EDS results showed that samples deposited at 100 °C had more closeness in weight % to the initial composition of

the alloy. There have been several reports on the large grain size in CuZnAl alloys which might be the case.

The adhesion of the film was tested using a scotch tape analysis where the difference in weight of the sample before and after the test is used as an indication. Table 2.4 shows the adhesion test results. It can be observed that the difference in weight was significant for the samples deposited without substrate heating. 17.6 mg of sample adhered to the tape, which indicated poor adhesion. Whereas the

**Table 2.4: Adhesion test results after Scotch tape analysis**

<i>Substrate Temperature (°C)</i>	<i>The weight of the tape before testing (mg)</i>	<i>The weight of the tape after testing (mg)</i>	<i>The weight of the adhered material (mg)</i>
Without Heating	178.4	160.8	17.6
100 °C	175.6	171.7	3.9

samples deposited with substrate temperature showed good adhesion. Very less sample of 3.9 mg adhered with the tape. The variation in adherence can be attributed to the presence of nucleation sites at higher temperatures. The deposition process can be divided into three steps, where the first step is to melt the metal. When the pellets are in a molten state, the current flowing through the tungsten boat is increased rapidly. The melt evaporates and propagates towards the substrate. The second and third process cannot be controlled. The evaporated material in vapour phase forms a continuous film on the substrate. The film is affected by the surface energy and the surface tension of the materials used. The surface energy of the substrate can vary with temperature[32].

**Table 2.5: Composition analysis from EDS of CuZnAl**

<i>Element</i>	<i>Cu (Atomic %)</i>	<i>Al (Atomic %)</i>	<i>Zn (Atomic %)</i>
Without Heating	67.87 %	1.63 %	30.5 %
At 100°C	65.3 %	1.6 %	33.1 %

Energy dispersive spectroscopy (EDS) was used for the composition analysis. An average of ten readings taken at different places on the samples is summarized in Table 2.5. The samples developed without substrate heating showed more percentage of copper, and there was a decrease in Aluminium percentage. However, with 100 °C, the average composition measured was in agreement with the initial composition.

At higher temperatures, the time take for the material in the vapour phase to form a film is longer. At room temperature, the film is formed rapidly and thus leading to inhomogeneous film [105]. However, it was not observed at higher temperatures, as the results displayed a homogenous film. Fig. 2.11, presents the XRD plot of all the samples developed. The samples deposited with substrate heating showed M18R peak, which was not observed with sample deposited at 100 °C. There were two martensite peaks M18R' at  $2\theta = 42^\circ 7'$ ,  $\beta$  phase formation observed at  $2\theta = 43^\circ 56'$ . Crystallite size was calculated using the Scherrer formula[106]: Where 'd' is for crystallite size,  $\lambda$  stands for wavelength of the X-Radiation used, B is the peak width at half the intensity, and  $\theta$  is the Bragg angle. Using the Scherrer formula, the calculated grain size of sample developed without substrate heating was found to be 18.41 nm, and with substrate heating was 12.45 nm respectively. The  $\beta$  (200) phase relatively has an ordered structure and has a lattice parameter of 0.58707 nm [107]. Here, the high temperature  $\beta$  phase is disordered bcc, but upon cooling it to ambient temperature ordering occurs into B2

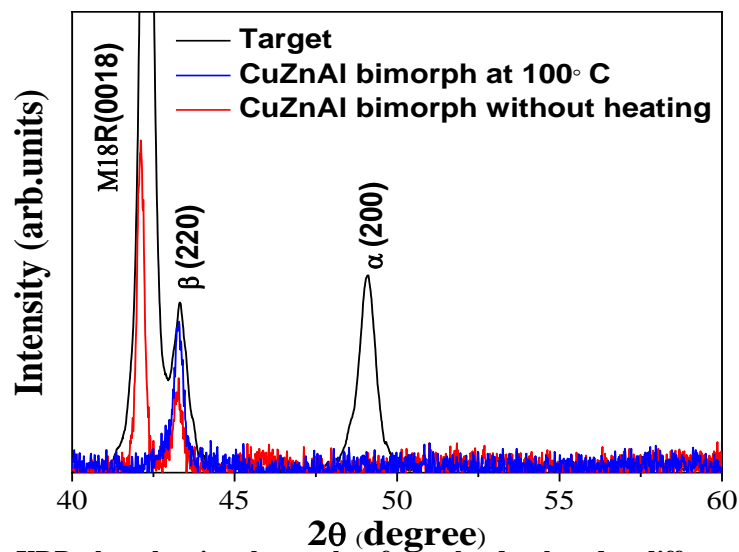


Figure 2.11: XRD plots showing the results of samples developed at different substrate temperatures.

or DO<sub>3</sub>, (or L2,) type structure, and then transforms into or 18R martensite with or without further cooling, depending on alloy composition [90,108]. When the Al content becomes higher, the  $\beta$  phase is susceptible to decomposition into  $\alpha$  fcc primary solid solution of Cu) and  $\gamma$  (Cu, Zn, cubic phase) at around 700 K. However at substrate temperature of 100 °C, the M18R peak was not visible and the  $\beta$  phase was more predominant [109]. This shows that the samples developed

had a prevalent  $\beta$  phase with a more crystalline structure. The diffractogram matched with the structural information of the initial target which had a major M18R peak. This might be due to the target preparation process.

#### **2.8.4 Outcomes of Physical Vapour Deposition of CuZnAl SMA**

CuZnAl/Polyimide composite structures were developed through thermal evaporation, and the structural and morphological studies were probed. The composition of the developed samples was in agreement with the initial composition and adhesion of the film to the substrate was excellent. The grain size was found to be less than 100 nm which has not been reported elsewhere for CuZnAl alloy. Further, the XRD results display the crystalline  $\beta$  phase formation which is a promising result to achieve shape memory effect. Further, the samples developed with substrate temperature showed better structural information. However, due to zinc low vapour pressure, the deposition process was contaminated results in poor reproducibility. Further, Zn melting point is 420 °C which makes it difficult to develop alloys with shape memory effect. As the alloys are highly sensitive to composition, the composition control with the deposition system was difficult.

#### **2.9 Approach for Developing CuAlNi Thin Films**

The preliminary results with CuAlNi displayed excellent structural and morphological properties were chosen for further studies. The primary limitation of CuAlNi shape memory alloy is its poor ductility, which leads to a drastic decline in its cyclic behaviour. The poor ductility is observed in bulk samples predominantly, which is due to high cooling rates for obtaining stable martensite structures. As the majority of thin film deposition techniques has rapid cooling rates, the issues with precipitates formation have not been observed widely. However, a deposition technique which satisfies the present requirements was chosen, and the investigations on deposition parameters were performed in detail. Fig. 2.15 shows the design of experiments that were performed in the present work for developing CuAlNi bimorphs. Parameters such as composition, substrate thickness, growth substrate temperature and the addition of a quaternary element

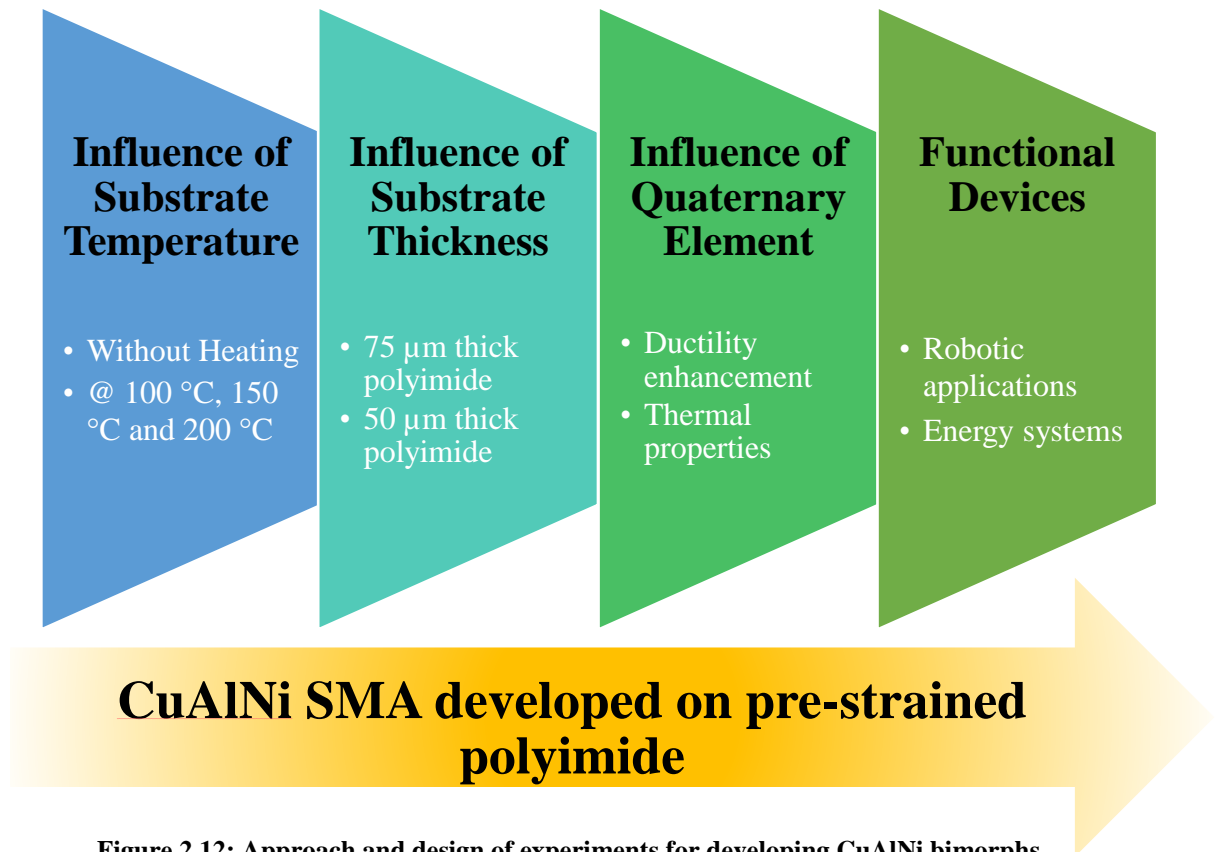


**Figure 2.12: Approach and design of experiments for developing CuAlNi bimorphs** to the ternary CuAlNi alloy could result in better overall properties. The problems related to training has been overlooked by using a pre-strained flexible substrate, which can assist during cyclic loading and unloading. Polyimide (PI) substrates are

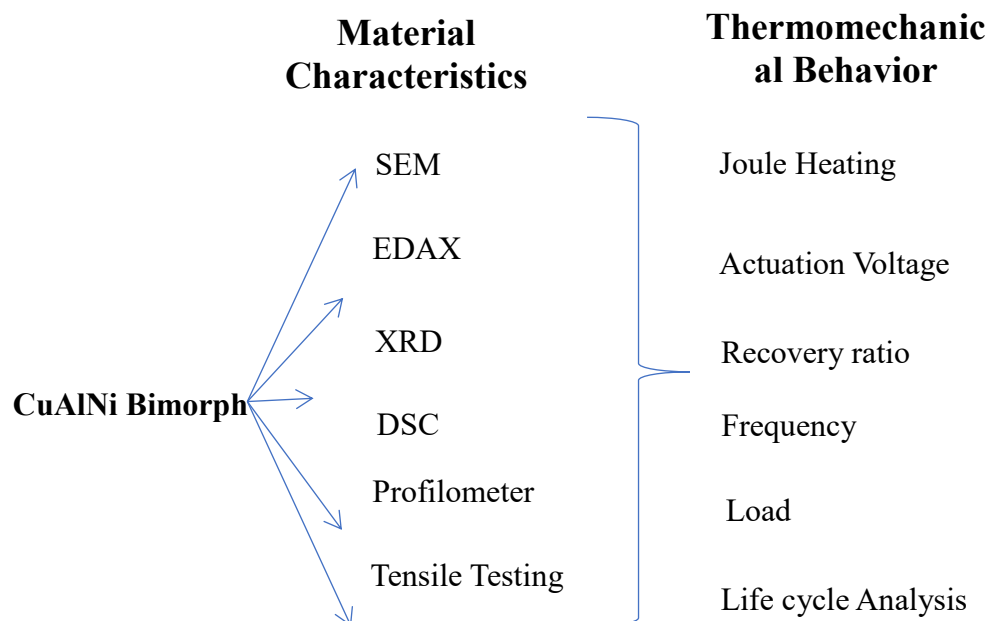


**Figure 2.13: Flow chart displaying the various characterization techniques and various thermomechanical parameters used for analysis.**

recently being used for the development of microactuators. SMA/Polyimide bimorphs are flexible films which are more suitable for microactuators, as the return stroke during the thermomechanical cycle is accomplished by the bias force of the flexible substrate. Further, the flexible substrates can be obtained in several other shapes according to the requirement and can be used in pre-strained condition during deposition to avoid the training process performed after deposition. Fig. 2.16 shows the various methodologies utilized for characterizing the developed CuAlNi bimorphs.

## **2.10 Summary**

The importance of obtaining stable martensite structures are fundamental in achieving shape memory effect. Further, the training process as report mostly for the bulk materials is practically impossible for thin film SMA. Further, the addition of a ternary and quaternary element to binary CuZn and CuAl is primarily performed to tune the transformation temperatures. The literature indicates the life cycle behaviour of copper-based alloys are hindered by several factors such as precipitates, composition, and brittleness. However, these issues are predominant in thin films due to rapid cooling rates with deposition techniques. The preliminary results with CuZnAl indicated the partial alloy formation with chemical technique. Further, with physical vapour deposition, maintaining the composition precisely was difficult due to Zn low melting point. CuAlNi, having significant advantages was chosen for analysis. The issue related to training was overlooked by utilizing a pre-strained polyimide sheet.

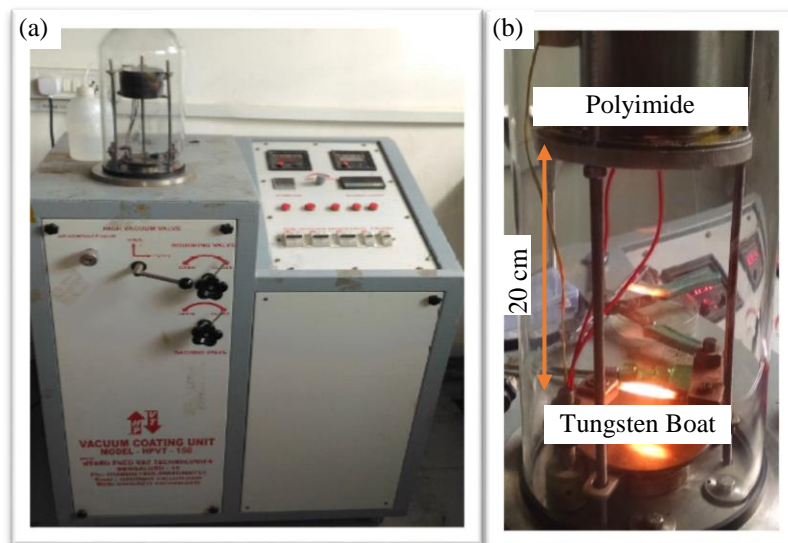
## Chapter 3

# Experimental Specifications and Theory of SMA Bimorphs

The thin film deposition was carried out by realizing a physical vapour deposition (PVD) technique. Among different techniques, PVD is considered to be one of the straightforward methods for developing thin film, where the material to be deposited was placed in a crucible and evaporated by resistance heating. The normally used crucible material is tungsten due to its high melting point. The influencing parameters of the deposition process include (i) the distance between the crucible (boat) and substrate (ii) rate of deposition (iii) nature of the substrate. This chapter will discuss the experimental procedure, pre-straining of polyimide, thermomechanical behaviour setup used for the actuation studies and the other material characterization techniques used.

### 3.1 Thermal Physical Vapour Deposition System

The thermal evaporation technique has a small chamber, which was vacuumized until 0.001 MPa through rotary and diffusion pumps. The material to be deposited was placed in the crucible, and the evaporation was carried out in two steps. The first step was to increase the temperature to melt the alloy pellets. The current was increased to the eutectoid temperature and left for 30 s until the material present in the crucible is entirely melted. The second step was to rapidly



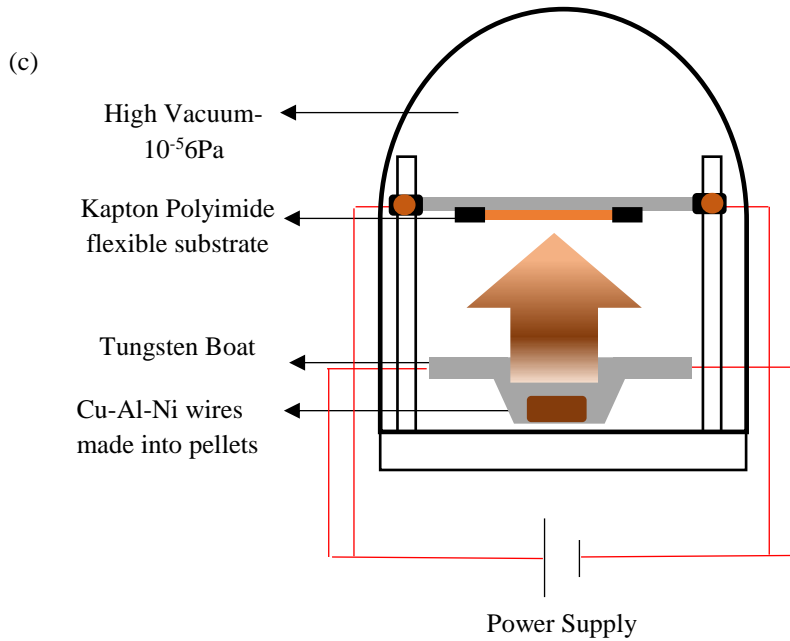


**Figure 3.5: Images showing (a) deposition unit (b) chamber with the crucible and substrate holder (c) block diagram of the thermal evaporation system**

increase the current flow to the crucible until the molten material was completely evaporated. By following this step by step process, the adhesion of the deposited film was excellent. Minor variations in the current resulted in poor quality films. Fig. 3.1 shows the images of (a) the deposition unit, (b) the electrodes, substrate holder and the crucible (c) the block diagram of the thermal evaporation system.

### 3.1.1 Deposition Parameters and Pellet Preparation

CuAlNi/polyimide bimorphs have been developed through direct thermal evaporation method. The alloy targets of composition Cu – 84.5 wt%, Al – 11.5 wt % and Ni – 4 wt % were procured and were of 99.99% purity. The alloy pellets were weighed to be 100 mg for each deposition process, as higher amounts resulted in poor adhesion of SMA film to the substrate. The substrates were cleaned with acetone and washed with distilled water. After drying, the substrates were baked in the oven at 200 °C for one hr. Further plasma etching was performed before the deposition process at much lower vacuum. Fig. 3.2 shows the images of (a) Cu-based SMA targets (b) Plasma etching setup.

The substrates were placed 20 cm above the crucible, as depositions carried out by placing substrates below 20 cm resulted in a black or improper deposition. Initially, three different substrates were taken for the deposition process. The suitability of conventional substrate in the alloy formation was probed, and

preliminary analysis by etching the substrate to obtain free-standing film was investigated. Table 3.1 shows the deposition parameters utilised in developing CuAlNi thin film on various substrates.

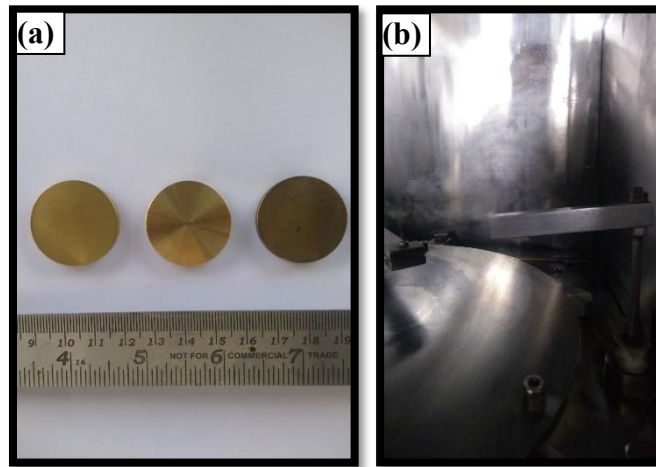


Figure 3.6: Pictures of (a) CuAlNi targets of various composition (b) Plasma etching used for cleaning the substrates

Table 3.1: Parameters used for the deposition process

<i>Parameters</i>	<i>Value</i>
Substrate	Polyimide Sheet
Thickness of deposited film	$\approx 100 \mu\text{m}$
Pellet Holder	Tungsten crucible
Distance between crucible and substrate	20 cm
Current	$\approx 140 \text{ A}$
Composition	Cu 84.5 wt%, Al 11.5 wt%, Ni 4 wt%
Substrate heating	Without Heating

### 3.2 Theory of SMA Bimorph

The principal reason for employing a flexible substrate was to obtain two-way shape memory effect without any post-processing. Shape training is often performed for obtaining two-way shape memory effect. Conventionally, the application of external load was preferred to avoid two-way training observed in an application such as micropumps. The SMA material used as a diaphragm will be at twinned martensite phase at room temperature. By the flow of liquid, the

diaphragm will be strained to form detwinned martensite. After a critical strain level, the SMA will be actuated to transform from detwinned martensite to austenite. Shape change accompanies the phase change, and the liquid will be pumped out. In the absence of external load in an application such as microgripper, the alloy has to be trained to remember different shapes at different phases to clamp and release objects. The training process involves constraining the alloy in the required shapes and exposing it to heating and cooling cycles. The thermal cycles have to be at the particular temperature, and it has to be carried out for 50 – 100 cycles. It remains practically impossible to train SMA thin films as it might disintegrate.

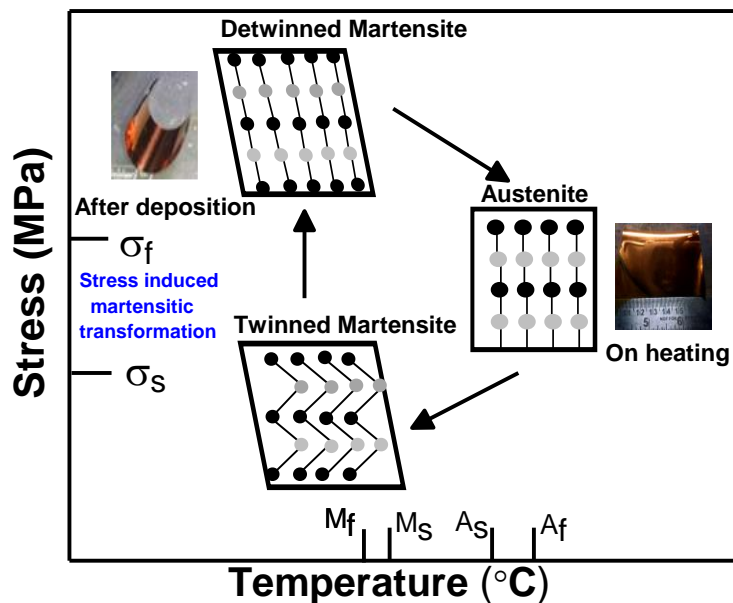


**Figure 3.3: Graph showing the different transformation temperatures, phase change and shape memory effect exhibited by sample developed at 150 °C without any post-processing**

To overcome the training process required after deposition, an approach of pre-straining the flexible sheets was chosen. The theory behind the actuation of pre-strained SMA/polyimide film is shown in Fig. 3.3. The flexible polyimide substrate has a curved shape, which was strained before depositing SMA thin film. The film deposited on the constrained polyimide will be in the twinned martensite phase. Once the constraints are removed after deposition, the flexible substrate will induce the shape change by returning to original shape and forming detwinned martensitic phase in SMA thin film. On heating, the film will try to relieve the stress induced due to the flexible substrate by changing to the austenite phase, and will eventually lead to shape change. On cooling, the flexible substrate will again try to regain its original shape and thereby inducing the stress required for cyclic

behaviour. The pre-straining of the polyimide during deposition is displayed in Fig. 3.4 (a) and (b). Further, the shape memory effect exhibited by the bimorphs during heating and cooling is shown in Fig. 3.4 (c) and (d). The method of pre-straining

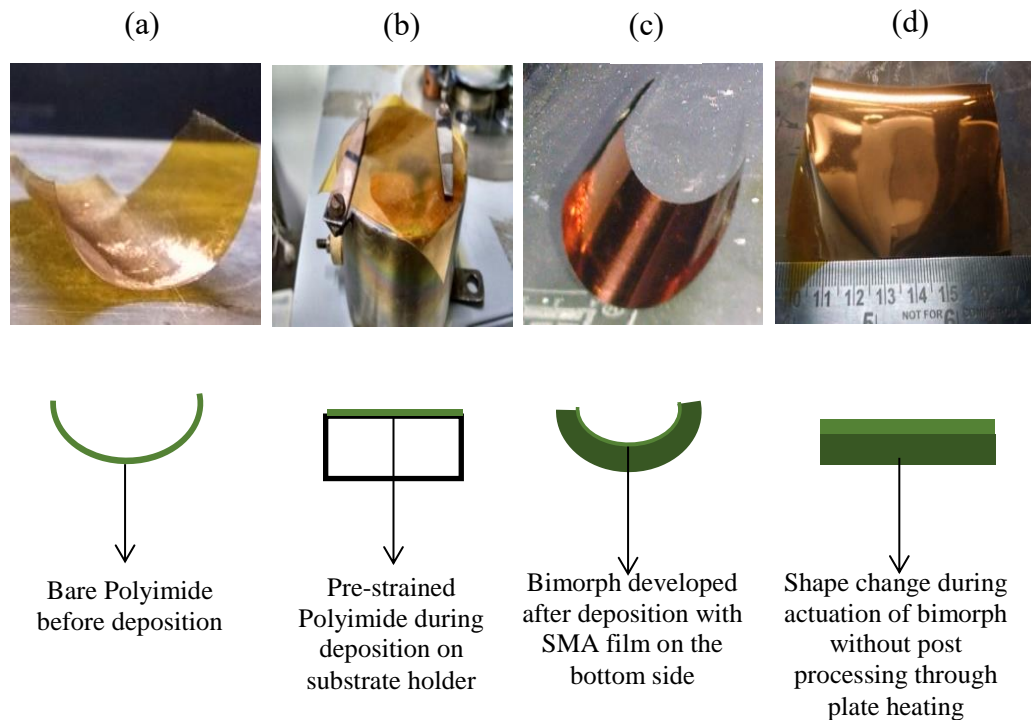


**Figure 3.4: Images showing (a) bare polyimide substrate (b) pre-straining (c) bimorph after deposition and (d) bimorph on actuation**

can be varied to obtain different shapes as required by the application.

### 3.3 Characterization Utilized for the Analysis

The developed samples were characterized with the techniques as shown in Fig. 3.5. The scanning electron microscopic (FE-SEM) and energy dispersive x-ray analysis (EDX) were carried out by SUPRA55 Zeiss for analysing the surface morphology and composition of the bimorphs. The samples were placed on a glass slide with the help of conductive tape. The composition was measured at five different locations, and the average values were considered. The surface morphology was inspected at a different magnification ranging from 100 X to 75 KX. The adhesion test was carried out using scotch tape analysis. The scotch tape of particular weight was stuck to the film with uniform pressure. After few minutes, the tape was removed and weighed. The material adhered to the tape was employed as a scale to measure the adhesively of the film. X-Ray Diffraction (XRD) patterns were recorded by RIGAKU SMARTLAB instrument using monochromatic Cu K $\alpha$  (1.541 Å) radiation. The measurement was conducted between 20° to 80° of 2 $\theta$

angle. The thickness of the samples was measured using Marsurf LD 130 Roughness and Contour profile measurement. The measurements are carried out at room temperature and atmospheric pressure. A stylus with a tip radius of 12.5 $\mu$ m was moved vertically in contact with the sample to a specified distance and specified contact force. The difference in height, between sample and needle, is measured and a step height profile is generated. The instrument can measure small variations in vertical stylus displacement, with a vertical resolution of 100 nm, as a function of position. Further, the transformation temperatures of the bimorphs were measured using both Four- probe Vander pauw method and differential scanning calorimetry (DSC – Netzch). The silver conductive paste was used for the four probe technique, and the heating rate was controlled at 5 °C/min. The sample was allowed to cool down to room temperature by natural convection. Samples weight of 10 mg was used for the DSC analysis, and the heating/cooling rate was maintained at 5 °C/min. The thermal analysis was extended by capturing thermal images from FLIR thermal camera.

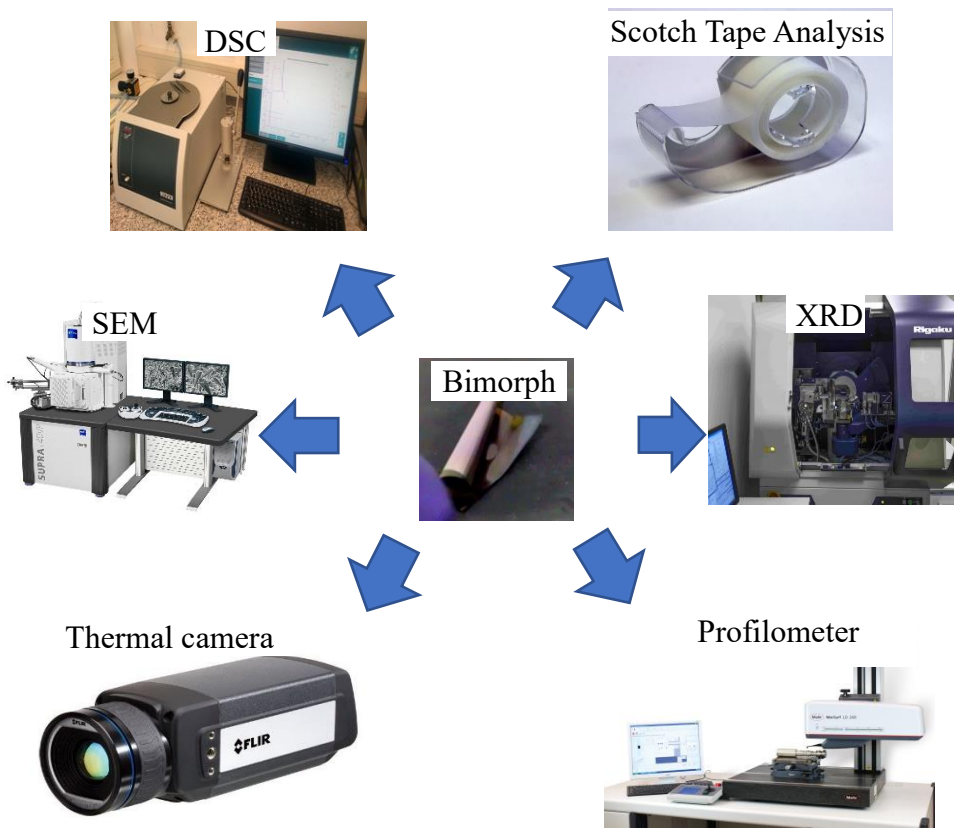


**Figure 3.5: Characterization techniques used for analyzing the bimorphs**

### 3.4. Thermomechanical analysis setup

The actuation behaviour of the bimorphs has to be investigated thoroughly before considering it for potential applications. To probe the suitability of the developed bimorph in MEMS microactuator application, two different actuation systems were utilised (i) Joule heating (ii) Plate heating. Joule heating was selected, as it can be used in wide range of applications.

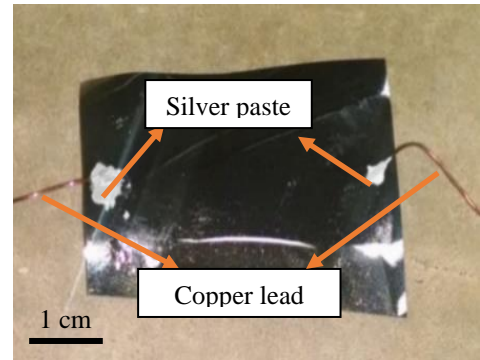


**Figure 3.6: Initial setup with silver paste and copper contacts.**

Initially, the bimorphs were connected with copper contacts using silver paste as shown in Fig. 3.6 for Joule heating. However, due to mechanical movement of the samples, the conductive paste was not withstanding the actuation for large cycles. Further, the temperature was also affecting the contacts. A flat mouth connector was clamped to the bimorphs without damaging the film, and the experiments were conducted.

#### 3.4.1 Joule Heating Setup

An image of the electrical actuation setup was utilised as shown in Fig. 3.7 (a). It consists of K-type thermocouple, data acquisition system with 22 channels (Model: 34970 A, Agilent) and programmable power supply. The heating and cooling cycles were recorded by a laser displacement sensor (Model: HLG108-A-C5, Panasonic). Different voltages were used for the analysis. Fig. 3.7 (b) shows the block diagram of the thermomechanical and life cycle analysis setup. Using the setup three different frequencies of 0.25 Hz, 0.33 Hz and 0.5 Hz was exercised. To obtain the maximum displacement of the bimorph at different voltages, 0.05 Hz was utilised. The fatigue life was tested for 15,000 cycles, and the results are summarized.

#### 3.4.2 Substrate Heating Setup

For the recovery ratio analysis, a plate heater was utilised to find out the maximum displacement. A graph sheet was placed behind the heater, and the change in curvature was photographed at a different temperature as shown in Fig.

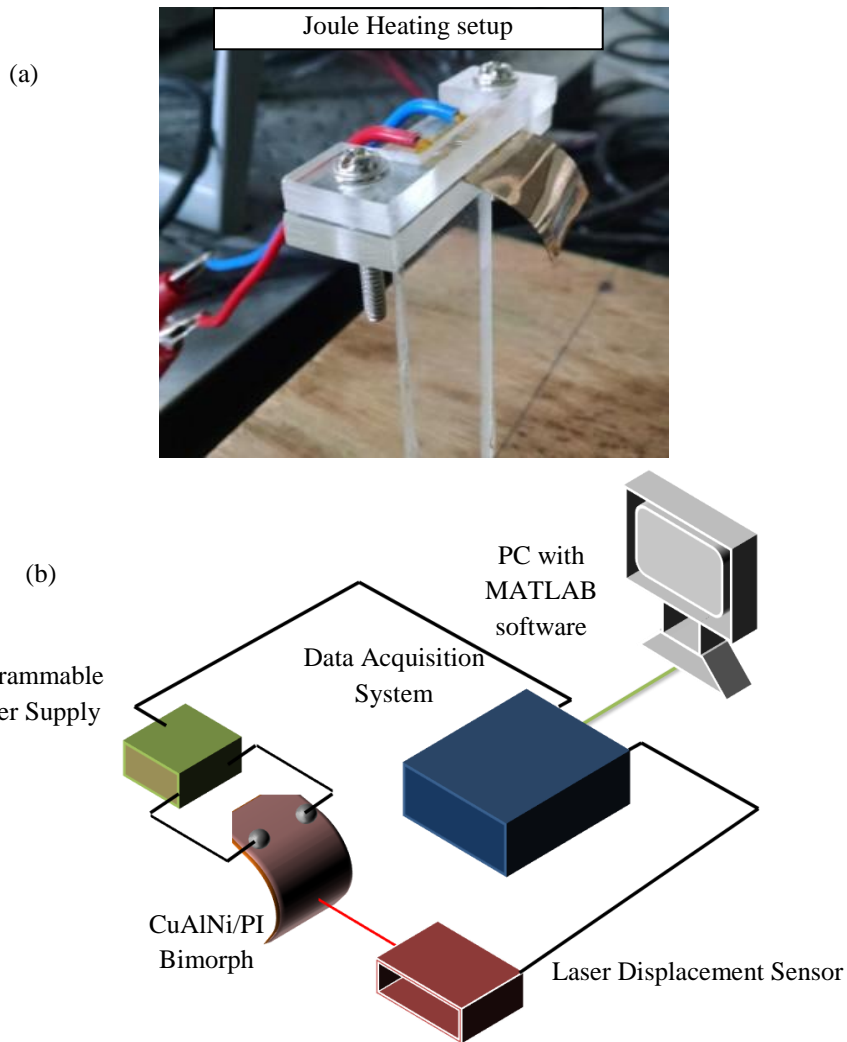


**Figure 3.7: Images showing the pictures of (a) the bimorph cut into small samples for electrical actuation (b) block diagram of the electrical actuation setup**

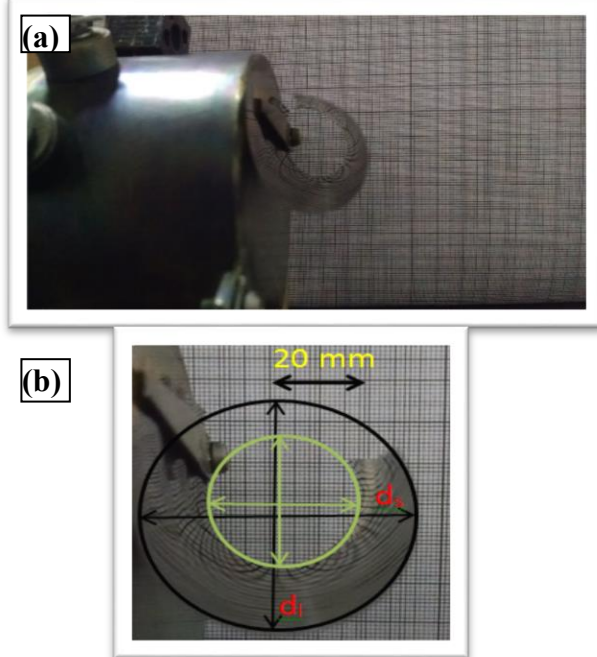


**Figure 3.8: (a) Bimorph heated with plate heater (b) the measurement used for recovery ratio analysis**

3.8 (a) and 3.8 (b). The experiments aided in finding out the change in curvature at

specified temperatures.

$$D_{temp} = (d_l + d_s)/2 \quad (4.1)$$

$$D_R = D_{temp}/D_{RT} \quad (4.2)$$

Where  $d_l$  and  $d_s$  are the length and breadth of the inner and outer surface and  $DR$  is the recovery ratio.  $D_{RT}$  and  $D_{temp}$  are the ratios at each temperature interval. Quantified analysis of the shape change and the temperature effect of phase transformation was possible with this technique.

### 3.5 Micro Universal Testing Machine

To analyse the stress-strain behaviour of the developed bimorphs, an in-house established tensile testing instrument was utilised. The clamps as shown in Fig. 3.9, were specially designed to exert uniform tension throughout the bimorph during operation. Fig. 3.10 (a) shows the block diagram of the tensile testing equipment and Fig. 3.10 (b) shows the image of the system with clamping design utilised for the testing process. The tensile testing equipment was employed with a commercially available load cell (Rudrra RS-302) of 5 kgf with a sensitivity of 2 mV/V to measure the applied load. A stepper motor and low-pitch lead screw interfaced with Arduino was utilised for smooth application of load.

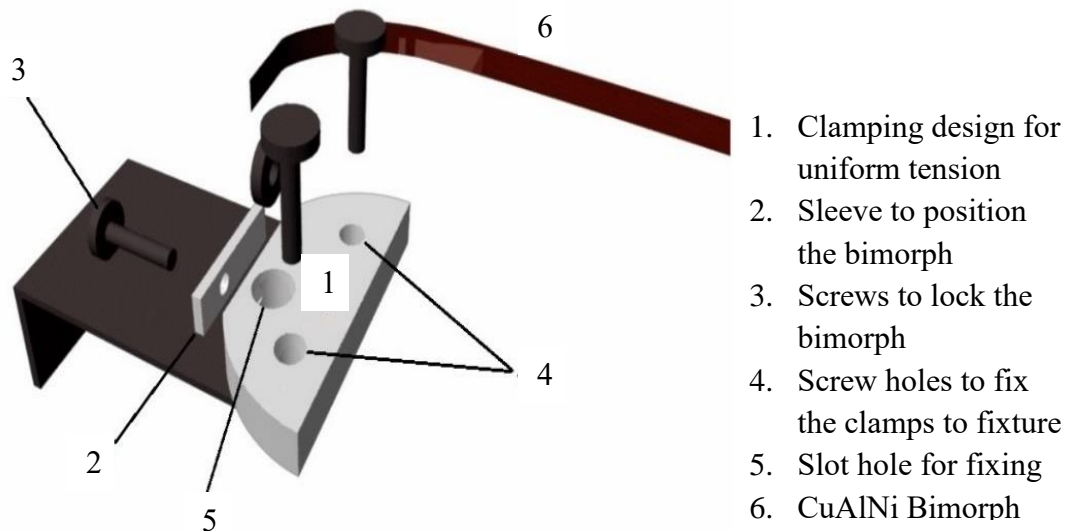


**Figure 3.9: Image shows the clamping design utilized for uniform tension**

The UTM includes the following components for specific functions:

1. Use of high precision load cell. with 5 kgf and sensitivity of 2 mV/V can be used to measure the applied load.

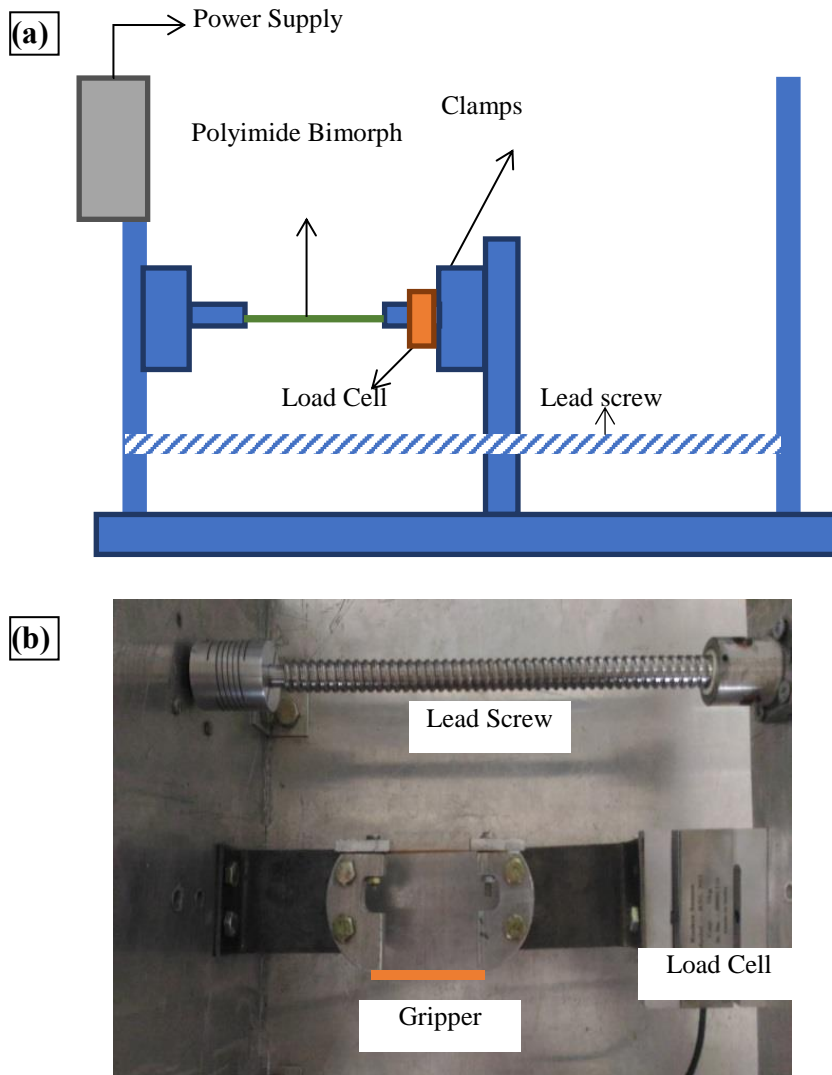


**Figure 3.10: (a) Block diagram of the micro tensile testing equipment (b) Image of the clamp utilized for the testing process.**

2. Amplifier: Instrumentational Amplifier was used to amplify the load cell signal and to reduce the error in signal processing to increase accuracy.
3. Stepper motor and low-pitch lead screw for smooth application of load.
4. Controller module: It was used as an interface between electronic system software and machine, as it takes value from the software and converts them into an electric signal to run the machine. Simultaneously, it also takes the signal from the load cell and sends them to software.
5. Displacement Measurement: The RPM of the motor can be used to calculate the linear displacement of the cross-head. In an alternate embodiment, the linear displacement of the cross-head can also be measured by incorporating non-contact type sensors such as laser displacement sensors or LVDT.

The steps involved in operating the UTM as shown in Fig. 3.11 are

Step 1: Switch on the power supply of the instrument and connect the USB cable from the microcontroller to the electronic system.

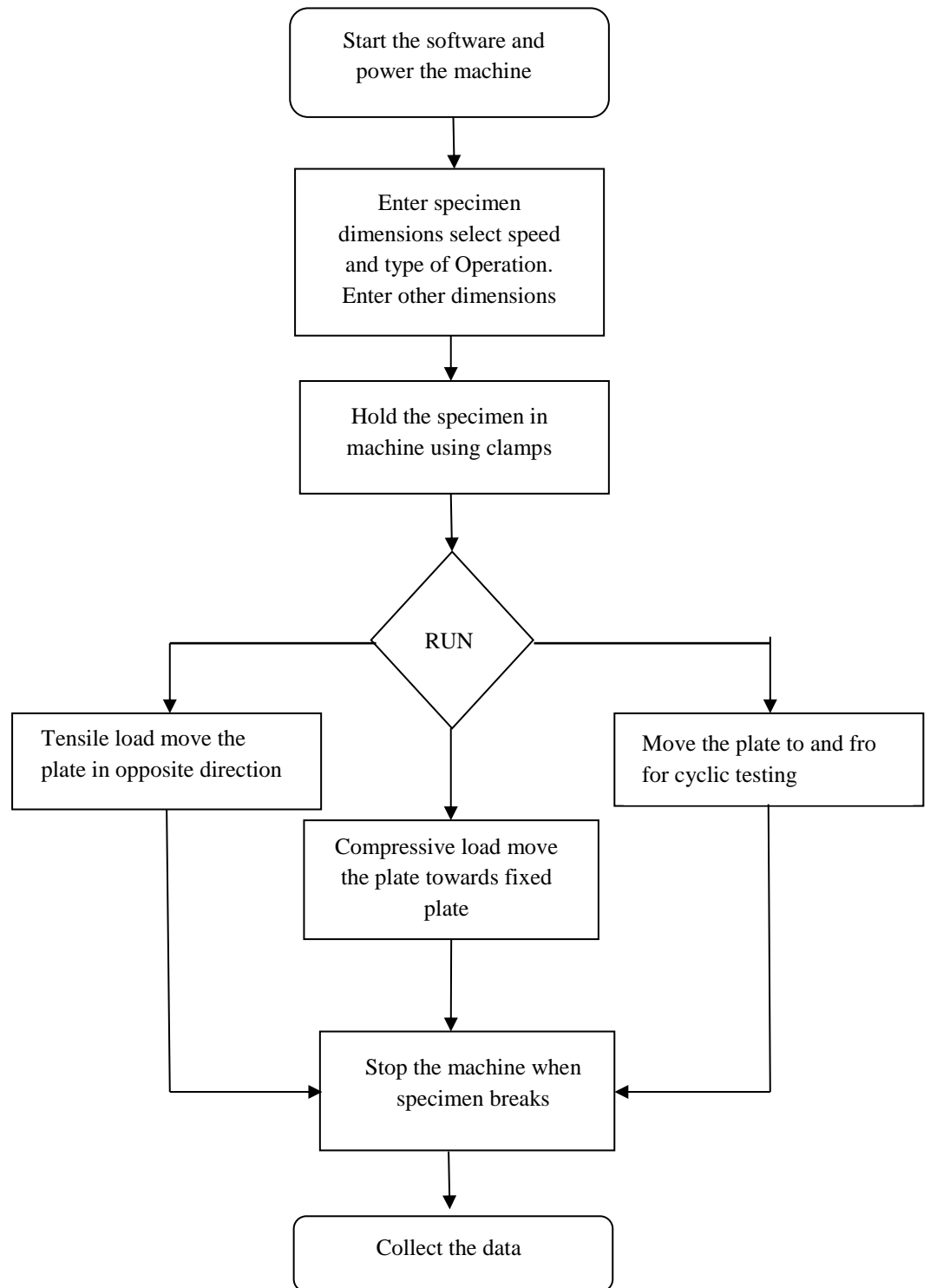


**Figure 3.11.** Illustrates the flow chart for the testing process using the UTM

Step 2: Using the interface on the electronic system enter the properties of the thin film sheet to be tested such as width, length, and thickness in the software window.

Step 3: Select the type of operation.

Operation 1 - Loading until failure to find out maximum tensile strength

Operation 2 – Compressive loading to find the compressive force

Operation 3 – Cyclic loading and unloading below maximum stress value

Step 4: Fix the polyimide sheet to the clamps, which provides uniform load distribution.

Step 5: Run the program.

Step 6: Once the program is complete, the data from the load cell will be saved.

### 3.6 Summary

- The physical vapour deposition system for developing bimorphs with 100 mg CuAlNi pellets was found suitable.
- Pre-cleaning methods with plasma etching were utilized before deposition on the deposition of 7 cm<sup>2</sup> bimorphs.
- The in-house developed Joule heating system for analysing the actuation behaviour with laser displacement sensor of 2 cm<sup>2</sup> bimorphs.
- Various actuation parameters such as voltage (1 V – 3 V), frequency (0.25 Hz – 3 Hz), and load (30 mg – 60 mg) was investigated in detail with the setup.
- The recovery ratio calculation through plate heating with curvature change of bimorphs of 7 cm.
- In-house developed micro-tensile testing system for study the mechanical property of 2 cm x 20 cm CuAlNi bimorph.
- The clamps were specially designed to exert uniform tension while testing.

## Chapter 4

---

# Parametric Investigation on Development of SMA Bimorph

### 4.1 Introduction

CuAlNi/polyimide SMA bimorph has been developed through direct thermal evaporation by depositing on Kapton polyimide sheet. The as developed bimorph exhibited two-way displacement without any post-processing, where the return stroke was achieved with the influence of flexible polyimide substrate. The influence of polyimide substrate thickness and the substrate temperature during deposition was investigated in detail. The developed samples were characterised using SEM, XRD, TGA, temperature vs resistance plot, and DSC. The recovery ratio was calculated for all the developed samples through plate heating. The custom-made setup with electrical heating was utilised to investigate the life cycle of the bimorph at different voltages ranging from 1 - 3 V and different frequencies.

### 4.2 Influence of Different Substrates

The preliminary experiments with three different substrates were conducted by placing all three substrates inside the chamber for deposition. The images of the developed samples are shown in Fig. 4.1 and it was evident the film was of poor quality with the glass substrate. The developed samples were characterised by scanning electron microscopy and X-ray diffraction analysis. The surface morphological analysis displayed uneven surface with peaks and troughs with film developed on a glass substrate. The film on silicon substrate had cracks in various

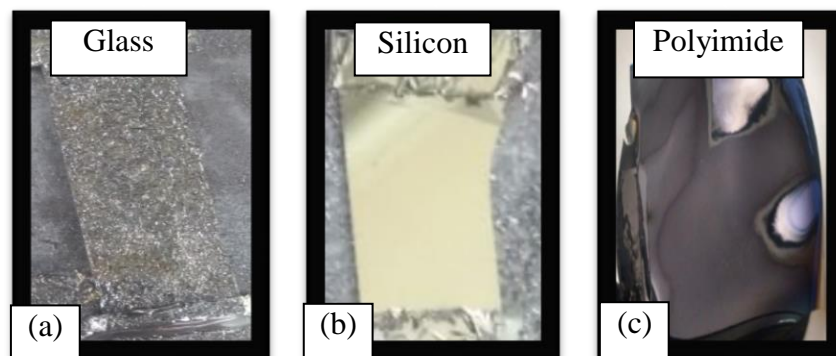
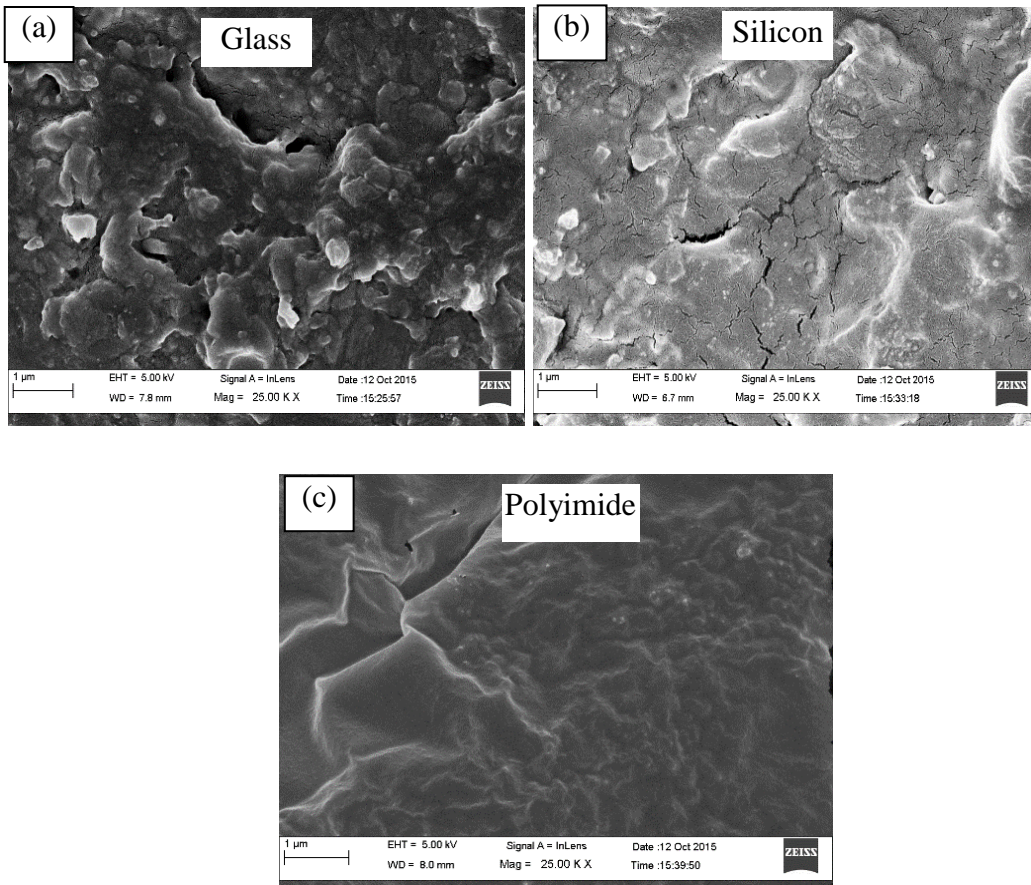
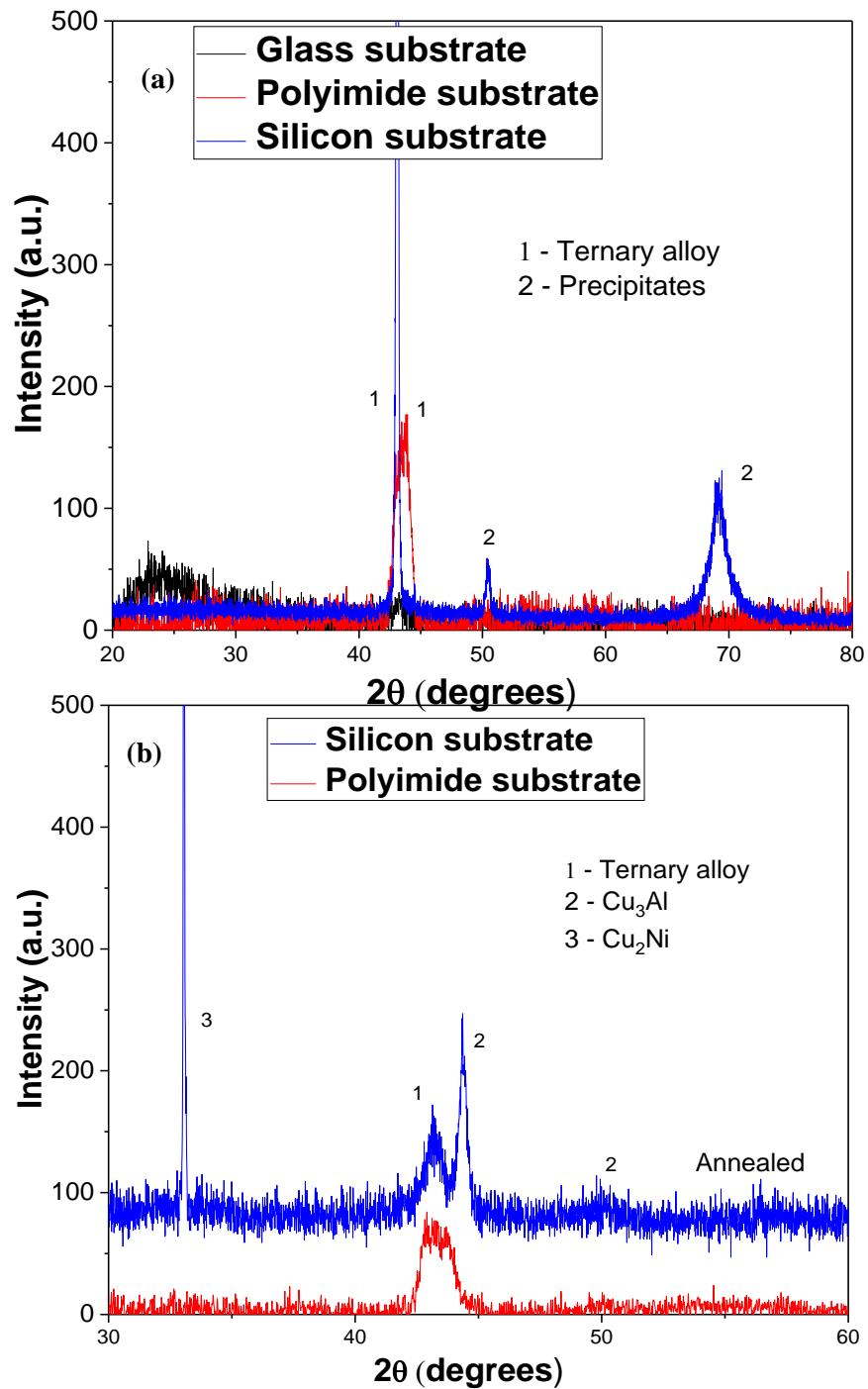


Figure 4.1: Images of the SMA film deposited on (a) Glass (b) Silicon and (c) Polyimide substrates.



**Figure 4.2: SEM images showing the surface morphology of (a) Glass (b) Silicon and (c) Polyimide substrates.**

places. However, the surface was smooth, and the adhesion was excellent. The polyimide substrate displayed excellent adhesive properties, and the morphology exhibited a smooth and uniform surface. Fig. 4.2 displays the scanning electron microscopic images of the film developed on (a) glass, (b) silicon and (c) polyimide substrate. The X-ray diffraction analysis displayed the absence of any significant pattern related to CuAlNi SMA. Generally, the  $\beta$  martensite phase responsible for shape memory effect is observed between  $40^\circ - 50^\circ$  C, as shown in Fig. 4.3 (a). However, the pattern obtained with silicon substrate displayed other secondary phase formation of CuAl. The results with polyimide displayed less intensity diffraction patterns at  $43^\circ$ , which primarily belongs the ternary alloy. To further investigate the alloy formation on a silicon substrate, the samples were annealed at  $400^\circ$  C for 90 min, and the resulting XRD plot is displayed in Fig. 4.3 (b). The diffraction pattern after annealing displayed improvement in ternary alloy formation with silicon substrates, with reduced precipitates. The polyimide samples displayed insignificant changes after annealing, and the XRD results indicated similar  $\beta$  phase formation.



**Figure 4.3: Plots showing the (a) XRD pattern obtained with three different substrates before annealing (b) XRD after annealing sample at 400 °C for 90 min.**

To further probe the transition temperature of the developed samples, thermal analysis with DSC was conducted. The phase transition was more evident with polyimide substrates than SMA film developed on silicon substrate. There was shape memory effect before annealing with the polyimide substrates. After annealing it was prominent. The martensite phase was more stable after annealing.

Further, the austenite transformation temperature found at approximately 185 °C for SMA film developed on the silicon substrate and 120 °C for

SMA/polyimide composite as displayed in Fig. 4.4 (a) and 4.4 (b). A minor transition peak was observed near 250 °C for SMA/polyimide composite, though the transition observed at 120 °C was prominent. The SMA film from silicon substrate was peeled off, and investigated for shape memory effect by actuating

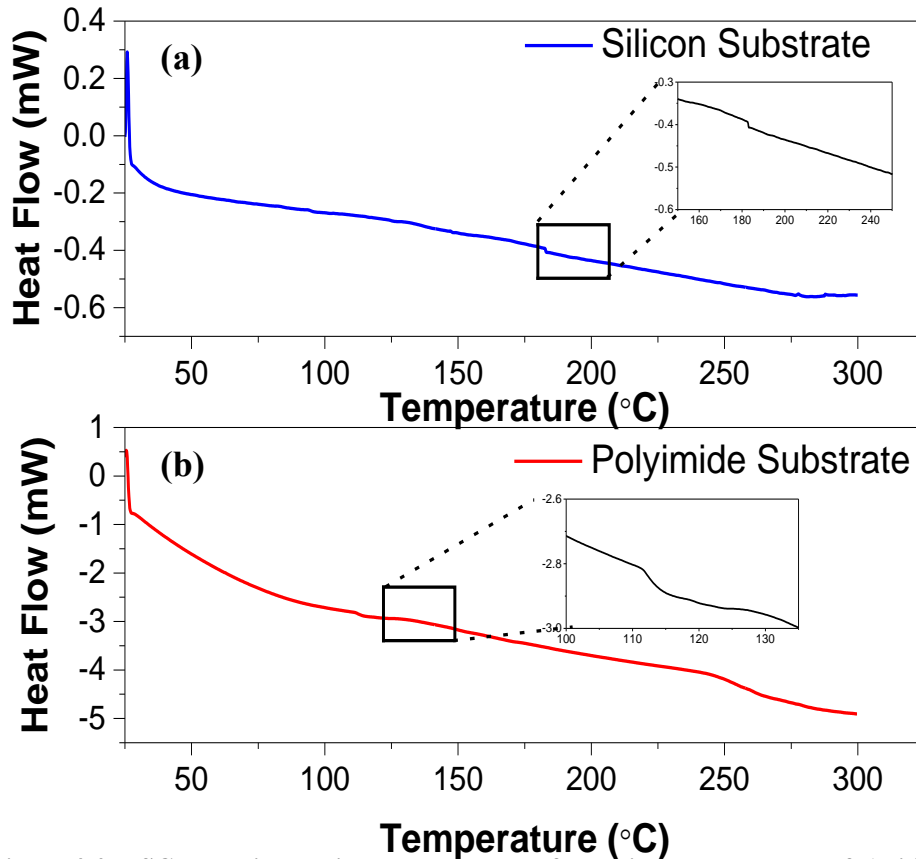


**Figure 4.4:** DSC analysis showing the phase transformation temperatures of a) silicon substrate (b) polyimide substrate

through plate heater. The peeled off film from silicon substrate displayed no shape change. However, the SMA/polyimide composite film actuated steadily as the temperature increased.

The results indicated the surface energy and the nucleation process is different for each substrate as the alloy formation was not identical. The minor alloy formation observed with SMA developed on silicon substrates indicate the need for further optimisation in a deposition. Further, the presence of precipitates observed with film developed on silicon substrates was evident after annealing, which could hinder the shape memory properties. This might be the primary reason for the absence of shape memory effect. Further, the film has to be strained to observe any shape change, which was impossible, as the films will disintegrate. The essential reason for the SMA/polyimide to actuate is due to the pre-strain

applied to the polyimide substrate. Further, optimisation could generate significant results, however etching the substrate and obtaining the film was unfeasible.

### 4.3 Influence of Substrate Thickness

Polyimide substrates of 25, 50 and 75  $\mu\text{m}$  were taken for the analysis. The influence of substrate thickness on morphological, structural, thermal properties and the fatigue life has been investigated in detail. Fig. 4.5 shows the images of the SMA bimorph developed at varying substrate thickness. As observed from the image, the 25  $\mu\text{m}$  polyimide curled excessively, making it difficult for further analysis. As the bimorph was unwrapped for characterisation, crack formation was observed. However, the tests were conducted with all the three bimorphs in possible places.

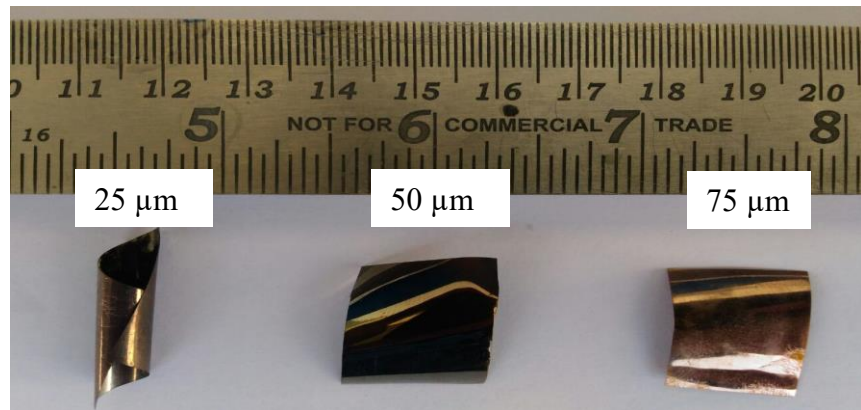
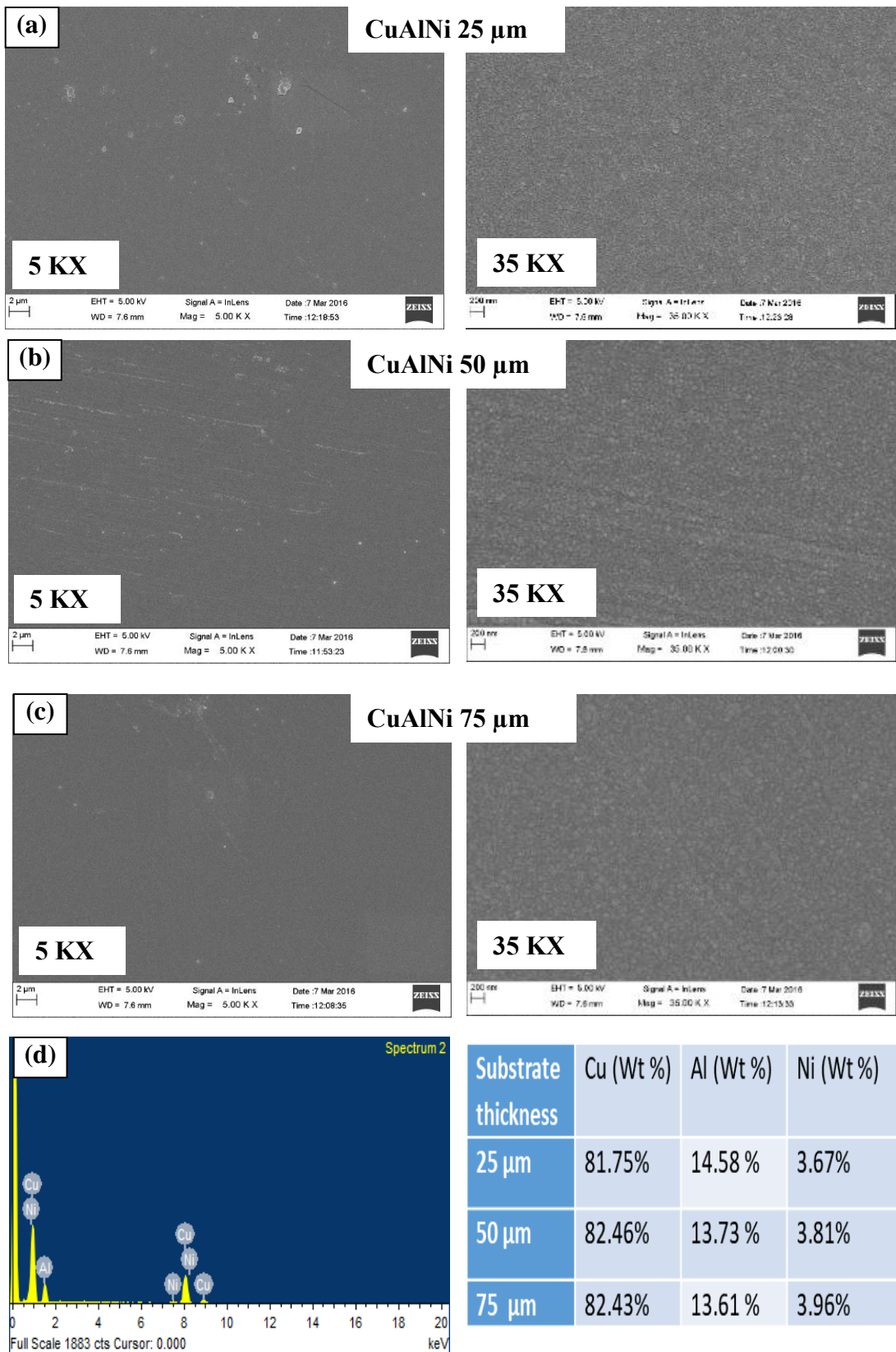


Figure 4.5: Images showing SMA film deposited on polyimide of varying substrate thickness

#### 4.3.1 Surface Morphological and Composition Analysis

The surface morphological analysis displayed a smooth and uniform film without any porosity or crack. The martensite texture was visible with all the three samples, and the grain size was found to be less than 100 nm, which is significantly less than the conventionally cast bulk samples. Fig. 4.6 shows the microscopic images of bimorph developed at (a) 25  $\mu\text{m}$ , (b) 50  $\mu\text{m}$  and (c) 75  $\mu\text{m}$ . The textures observed, varied with the substrate thickness belonging to the  $\beta$  martensite phase. The composition analysis exhibited minor variations in Al % as compared to the initial values. The percentage of Al was observed to be higher than 14 % for samples developed with 25  $\mu\text{m}$ . The variation in the composition could be due to the presence of precipitates and binary phases, though such precipitates were not observed from the SEM analysis. Fig. 4.6 (d) shows the EDS spectrum of

the sample developed on 50  $\mu\text{m}$  polyimide and the table shows the composition of the bimorphs at different substrate thickness.



**Figure 4.6: Images showing the (a) morphology of SMA film deposited on 25  $\mu\text{m}$  polyimide (b) morphology of SMA film deposited on 25  $\mu\text{m}$  polyimide (c) morphology of SMA film deposited on 25  $\mu\text{m}$  polyimide (d) EDS analysis showing the composition of samples deposition on polyimide of varying thickness**

### 4.3.2 Adhesion and Roughness Analysis

The adhesion tests were conducted by scotch tape analysis. The tape was stuck to the bimorph with uniform pressure, and it was made sure there were no air gaps. Fig. 4.7 shows the images of the scotch tape analysis. The results indicated the poor adhesion of 25  $\mu\text{m}$  samples to some extent. The significant reasons originated while unwrapping the bimorph, which created minor cracks.

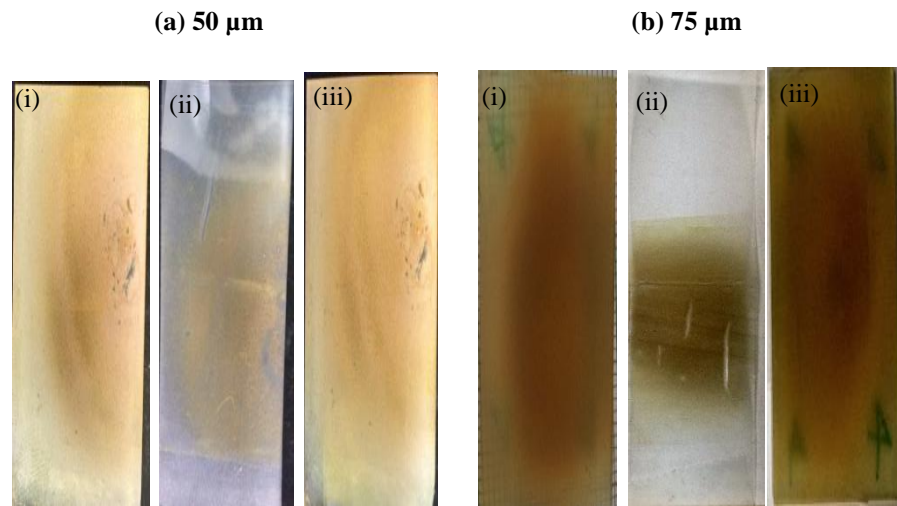


Figure 4.7: Images showing the scotch tape analysis performed on varying polyimide thickness (i) sample before testing (ii) scotch tape after testing (iii) sample after testing

Table 4.1: Results of Scotch Tape analysis

Substrate Thickness ( $\mu\text{m}$ )	The weight of the tape before testing (mg)	The weight of the tape after testing (mg)	The weight of the adhered material (mg)
25	57.9	58.8	0.9
50	57.4	57.9	0.5
75	57.6	58.1	0.4

The roughness of the samples was performed with Veeco optical profilometer, at different locations. The results show the roughness of both 50  $\mu\text{m}$  and 75  $\mu\text{m}$  the samples were in micron order. Fig. 4.8 shows the results of the roughness analysis. The arithmetic mean Ra value displayed 2.15  $\mu\text{m}$ , 1.6  $\mu\text{m}$  and 181 nm for 25  $\mu\text{m}$ , 50  $\mu\text{m}$  and 75  $\mu\text{m}$  polyimide sheets. The maximum height of the profile Rt displayed 37  $\mu\text{m}$ , 72  $\mu\text{m}$  and 8  $\mu\text{m}$  as displayed in Table 4.2. The root mean square roughness was high with samples developed on 75  $\mu\text{m}$ . Roughness plays a vital role in determining how the film interacts with surroundings during actuation.

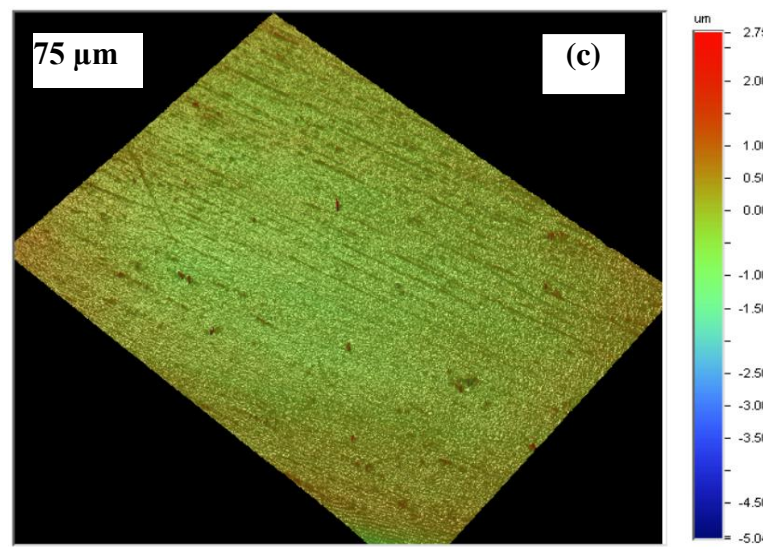
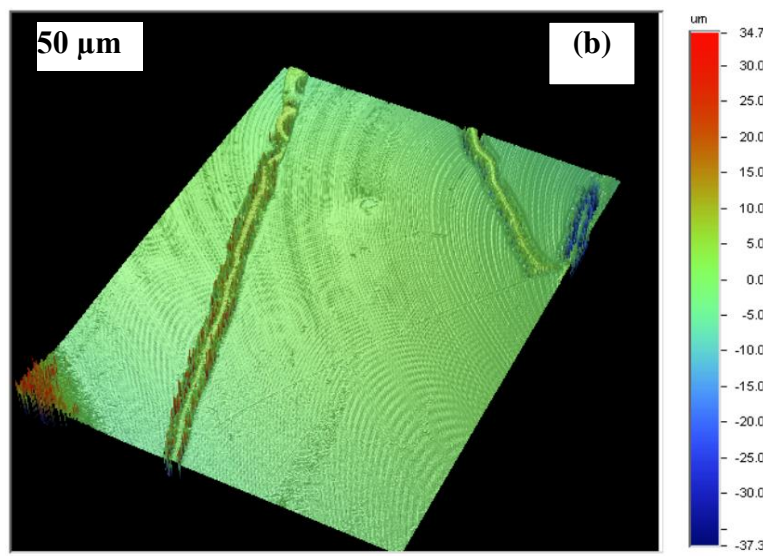
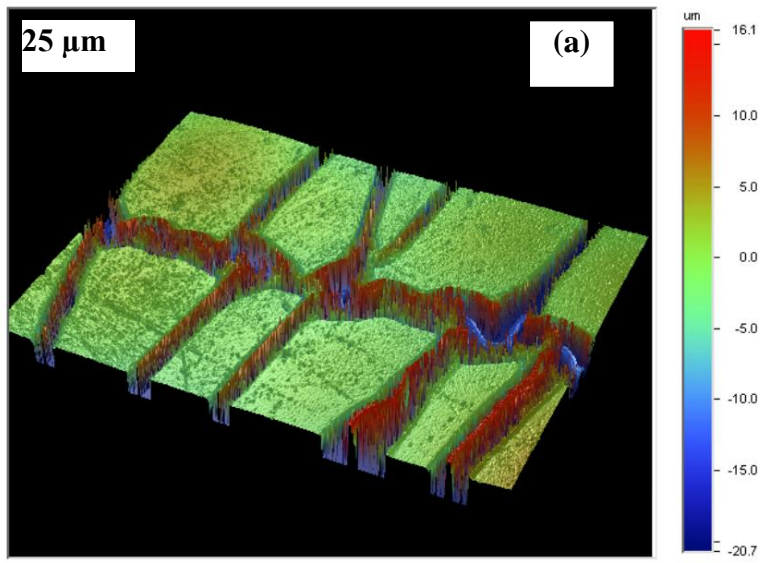


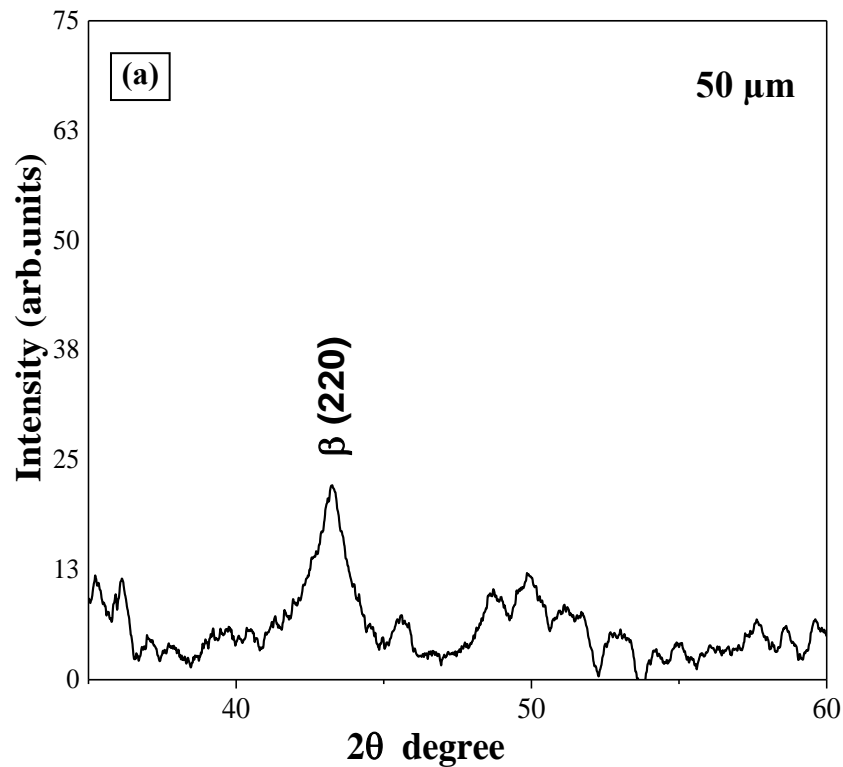
Figure 4.8: Roughness profile of SMA bimorph with varying polyimide thickness

**Table 4.2: The results of Roughness analysis**

<b>Substrate Thickness</b>	<b>Ra</b>	<b>Rq</b>	<b>Rt</b>
25 $\mu\text{m}$	2.15 $\mu\text{m}$	3.59 $\mu\text{m}$	36.74 $\mu\text{m}$
50 $\mu\text{m}$	1.60 $\mu\text{m}$	2.39 $\mu\text{m}$	71.99 $\mu\text{m}$
75 $\mu\text{m}$	181.90 nm	245.59 nm	7.79 $\mu\text{m}$

### 4.3.3 Structural Analysis

The analysis with 25  $\mu\text{m}$  was difficult for further processing and the results displayed ambiguous data. Figure 4.9 (a) and (b) shows the X-Ray diffraction pattern of 50  $\mu\text{m}$  and 75  $\mu\text{m}$  samples. It can be observed that the evolution of crystalline peak corresponding to  $\beta$  (220) monoclinic structure was observed in both the samples and (ICSD pattern, card no: 01-072-3498) and other  $\alpha$  and  $\gamma$  phases were present in samples developed on 75  $\mu\text{m}$  bimorph [73,110]. However, the signal from the XRD was very coarse, and the evolution of other martensite peaks was not evident. The crystallite size calculated using Scherrer formula was 6.67 nm. The transformation between the phases depends on the structural



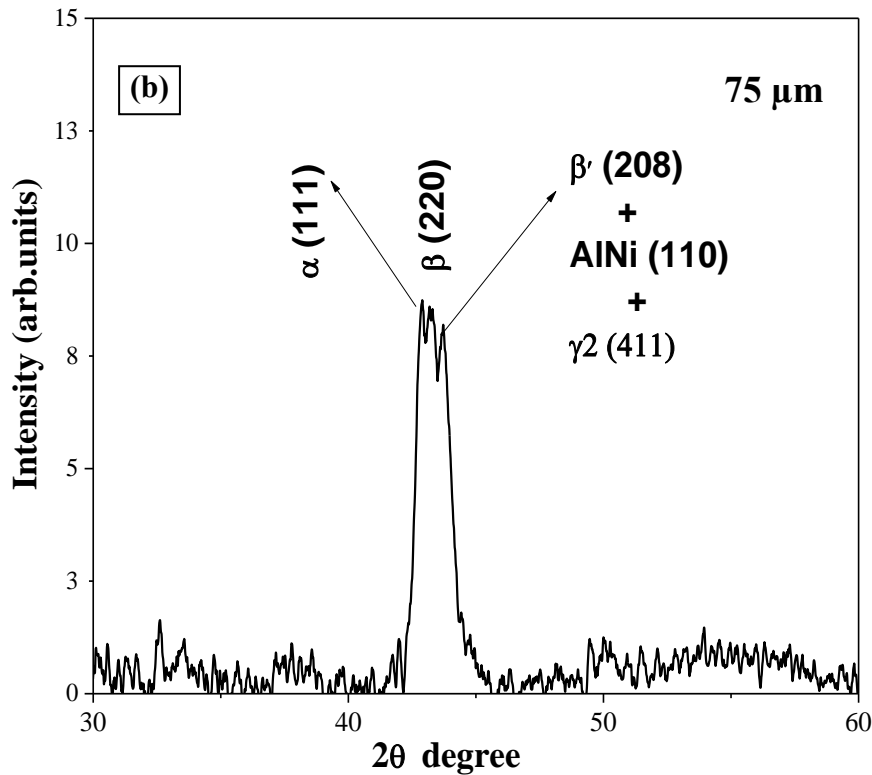


**Figure 4.9:** XRD pattern of SMA bimorph with varying polyimide thickness (a) 50  $\mu\text{m}$  (b) 75  $\mu\text{m}$

properties and the composition of the alloy [111]. Structural properties such as single crystal or polycrystalline alloys affect the shape memory effect vastly as single crystal shape memory alloys are better because of the defined transformation between one phase to another [112–114]. Whereas, polycrystalline alloys have difficulty in remembering their low-temperature structure as the probability of cycling between two different phase are high [115]. Furthermore, polycrystalline alloy shows recoverable strains up to 5% only, corresponding to brittleness and order less phase transition, which reduces the shape recovery significantly [54,116,117]. The lattice parameters of the product phase are  $a = 4.382 \text{ \AA}$ ,  $b = 5.356 \text{ \AA}$  and  $c = 4.222 \text{ \AA}$ . Parameters such as heat treatment, ageing, the addition of other materials and training of the polycrystalline alloys at two particular phases [50,118–122] can have a significant effect on the shape memory effect.

#### 4.3.4 Thermal Analysis

Thermogravimetric analysis was performed for 50  $\mu\text{m}$ , and 75  $\mu\text{m}$  bimorphs and the results are displayed in Fig. 4.10. The results exhibit the TGA analysis of the bimorph as well as the bare polyimide sheet where single stage

decomposition was observed. Sample weight of 5 mg was used for the analysis, and the heating rate was maintained at 10°C/min. The samples started degrading gradually from 390 °C, and the initial decomposition rate (IDR) of both the samples was less than 5 % till 500 °C. From 505 °C the CuAlNi bimorph sample weight loss was rapid, and the bimorph decomposed entirely at 670 °C. The maximum rate of decomposition temperature (MRDT) was found to be in the range of 500 °C - 670 °C. However, the bare polyimide exhibited a different decomposition rate, and the sample got decomposed entirely at 725 °C. Similar results were observed with 75 μm polyimide samples and there were not significant vibrations.

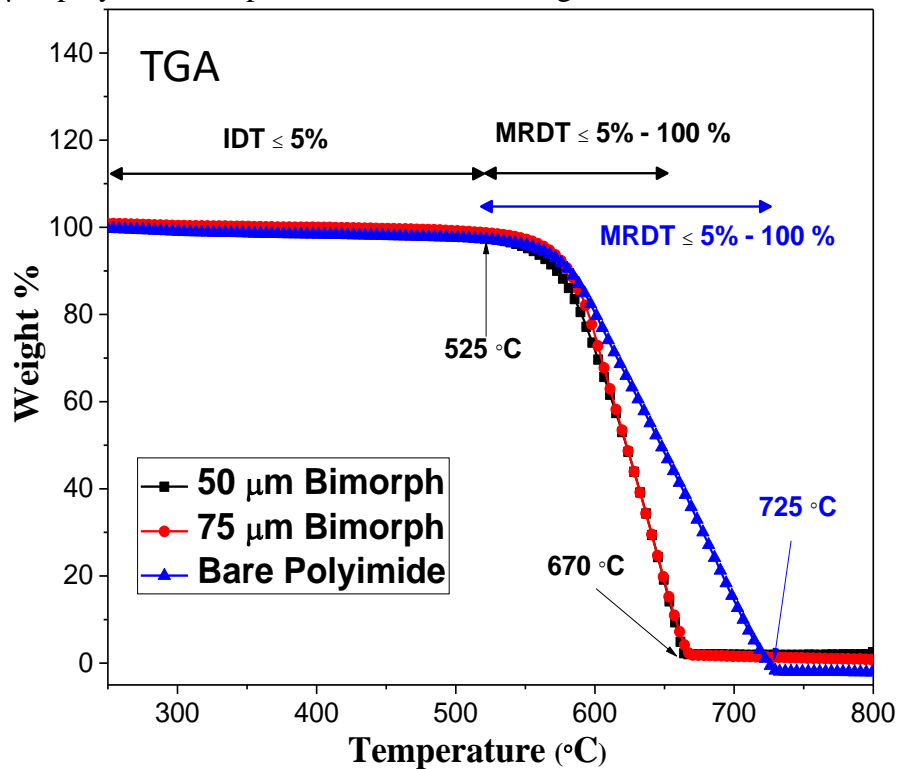


**Figure 4.10: Thermogravimetric analysis showing the decomposition of different polyimide samples**

The rapid decomposition of CuAlNi bimorph samples may be attributed to the ability of the alloys to absorb heat which might result in the conduction of the polyimide samples. The decomposition range assisted in relating the voltage required during electrical actuation. To further locate the phase transition temperature of the developed bimorphs, a four probe Van der Pauw method which provides temperature vs resistance measurements was utilized [69]. The samples were cut in 2 × 2 cm<sup>2</sup> sheets, and silver conducting paste (1-3 × 10<sup>-5</sup> Ω-cm) was used to make the contacts. Heating was controlled at 5°C/min, and the analysis was conducted in an argon atmosphere. Figure 4.11 (a) and (b) shows the temperature

vs resistance measurement of 50  $\mu\text{m}$  and 75  $\mu\text{m}$  bimorphs. The austenite start and finish temperatures were observed at  $A_s$  - 225  $^\circ\text{C}$  and  $A_f$  - 250  $^\circ\text{C}$  for samples developed on 50  $\mu\text{m}$  polyimide. The 75  $\mu\text{m}$  polyimide bimorph had  $A_s$  - 215  $^\circ\text{C}$  and  $A_f$  - 240  $^\circ\text{C}$  and the transition was distinct from the samples. The cooling curve was not displaying any transition as the samples were cooled down by natural convection.

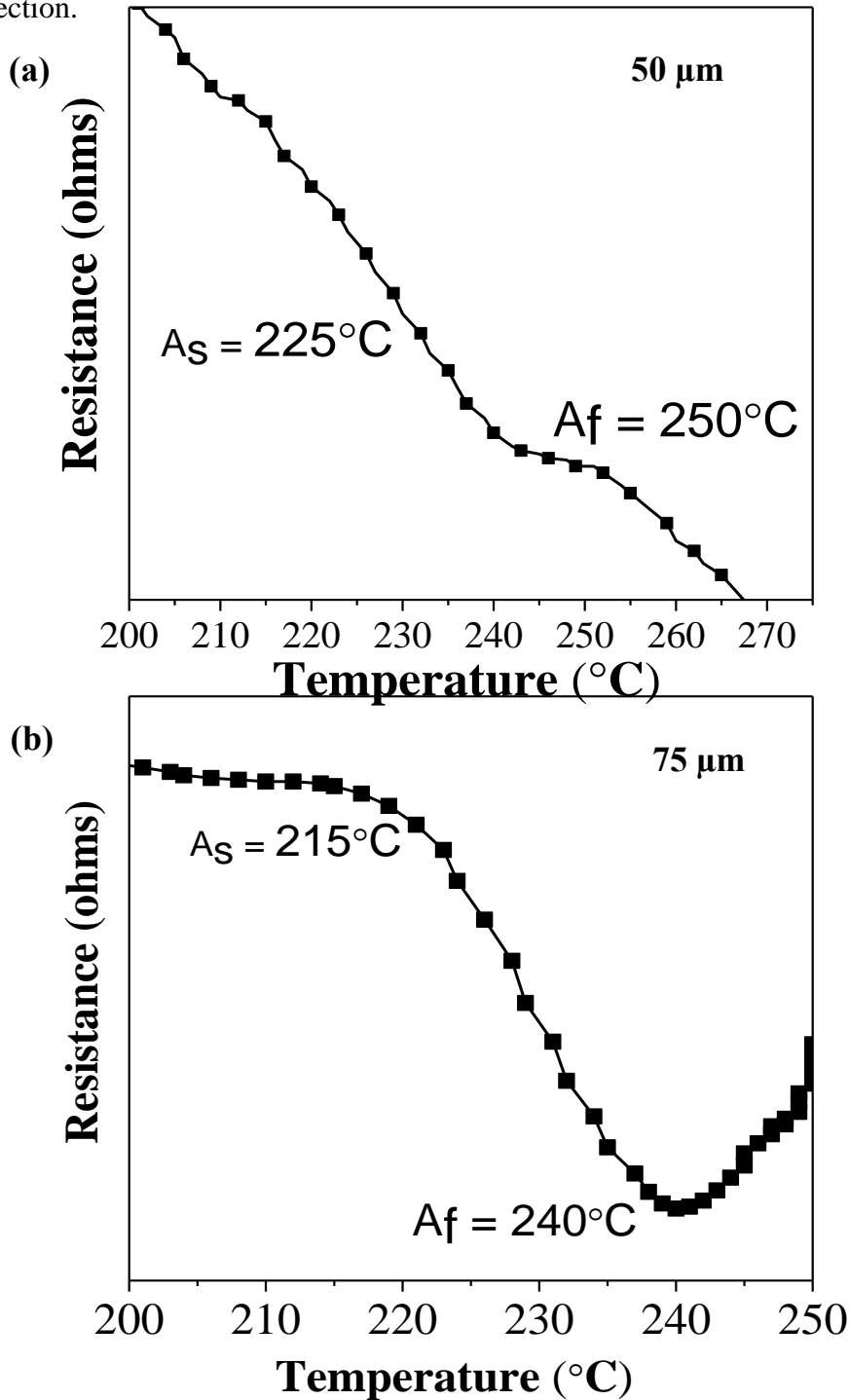


Figure 4.11: Temperature vs Resistance plot showing the transformation temperatures of SMA bimorph of varying thickness.

#### 4.3.5 Shape Recovery Ratio Analysis

To investigate the shape recovery ratio and maximum displacement from the edge of the bimorph a test bench with substrate heating was designed to heat and cool the bimorph as shown in Fig. 4.12. A sample size of  $7 \times 2 \text{ cm}^2$  CuAlNi/polyimide sheet was clamped to a substrate heater with thermal tape. It was found that the maximum displacement was achieved only with substrate heating as the contact points reached the degradation temperature at higher voltages with electrical actuation. Fig. 4.13 (a) shows the shape recovery ratio  $D_R$  vs temperature plot. The recovery ratio increases during heating, and it returns to its original value as the bimorph transforms from high-temperature austenite phase to low-temperature martensite phase.  $75 \mu\text{m}$  bimorphs exhibited a higher recovery ratio of 1.38, whereas  $50 \mu\text{m}$  sheet exhibited only 1.21 ratio. The recovery ratio was calculated by finding the diameter of the curved bimorph structure at various temperatures. The

recovery ratio gradually decreased during cooling as the sheet recovered to its original developed CuAlNi/polyimide bimorph has two-way shape memory effect, with polyimide acting as a bias force during cooling. The recovery ratio is higher than previously reported works on shape memory alloy/polyimide bimorph.

Fig. 4.13 (b) shows the time vs displacement and time vs temperature plots of the samples deposited on  $75 \mu\text{m}$  sheets. It can be observed that a maximum displacement of 19 mm was observed. The time required to reach this maximum displacement during heating was 37 seconds. The cooling cycle takes more time as

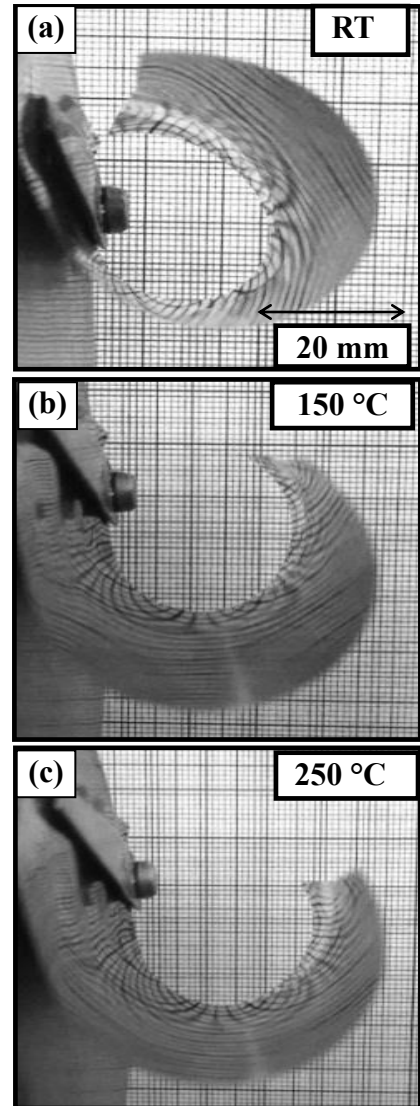


**Figure 4.12: Images showing the actuation of the bimorph at different temperature obtained through plate heating**

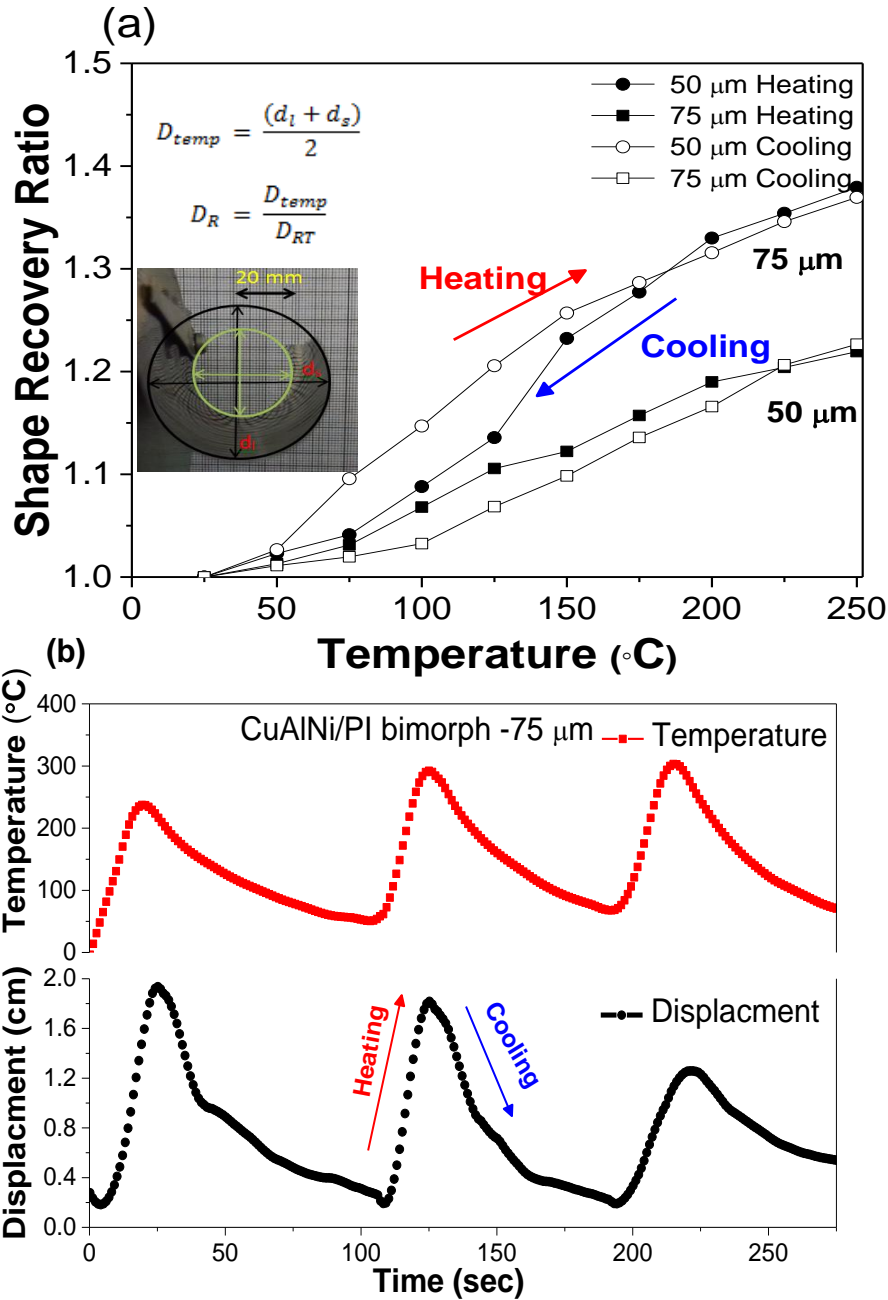


Figure 4.13: (a) shows the recovery ratio of both the bimorph, (b) cycling heating and cooling to find the maximum displacement of the bimorph

natural heat convection was allowed to cool the sample. The cooling time was approximately 75 s and the film returned to its original position after 110 s, without any plastic deformation. As the temperature was increased to 300°C, the displacement of the bimorph reduced to 15 mm, and the retraction took the same time as the first cooling cycle. When the temperature was raised above 300 °C, as seen in the third cycle, the maximum displacement was only 12 mm, and the film did not return to its original position. The return stroke was limited to 6 mm due to

plastic deformation of the bimorph. Therefore, 230 °C - 250 °C is the appropriate actuation temperature range, where the maximum displacement was observed.

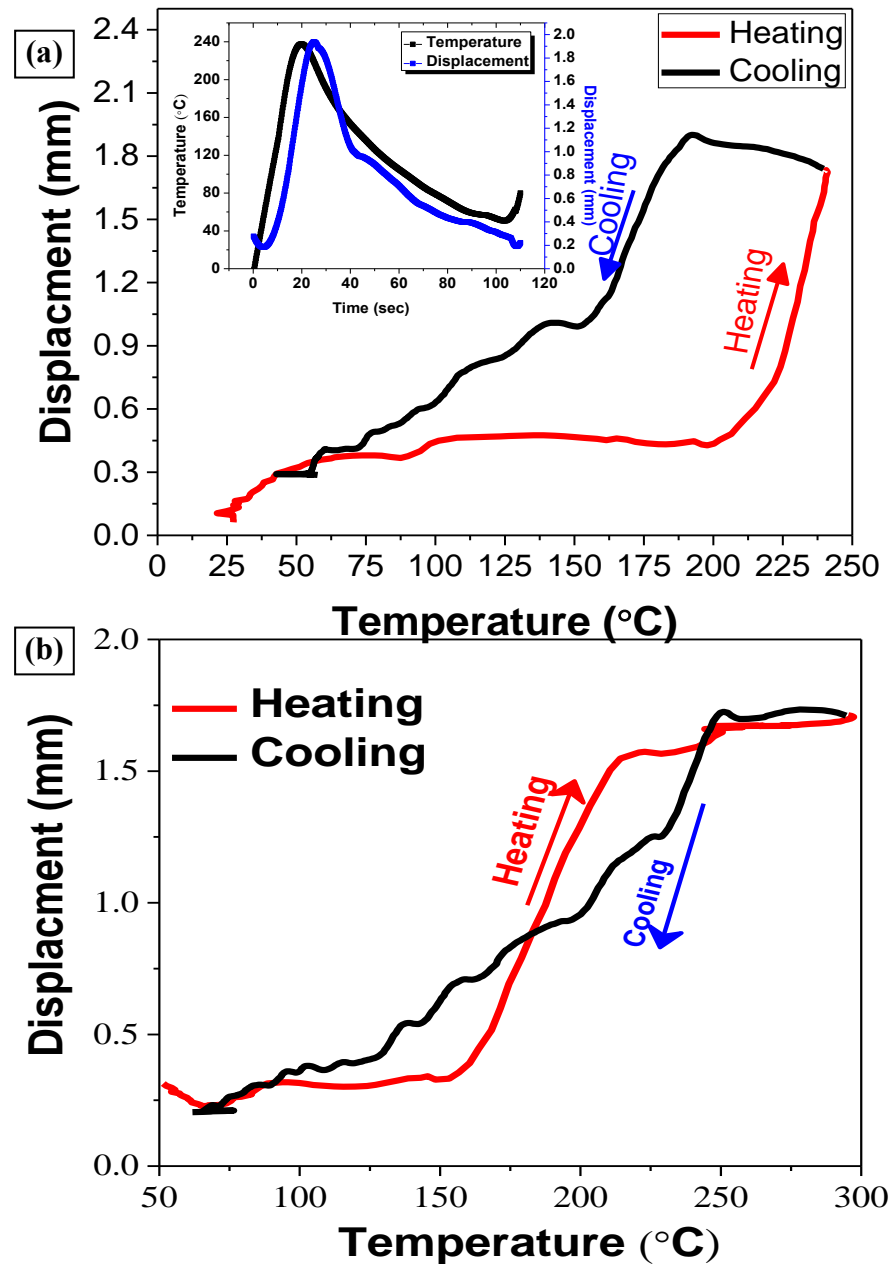


Figure 4.14: Plots obtained from 50 μm PI displaying the (a) hysteresis curve showing the time lag which was high at initial stages, (b) Hysteresis plot after attaining maximum displacement

Fig. 4.14 (a) shows the hysteresis curve of the first two cycles of the bimorph structure. In the first cycle, it can be noticed that the displacement continues to increase, even after the heating is stopped. On the contrary, the second cycle as shown in Fig. 4.14 (b), exhibited a minimal hysteresis, as the maximum displacement was achieved in the previous cycle and the bimorph was more

sensitive to the change in temperature. This proves that it is better suited to employ the bimorph structures at the fully extended position for fast heating and cooling.

#### 4.3.6 Thermomechanical and Life Cycle Analysis

The thermomechanical analysis of the developed bimorphs was conducted with Joule heating setup, and the experiments were performed at various voltages.

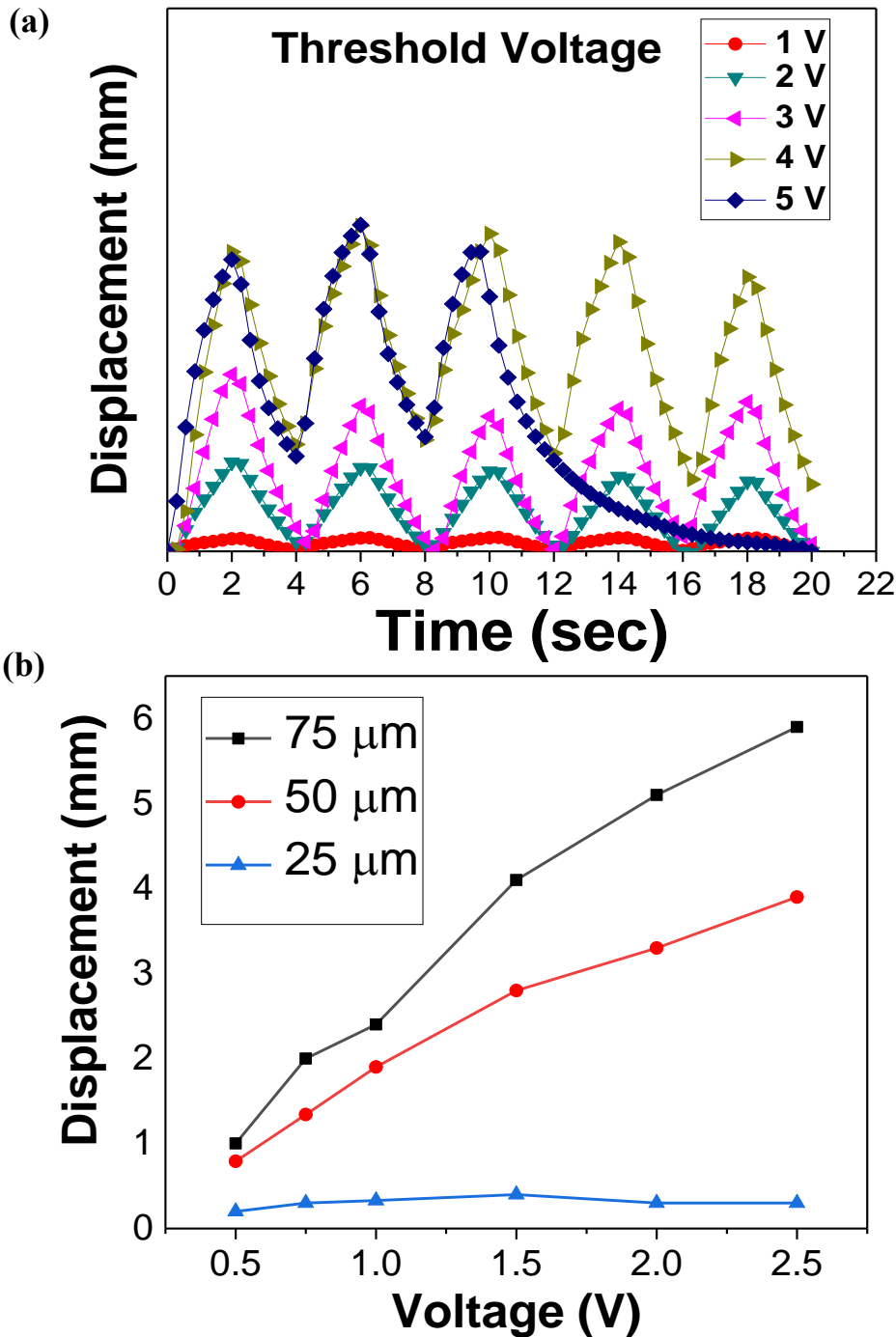


Figure 4.15: (a) Time vs displacement plot at varying voltages (b) Variation in displacement of all the three bimorphs at varying voltage

It was observed that the amount of actuation displacement is a function of applied voltage, as well as the frequency of actuation of the film. CuAlNi bimorph actuators at higher voltages show maximum linear displacement but found to have a very short lifespan, due to overheating. Fig. 4.15 (a) shows the displacement of the bimorph at a different voltage. It can be observed from the results, for actuation voltages from 1 V to 3V, exhibited return stroke same as that of actuation stroke. The composite film comes back to its initial position by the bias force of pre-stained polyimide during the cooling cycle. Beyond 3 V composite, the bimorph failed to return to its initial position on cooling cycle's and damages the bimorph near contacts affecting the electrical conductivity. The bimorph failed to return at 4 V and failed to actuate after few cycles at 5 V. Therefore most of the experiments were conducted below 3 V. Further, preliminary experiments with varying thickness bimorph exhibited the inability of 25  $\mu\text{m}$  bimorphs to actuate under varying voltages. Whereas, 50  $\mu\text{m}$  and 75  $\mu\text{m}$  bimorphs displayed excellent actuation with Joule heating. Fig. 4.15 (b) shows the response of bimorphs of varying thickness.

To investigate the cyclic behaviour and the fatigue life of the developed structures, electrical actuation was employed. Three different voltages of 2 V, 2.5 V and 3 V were selected, and two different frequencies of 0.05 Hz and 0.5 Hz were used for the investigations. 0.05 Hz was used to find the maximum displacement at different voltages, and 0.5 Hz was used as an initial value to study the suitability of the bimorph in MEMS actuators. Fig. 4.16 (a) shows the maximum displacement graph for samples deposited on 50  $\mu\text{m}$  polyimide sheet. The maximum displacement achieved with 2 V, 2.5 V and 3 V was 2.8 mm, 4.1 mm and 4.6 mm respectively. For 2 V and 2.5 V, the bimorph returns to its original position without any deformation. However, at 3 V, the cycle was incomplete as the bimorph showed a loss of 0.5 mm in displacement during cooling. The first cycle had larger displacement however once the actuation frequency was attained the maximum displacement was 2.5 mm, 3.4 mm and 3.8 mm respectively. Fig. 4.16 (b) shows the maximum displacement graph for samples deposited on 75  $\mu\text{m}$  polyimide sheets. The plots displayed similar behaviour as compared to 50  $\mu\text{m}$  sheet where the bimorph failed to return to original position during cooling. Nevertheless, the

maximum displacement achieved with different voltage was 4.1 mm, 7.2 mm and 9.2 mm.

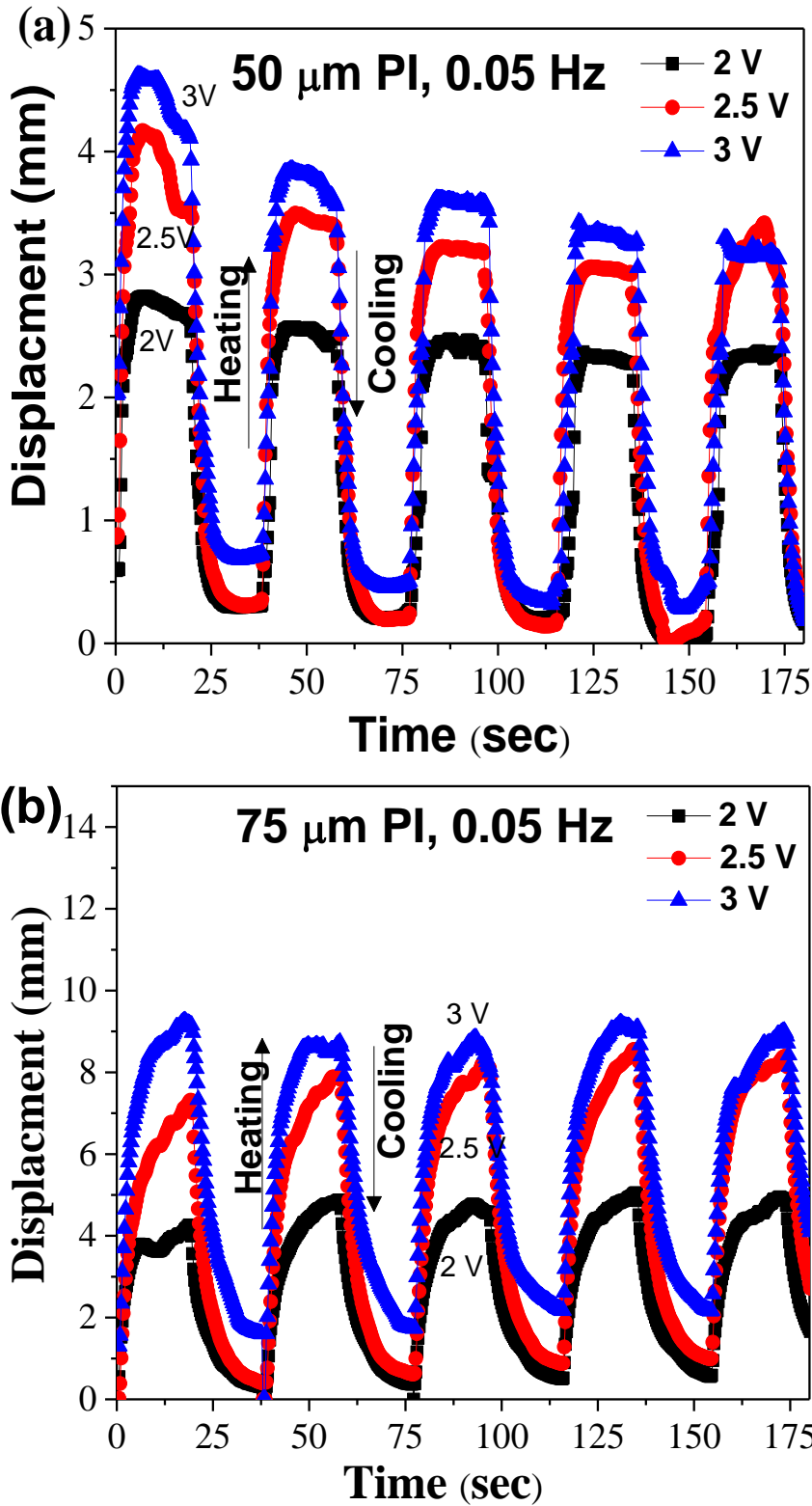


Figure 4.16: (a) Maximum displacement obtained through electrical actuation for 50  $\mu\text{m}$  bimorph, (b) Maximum displacement obtained through electrical actuation for 75  $\mu\text{m}$  bimorph

The bimorph was tested for its fatigue life at 0.5 Hz for 500 cycles. Figure 4.17 (a) and 4.17 (b) shows the life cycle of samples deposited on 50  $\mu\text{m}$  and 75  $\mu\text{m}$  polyimide sheet. The bimorph showed minor fluctuations in displacement. However, an average displacement of 0.5 mm, 0.6 mm and 0.65 mm was observed with different voltages. 75  $\mu\text{m}$  thick CuAlNi/polyimide bimorph showed no signs of fatigue and showed a consistent and average displacement of 0.75 mm, 1.05 and 1.4 mm.

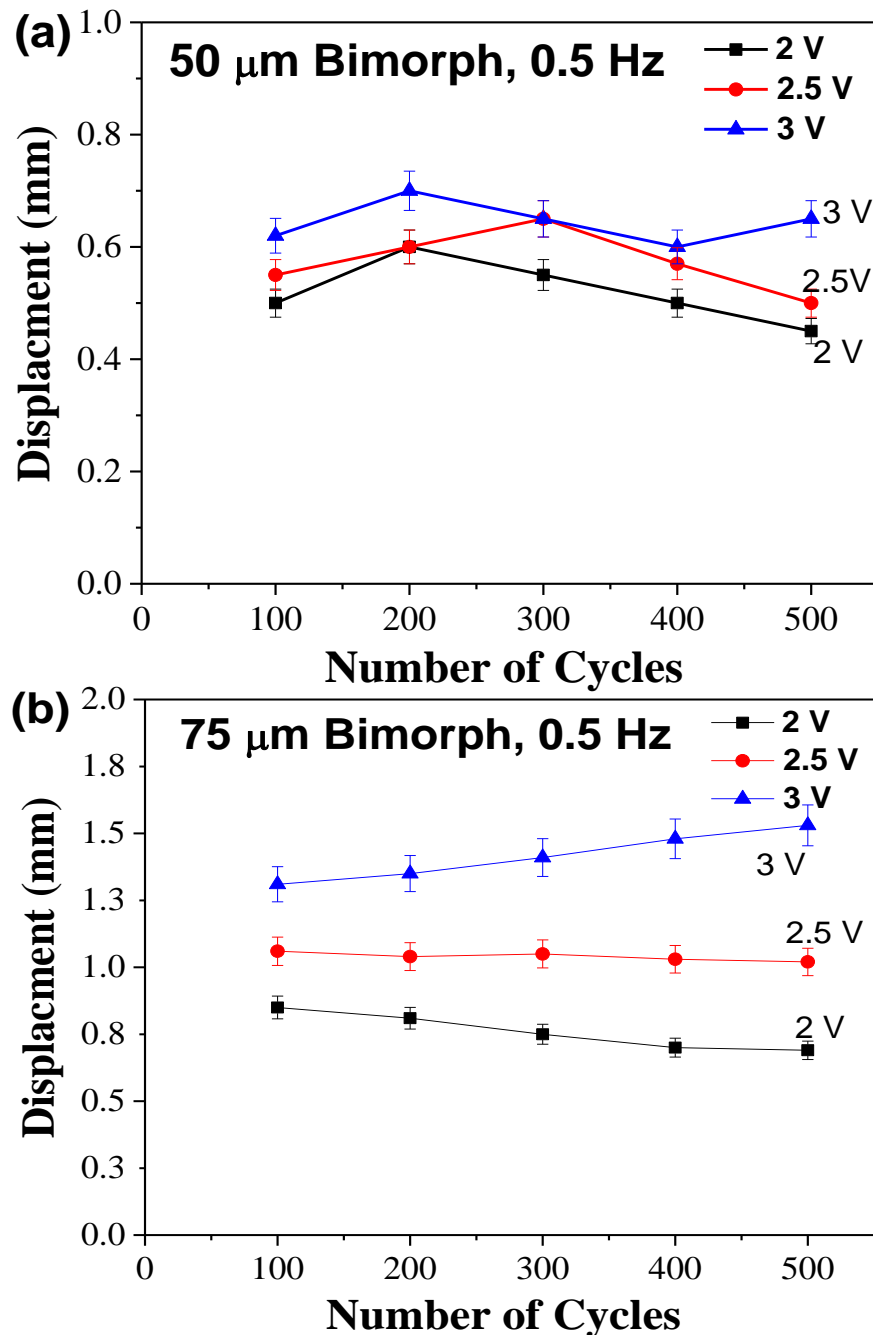


Figure 4.17: (a) Life cycle analysis of 50  $\mu\text{m}$  bimorph, (b) Life cycle analysis of 75  $\mu\text{m}$  bimorph

The stiffness of 50  $\mu\text{m}$  polyimide sheets is lower than 75  $\mu\text{m}$  sheets, which directly affect the magnitude of pre-strain applied to the sheets. After deposition, the developed films generate compressive stress, which tends to act against the stiffness of the polyimide substrate. The stiffness variation was distinct, as there was an increase in curvature of the bimorph. Further, the radius of curvature of 50  $\mu\text{m}$  sheets was higher due to its low stiffness. As observed from the shape recovery ratio graphs the shape memory effect of 50  $\mu\text{m}$  bimorph sheets, was not sufficient to recover from the compressive stress completely. Also, the inability of 50  $\mu\text{m}$  to overcome the stress, with the given actuation conditions was evident from the fluctuations observed in the life cycle analysis. Whereas in case of 75  $\mu\text{m}$  sheet the stress induced in the SMA film was recovered with all the actuation conditions. Stiffness and the residual stress was optimum for the SMA film to recover its shape effortlessly. As it can be observed from the life cycle analysis, 50  $\mu\text{m}$  CuAlNi/polyimide bimorphs has unstable actuation behaviour with fluctuations. The displacement was constantly varying during actuation at varying frequencies and voltage. There was no saturation attained even after 500 cycles. However, 75  $\mu\text{m}$  bimorphs displacement presented a steady and stable actuation behaviour throughout the 500 cycles.

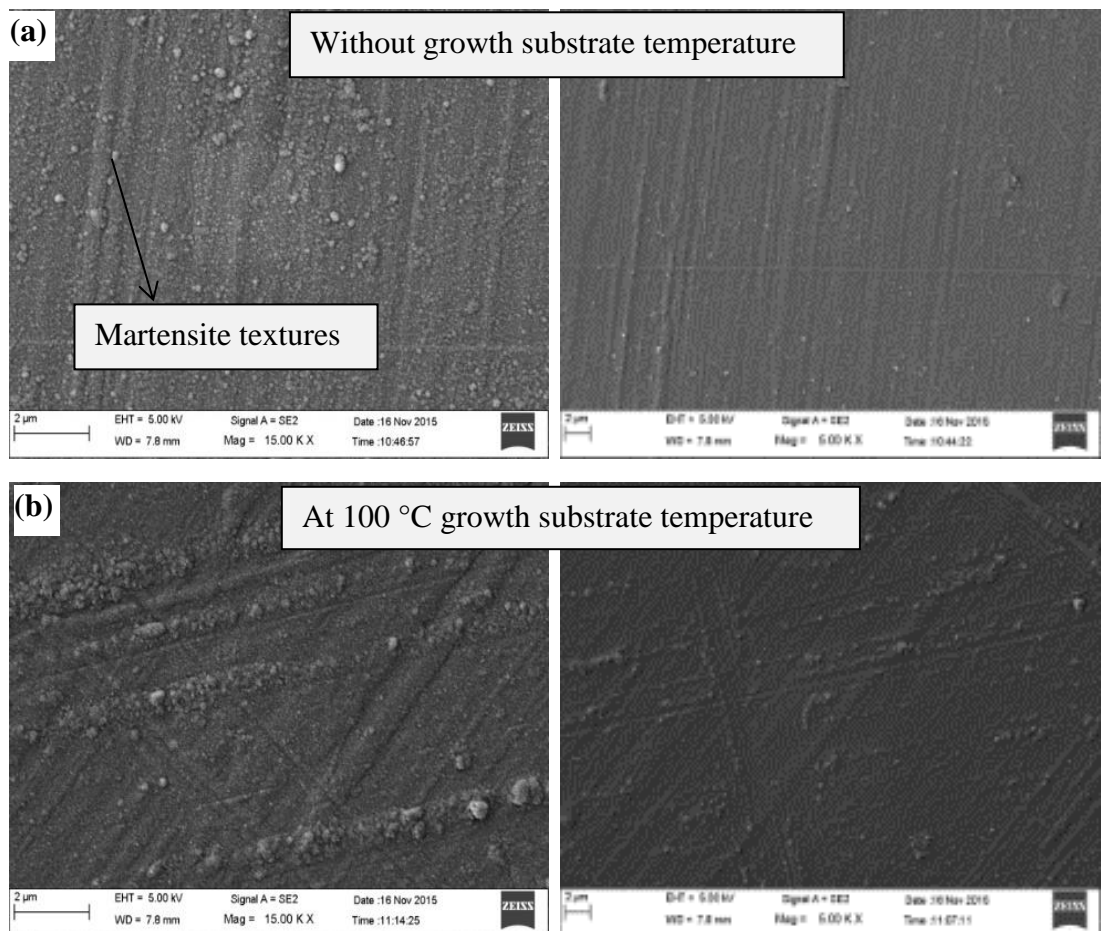
#### **4.4 Influence of Substrate Temperature**

The influence of growth substrate temperature on the development of CuAlNi shape memory alloy (SMA) over Kapton Polyimide sheet and its effect on tuning the thermomechanical behaviour has been investigated. The substrate temperature during deposition plays a vital role in the crystallinity of the developed film. There have been several reports of deposition on heated substrates which facilitates in avoiding the high-temperature annealing required after deposition [73,123]. High-temperature surfaces can be an effective place for nucleation, and further, it can improve the diffusion process leading to enhanced crystallisation. The SMA bimorph was synthesized at varying substrate temperatures ranging from 100  $^{\circ}\text{C}$  – 200  $^{\circ}\text{C}$ . To investigate the life cycle behaviour of the as developed SMA bimorph with Joule heating as actuation source. The cyclic behaviour was investigated for 500 cycles, at three varying voltages ranging from 2V, 2.5V and 3V at an actuation frequency 0.5 Hz. To probe the influence of substrate temperature in tuning the thermomechanical behaviour, an analysis of the

structural, morphological, and thermal properties of the bimorphs has been investigated in detail.

#### 4.4.1 Surface Morphological Analysis

The samples were characterised using scanning electron microscope to analyse the morphology of the developed films. Fig. 4.18 shows the SEM images of the samples developed at different substrate temperatures. All the developed films displayed a texture pattern which is possibly the martensite structures. The overall morphology of the film was smooth without any pores or hollows. However, there were precipitates of CuAl found in different places. 4.18 (a). The average grain size of the film developed without substrate temperature was found to be less than 100 nm. Similarly, the grain size was noticed to be less than 100 nm for samples developed at 100 °C and 150 °C and Cu<sub>3</sub>Al precipitates were in very fewer amounts as observed from Fig. 4.18 (b) and (c). At 200 °C, as observed from Fig. 4.18 (d), the film had cracks and the surface discontinuous in nature. The precipitates were found in large amounts throughout the film.



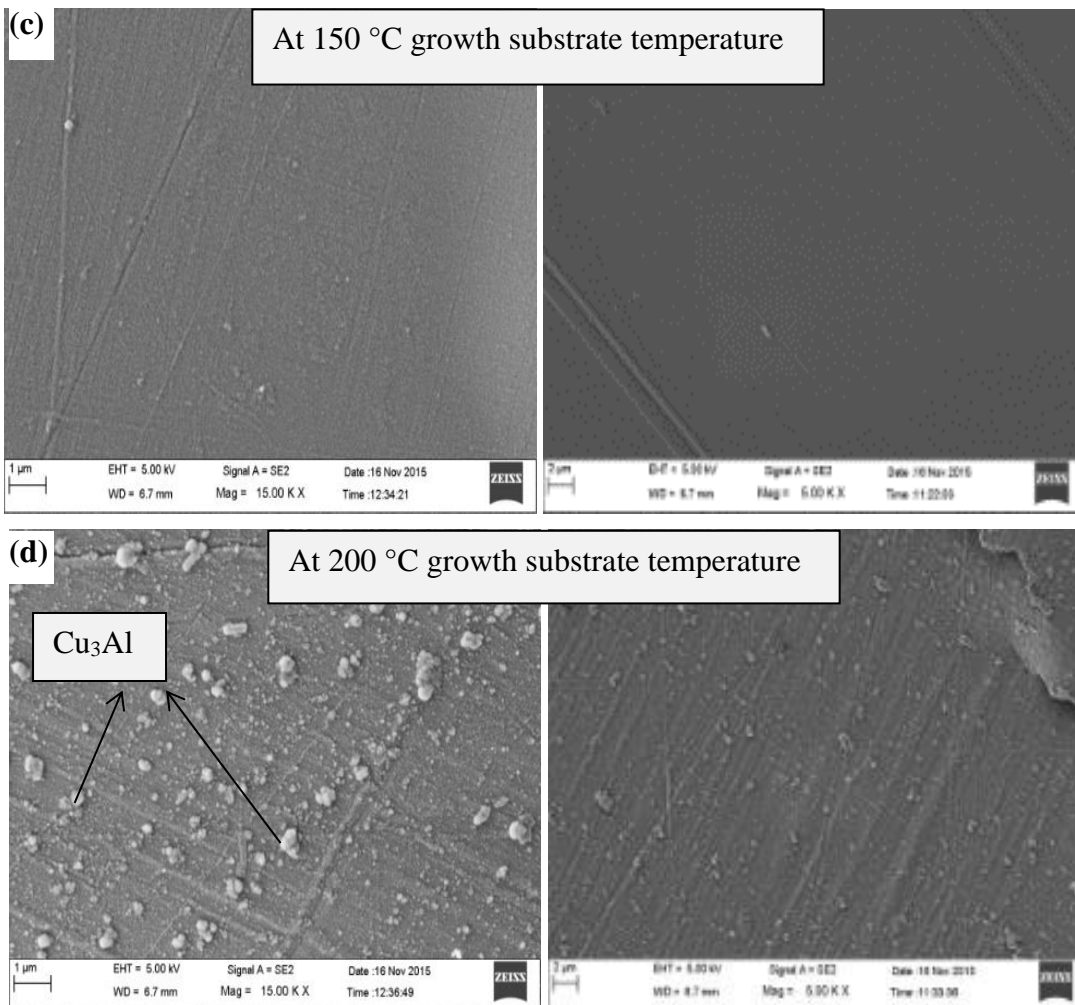


**Figure 4.18: Scanning Electron Microscope images showing the morphology of the developed films (a) Without substrate heating (b) at 100°C (b) at 150 °C (c) 200°C**

The samples developed without growth substrate temperature displayed textured martensite structures as observed from the SEM images.  $\text{CuAl}$  precipitates were observed at different points in the film. Similar precipitates of varying size have been identified by other researchers which were found to be ordered martensite of  $\text{Cu}_3\text{Al}$  [110]. The samples developed at a growth temperature of 100 °C displayed a smooth film with textures. The precipitates reduced as the growth temperature was increased to 150 °C which might be due to the effect of crystallisation temperature of polyimide which was found to be in the region of 150 °C – 200 °C. The polyimide in the semi-crystalline state tends to have different surface energy and thermal properties which might affect the nucleation process [98,124–126]. As the growth substrate temperature was increased to 200°C, additional  $\text{Cu}_3\text{Al}$  precipitates were formed which shows the growth temperature

was high to form an alloy with the required composition. The film was coarse, and the adhesion was also weak as compared to other developed films.

#### 4.4.2 Adhesion and Compositional Analysis

The composition of the films was acquired through energy dispersive spectroscopy analysis (EDS). Table 4.3 shows the results of the EDS analysis. The composition of the sample was taken at ten different locations, and the average value is presented in the table. There was a minor deviation from the initial composition measured before deposition. The samples exhibited a higher percentage of Al than the initial value, except for the samples developed at 150 °C. As observed from the EDS results, the high composition of Al results leads to  $\gamma$  phase [101,127,128], which was apparently observed from the samples developed without growth temperature. From the EDS analysis, it can be observed, the percentage of Al is above 13 % [129], confirming the transition from primary  $\beta_1$  to  $\gamma$  phase and for composition below 13 %, both  $\beta'_1$  and  $\gamma$  were present together. This shows that samples developed at 100 °C and 200 °C might have unstable shape memory characteristics.

**Table 4.3: EDS analysis displaying the composition of the developed samples**

<b>Element</b>	<b>Without Heating (Atomic %)</b>	<b>100 °C (Atomic %)</b>	<b>150 °C (Atomic %)</b>	<b>200 °C (Atomic %)</b>
Al	13.91	11.82	11.43	12.54
Ni	3.63	3.58	3.78	3.85
Cu	82.46	84.60	84.79	83.61

The adhesion test was carried out by scotch tape analysis on 5 cm<sup>2</sup> samples. The scotch tape of specific weight was used to stick to the film without any air gaps. The tape was removed from the sample and weighted to check the amount of material adhered to it. Table 4.4 shows the results of the scotch tape analysis. The samples developed without growth temperature, 100 °C and 150 °C showed excellent adhesion as there was less than 0.2 mg of material adhering to the tape. This confirmed the adhesion of the film was excellent with the polyimide substrate. Further, the film did not peel off from the substrate even at high temperatures as observed from substrate heating. The adhesion of samples developed at a growth temperature of 200 °C was slightly poor as, 0.5 mg of material adhered to the tape.

**Table 4.4: Scotch tape analysis showing the adhesion results**

<b>Substrate Temperature (°C)</b>	<b>The weight of the tape before testing (mg)</b>	<b>The weight of the tape after testing (mg)</b>	<b>The weight of the adhered material (mg)</b>
Without Heater	86.6	86.8	0.2
100	86.5	86.6	0.1
150	87.2	87.3	0.1
200	86.3	86.8	0.5

#### 4.4.3 Structural Analysis

The samples were characterised by X-ray diffraction to find the present phases. Fig. 4.19 shows the X-Ray diffraction pattern of the phases present in the bimorphs. The crystal structures were identified as  $\beta'_1$ ,  $\alpha$  and  $\gamma_2$ . It can be observed that the evolution of crystalline peak corresponding to  $\beta'_1$  18R (220) +  $\beta'_1$  (0018) martensitic was visible, approximately at  $2\theta = 43.5^\circ$  for samples developed without substrate heating, 100 °C and 150 °C. The  $\beta'_1$  peak was found to be monoclinic in nature. The other martensite peak observed was  $\beta'_1(208)$ , and  $\gamma_2$  (330) which were observed only for samples developed without growth substrate temperature and at 200 °C. The observed results were in agreement with the results reported by other researchers [73,110]. As the growth temperature was increased to 200 °C, the formation of  $\alpha$  (111) phase was also evident. The average crystallite size of 6 nm was calculated using the Scherer equation

$$d = \frac{K\lambda}{\beta \cos\theta} \quad (4.1)$$

Where  $d$  is the grain size,  $K$  is constant (0.89);  $\lambda$  is the Cu-K $\alpha$  wavelength (1.54 nm),  $\beta$  is the FWHM (0.372), and  $\theta$  (43.18°) is the diffraction angle.

The  $\gamma$  phase gradually decreases as the growth temperature was increased and the formation of  $\beta'_1(220)$  was prominent with samples developed at growth temperatures of 100 °C and 150 °C. The  $\beta$  phase undergoes eutectoid decomposition to form  $\beta'_1$ ,  $\alpha$  and  $\gamma$  phases [130–132]. XRD peaks show the diffraction pattern of  $\beta'_1$  (208) orientation which might be caused by the deficiency

of Al atoms in  $\text{Cu}_3\text{Al}$ . The phase transformation process observed during the increase in growth temperature can be established as,  $\beta_1 \gg \beta'_1 + \gamma_2 \gg \beta'_1$ . The parent phase transforms to develop ordered martensite structure to form  $\beta'_1 + \gamma_2$  without growth substrate temperature. As the temperature increases,  $\beta'_1 + \gamma_2 \gg \alpha$  phase which was observed at a growth temperature of 200 °C. The low intensity might be due to the presence of untransformed austenite phase. However, the  $\gamma$  peaks are present at a very close  $2\theta$  to the  $\beta'_1$  phase. Previous reports suggest the absence of the intermetallic peaks might be due to the extended solid solubility of elements such as Al and Ni in the molten metal matrix [133].

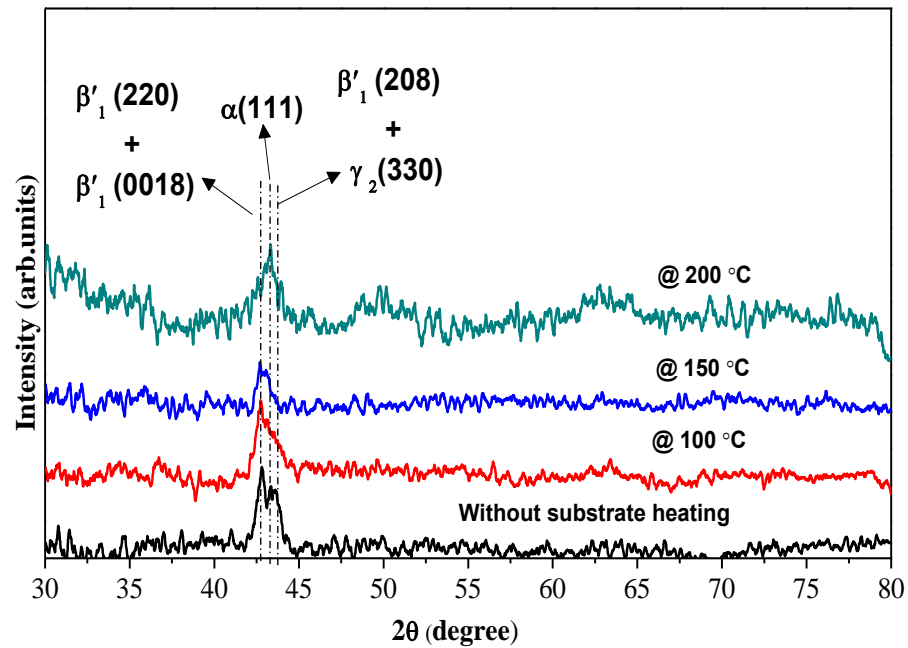


Figure 4.19: X-ray diffractogram showing the different phases observed from the film.

#### 4.4.4 Thermal Analysis

The samples were characterised with van der Pauw method to find the phase transition temperature. All the developed samples displayed austenite transition temperature. The samples developed with substrate heating had identical results as before with  $A_s - 200$  °C and  $A_f - 245$  °C. The samples developed with 100 °C, 150 °C and 200 °C had  $A_s - 222$  °C, 195 °C, and 200 °C and  $A_f - 284$  °C, 265 °C, and 265 °C. The results as shown in Fig. 4.20 (a) – (d), displayed large hysteresis between the austenite start and austenite finish temperature. Further, the samples were damaged after the analysis. Shape change is probable during the process, which might affect the readings. The minor deviation in readings can also be due to the movement of the SMA film during analysis. Further, the analysis was conducted only till 350 °C, and a well-defined austenite finish temperature was not

observed. The martensite start and finish temperature were not significant due to the extensive cooling time by natural convection.

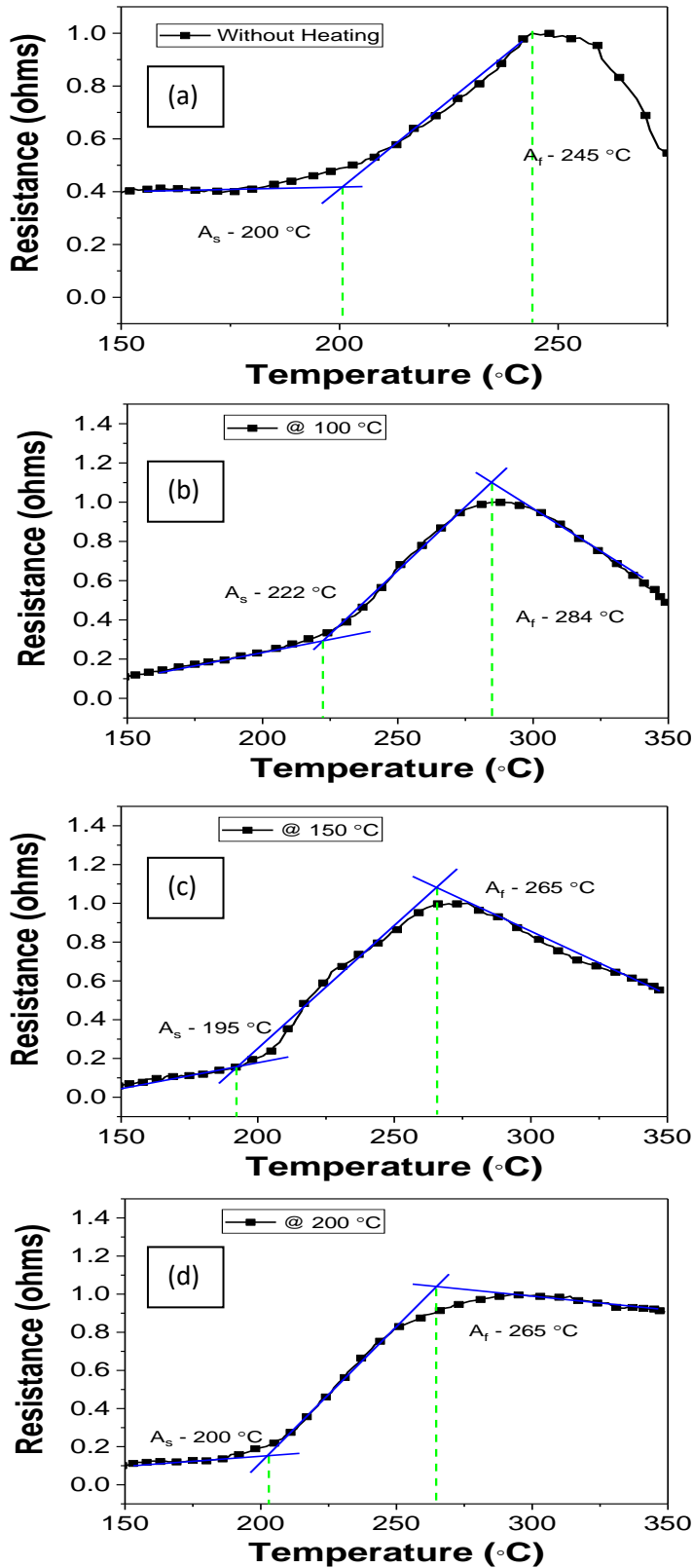


Figure 4.20: Resistance vs temperature plots of samples developed at (a) without growth substrate temperature (b) @ 100 °C (c) @ 150 °C and (d) 200 °C.

To find out the transformation temperature precisely, the samples were further characterised by differential scanning calorimetry. For the analysis, the samples were into samples pieces less than 2 mm and approximately 10 mg of such samples were loaded in the crucible. Crucible of 35  $\mu$ l was used for the analysis, and the analysis was conducted at argon atmosphere. Fig. 4.21 shows the DSC measurements of CuAlNi bimorphs developed at different substrate temperatures. The heating and cooling rate were controlled at 10  $^{\circ}$ C/min for 10 mg sample. The sample deposited without growth substrate temperature displayed a sharp dip indicating the austenite transformation temperature  $T_A = 224.07$   $^{\circ}$ C. During the exothermic reaction, a trivial peak representing the martensite transformation temperature  $T_M = 223^{\circ}$ C was present. With growth temperature of 100  $^{\circ}$ C, the transformation temperatures were found to  $T_A = 264^{\circ}$ C and  $T_M = 239$   $^{\circ}$ C. The sample developed at 150  $^{\circ}$ C had a composition close to the initial percentage, and the transition temperature was observed at  $T_A = 248.12$   $^{\circ}$ C and  $T_M = 224.09$   $^{\circ}$ C.  $T_M$  of the samples deposited at 200  $^{\circ}$ C was at 163.12  $^{\circ}$ C, significantly away from  $T_A$ . The hysteresis of the samples developed at 200  $^{\circ}$ C was highest of the developed samples. All the samples developed with substrate growth temperature displayed a well-defined austenite transformation peak. The deduced transformation temperatures from the DSC graphs are summarised in Table 4.5. The transformation hysteresis of the samples increased with increase in substrate heating temperature. The exothermic plot during cooling as shown in Figure 4.21 (b) showed minor signs of martensite transformation.

**Table 4.5: Transformation temperatures from DSC and Van der Pauw method**

Samples	Heating (DSC)			Cooling (DSC)				Heating (Four probe)	
	$A_s$ ( $^{\circ}$ C)	$A_f$ ( $^{\circ}$ C)	$T_A$ ( $^{\circ}$ C)	$M_s$ ( $^{\circ}$ C)	$M_f$ ( $^{\circ}$ C)	$T_M$ ( $^{\circ}$ C)	$T_A - T_M$ ( $^{\circ}$ C)	$A_s$ ( $^{\circ}$ C)	$A_f$ ( $^{\circ}$ C)
WH	223.52	225.16	224.07	226.36	219.58	223.90	0.17	200	245
100 $^{\circ}$ C	259.81	284.95	264.02	240.27	236.75	239.13	24.89	222	284
150 $^{\circ}$ C	243.91	261.99	248.12	226.79	221.52	224.09	24.83	195	265
200 $^{\circ}$ C	243.77	271.91	254.20	163.95	161.50	163.12	-137.7	200	265

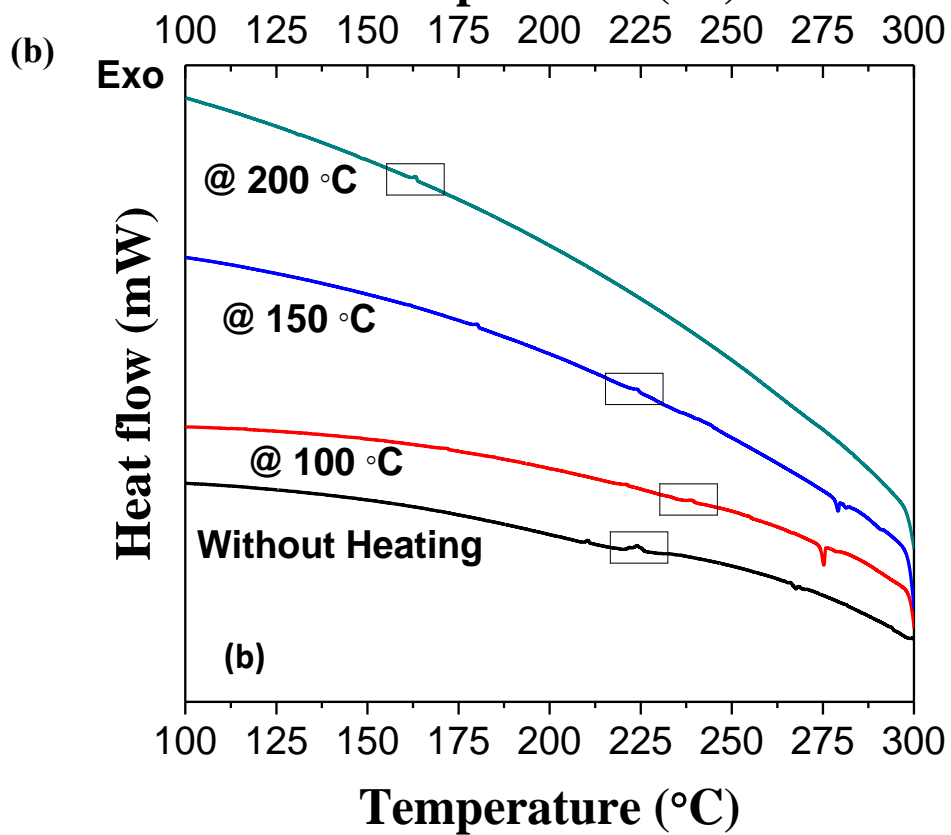
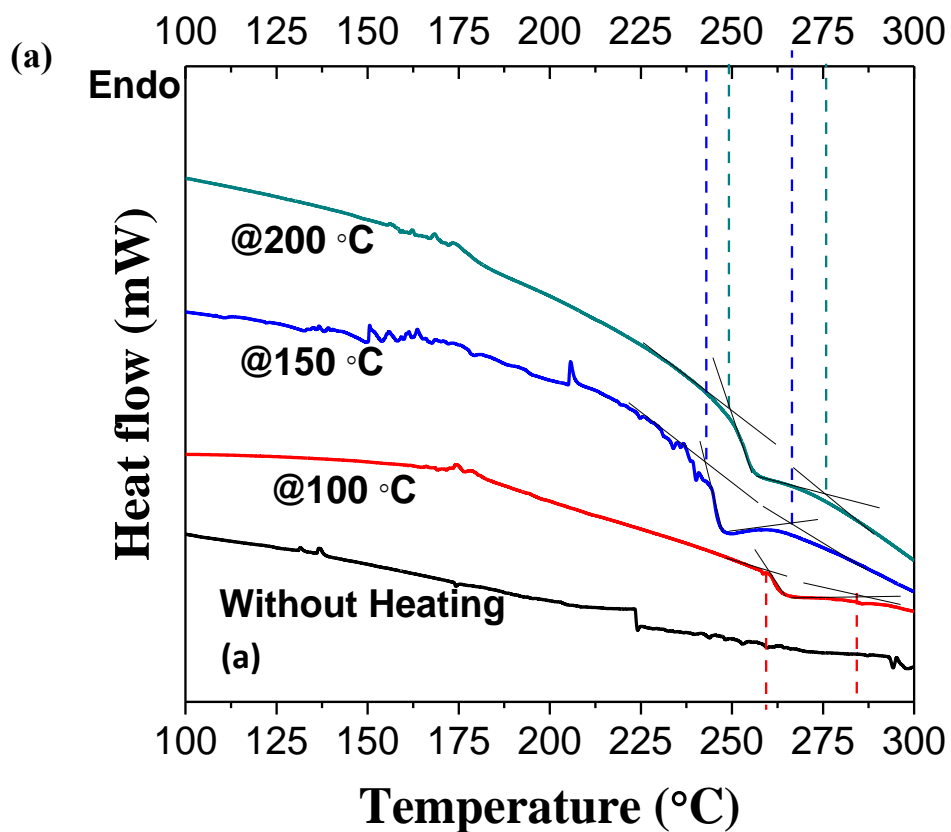


Figure 4.21: Differential Scanning Calorimetry graphs showing the phase transition of the composite films. (a) Endothermic plot, (b) Exothermic plot

The transformation temperature  $T_A$  and  $T_M$  altered for each sample, which might be attributed to the change in the composition, as observed from EDS results. Further, the thermal history of the substrate also affects the transition temperatures. From the DSC plots the endothermic plots showed several small exothermic peaks, which might be due the crystallisation or glass, transition of the polyimide substrate. There were sharp endothermic peaks at 275°C, which might be due to rapid volatilisation of trapped gases. Further, it can be observed from the depth of the transformation peak, the percentage of crystallinity is higher for samples developed at 150 °C than other samples. Quantitative analysis can be made when there is prominent peak during the exothermic reaction. As observed from Table 4.5 the results from four probe van der paw method and differential scanning calorimetry are having rather identical results. The austenite finish temperature of the all the four samples displayed values similar to DSC. However, the thermal hysteresis between the austenite start and finish is large with the van der paw results. The change in resistance can be affected by other parameters, and the repeatability of the results are not significant. Therefore, van der paw analysis was neglected for the further analysis.

#### **4.4.5 Shape Recovery Ratio**

The bimorphs were attached to a plate heater, and the displacement concerning increase in temperature was calculated. Based on the observed results the recovery ratio was estimated. The samples were cut to 7 cm × 2 cm sheets for the analysis. The curvature of the bimorphs at room temperature was used as the reference, and the change in curvature was noted for every 25 °C. The heating rate was maintained at 10 °C/min. The diameter of both vertical and horizontal axis was considered, as the bimorphs had a non-uniform structure. The results of the recovery ratio can be seen in Fig. 4.22. It can be observed, the recovery ratio was superior with 1.71, for sample developed at 150 °C substrate temperature. All the other bimorph heating displayed a ratio between 1.4 and 1.5. Further, the bimorph developed at 200 °C substrate temperature exhibited better recovery characters as compared to bimorphs developed with heating and 100 °C substrate temperature. However, as the temperature increased, recovery properties of bimorphs developed at 200 °C substrate temperature subsided, and bimorphs developed at 100 °C

exhibited better stability at high temperatures. Bimorphs developed at 150 °C substrate temperature displayed no signs of deformation as temperature increased.

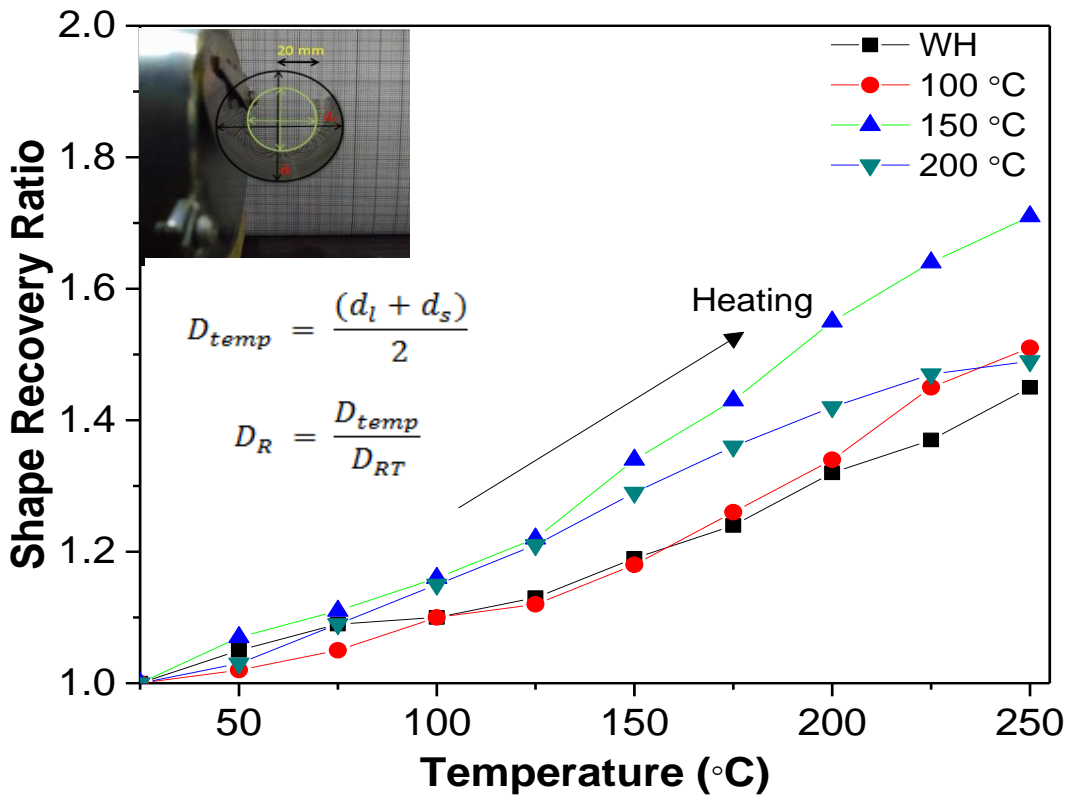


Figure 4.22: Recovery ratio calculation during heating

#### 4.4.6 Life Cycle Analysis

The bimorphs were actuated using Joule heating, and the life cycle behaviour of the films was tested up to 500 cycles. Fig. 4.23 shows the results of life cycle analysis probed using three different voltages ranging from 2 V- 3 V. The film was actuated at a frequency of 0.5 Hz at 2 V and the results are displayed in Fig. 4.23 (a). The displacement obtained with samples deposited at 150 °C was very high, as compared with other samples and an average displacement of above 1 mm was observed for 500 cycles. The samples obtained without substrate heating exhibited better fatigue as compared to samples obtained at 100 °C and 200 °C. At 2.5 V the samples developed at 200 °C substrate temperature displayed a decline in displacement from 0.9 mm to 0.5 mm. The samples grown without substrate heating and at 100 °C showed no signs of fatigue. However, with samples developed at 150 °C there were minor fluctuations in displacement and an average

displacement of 2.25 mm was observed. The results from electrical heating of the

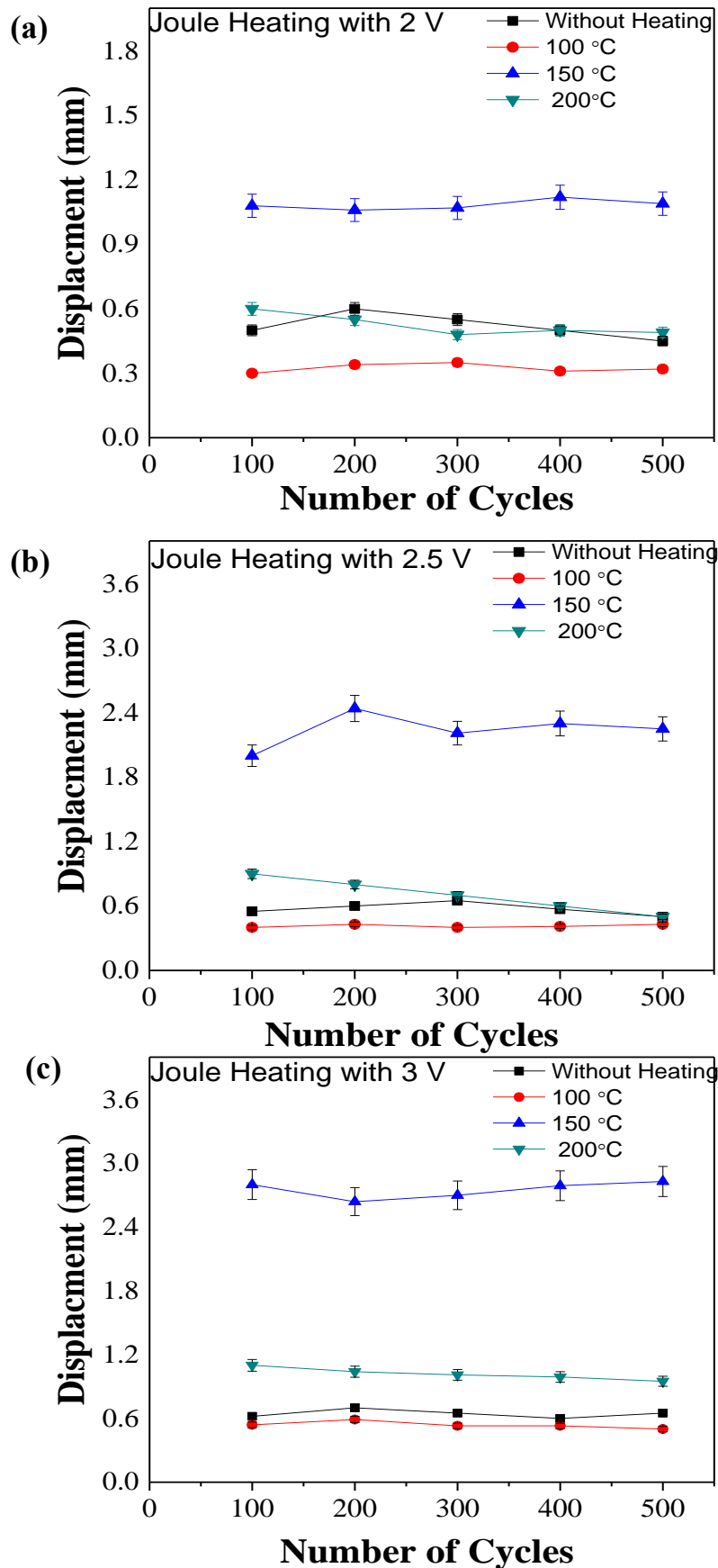


Figure 4.23: Life Cycle Analysis graphs showing the change in displacement for 500 cycles. (a) Joule heating with 2 V (b) Joule heating with 2.5 V (c) Joule heating with 3 V

films at 3 V showed similar results with an increase in average displacement. The samples developed at 150 °C showed an average displacement of 2.6 mm. After 200 cycles, there was a minor decrease which was not seen in the next 300 cycles as there was a steady increase. The samples developed without substrate heating, 100 °C and 200 °C showed an average displacement of 0.6 mm, 0.45 mm and 0.92 mm respectively. There was a minor decrease in displacement of the samples grown at 100 °C after 500 cycles.

The life cycle analysis determined that samples developed at 150 °C growth substrate temperature had superior properties, which could be attributed to a large amount of martensite fraction to transform. Further, the samples developed at 150 °C had an exact composition and finer grains without precipitates. The recovery ratio also suggests that 150 °C substrate heated samples revealed better shape memory effect than the rest. Except for the samples developed at 150 °C growth temperature, the other samples exhibited a trivial displacement curve after 500 cycles. This can be assigned to the presence of  $\alpha$  and  $\gamma$  phases, which can hinder the stability in prolonged working conditions. The samples grown without substrate heating exhibited better life cycle than samples grown at 100 °C and 200 °C substrate heating. However, the recovery ratio implies, 100 °C substrate heated samples are second best to exhibit better shape memory effect. Moreover, the samples developed at 100 °C displayed a steady displacement plot, which was the best of all the samples. The optimum parameters for Joule heating were found to be 3 V without any decrease in displacement for all the samples.

From the results, it is evident that thermomechanical behaviour of CuAlNi Polyimide bimorph can be varied by changing the growth substrate temperature. A substrate temperature of 150 °C is best suited to develop CuAlNi/Polyimide bimorphs, beyond which different phase coexist which will hinder the stability of shape memory effect. The second-best growth temperature was found to be 100 °C, which displayed excellent Recovery ratio and stable  $\beta'_1$ . Even though the displacement was less, the bimorphs developed at 100 °C is best suited for applications as it displayed a steady displacement throughout the 500 cycles. Temperature sensing applications like a circuit breaker and viscous fluid temperatures can be monitored with the help of developed bimorphs. The load-

bearing capacity of the bimorphs is also in good agreement with the proposed applications.

#### **4.5 Summary**

The influence of substrate thickness and growth substrate temperature on the material, thermomechanical and life cycle behaviour of the developed CuAlNi bimorphs was explored in detail, and the results can be summarised as

##### **Varying Substrate Thickness**

- The adhesion between CuAlNi and polyimide was tested using scotch tape analysis, and there was no removal of the deposited SMA film.
- XRD results indicate a high-intensity peak corresponding to  $\beta$  (220), and the crystallite size was found to be 6.67 nm, which shows the crystallinity of the developed structures.
- SEM images showed a continuous film with a grain size of approximately 100 nm.
- The thermal decomposition of the Cu-Al-Ni/Polyimide bimorph was rapid when compared to bare polyimide sheet as confirmed by TGA analysis.
- The austenite transformation temperature was found to be  $A_s = 215$  °C and  $A_f = 240$  °C measured by temperature vs resistance plots.
- The bimorph structures without any post-processing and training showed maximum displacement of 19 mm during both heating and cooling cycles.
- The shape recovery ratio was calculated, and it was found that 75  $\mu$ m polyimide sheet had better recoverability of than 50  $\mu$ m.
- The bimorph developed at various substrate thickness was tested for 500 cycles, and the bimorph showed minor signs of deviation from the average displacement.
- 75  $\mu$ m thick polyimide substrate has a stable life as compared to 50  $\mu$ m sheets and has better applicability in devices

##### **Varying Substrate Growth Temperature**

- There were precipitates of ordered Cu<sub>3</sub>Al precipitates, which were less at 150 °C. Beyond 150 °C, the morphology was textured with large grains.

- Composition analysis showed 150 °C had values close to the initial composition.
- Adhesion was excellent for all the samples, with less than 0.3 mg adhering to the scotch tape.
- XRD results presented the crystalline  $\beta_1 \gg \beta'_1 + \gamma_2 \gg \beta'_1 \gg \alpha$  phase formation.
- Further, the XRD results showed stable  $\beta'_1$  without  $\alpha$  and  $\gamma$  phases at growth temperatures of 100 °C and 150 °C.
- DSC graphs exhibited a well-defined transition peak as the sample developed at 200 °C exhibited large hysteresis while the samples developed without substrate heating showed minimal hysteresis.
- Recovery ratio calculation presented that samples developed at 150 °C substrate temperature had the capability to exhibit substantial shape memory effect.
- The samples developed at 100 °C growth temperature was the second best among the tested conditions.
- The developed samples were tested for life cycle, which displayed no signs of fatigue for samples developed with substrate heating.
- The samples developed with 150°C growth temperature had a superior displacement as compared to other samples.
- Due to the presence of  $\alpha$  and  $\gamma$ , the samples developed at 200 °C showed a decline in displacement after 500 cycles.
- The samples developed without growth temperature, and 100 °C growth temperatures can be suitable for applications, which require minimal displacement as the films displayed a stable and steady actuation behaviour.

## Chapter 5

---

# Theoretical Simulations on Structural and Thermal Behaviour of SMA Composite

CuAlNi shape memory effect exhibited by thin films developed on Kapton polyimide substrate is a complex process to analyse. The curvature of the polyimide plays a vital role in two-way shape memory effect. There are few literatures with NiTi SMA theoretically simulated with known properties. Through simulation, it is difficult to reproduce the shape memory effect displayed by copper-based alloys, as there is very less work with thin films. In this chapter, the structural and thermal properties of the bimorphs under different loading conditions was studied through simulation. The simulation was carried out using COMSOL Multiphysics software, and structural mechanics module was utilized for the analysis. Further, the emissivity of the thin film was varied from 0.1 to 0.9, and the temperature profile was obtained at varying current flow. The simulations utilised in understanding the behaviour of bimorph under Joule heating which is later compared with the experimental results.

### 5.1 Simulation Parameters

COMSOL software was used to study the stress profile when a fixed constrained is given at the centre during simulation. The actuation parameters are neglected for the simulation analysis and the flow chart illustrating the steps involved is shown in Fig. 5.1. The structural was used to compare with the experimental results to find the load-bearing capacity of the bimorph without the SME. By doing so, the percentage of recoverable strain can be approximated.

The steps used in this simulation are based on the following assumptions;

- The elastic strain should not be ignored because it plays a vital role in two-way SMA Bimorph actuation.
- The principal directions of stresses are oriented along the X, Y, and Z directions of the bimorph.
- The Bauschinger effect that prevails and pertinent due to bending–unbending cycles can be neglected because results are minimal when the

ratio between bending radius and bimorph thickness is  $\geq 6$ . Thus, the isotropic hardening is considered.

- The bimorph wall is considered to be straight.
- The shear stresses in the bimorph can be neglected because it is minimal.
- The plane strain conditions are considered both side of the clamped bimorph since the strains in the Y direction are zero.
- The Young modulus is considered constant while increasing plastic strain.
- The top surface of the bimorph materials used for node set and stress analysis.
- The coefficient of friction between PI and SMA thin film is considered to be 1.0.
- The actuation parameters of SMA are neglected for the simulation analysis.
- The developed composite films had a semi-circular shape after deposition.

## 5.2 Structural Analysis

The bimorph was considered as a cantilever beam, and the structural analysis was performed, when there is an external load applied to the free ends. By consider this structural form, the stress acting on the composite structure and load-bearing capacity can be probed. The simulation is conducted without considering the shape memory effect as a normal composite structure. The governing equations using free body diagram as shown in Fig. 5.2 for a single beam cantilever is given below

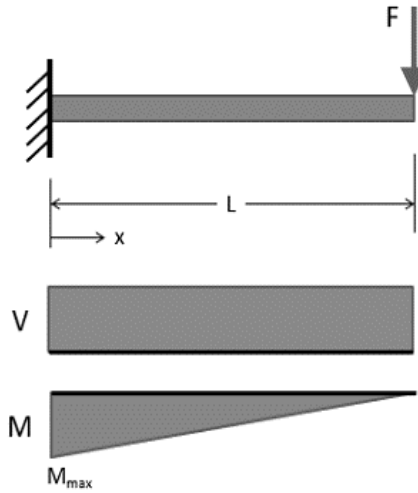


Figure 5.1: Single beam cantilever

The curvature of Neutral Surface ( $1/\rho$ ) is described by the moment and the flexural rigidity of the composite

$$(1/\rho) = (M/EI) \quad (5.1)$$

### 5.2.1 In case of the transverse loading

$$(1/\rho) = (M(x)/EI) \quad (5.2)$$

$$M(x) = -Px \quad (5.3)$$

$$(1/\rho) = (-Px/EI) \quad (5.4)$$

### 5.2.2 The equation for the elastic curve

$$1/\rho = ((\frac{d^2y}{dx^2})/([1 + (\frac{dy}{dx})^2]^{3/2})) \quad (5.5)$$

$$1/\rho = (\frac{d^2y}{dx^2}) \quad (5.6)$$

$$(\frac{d^2y}{dx^2}) = (M(x)/EI) \quad (5.7)$$

### 5.2.3 Equation related to Solutions

*Deflections*

$$\delta = (-) \frac{Fx^2}{6EI} (3L - x) \quad (5.8)$$

$$\delta_{max} = (-) \frac{Fx^2}{6EI} ; \text{at } x = L \quad (5.9)$$

*Slope*

$$\theta = (-) \frac{Fx}{2EI} (2L - x) \quad (5.10)$$

$$\theta_{max} = \frac{FL^2}{2EI} ; \text{at } x = L \quad (5.11)$$

*Moment*

$$M = -F(L - x) \quad (5.12)$$

$$M_{max} = -FL; \text{at } x = 0 \quad (5.13)$$

Where,  $\rho$  –is the radius of curvature, M is Moment, E is Young's modulus, I is the second moment of area, and L is the length of the composite structure.

### 5.2.4 Von Mises Stress

As the object is under applied force and that given stress satisfies certain nominated criteria such as yield criteria, then a plastic component of strains are produced, and that is called deformation strains. Moreover, one such criterion, which needs to be qualified for the plastic deformation, is the Von Mises yield criteria. The von Mises yield criterion states that the von Mises stress of material under acted load condition should be neither equal nor greater than the yield limit

of the material under uniaxial stress. The Von Mises stress is criteria for yielding, which states that component will fail or yielding will occur in a body if the acting stress component on the object is greater than criteria as mentioned in equation (3.20).

$$[(1/6)\{(\tau_{11}-\tau_{22})^2+(\tau_{22}-\tau_{33})^2+(\tau_{33}-\tau_{11})^2+6(\tau_{21}^2+\tau_{22}^2+\tau_{21}^2)\}]=k^2 \quad (5.14)$$

Where; the constant k is defined through experiment and  $\tau$  is the principle stress tensor. Therefore, the Von Mises yield criterion is mentioned as equation (3.21):

$$S_y = \frac{\sqrt{((\tau_1-\tau_1)^2+(\tau_1-\tau_1)^2+(\tau_1-\tau_1)^2)}}{2} \quad (5.15)$$

If octahedral stress is higher than the simple stress yield limit is expected to occur as mentioned in equation (5.15).

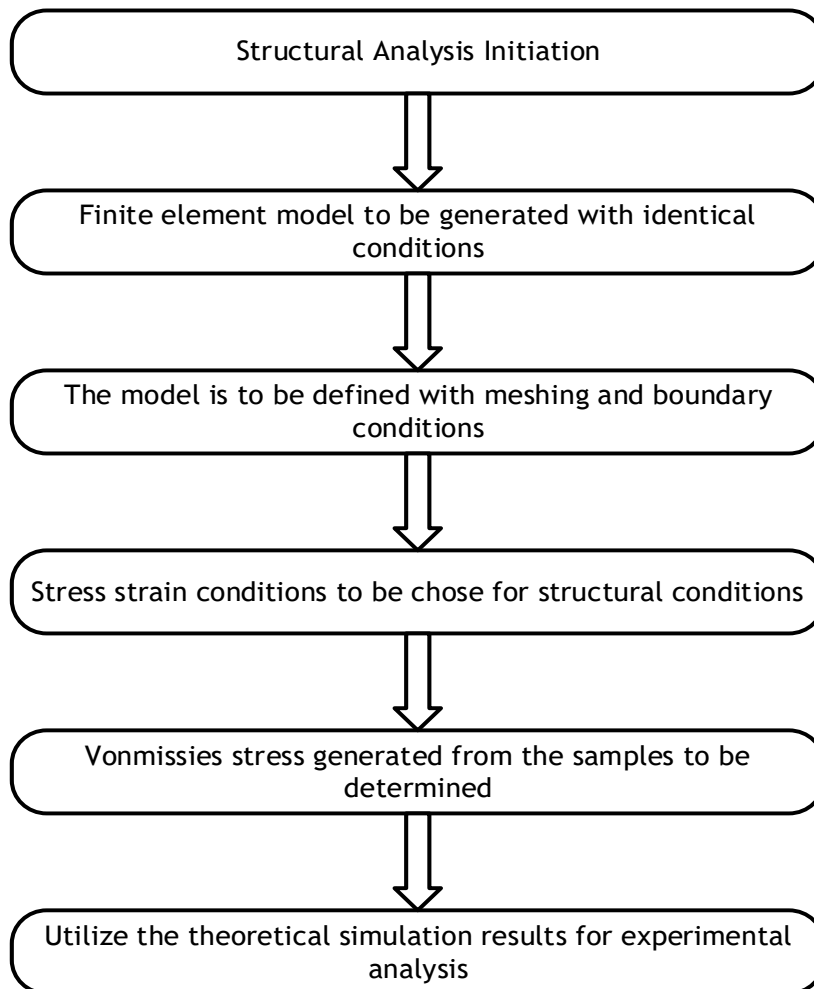


**Figure 5.2: Flow chart of the structural analysis**

### 5.3 Joule Heating Equations

The composite structure was further analysed for thermal behaviour with Joule heating. Copper contact was used an identical material, and meshing properties were used for the analysis. Further, the effect of emissivity on temperature with variation in current flow was analysed. Fig. 5.3 shows the flowchart of thermal analysis. The governing equation for the simulation is given below.

The direct current equation used for Joule heating

$$\Delta J + Q_{j.v} \tag{5.16}$$

$$J = \sigma E + J_e \tag{5.17}$$

Temperature time reaktion in SMA/polyimide

$$T = \frac{P}{h_c A_c} \left(1 - e^{-\frac{t}{\tau}}\right) + T_a \tag{5.18}$$

Heat transfer in solids

$$\rho C_p u \cdot \nabla T + \Delta q = Q + Q_{ted} \tag{5.19}$$

$$q = -k \nabla T \tag{5.20}$$

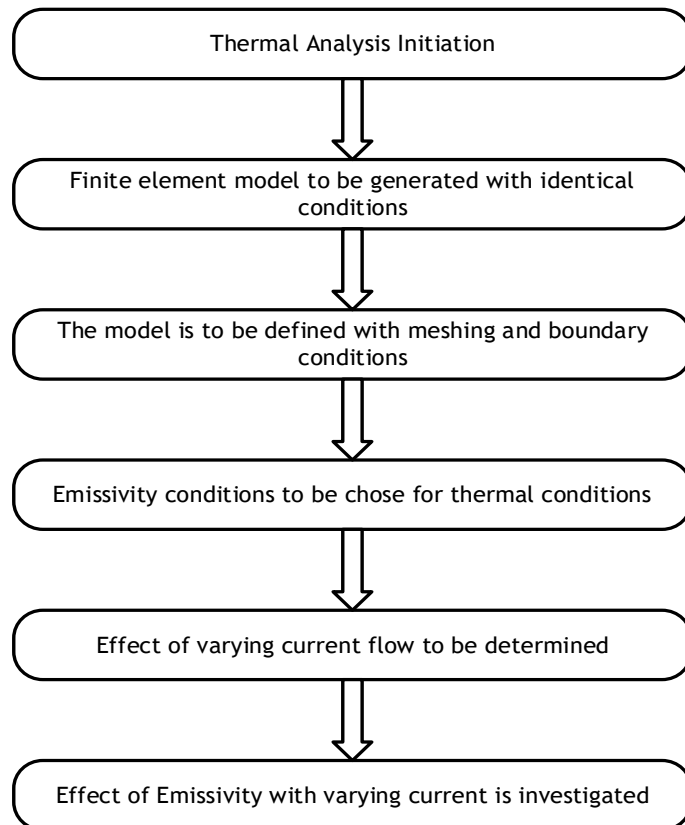


**Figure 5.3: Flow chart of the thermal analysis.**

## 5.4 Material Properties and Global Definition

The material properties for the simulation are given in Table 5.1. The developed composite films had a semi-circular shape after deposition, and similar conditions were considered for the simulation. The electrical contacts were placed at the edges from the epicentre. During actuation both the free ends exhibited displacement and in structural analysis, loads were applied to both the free ends and the composite structure was constrained at the centre as shown in Fig. 5.4.

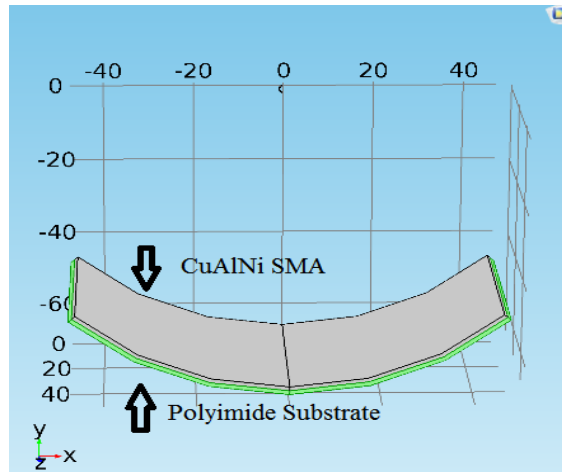


Figure 5.4: Global definition and part modelling of bimorph

Table 5.1: Material properties of CuAlNi and polyimide

<i>Description</i>	<i>Name</i>	<i>CuAlNi</i>	<i>Polyimide</i>
Density	<b>SMA_rho</b>	7150 kg/m <sup>3</sup>	1420 kg/m <sup>3</sup>
Heat capacity at constant pressure	<b>SMA_Cp</b>	400 J/(kg·K)	1090 J/(kg·K)
Thermal Conductivity	<b>SMA_K</b>	50 W/(m·K)	0.12 W/(m·K)
Electrical Conductivity	<b>SMA_sigma</b>	8.33E6 S/m	7.142E-16 S/m
Relative Permittivity	<b>SMA_epsilonr</b>	0.9	3.5
Resistivity	<b>SMA_res</b>	1.2E-7 Ω·m	
Young's Modulus	<b>SMA_E</b>	9E10 Pa	2.5E9 Pa
Coefficient of thermal expansion	<b>SMA_alpha</b>	17 1/K	7.299E-8 1/K
Endurance limit	<b>SMA_sigmae</b>	3.5E8 Pa	
Poisson's Ratio	<b>P_nu</b>	1.7	

Emissivity	<b>SMA_emissivity</b>	0.2
Initial Current	<b>I</b>	0.6 A
Initial voltage	<b>V</b>	2 V

### 5.5 Boundary Conditions

The boundary as shown in Fig. 5.5 displays the constrained SMA Bimorph used in the simulation. Fig. 5.5 (a) demonstrates the centreline of the bimorph along the Z-axis. After constraining Z axis of the modelled bimorph, it is transformed into double symmetric cantilever and the SMA and polyimide interface and is fixed. Fig. 5.5 (b) demonstrates the linear constraints, top nod constraints, centre, and bottom nod constraints. Moreover, the central line (SMA/PI) interface line is

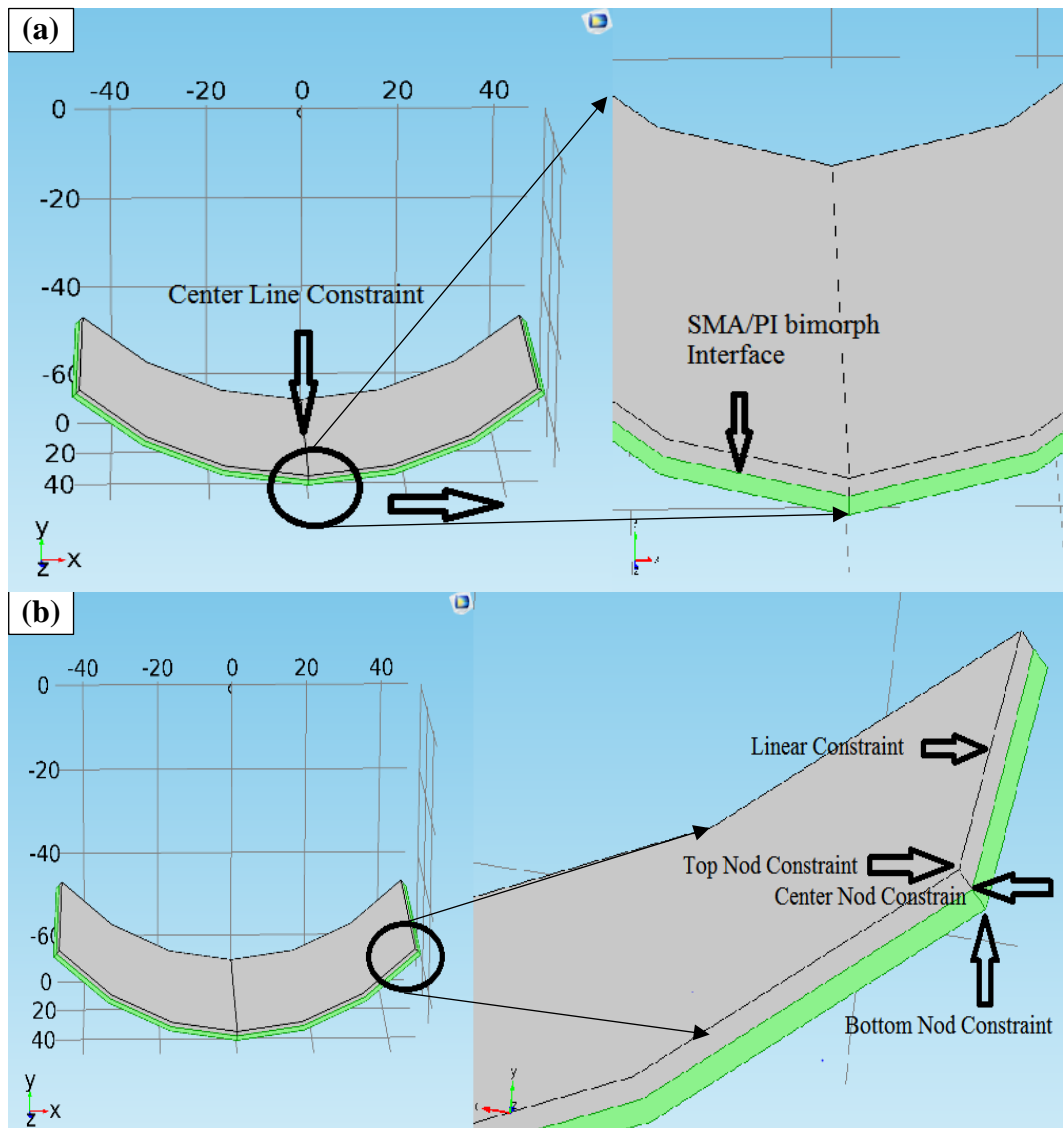


**Figure 5.5: Boundary conditions and the constraints implemented in bimorph simulation**

also constrained for the tip displacement (arc length displacement) at different load varying from 10 mN to 50 mN.

**Boundary conditions 1:** Can be used to specify the values of all primary solution variables (displacements, rotations, warping amplitude, and connector material flow) at nodes.

**Boundary conditions 2:** Given as “model” input data (within the initial step in COMSOL) to define zero-valued boundary conditions, and boundary conditions specify the Degree of Freedom allowed for a part also in history non-zero values.

**1. SMA/PI Bimorph in step-1,** Boundary condition imparted to reference point of the bimorph. This boundary condition is imparted in the initial step of simulation procedure so that bimorph gets zero degrees of freedom and remains static throughout the procedure.

**2. Load application in step-2,** Boundary Condition imparted to Reference Point of bimorph is its arc displacement concerning applied force  $F1=0$  mN,  $V2= -50.0$  mN and rotation = 0. This boundary will move the bimorph curve tip from the initial position to 18 mm towards outer periphery.

### **3. Interaction properties**

Most contact problems are modelled by using surface-based contact. Contact between a rigid constraint point and a deformable body. The structures can be either two or three dimensional, and they can undergo either small or finite sliding. Examples of such problems include cantilever bending simulations.

There are three steps in defining a constraint nod based contact simulation in COMSOL simulation

- Defining the surfaces of the bodies that could potentially be in contact;
- Specifying the node and force point interact with one another;
- Specifying the node of the tip and which node of the PI/SMA interface line and point intersection connected with one another.
- Defining the mechanical and thermal property models that govern the behaviour of the surfaces when they are in contact.

## 5.6 Meshing Properties

Fig. 5.6 shows the meshing profile in which the minimum element size was 1.34 mm. The tetrahedral mesh with total elements 26519 and triangular mesh with total elements 14128 was used with a minimum element size of 1.34 units and element growth rate of 1.45. The diffuse surface radiation heat transfer analysis is carried out, and the temperature profile is obtained. Table 2 shows the meshing properties and elements present.

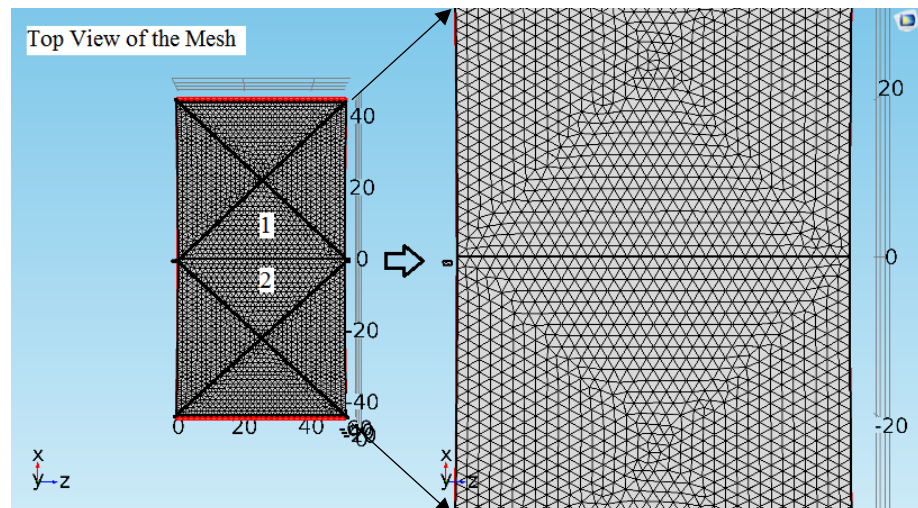


Figure 5.6: Tetragonal meshing used in simulation

Table 5.2: Meshing properties and the elements present after meshing

<i>Description</i>	<i>Value</i>
Minimum element quality	0.1409
Average element quality	0.6919
Tetrahedral elements	26519
Triangular elements	14128
Edge elements	665
Vertex elements	24
Maximum element size	10.7
Minimum element size	1.34
Curvature factor	0.5
Resolution of narrow regions	0.6
Maximum element growth rate	1.45

### 5.7 Effect of Von Mises Stress

The results indicate the SMA/PI bimorph in an initial state of equilibrium or un-deformed condition is acted with internal and external force and the stress

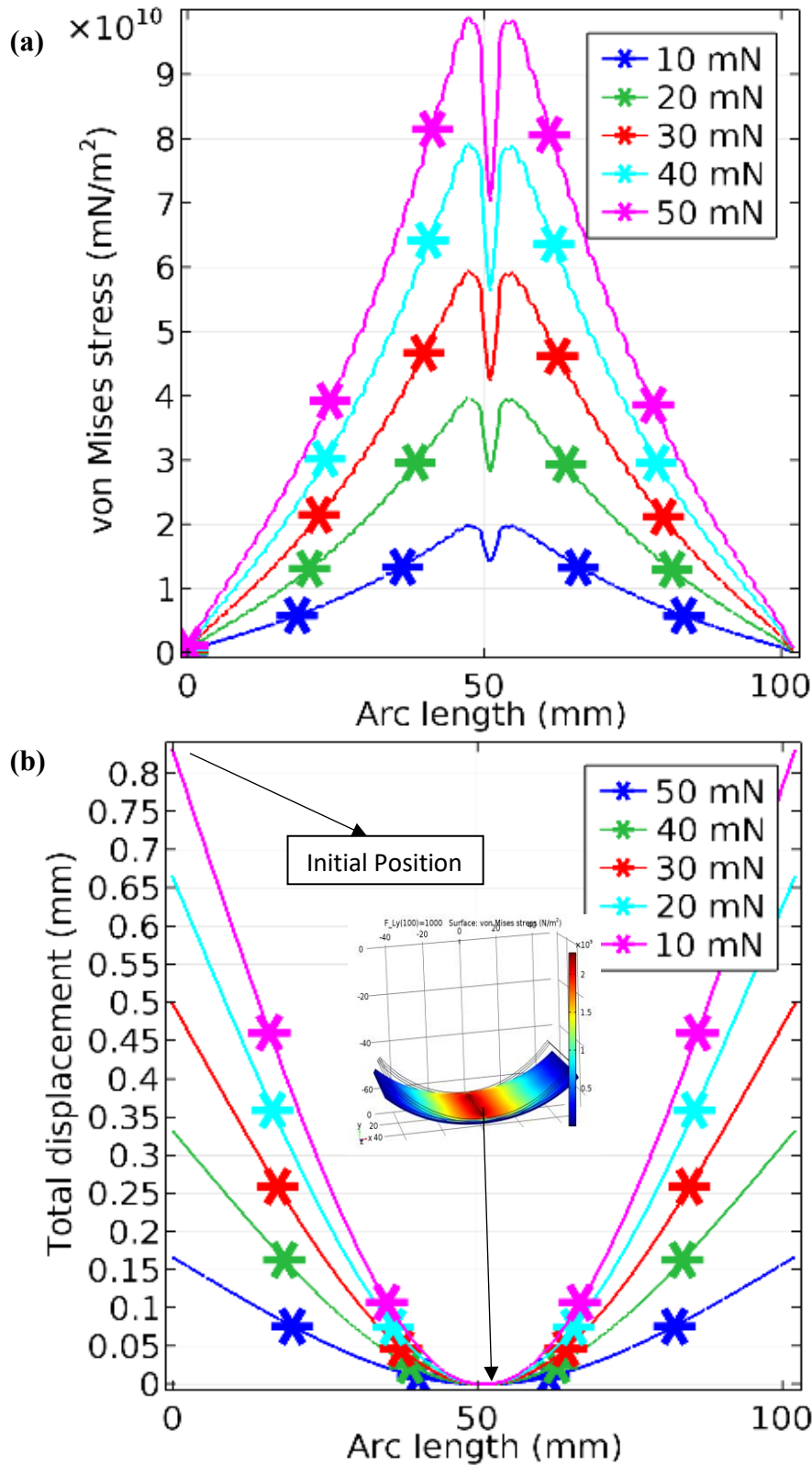
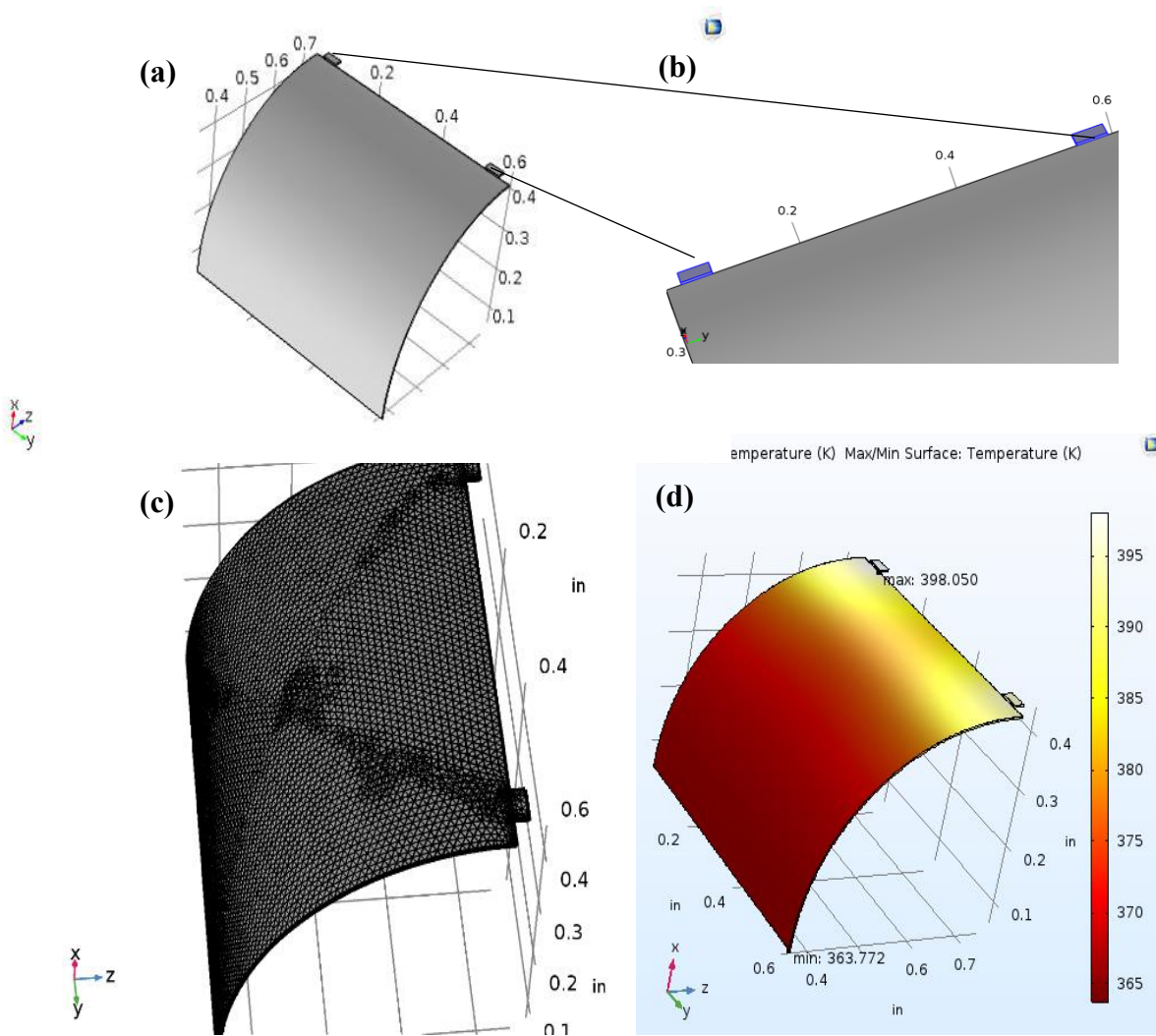


Figure 5.7: (a) Von misses stress variation across length as the load is increased (b) Variation in displacement with reversed arc length under varying loads at the tip of the bimorph.

profile with reversed arc length is given in Fig. 5.7 (a). The composite film deforms subsequently until the object attains another mechanical equilibrium states. The internal forces are the resultant of force fields like gravity and surface forces are the resultant forces appears by contact force of another body. The external forces characterise stress, internal deformation characterises strain, and the resultant cumulative effect is called Stress-Strain relations. These constitute relation because it represents properties of the materials composed of the subjected body. An initial load of  $10 \text{ mN/m}^2$  or  $10 \text{ MPa}$  displayed the stress profile increase from the free to the centre of the composite. There was a minor reduction in stress at the constraints. As the load increased the stress generated in the film increased. Fig. 5.7 (b) shows that a maximum of  $0.65 \text{ mm}$  approximately change is displacement will be induced due to the  $50 \text{ mN}$  load.

### **5.8 Effect of Emissivity**

The dimensions of the bimorph are modified for the thermal analysis for straightforward comparison with experimental results. The shape is similar to that of single beam cantilever, where one side of the bimorph is chosen for the analysis as shown in Fig. 5.8 (b). Joule heating with copper contacts as displayed in Fig. 5.8 (b) was utilised as the actuation source, and the temperature profile of the bimorph at varying current flow was studied concerning different emissivity. Boundary and meshing conditions were similar as shown in Table 5.1 and 5.2. Fig. 5.8 (c) and (d) shows the meshing and model of the created model. The objective was to find out the maximum working temperature of the bimorph and use the same for experimental analysis as shown in Fig 5.8 (d). Further, later in the experimental section, the addition of Mn has induced significant changes in thermal and electrical properties. Although the quaternary alloys are not studied through simulation, the ternary CuAlNi simulation results were compared with the experimental results.



**Figure 5.8: (a) Single beam cantilever model of bimorph for thermal analysis (b) copper contact for Joule heating (c) Tetragonal meshing of bimorph and (d) heat transfer profile during Joule heating.**

### 5.8.1 Temperature profile at Varying Emissivity

The emissivity vs temperature profile of CuAlNi bimorph is showing in Fig. The results as shown in Fig. 5.9, exhibits there is no significant change in temperature as the emissivity changes at low current. However, as the current flow is increased to 0.8 amps and above, the temperature is high at  $\epsilon = 0.1$  and 0.2. This trend is similar for most of the metals, where  $\epsilon$  is 1 for black bodies, theoretically stating that the body absorbs all the heat. Therefore, the temperature is less at  $\epsilon$  values beyond 0.3. It can be observed that at two amps the temperature reaches 250 °C with  $\epsilon$  of 0.8. Mostly thin films have highly reflecting surface, and there can be variation in emissivity during phase transformation. The simulation results also

indicate the suitable range for actuation was with less than one amps, as the temperature reaches marginally above 200 °C with  $\epsilon$  as 0.2.

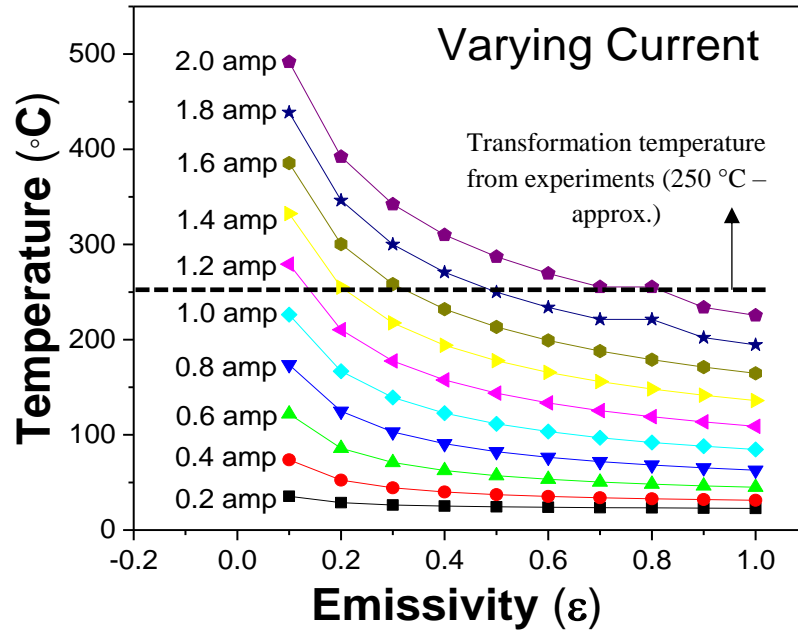


Figure 5.9: Results displaying the temperature vs Emissivity at varying current

### 5.8.2 Temperature Profile at varying current

The simulation was further extended with studies on temperature profile with the different current flow. The results as shown in Fig. 3.11 display the significant variation in temperature between emissivity of 0.1 and 0.2. The

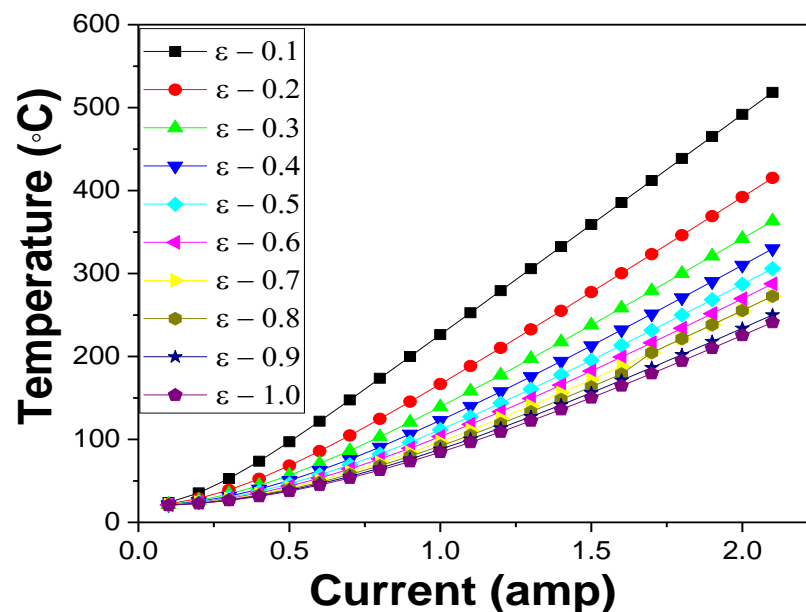


Figure 5.10: Results displaying the temperature vs current at varying emissivity

temperature reaches 250 °C at one amp for  $\epsilon=0.1$ , whereas the temperature is only 150 °C at  $\epsilon=0.2$ . The variation is not substantial as emissivity reaches 1. The minimum temperature at maximum current was observed with  $\epsilon=1$  reaching approximately 250 °C. Both the results prove the current values less than 0.8 amperes should be sufficient to actuate the film assuming that the emissivity is less than 0.3.

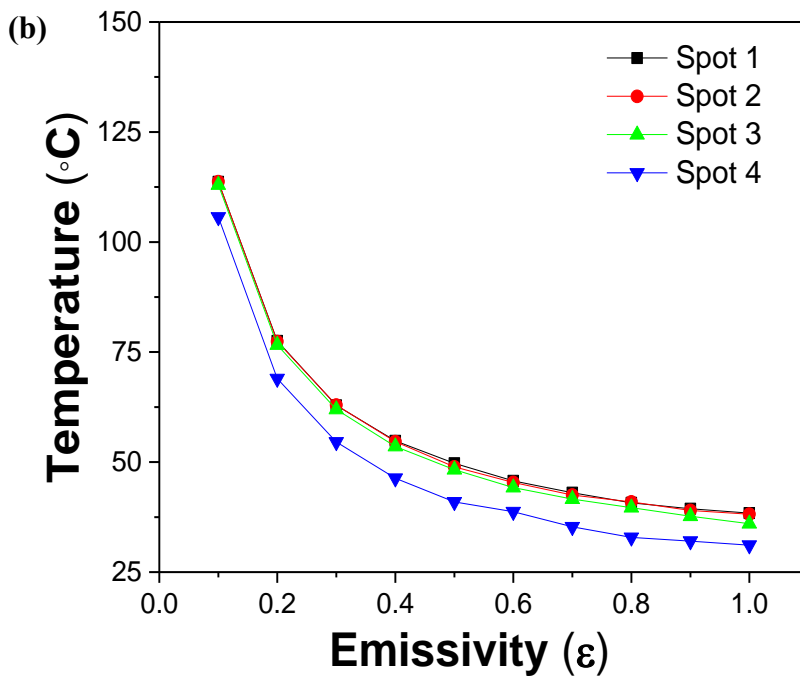
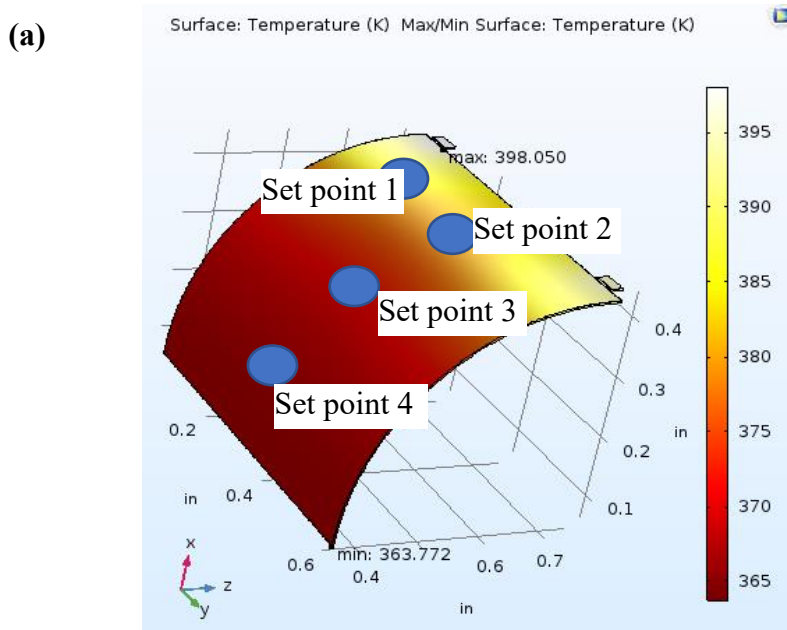


Figure 5.11: (a) Temperature profile obtained by Joule heating and the various set points taken (b) Temperature vs emissivity at varying set points

### 5.8.3 Temperature Profile at various spots during Actuation

Different spots on the bimorph were selected to analyse the heat transfer profile during the actuation. Analysing the heat transfer profile at different spots displayed the variation in temperature moving away from the contacts. Fig. 5.11 (a) shows the image of the different locations at the bimorph for the analysis and Fig. 5.11 (b) shows the variation in temperature for all four spots at an emissivity of 0.8. The results show that there is not much variation in the temperature profile at different spots. However, the shape memory effect is observed where residual stress is reduced on the application of heat. There will be a high amount of heat required for the process of phase transition. Therefore there will be a difference in temperature profile at different spots on the bimorph. The structural and thermal analysis will benefit in understanding the shape memory effect of the bimorph.

### 5.9 Summary

- The theory behind TWSME in SMA thin films deposited on the Kapton polyimide flexible substrate was discussed.
- Theoretical simulations on the structural properties of the bimorph were performed.
- The Von Mises stress effect displayed the effect of loads beyond 20 mN at the free ends of the bimorphs is the threshold limit.
- However, it was observed that the bimorphs could work with loads up to 50 mN
- Beyond 20 N the bimorphs will fail in real time
- The thermal analysis displayed the bimorphs to have an emissivity around 0.2 to 0.3.
- The effect of Joule heating was investigated, and the results exhibited the ability of the bimorphs to work efficiently under 0.6 amps.
- However, to control the current in real time for SMEs are particularly challenging due to variation in properties as temperature increases.
- The theoretical simulations were considered as a preliminary parameter set for further real-time experiments.



## Chapter 6

---

# Investigations on Inclusion of Mn in CuAlNi SMA Bimorph

### 6.1 Introduction

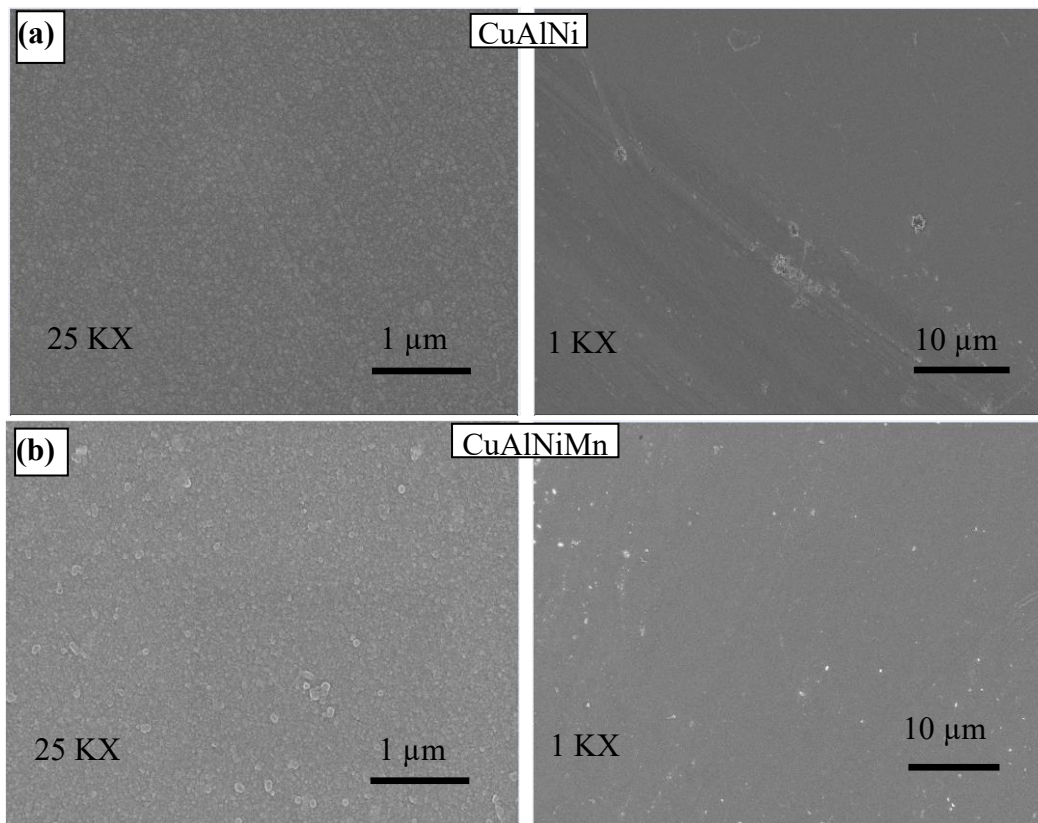
Copper-based shape memory alloys exhibit low hysteresis and have prominent electrical and thermal properties [134–138]. Particularly Cu-Al-Ni has higher thermal stability than other Cu-based alloys and holds the potential to be utilised in MEMS applications. Binary Cu-Al at high temperature has disordered  $\beta$  parent phase ( $\beta_1$  and  $\beta_2$  with D0<sub>3</sub> and B2 structures) which undergoes eutectoid decomposition at a temperature beyond 500 °C and forms  $\alpha$  phase with FCC structure and  $\gamma$  ( $\gamma_1$  with 2H martensite) phases.  $\beta$  phase stabiliser such as Ni is added to suppress the precipitate formation, and compositional changes with Al can be utilised to vary the transformation temperature. However, there is a loss of thermomechanical and pseudoelastic behaviour mainly due to the brittleness and large elastic anisotropy. The brittleness of these alloys is because of inherent coarse grains, precipitates and high anisotropy ratio which results in strain incompatibility at the grain boundaries [139]. Quaternary alloy, primarily manganese, has been proved to improve the shape memory and thermomechanical properties. Even though there are enough reports on CuAlNi bulk samples, the properties of SMA at micro and nanoscale is not similar. *San Juan et al. (2008)* has investigated the pseudoelastic behaviour of CuAlNi at the nanoscale. However, the improvement in ductility by Mn addition and the aftereffect on the thermomechanical and life cycle behaviour have not been experimentally investigated. The optimized results from previous analysis was used for further processing.

Two-way displacing CuAlNi/polyimide SMA bimorphs, which can operate for a large number of cycles was developed. However, the alloy is brittle in nature and fails subsequently when higher loads are applied. In order to enhance the cyclic repeatability and thermomechanical behaviour of CuAlNi, quaternary element manganese was added. To assess the improvement in material thermomechanical properties, the bimorphs was attached to mechanical loads, and the thermomechanical behaviour was investigated at different actuation conditions.

The life cycle of the developed samples was studied at particular loading conditions for a large number of cycles. Further, the samples were characterised by XRD, FE-SEM, EDAX, and DSC and the actuation behaviour has been associated with the structural, morphology and thermal properties.

## 6.2 Surface Morphological Analysis

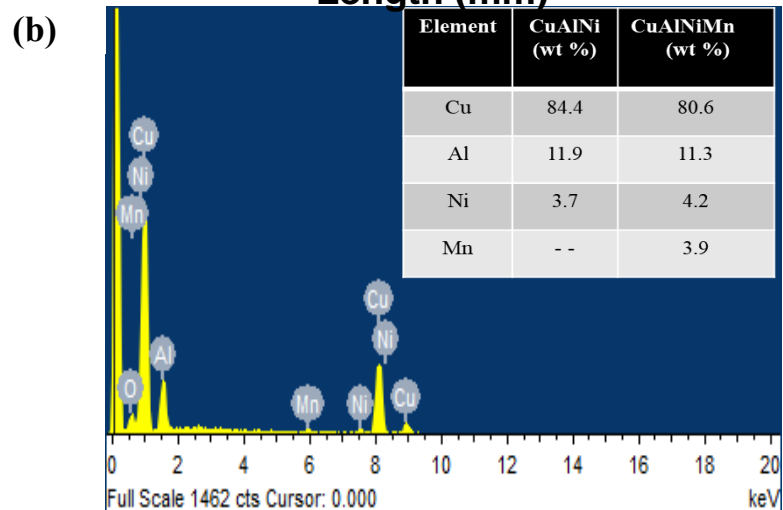
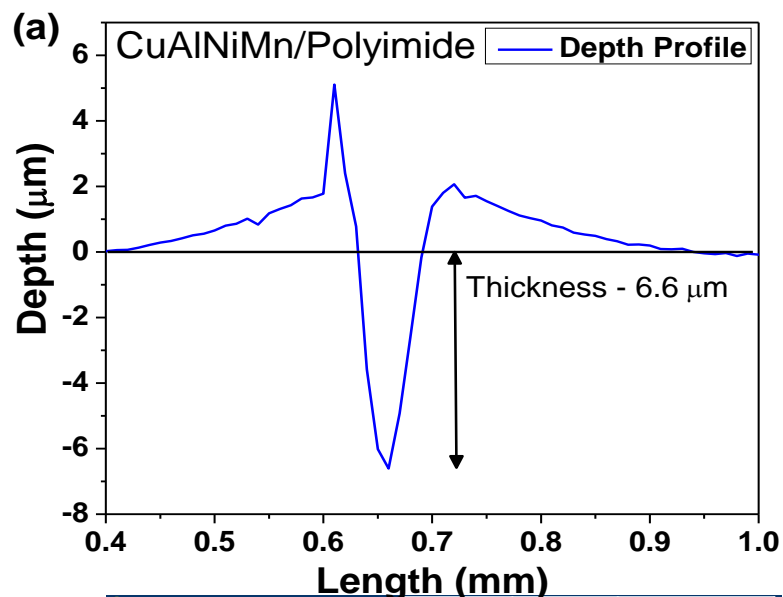
The scanning electron microscopic images present a smooth and uniform surface without any pores or cracks. The average grain size was calculated to be less than 150 nm for the developed samples. Fig. 6.1 (a) shows the surface morphology of CuAlNi/polyimide bimorph and Fig. 6.1 (b) shows the composition of the samples, measured by EDAX. The reduction in grain boundaries without any porosity or cracks was clearly visible from the SEM images. Further, the textures with martensite were evident from the lower magnification images.



**Figure 6.1: Images showing the (a) SEM image of CuAlNi at 25 KX and 1 KX and (b) CuAlNiMn bimorph at 25 KX and 1 KX**

### 6.3 Thickness, Composition and Roughness Analysis

The thickness of the bimorph was measured by scratching a line using a diamond cutter with uniform pressure, and the profiling was conducted at different places. The raw profile showed 6.6  $\mu\text{m}$  depth for the developed bimorphs. Fig. 6.2 (a) shows the results of the thickness measurement. The EDS analysis of CuAlNiMn was performed at five different locations, and the average composition results are summarised in Fig. 6.2 (b). The composition analysis presented a minor reduction in copper, nickel and manganese content. However, there was an increase in the atomic percentage of aluminium. Further, the adhesion of the samples was characterized by employing scotch tape tests. The scotch tape of particular weight was cut and stuck to the bimorph without air gaps. Uniform pressure is applied, and the sample was left for few minutes.



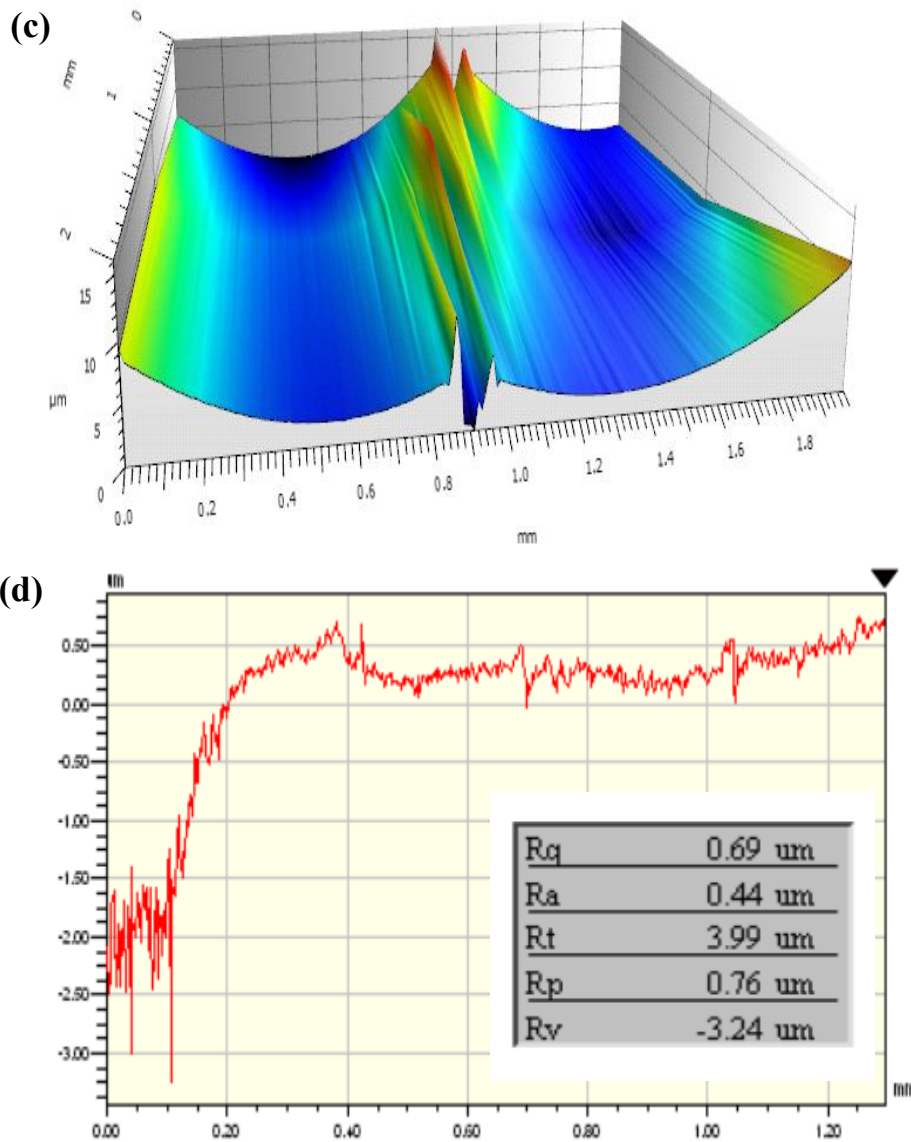


Figure 6.2: Results of (a) Thickness measurement, (b) Composition analysis from EDS (c) Roughness profile after scratching (d) Roughness plot of CuAlNiMn

Table 6.1: Results of the scotch tape analysis

Material	The weight of the tape before testing (mg)	The weight of the tape after testing (mg)	The weight of the adhered material (mg)
CuAlNi	54.2	54.7	0.5
CuAlNiMn	51.8	52.3	0.5

The scotch tape was removed gradually, and it is weighed again. There was less than 0.1 mg of sample adhering to the tape, demonstrating the excellent adhesion as shown in Table 6.1. Fig. 6.2 (c) and (d) shows the roughness profile of

the composite film. The abrupt change in the roughness the profile was observed with the developed bimorphs, and the  $R_t$  was found to be approximately 4  $\mu\text{m}$ .

#### 6.4 Structural Analysis

The XRD diffractogram displayed the presence of crystalline  $\beta'_1$  martensite peak belonging to monoclinic structure, with CuAlNiMn samples. The presence of crystalline  $\beta'_1$  (128) peak was evident from the results. Fig. 6.3 shows the XRD results of the bimorphs. It was found that the pattern peaks of the quaternary alloy were shifted towards a higher angle with variation in their shape and intensity. Similar results regarding the peak shift have been reported by other research groups [51,140]. The FWHM values obtained by peaks curve fitting using the Gaussian fit method. The crystallite size calculated using the Scherrer formula was found to be 23.5 nm for the samples.

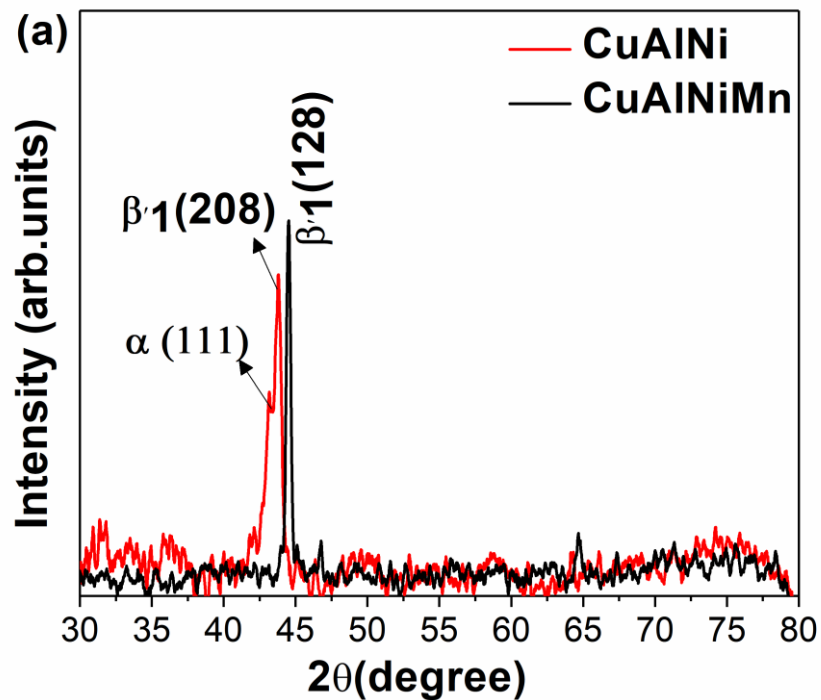


Figure 6.3: X-ray diffraction displaying the martensitic phase present in CuAlNiMn bimorph

#### 6.5 Thermal Analysis

Phase transformation temperature of CuAlNiMn samples was measured by DSC. Sample weight of 15 mg was used for analysis, and the heating rate was maintained at 10  $^{\circ}\text{C}/\text{min}$ . The results show that quaternary alloy had

reduced transformation temperature as compared to the ternary alloy. Fig. 6.4 (a) shows the DSC results of the samples. The austenite transformation temperature was found to be  $A_s$  - 221 °C and  $A_f$  - 235 °C respectively and there was no evidence of martensite transformation during cooling cycle for the samples. This might be due to the effect of the polyimide substrate, which might affect the cooling rate. There were other minor peaks present in the sample at 150 °C, which might be due to the stresses incurred during the deposition process [51,141]. Further, these peaks might also be present because of other impurities, trapped gases or the glass transition of the polyimide substrate. The TA of samples was found to be at 229 °C, as indicated by the green line in Fig. 6.4.

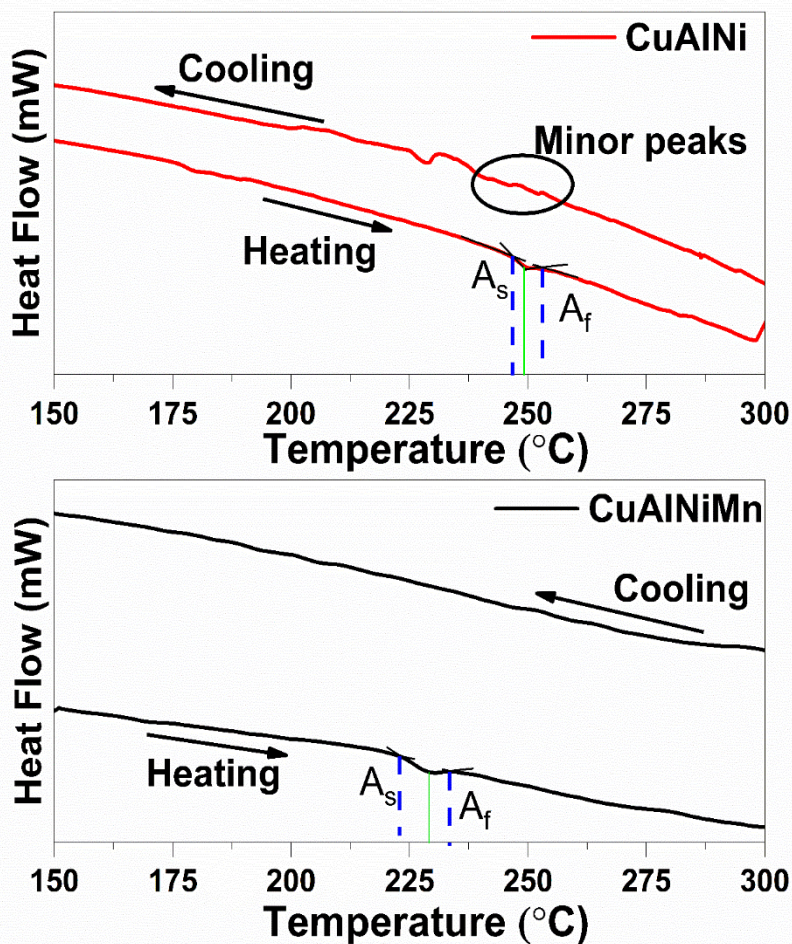


Figure 6.4: Images showing the results of transformation temperature of the samples as measured from DSC

The TGA results exhibited the decomposition temperature of Mn added bimorphs. The decomposition temperature was found to be 540 °C for CuAlNiMn bimorphs, whereas it was only 525 °C for CuAlNi bimorph. The results of the TGA

analysis is given in Fig. 6.5. The improvement in thermal conductivity might be due to increase in grain size and the reduction in  $\text{Cu}_3\text{Al}$  precipitates.

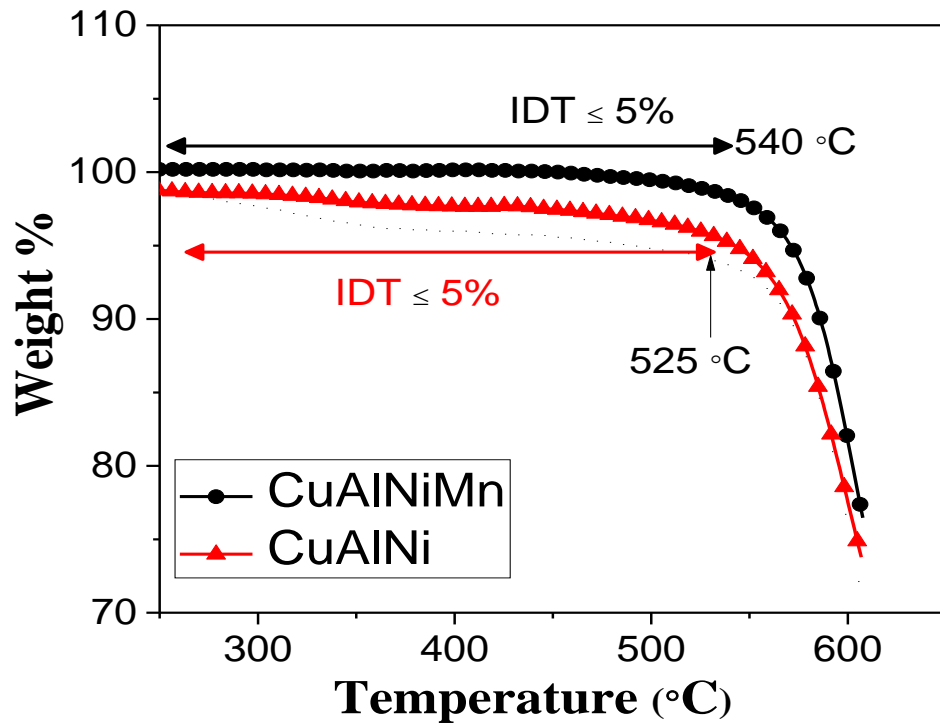
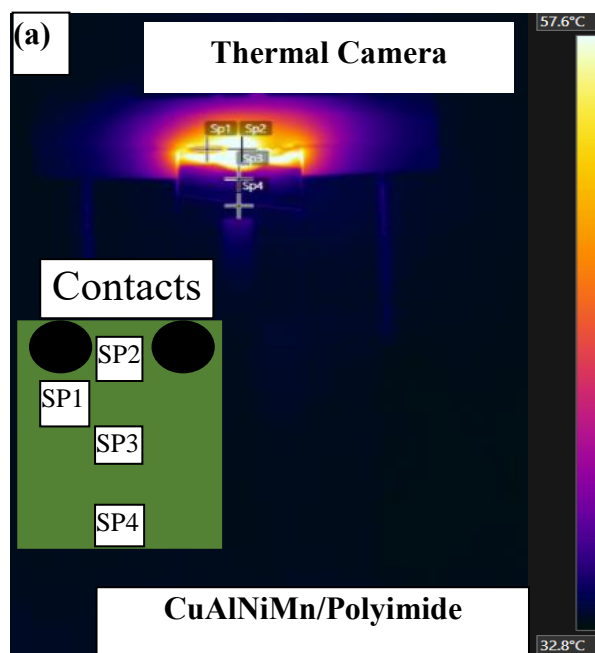
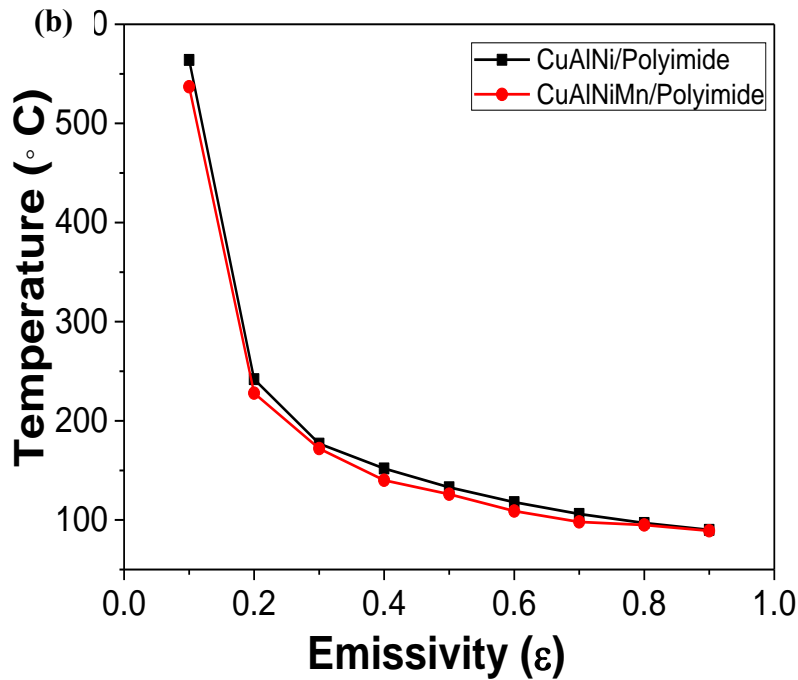


Figure 6.5: Graphical plot displaying the results of TGA analysis

Further to probe the heat transfer profile, thermal images of the samples were recorded using Forward Looking Infra-Red (FLIR) thermal camera, as the film was actuated for 100 seconds continuously as shown in Fig. 6.6 (a). The electrical actuation setup was placed inside, and a black cardboard box and





**Figure 6.6: Images showing the (a) Thermal image of CuAlNiMn bimorph during actuation and various set points (b) variation in temperature with change in emissivity**

reference emissivity of 0.98 was taken[142–144]. As the temperature difference was visible with all the emissivity values, a reference emissivity of 0.8 was taken for the analysis and the temperature profile of the bimorphs has been plotted for four different locations in the film. The maximum temperature of the bimorphs during actuation at an emissivity of 0.8 is plotted in Fig. 6.6 (b). SP1 indicates the set point placed near the contacts, SP2 is placed in-between the contacts, SP3 is placed at the centre of the film and SP4 is placed at the edge of the film. The inset in Fig 6.6 (a) shows the locations of the set points as recorded from the thermal camera. The temperature profile shows the SP2 temperatures is higher than the rest. SP1 temperature readings are slightly lower than SP2 with both the samples. SP3 and SP4 displayed less than 20 °C difference from room temperature. It was evident from the analysis that the temperature was higher in-between the contacts and there was no heat transferred to the free end of the film. Fig. 6.7 (a) and (b) shows the results of the temperature vs time at varying set points of CuAlNi and CuAlNiMn bimorphs.

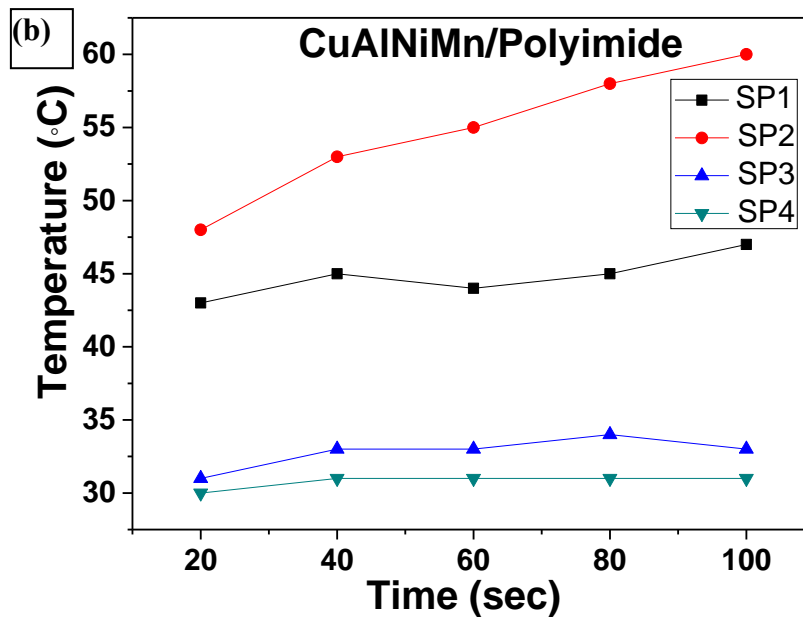
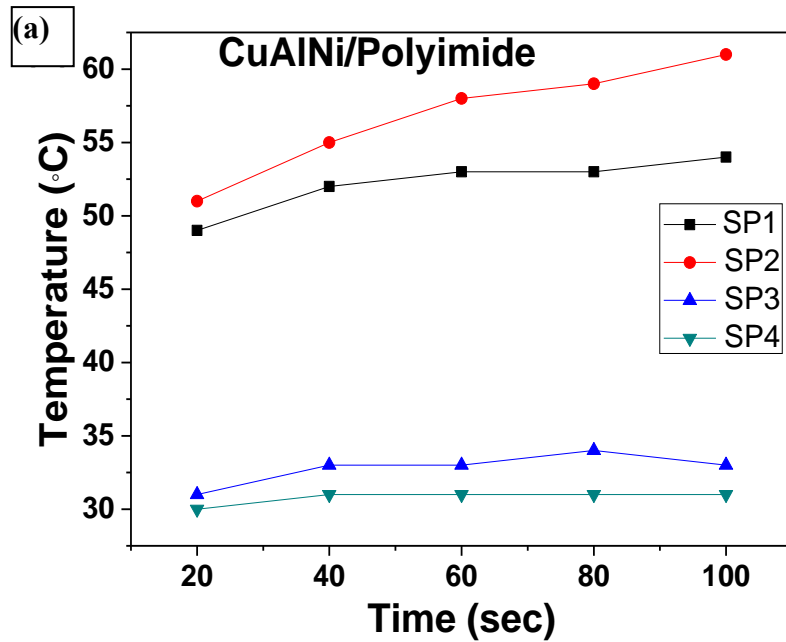


Figure 6.7: Results of thermal images showing the temperature vs time plots at various set points of (a) CuAlNi bimorph (b) CuAlNi

## 6.6 Thermomechanical Analysis

The thermomechanical behaviour of the developed bimorph was tested at different voltages such as 1 V, 1.5 V and 2 V and varying frequencies of 0.5 Hz, 0.33 Hz and 0.25 Hz for each loading conditions and the results are summarized.

### 6.6.1 Maximum Displacement

The bimorphs were tested with large heating and cooling cycle of 16 seconds to find the maximum displacement under different loading conditions. Fig.

6.8 (a) to 6(c) shows the maximum displacements comparison plots under different actuation conditions. The plots reveal the significant displacement exhibited by the quaternary alloy samples. It can be seen that CuAlNiMn film takes more than 0.5 seconds to actuate under higher loads, indicating the time required to reach austenite phase. The response time of CuAlNiMn added samples were significant, as the samples actuate rapidly, and the film shows quick displacement till 5 seconds. As the rate of displacement slightly decreases the curve tends to be flat after 7.5 seconds of heating. As the load increases to 60 mg, the difference in displacement increased to 5.3 mm at 2 V.

The samples exhibited faster heating and cooling rate as compared to ternary copper-based alloy and thereby actuating for extended periods. The cooling curve showed the bimorphs returned to its original position in most of the actuation conditions with an exceptionally minor loss in displacement. It can be observed from the graphs that load carrying capacity of CuAlNiMn film is less as load increases to 60 mg. The maximum displacement of the bimorph under different loading conditions are given in Table 6.2. The heat transfer profile exhibited the effect is Joule heating which is majorly till set point three, which might be one of the reason for reduced displacement as the samples displayed larger displacement with plate heater.

**Table 6.2: Maximum displacement results at different loads and different voltages**

<i>Load</i>	<i>Voltage</i>		
	<i>1 V</i>	<i>1.5 V</i>	<i>2 V</i>
<i>30 mg</i>	0.6 mm	2.3 mm	4.3 mm
<i>45 mg</i>	1.6 mm	3.3 mm	4.9 mm
<i>60 mg</i>	1.7 mm	3.5 mm	5.3 mm

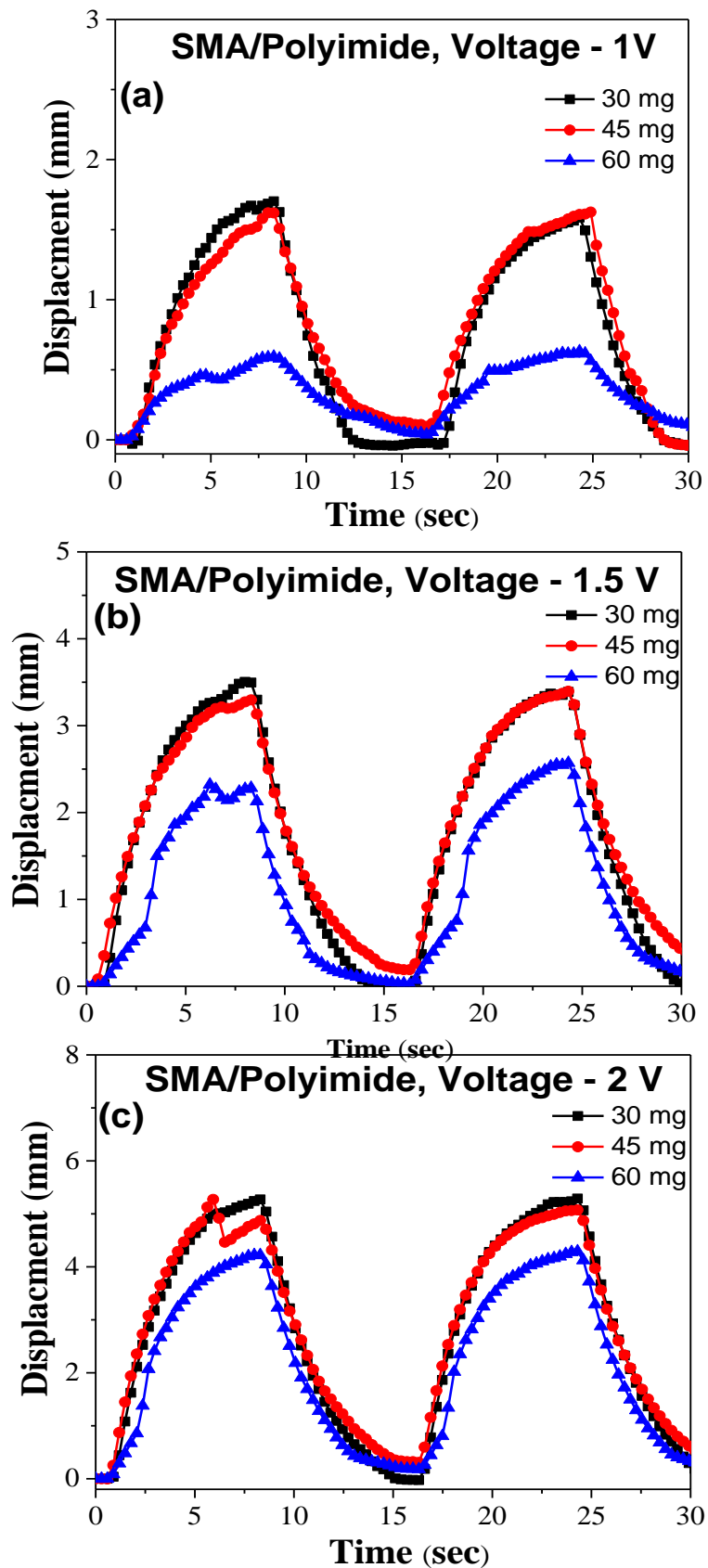


Figure 6.8: Images showing the results of Maximum Displacement of (a) CuAlNiMn/polyimide at 1 V and three different loads (b) CuAlNiMn/polyimide at 1.5 V and three different loads (c) CuAlNiMn/polyimide at 2 V and three different loads.

### 6.6.2 Frequency Actuation with 30 mg Load

The thermomechanical behaviour of the developed bimorphs was tested at different voltages such as 1 V, 1.5 V and 2 V and varying frequencies of 0.5 Hz, 0.33 Hz and 0.25 Hz for each loading conditions and the resulting graphs are plotted below in Fig. 6.9. The maximum displacement of 2.5 mm, 3.2 mm and 3.5 mm was observed from CuAlNi bimorphs for three different frequencies. Whereas, CuAlNiMn samples showed 6.1 mm, 5.7 mm and 6.05 mm was observed at frequencies of 0.5 Hz, 0.33 Hz and 0.25 Hz. Both the bimorphs displayed steady actuation behaviour at 0.25 Hz and 0.33 Hz, and there was no deviation in displacement. With 1.5 V and 2 V at 0.5 Hz Fig. 6.9 (a), 9(c), and 9(e) shows the results obtained with CuAlNi/Polyimide bimorphs and Fig. 6.9 (b), 6.9 (d), and 6.9 (f) displays the results with CuAlNiMn/polyimide bimorphs, under varying voltages and frequency for 20 seconds at 30 mg load. It is evident from the results that CuAlNiMn/Polyimide bimorph has higher displacement than samples developed without Mn. At 2 V and 0.25 Hz as shown in figure 6.9 (e) and 6.9 (f), the displacement of Mn added samples were approximately 3.7 mm for one cycle, whereas samples developed without Mn exhibited a maximum of 2.07 mm displacement. The displacement of both the samples reduced as the frequency was increased. On first heating cycle with 1 V and 0.5 Hz, both the bimorphs displayed similar displacement readings however the displacement varied on subsequent cycles, as the film would have been at a higher temperature than room temperature due to slow cooling through air convection. After few cycles, the displacement of the samples was consistent, and a CuAlNi/Polyimide bimorphs displayed minor fluctuation which was not observed with Mn added samples. However, the fluctuations were not distinct in large no of cycles. Mn added samples exhibited higher displacement and steady actuation behaviour with 30 mg load.

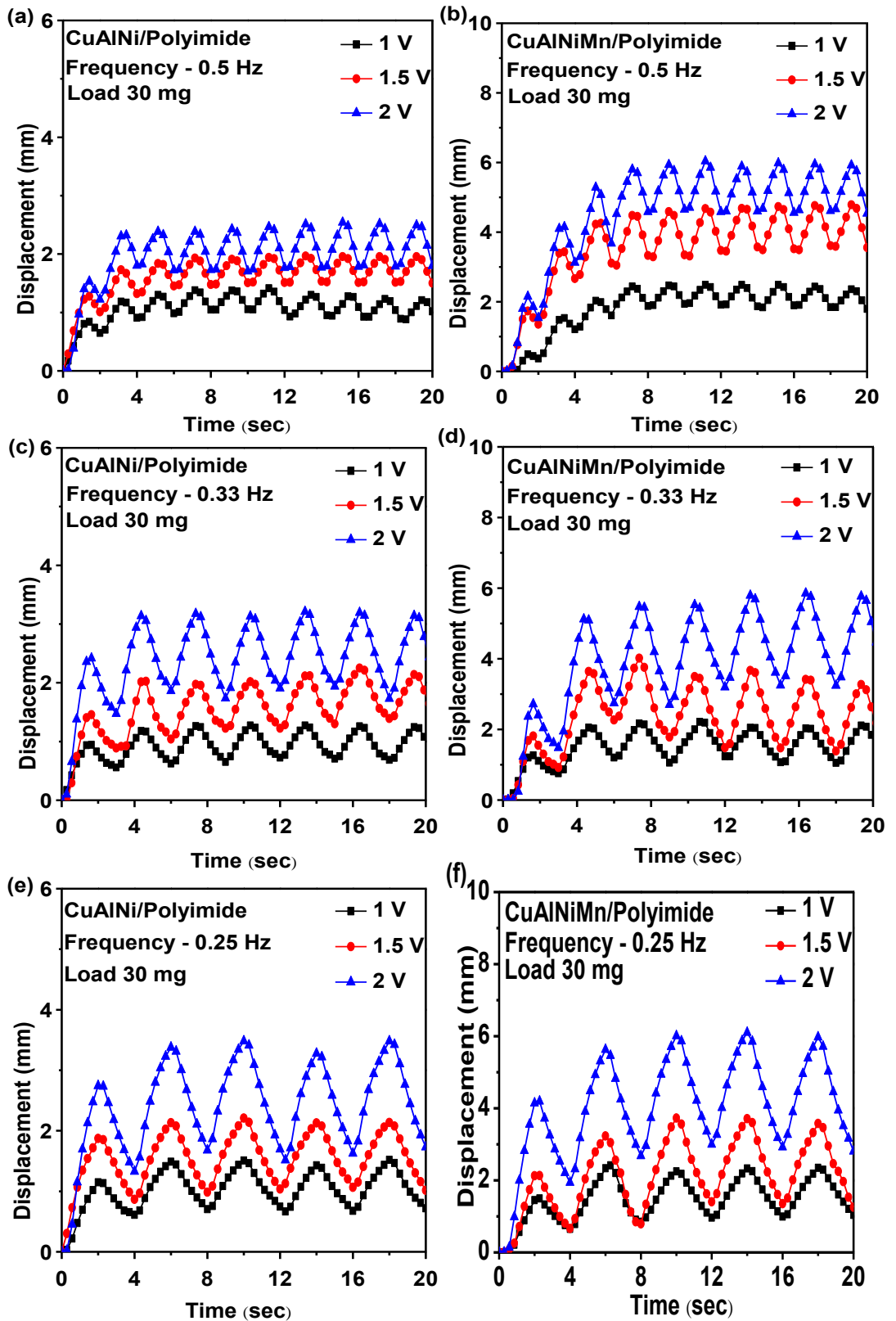


Figure 6.9: Electrical actuation results with 30 mg load at different voltages of 1 V, 1.5 V and 2 V (a) CuAlNi/Polyimide at 0.5 Hz (b) CuAlNiMn/polyimide at 0.5 Hz (c) CuAlNi/Polyimide at 0.33 Hz (d) CuAlNiMn/polyimide at 0.33 Hz (e) CuAlNi/Polyimide at 0.25 Hz (f) CuAlNiMn/polyimide at 0.25 Hz

### 6.6.3 Frequency Actuation with 45 mg Load

As the load was increased to 45 mg, CuAlNi/Polyimide samples displayed a steady actuation behaviour without any fluctuations. At voltages of 2 V, the recorded displacement values for one cycle was 0.67 mm, 1.22 mm and 1.44 mm at varying frequency. There was no drastic variation with change in frequency as observed from Fig. 6.10 (a), (c) and (e). The samples developed with Mn addition displayed improved displacement as compared to samples developed without Mn and displacement of 1 mm, 2.17 mm and 2.82 mm was observed at 2 V and three frequencies for one cycle as shown in figure 6.10 (b), (d) and (f). However, with a higher frequency of 0.5 Hz, the bimorphs developed with Mn addition had difficulty in lifting the load and the on/off control was not sufficient to have precise control. For one cycle at 1 V and 0.5 Hz, the displacement was 0.58 mm for samples with Mn and 0.32 mm for samples without Mn addition. The displacement was fluctuating; nevertheless, there was no evidence of failure. Even though the ability to lift weights of 45 mg was not significant as compared to samples developed with Mn addition, Cu-Al-Ni/Polyimide samples exhibited steady and stable behaviour.

### 6.6.4 Frequency Actuation with 60 mg Load

The samples developed with Mn addition displayed a major difficulty in actuating under 60 mg loads. Fig. 6.11(b), (d) and (f) shows the results of CuAlNiMn/ Polyimide bimorph at varying actuation conditions. This behaviour was evident at all the three frequencies with 1 V. As the voltage was increased to 2 V, there was sufficient shape memory effect to lift the load, and further, the results displayed steady actuation behaviour. The displacement under 60 mg loads was found to be approximately 0.08 mm, 0.28 mm and 0.35 mm at 2 V for one cycle. The effect of frequency on the samples was major, as all the samples exhibited increased displacement under varying actuation voltages. The samples developed without Mn addition, exhibited steady actuation properties at all conditions. Even at lower voltages of 1 V, the thermomechanical behaviour was definite with well-defined heating and cooling cycles. The average displacement at three different frequencies with 2 V was noticed to be 0.4 mm, 0.45 mm, and 0.52 mm for samples developed without Mn. The effect of frequency was minor at loads of 30 mg and 45 mg as observed from the thermomechanical analysis. Further,

from the analysis, the improvement of actuation was evident. However, the ability to actuate under higher loads was poor for samples developed with Mn. The primary reason might be the loss of toughness as the ductility increases.

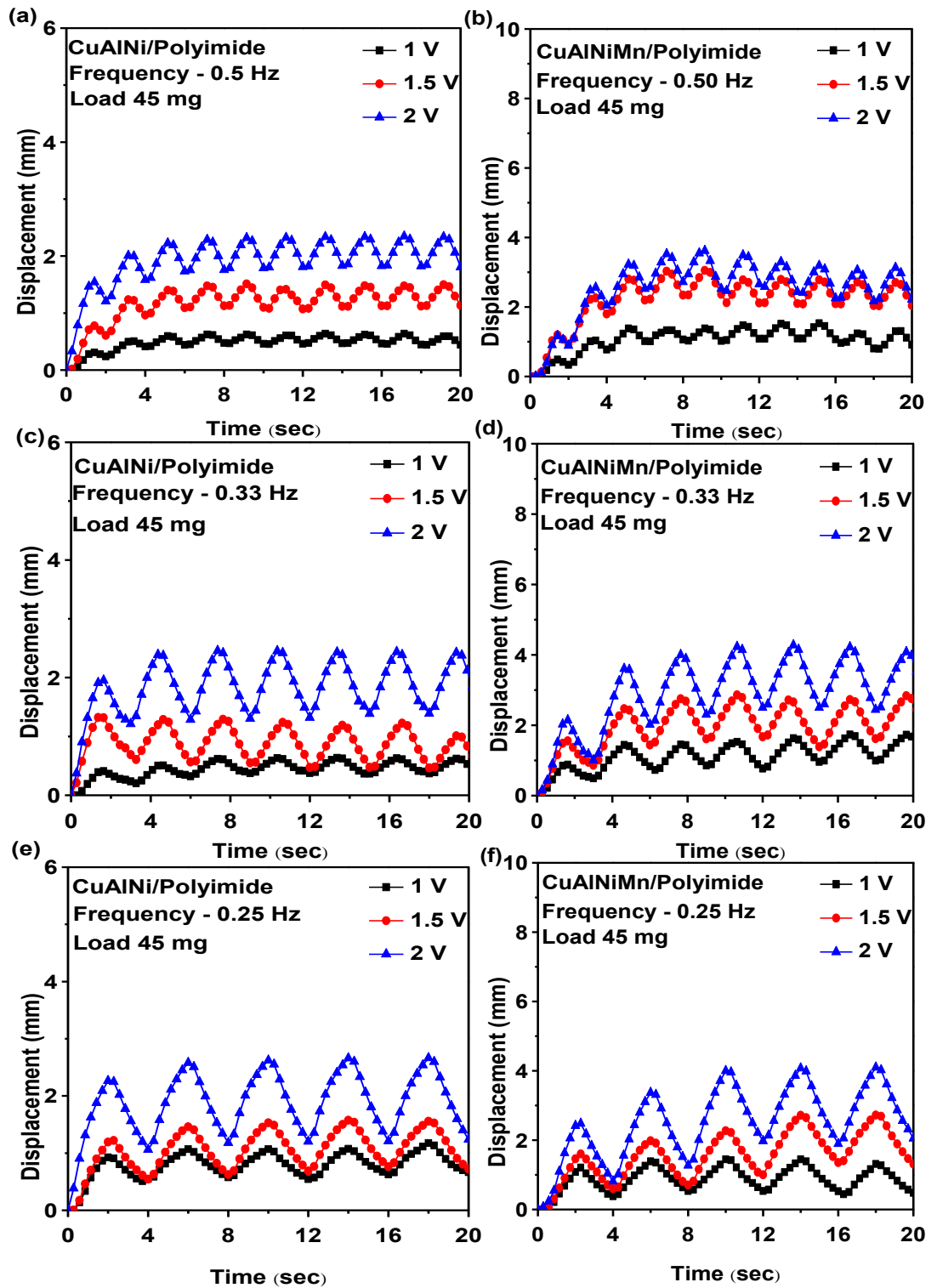


Figure 6.10: Electrical actuation results with 45 mg load at different voltages of 1 V, 1.5 V and 2 V (a) CuAlNi/Polyimide at 0.5 Hz (b) CuAlNiMn/polyimide at 0.5 Hz (c) CuAlNi/Polyimide at 0.33 Hz (d) CuAlNiMn/polyimide at 0.33 Hz (e) CuAlNi/Polyimide at 0.25 Hz (f) CuAlNiMn/polyimide at 0.25 Hz

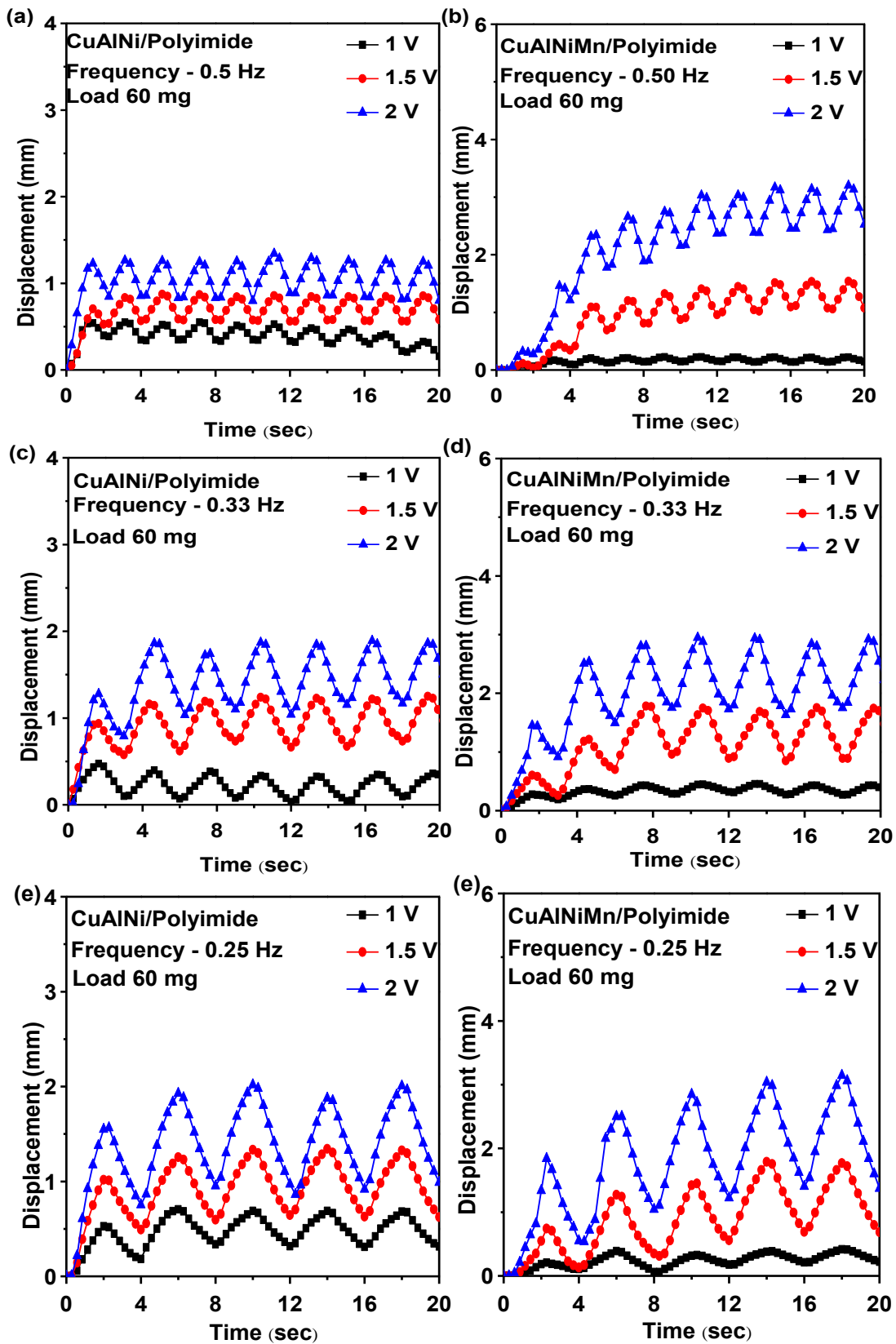


Figure 6.11: Electrical actuation results with 60 mg load at different voltages of 1 V, 1.5 V and 2 V (a) CuAlNi/Polyimide at 0.5 Hz (b) CuAlNiMn/polyimide at 0.5 Hz (c) CuAlNi/Polyimide at 0.33 Hz (d) CuAlNiMn/polyimide at 0.33 Hz (e) CuAlNi/Polyimide at 0.25 Hz (f) CuAlNiMn/polyimide at 0.25 Hz

## 6.7 Life Cycle Analysis

To verify the life cycle of the bimorphs, an actuation condition of 2 V and 60 mg which has a high probability of failure was taken for the analysis. Eight samples were taken for the analysis, and the samples were actuated till the displacement reduced less than 50 % of the initial value. Fig. 6.12 (a) and (b) shows the reliability results with the developed bimorphs for eight samples. It was evident that most of the samples had life more than 20,000 cycles before losing 50 % of the displacement. The life cycle analysis exhibited the property of the composite

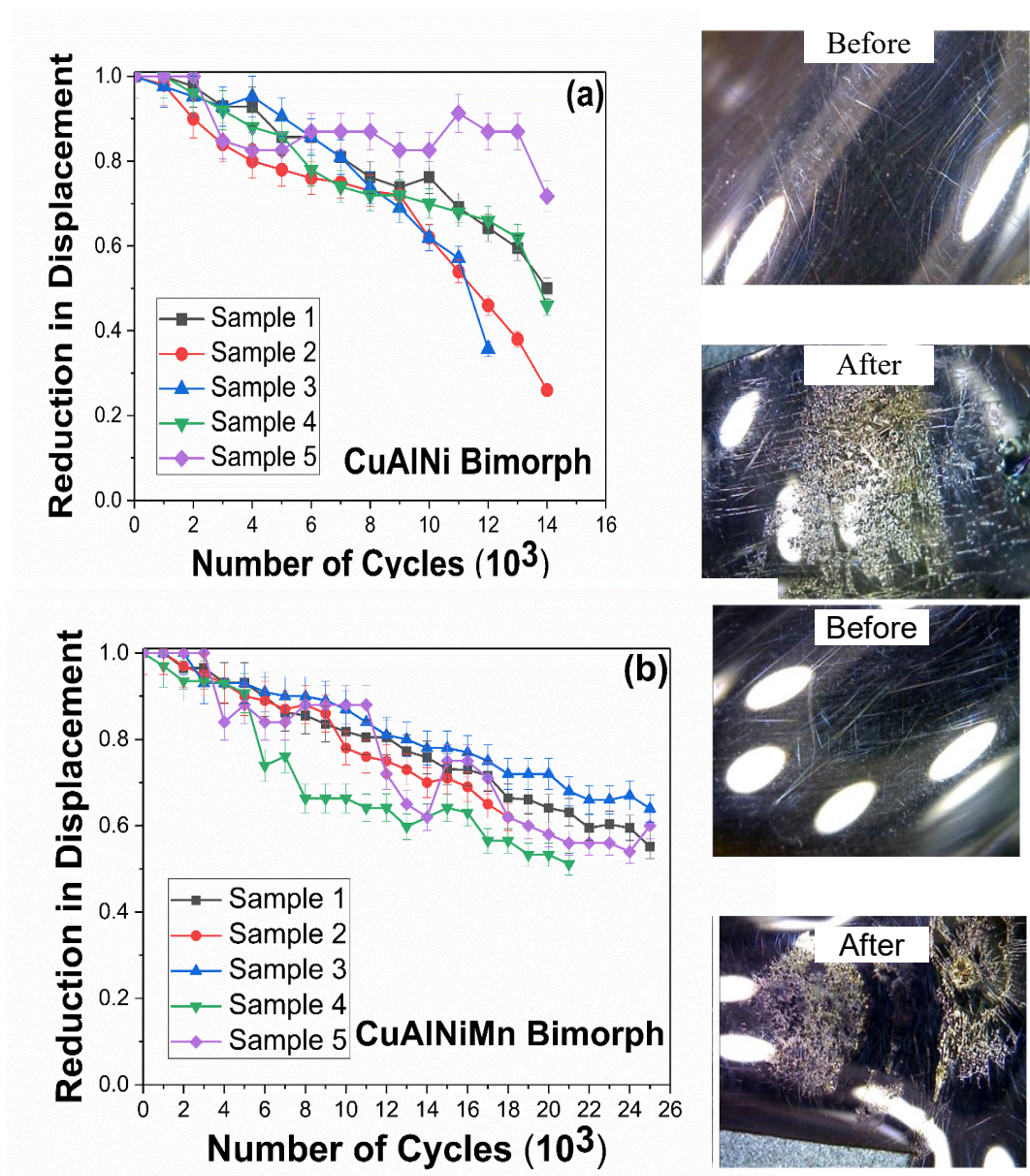


Figure 6.12: Life cycle behaviour of five typical samples of CuAlNi and the before and after images of the bimorphs

films to actuate under high loads for more number of cycle, making it a suitable for microactuators.

**Table 6.3: Results of the life cycle analysis of CuAlNi and CuAlNiMn bimorphs**

Sample No	CuAlNi Cycles to failure	CuAlNiMn Cycles to failure
1	13534	25000
2	13283	18678
3	11657	17892
4	13967	15675
5	15000	1359
6	10768	25000
7	15000	21263
8	5862	25000

## 6.8 Discussion

Mn addition has increased the grain size of the material as observed from the SEM images as shown in Fig. 6.1 indicating the reduction in grain boundaries per area. Further, the XRD as displayed in Fig. 6.3 displayed a more significant crystallite size as compared to samples developed without Mn addition. The increase in grain size can affect the three significant properties (1) electrical properties (2) mechanical properties (3) thermal properties [145]. Primarily the increase in grain size indicates the reduction in grain boundary per area. Increasing the free flow of current in material and this might be one of the reasons for the improved displacement as observed with Mn added samples. The conductivity of the film plays a vital role in electrical heating as there is more flow of current at higher voltages. The power generated in the film is proportional to the square of current, hence small increase in current drastically increases the internal temperature of the film and results in higher shape recovery. In the case of samples developed without Mn, the flow of current in the film is hindered by more grain boundaries and therefore lower displacement [22,116,146,147]. The increase in electrical conductivity was further evident from the thermal images as Mn added samples displayed reduced temperature at SP1 and SP2. As the grain size increases

both thermal conductivity and electrical conductivity increase. This shows the current flows freely inside the material and heat radiation is less [52,116,146–150]. The samples developed without Mn has higher resistance and thereby dissipating the electrical energy in the form of heat radiation. As the resistance is high, the heat generation is large resulting in high temperatures on the surface as observed from samples developed without Mn.

The dark spots seen in lower magnification images in SEM as displayed in Fig. 6.1 exhibits the presence of precipitates which was further confirmed by XRD as shown in Fig. 6.3. The diffractogram revealed the crystalline monoclinic peak without any  $\alpha$  or  $\gamma$  phases for the samples developed with Mn, while the samples developed without Mn had secondary phase. The dark spots indicating the secondary phase might arise due to diffusion of Al[151–153], which was not observed predominantly with Mn added samples. Further to this, there was no evidence of secondary phase with Mn added samples indicating the grain refinement by suppressing the  $\gamma$  phase origination. This shows the improved structural properties of Mn added samples to have better cyclic repeatability without any intergranular fracture.

The ductility of the samples developed with Mn was higher than samples developed without Mn [39,154,155]. This might be the second reason for the improved actuation with Mn added samples. The ability to accommodate external stress was better for samples developed with Mn. However, the load-bearing capacity of Mn added samples were affected due to the increase in grain size as observed from the results obtained with 60 mg loads. As the grain size increases the ductility improves and the toughness of the samples decreases. This was distinct with the experiments to find the maximum displacement. Mn added samples failed to bear higher loads, and their actuation was not significant as compared to CuAlNi/polyimide samples. Additionally, it was evident from the tensile test results, which displayed lower yield strength for samples developed with Mn. This shows the ductile nature of CuAlNiMn SMA as it requires less force for elongation as compared to the force required for elongation of CuAlNi SMA with the same amount. The thermal analysis exposed a lower transformation temperature which may possibly be the reason for their superior rate of actuation during heating and cooling cycles. The thermal analysis showed a difference of 20

°C between the two samples which might affect the sensitivity of samples, as witnessed from the frequency actuation. The bare polyimides thermal history will also affect the sensitivity drastically[124]. The large duration of actuation for the CuAlNiMn film is predominantly due to their wide range of austenite transformation temperature and high conductivity. From the Joule heating analysis, the effect of Mn addition has enhanced the thermomechanical response of copper-based shape memory alloys. The results exhibit the enhancement of grain size which leads to improvement in electrical and thermal conductivity. Ductility has improved. However, the ability to work with higher loads at lower voltage was better for samples developed without Mn. The displacement of the samples at 1.5 V and 2 V notably exhibited increased displacement with two orders higher than samples developed without Mn. Further, the enhancement was also observed in the cyclic behaviour as Mn added exhibited 50 % reduction in displacement only after 20,000 cycles.

## 6.9 Summary

The investigations on the thermomechanical behaviour of CuAlNiMn/polyimide composite films exhibited excellent characters to be utilised in microactuators. The actuation through Joule heating displayed the resolute characteristics with a maximum displacement of at 4 mm with 2 V at 60 mg load. The results can be summarised as

- The microscopic images revealed the presence of smooth and uniform surface morphology with composition with minor variation to the initial value.
- The  $\beta(128)$  martensite is mainly responsible for the shape memory effect along the pre-straining.
- The maximum displacement of the samples under different loading conditions exhibited the thermomechanical properties of with a maximum displacement of 4.3 mm achieved with 2 V and 60 mg.
- The frequency actuation exhibited the inability of the quaternary alloy to work with high loads at high frequency.
- The life cycle analysis displayed the ability of the bimorphs to work more than 24,000 cycles without significant loss.

The preliminary results with the micro flapper are promising as a maximum of 20 Hz was achieved under loads. The force generated by the bimorphs were found to less than 1 N for 5  $\mu\text{m}$  film on 75  $\mu\text{m}$  polyimide sheet. This can be further improved by improving the thickness of the SMA film on the flexible substrates. The higher force will facilitate better load bearing abilities, primary for microactuators. The quaternary alloy of copper-based SMA on flexible substrates are an excellent alternative to the conventional nickel – titanium binary system.



## Chapter 7

---

# Suitability of CuAlNiMn Bimorph towards Micro-Robotic and Energy Systems

### 7.1 Introduction

Shape memory alloy bimorphs can be an excellent actuator due to their ease of developing and excellent properties as discussed in previous chapters. Specifically, copper-based shape memory alloys developed on Kapton polyimide sheets can be used in high-temperature applications beyond 250 °C. However, these applications require proper control of the bimorphs to use it efficiently as an actuator. The suitability of the developed bimorphs in various actuator and sensor applications have been explored. Further, to control the displacement of the bimorph while transforming from martensite to austenite on heating, the temperature was indirectly controlled by governing the current flow through PID response. The developed of SMA belt with CuAlNi/polyimide has also been probed.

### 7.2 Microflapper with Bimorphs

High-frequency actuation of SMA is of importance in several actuators. As the literature suggests, SMA have an excellent energy density. However, the frequency at which they can work is limited. Reports suggest NiTi SMA reaching up to 3 Hz. Further, at micro scale the rate of heat transfer during cooling will be faster. This aids in developing high power output in devices such as micropumps. In this section, the bimorph is tested for high-frequency actuation through the previously discussed experimental setup further extended with Arduino programme for developing micro flapper. The programmable was not able to switch at high frequencies. The micro flappers can be utilized a wing in micro aerial robots. Further, the force generated during displacement is calculated by taking the bimorph displacement as a deflection in single beam cantilever. There are 3 major types of Shape Memory Alloy actuators-

- Shape Memory Alloy Bimorphs
- Shape Memory Alloy Wires
- Shape Memory Alloy Springs

The flight mechanism of Micro-Aerial-Ornithopters requires reciprocating motion which is difficult to achieve using SMA wires or springs, given the size constraints. Also, SMA springs and SMA wires, in most cases, only show One Way Shape Memory Effect, which cannot give the required reciprocating motion. Hence SMA Bimorphs are most suitable to be used as actuators for the flight mechanism.

The advantages of using SMA Bimorph Actuators over SMA Springs/Wires are-

- SMA Bimorphs exhibit the ‘Two-way Memory Effect’.
- Unlike SMA Springs/Wires, SMA Bimorphs need not be trained to remember the shapes.

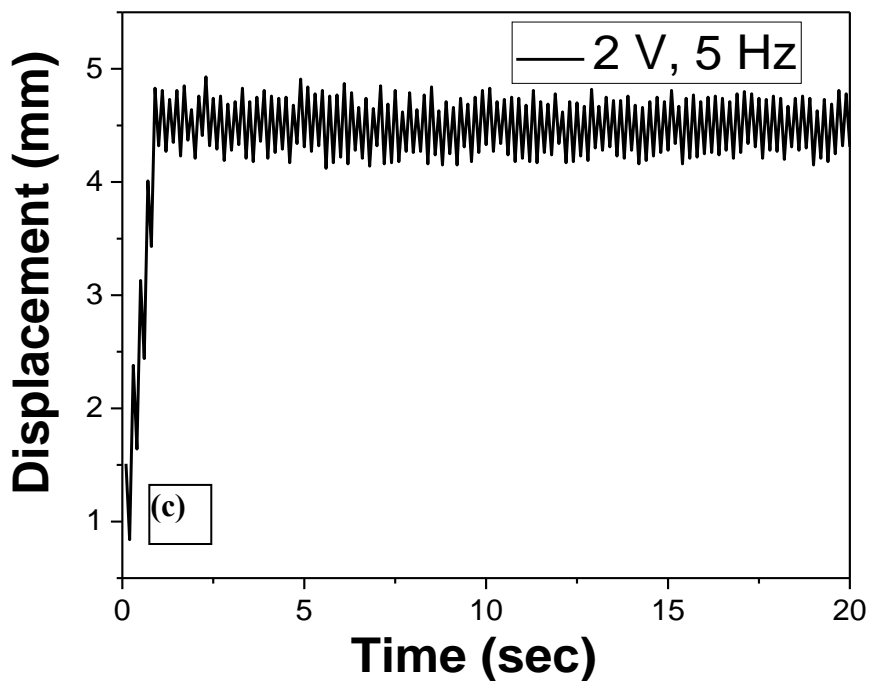
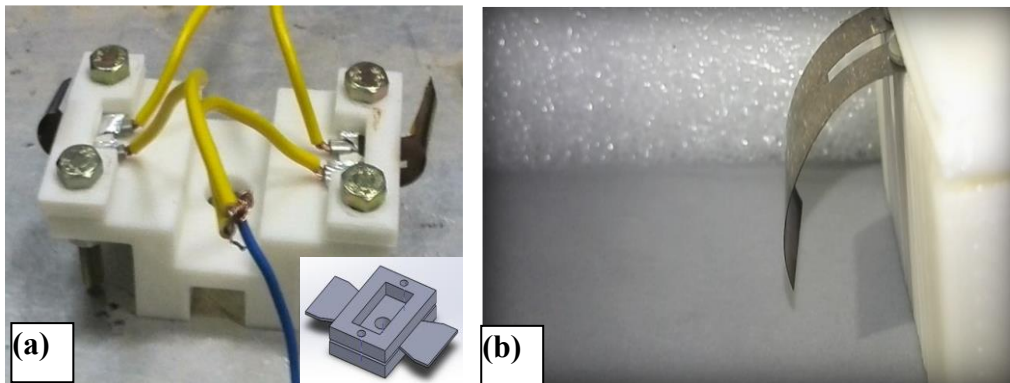


Figure 7.1: (a) Picture of the analysis setup with flapper (b) CAD model of the proposed microflapper setup with bimorph (c) Result showing the displacement at

- While using Joule heating, SMA Bimorphs can be actuated at a lower voltage than SMA Springs/Wires. They also require comparatively lesser time for cooling due the availability of a larger surface area.

The experimental setup was similar to the one used in the thermomechanical analysis. Fig. 7.1 shows the initial experiments with micro flapper (b) design of the proposed flapper and (c) displacement of bimorphs at 5 Hz. The frequency of actuation was varied, and the resulting displacement was measured using laser displacement sensor. From the analysis, it was observed the bimorphs were actuating at frequencies higher than 5 Hz. However, the resolution of the displacement sensors was not enough to measure the variation precisely. Further, the force generated during actuation was also an essential parameter in analysing the load-bearing capacity.

### 7.2.1 Force Generated by Bimorphs during Actuation

As the voltage is applied to heat the SMA film of the composite structure, it attempts to transform to its parent shape, and during such transformations, a force is generated. We can consider this force as uniformly distributed over the span of composite and as we measure the displacement of the composite at its free end by making it cantilever[24]. The total force generated by the composite can be calculated using the basic differential equation governing the deflection of the beam.

$$\frac{d^2v}{dx^2} = \frac{M}{EI} \quad (7.1)$$

Where M is Bending moment, E is Modulus of elasticity, I is Moment of Inertia of cross section about its neutral axis. On integrating the basic differential equation for the deflection curve of the beam twice, we get the expression for deflection at any point along the span of the beam.

Thus, the equation for deflection at the free end of the uniformly distributed cantilever beam is given by,

$$V = WL^3 / 8EI \quad (7.2)$$

Where, V is deflection at the free end of the beam and W is Total load/force on beam. Using above deflection equation of beam, the total force applied by composite by measuring the displacement at free end can be found. However, flexural rigidity (EI) of the composite beam is found by adding the values of each individual material. Fig 7.2 shows the force generated by the composite film during various displacements.

The force produced due to the actuation in the sheet is given by:

$$F = \frac{(3 \times E \times I)}{L^3} \quad (7.3)$$

$$\frac{(E \times b \times t^3)}{4 \times L^3} = K \quad (7.4)$$

Therefore,  $F = K \times d$

Where,

E = Young's Modulus of Elasticity for the given sheet,

I = its second moment of Inertia,

d = displacement of the free edge,

t = thickness of the SMA,

b = width of the cantilever, and

L = length of the cantilever

For the Cu-Al-Ni-Mn sheets, we have taken

$$E = 2.5 \text{ GPa}$$

The dimension of bimorph sheet used for this experiment was

$$t = 0.000006 \text{ m}, b = 0.02 \text{ m}, L = 0.02 \text{ m}$$

Also, to calculate the maximum value of 'F', the maximum attained value of 'd' through experimental procedures must be used.

This gives

$$d = 0.005 \text{ m}$$

Using these values in the above formula, we get,

$$F = 1.518 \times 10^{-3} \text{ N}$$

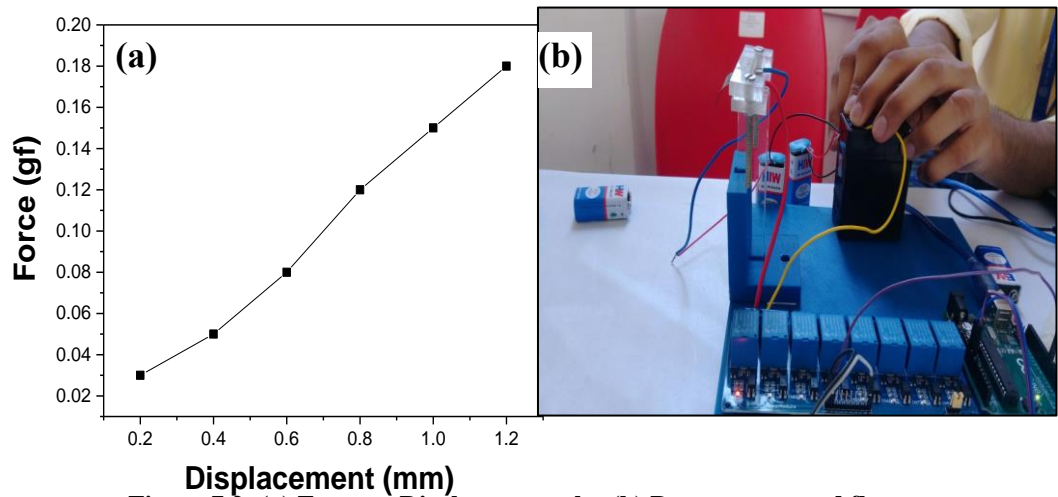


**Figure 7.2: (a) Force vs Displacement plot (b) Battery operated flapper setup**

Fig. 7.2 (a) shows the force vs displacement plot of the bimorphs. Further to the force calculation, a mobile setup with batteries was developed with 3 D printed structures and the same was used for demonstration as shown in Fig. 7.2 (b). In order to develop aerial robots with the developed bimorphs, suitability for controlling it was explored.

### 7.2.2 Control System Design

There are a number of different standard types of control systems that have been studied extensively. These controllers, specifically the P, PD, PI, and PID controllers are very common in the production of physical systems, but each has its own advantages and this the selection of appropriate controller is important. Control Loop is a “management system” to regulate the process, the controller decides whether to make an adjustment and the adjustment change affects the process. Fig. 7.3 shows the process control schematic layout. The set point gives the control to the process, and the controller takes the task of making the system reach the set point.

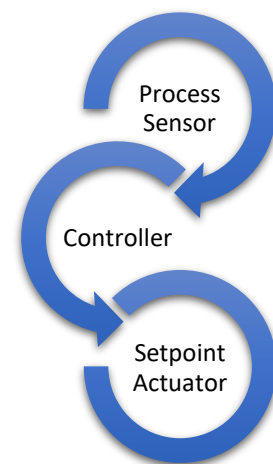


**Figure 7.3: Block diagram of Process control**

### 7.2.3 Controller Selection

Proportional controllers are merely gain values. Fig. 7.4 shows the different controllers that can be utilized. The gain value lets the system reach the set point quickly but may or may not be stable. The derivative controllers are implemented to account for future values, by taking the derivative and controlling based on where the signal is going to be in the future. Derivative controllers should be used with care because, even a small amount of high-frequency noise can cause very large derivatives, which appear like amplified noise. Also, derivative controllers are challenging to implement entirely in hardware or software, so frequently solutions involving only integral controllers or proportional controllers are preferred over using derivative controllers. Hence used as PD or PID. Integral controllers of this type add up the area under the curve. In this manner, a PI controller (and eventually a PID) can take account of the past performance of the controller, and amend based on past errors. PID controllers are combinations of the proportional, derivative, and integral controllers. Because of this, PID controllers have large amounts of flexibility. The transfer function for a standard PID controller is an addition of the Proportional, the Integral, and the Differential controller transfer functions. Also, we give each term a gain constant, to control the weight that each factor has on the final output:

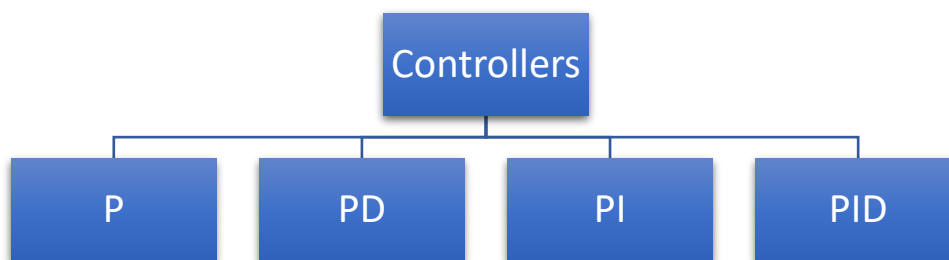


**Figure 7.4: Block diagram of types of controller**

### 7.2.4 PID Tuning

The process of selecting the various coefficient values to make a PID controller perform correctly is called PID Tuning. There are some different methods for determining these values,

- 1) Direct Synthesis (DS) method
- 2) Internal Model Control (IMC) method

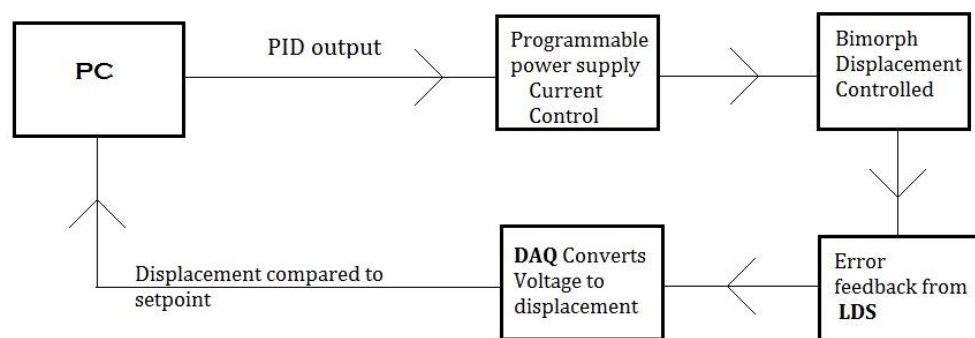
- 3) Controller tuning relations
- 4) Frequency response techniques
- 5) Computer simulation
- 6) On-line tuning after the control system is installed
- 7) Trial and error

### 7.2.5 PID Controller

The PID is one of the most opted control systems because of its distinctly stated better performance. It is because of its ease of use as its dependent on three parameters only viz. K, Ti, Td. The three parameters were changed for 3 V control on a trial and error basis in order to create the most plausible control for the bimorphs and for 4 V control Zeigler Nichols technique was used. To compare the response of the materials for the control system, Kapton sheets of thickness 50  $\mu\text{m}$  and 75  $\mu\text{m}$  was studied. The responses were almost similar, but the 75  $\mu\text{m}$  sheet displaced higher and had better control. For implementing the control system, the Virtual Instrument platform LabVIEW was used.

### 7.2.6 Design of the Control System

The parameter to be controlled for the bimorph is its displacement. The displacement is produced as the result of shape memory effect concerning temperature. In this case of Joules heating, the temperature is produced by the current. Thus, the parameter to be controlled was taken as current. The control system can be hence lined up as shown in Fig. 7.5.



**The Control Sequence**  
**Figure 7.5: Block diagram of the control system**

The system was designed to control the current and hence control the displacement as per requirement. PID in real time as discussed before involves three parameters: K, Ti, Td. The time unit to be used should be consistent with its response curve. The relationship with the sample period  $\Delta t$  can be obtained, after the discretisation of the PID controller. Fig. 7.6 shows the feed control system schematic.

### 7.2.7 Ziegler Nichol's PID Controller

It is performed by setting the 'I' (integral) and 'D' (derivative) gains to zero. The "P" (proportional) gain,  $K_p$  is then increased (from zero) until it reaches the ultimate gain  $K_u$ , at which the output of the control loop has stable and consistent oscillations.  $K_u$  and the oscillation period  $T_u$  are used to set the P, I, and D gains depending on the type of controller used are given in Table 7.1

**Table 7.1: Parameters of PID Controller**

Controller type	$K_p$	$T_i$	$T_d$
Classic PID	$0.6K_u$	$T_u/2$	$T_u/8$

The three parameters used to establish the correction  $u(t)$  from the error  $e(t)$  is given by,

$$u(t) = K_p e(t) + \frac{K_p}{T_i} \int_0^t e(\tau) d\tau + K_p T_d \frac{de(t)}{dt} \quad 7.5$$

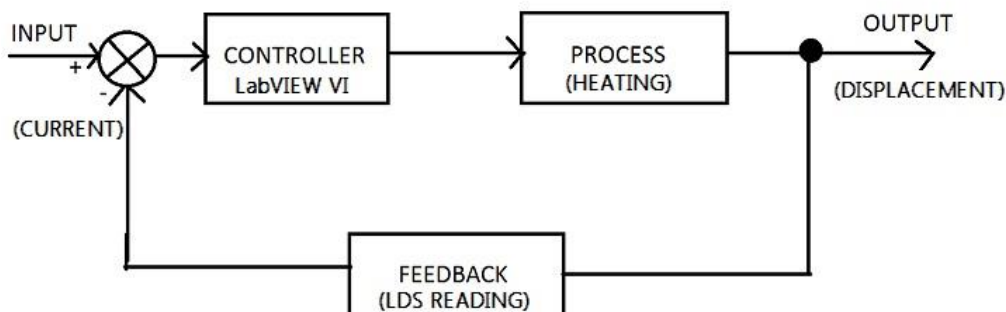


**Figure 7.6: Block diagram of the feedback control system**

## 7.2.8 Experimental Setup

The VI generated by the LabVIEW was run on the computer system uninterruptedly to provide the required control. Since the bimorphs follow Joules effect, the heat control was done by the current supplied from the RIGOL Programmable Power Supply. The power supply was interfaced to the PC by means of Ultra Zigma. During actuation, the displacement was to be studied and hence a laser displacement sensor was utilized. It provided the output in terms of Voltage, and the Data Acquisition (DAQ) Agilent 34970A was used to read and convert the voltage data to displacement. The DAQ was interfaced to the computer by means

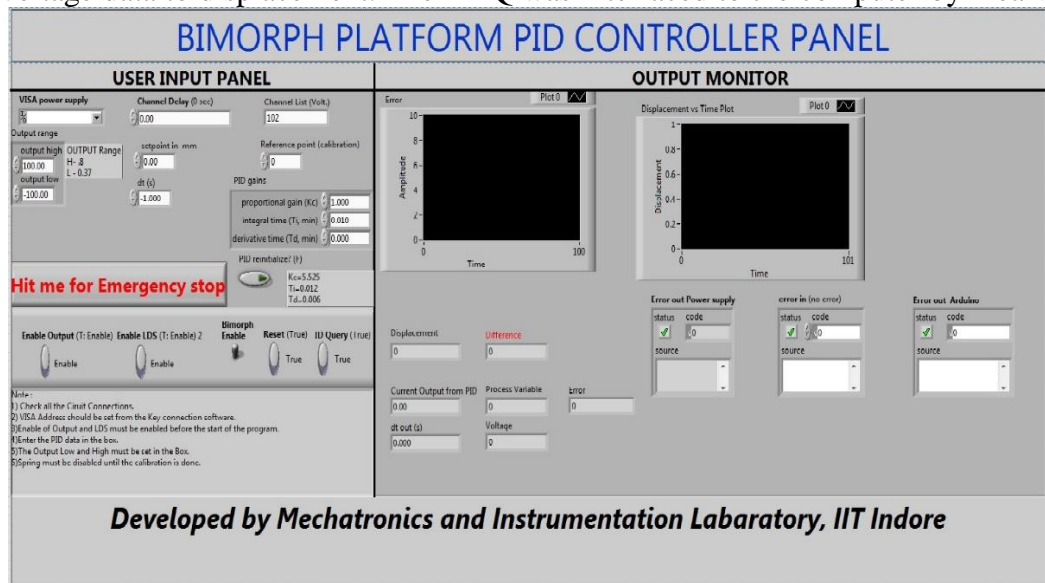


Figure 7.7: Screenshot of the LabVIEW program used for control

of Keysight Connection Expert. The displacement data was read, and the error compensation was done by the PID control system on the Computer (LabVIEW) as shown in Fig. 7.7. Though the VI generated values were used to control the current, the on and off control was given by means of an Arduino UNO development board connected to a 5 V-230 V relay.

## 7.2.9 Results and Discussion

For a 75  $\mu\text{m}$  Kapton coated with 100 mg of CuAlNi, the control was difficult because of the rapid cooling rate of the SMA. Hence the improvised SMA Bimorph with CuAlNiMn was studied. Comparatively, the control was implemented with ease for the latter because of the better displacement. The Gain value  $K_p$  was increased until the displacement reached the set point and then the  $T_i$  was increased in order to increase the precision and then the  $T_d$  was increased

to reduce the overshoot. Similarly, the controller parameters were designed for the other SMA bimorphs.

By Zeiger Nichol’s method, the displacement of CuAlNiMn bimorph was tried. The gain  $K_p$  was increased from 1 till it produced quasi-stability. The ultimate time (Critical time period) for the oscillation was found as 5s. i.e. the Time-gap between two consecutive peaks of the displacement plot. According to the Zeigler Nichol’s method using the critical time and critical gain, the  $K_p$ ,  $T_i$ ,  $T_d$  values were set, and the output was studied. Since the error was high, the next best gain  $K_p=10$  was chosen and the Critical period and Critical gain was chosen. The disturbances were more, and hence the peaks studied were for the gain values from

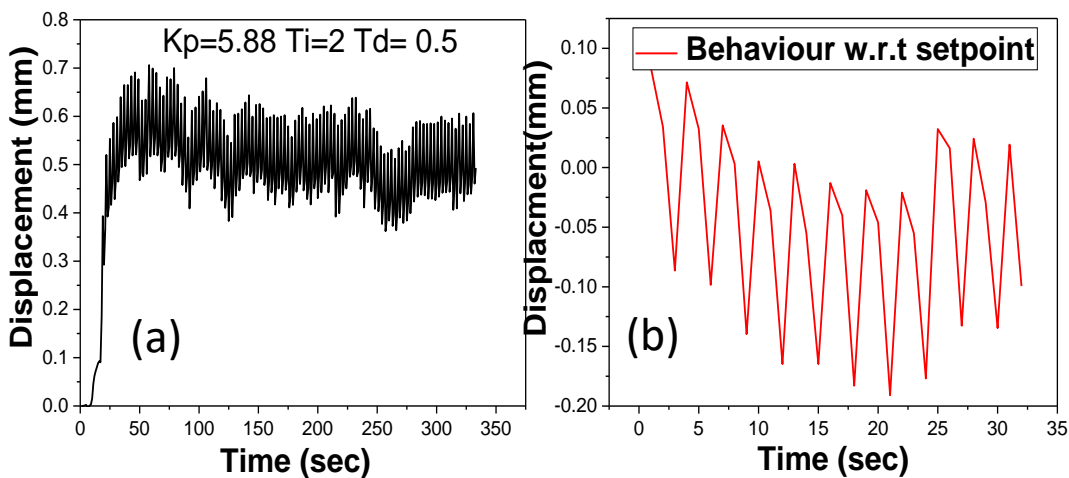


**Figure 7.8: Plots showing the (a) Control achieved with  $K_p$  - 5.88,  $T_i$  - 2 and  $T_d$  – 0.5 (b) Error plot showing minimum fluctuation during control**

9.74 to 9.85, and the best value was 9.8. The critical period  $T_u=4s$  and critical gain are  $K_u=9.8$ , and hence the controller parameters were found to be,  $K_p=5.88$   $T_i=2$   $T_d=0.5$  as shown in Fig. 7.8 (a) and (b).

### 7.3 Micro Circuit Breaker

Transformer oil temperature can be utilised as a primary parameter in monitoring the life of the transformer. At present, the electrical approach is taken which might be vulnerable to electromagnetic interference and are limited by sensors lifetime. Other non-contact techniques are ineffective due to difficulties in processing the output signal. CuAlNi/polyimide shape memory alloy bimorphs were applied to act as a temperature sensor in mineral oils. The developed films are employed in a custom-made oil rig, and the suitability of using it as a circuit breaker in temperature sensing application has been probed. The circuit breaker can be triggered by measuring the displacement of the bimorph using laser

displacement sensor. The measurement is of a non-contact type, and the temperature can be monitored at regular intervals. For comparison a procure Nickel-Titanium spring with transformation temperature less than 100 °C is also used for the studies. The results show that the developed bimorphs have a good sensitivity of 0.2 mm/°C and the output displacement is significant. Further, the effect of contamination in the mineral oils is also probed by adding known amounts of impurities, and the ageing effect was studied. A higher resolution measuring system using interferometry has been proposed.

### 7.3.1 Oil test rig

CuAlNi bimorph was used for high-temperature measurement of transformer oil. Mineral oil of 1 it was filled in a Borosil container and was heated using a hot plate. The bimorph was fixed to the container using the clamp as shown in Fig. 1(a). Heating of the oil was conducted for 30 minutes, followed by 1-hour cooling. The temperature of the oil was measured using both thermocouple and

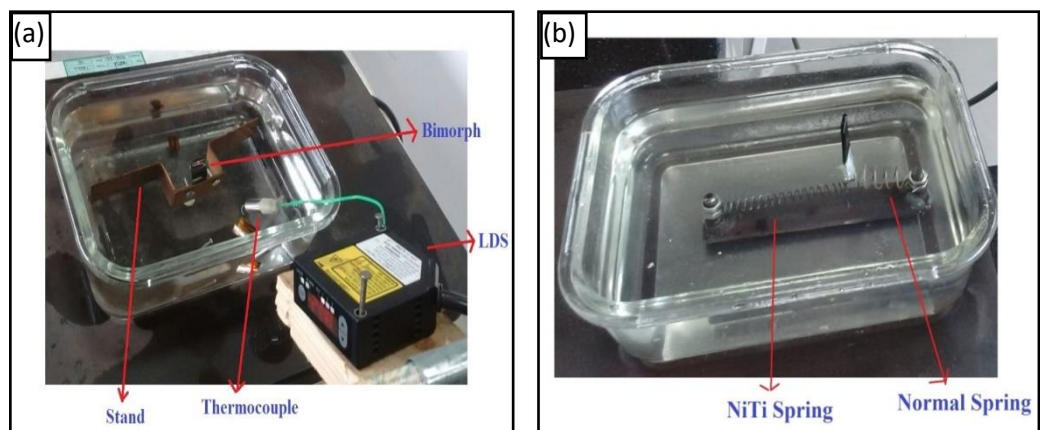


**Figure 7.9: (a) Setup with bimorph for transformer oil temperature sensing (b) Setup with NiTi Spring**

bimorph. Data were taken through Data Acquisition System interfaced to the computer. Fig. 7.9 (a) CuAlNi bimorph along with the laser displacement sensor. (b) NiTi spring along with the indicator for displacement measurement.

### 7.3.2 Displacement measurement

With the combination of Ni-Ti Spring and CuAlNi bimorph, two different temperature ranges were probed for measurement. For Low temperatures (40 °C - 90 °C) Ni-Ti spring and for temperatures beyond 100 °C, CuAlNi bimorphs has been used. The results show that CuAlNi bimorph was able to detect the temperature rise in transformer oil. However, the measurement contains some noise due to the environment, which can be eliminated by either a different orientation

or by using other higher resolution techniques. In this case, heating of oil is detected by Cu-Al-Ni Bimorph, although the displacement is of lower magnitude than Ni-Ti spring, the results show a promise in sensing the transformer oil with a low cost and efficient method.

The results indicate that both alloys are suitable for temperature sensing. However, there has to be better methods to sense the minor changes in deflection for precise operation. NiTi springs displayed higher displacement than CuAlNi bimorphs which could be utilised in low-temperature sensing. The sensitivity of the alloys was found to be in the range of 0.2 mm/°C. Table 2 summarises the preliminary sensor properties.

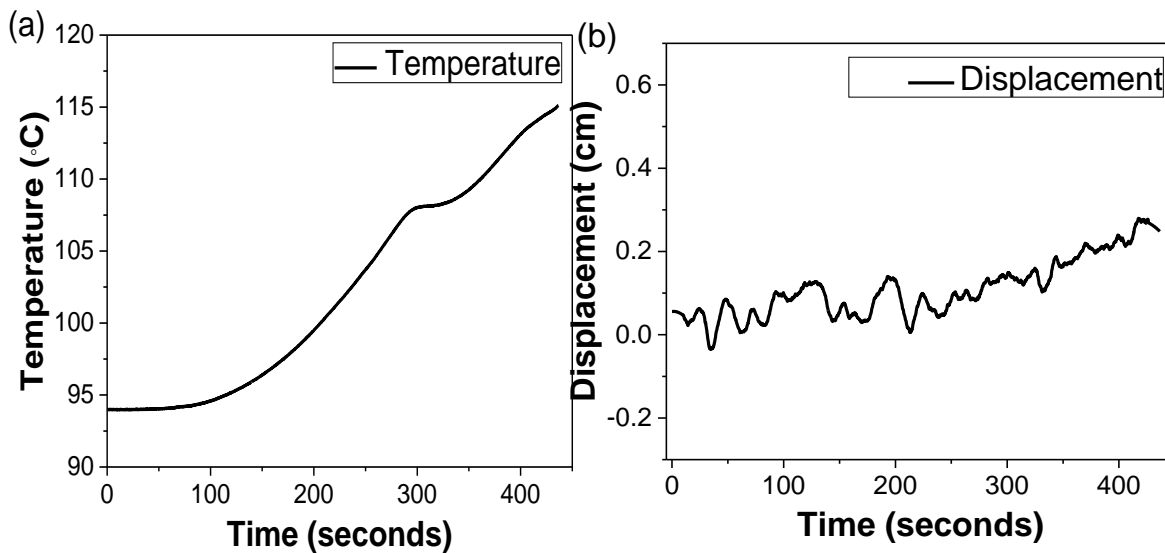


Figure 7.10: Results indicating the (a) temperature profile of CuAlNi bimorph (b) the displacement of CuAlNi bimorph

Table 7.2. Preliminary sensor properties

Shape memory alloy/ Parameter	Maximum Displacement	Sensitivity	Temperature Range
Ni-Ti Spring	15 mm	0.29 mm/°C	60° C – 100 °C
CuAlNiMn Bimorph	0.5 mm	0.2 mm/°C	90 °C – 140 °C

### 7.3.3 Contamination test

Further to probe the effect of contamination of the transformer oil, a laboratory level testing with simulated conditions have been carried out. The samples were left to age in the contaminated mineral oils for ten days.

(i) Test with acid: -

1 mL of 37% concentrated HCL acid was added to the transformer oil and was heated up to 100 °C. After few days the colour of oil changed from transparent to pale yellow and its flash point also decreased from 130 °C to 115 °C. 0.02 mg KOH/gm of oil was introduced.

(i) Test for moisture effect: -

2 mL of water was added to 80 mL oil and was heated up to 100 °C and was kept for 10 days. Although the colour change of the oil was not observable, a significant decrease in flash point and the temperature was noted to be 10 °C.

Figure 4 shows the pictures of the tests conducted with acid and moisture. The results of the contamination results are summarised in table 2. Further analysis of the structural and morphological characteristics must be conducted to confirm the effect of acids.

Table 7.3. Contamination test results

Contamination	Effect on Bimorph	Effect on Spring
Water	Measurable Effect	Measurable Effect
Acidity	The acid reacts with CuAlNi film	No Effect
Gases	No Effect	No Effect

The results show that shape memory alloy bimorphs are suitable for temperature sensing. Further, the sensitivity of the developed bimorphs is appropriate for temperature beyond 100 °C. Cu-Al-Ni Bimorph is tested for 22 cycles and NiTi spring for 15. The sensitivity of the alloys was found to be in the range of 0.2 mm/°C at different temperature zones. The contamination shows that acids are affecting the CuAlNi thin films. Further analysis of the concentration of the acid

and the contaminations is under study. Using both, Cu-Al-Ni Bimorph & NiTi Spring improves the sensing of oil temperature. However, there are difficulties in measuring the displacement of the SMA through laser displacement sensor.

An interferometry based technique with higher resolution is proposed for sensing in such robust environments. The schematic of the experimental set-up for measurement of vibrations using shear plate interferometer is shown in the figure. The fringe pattern formed due to defocusing of a collimating lens in lateral shearing interferometer falls on a CuAlNi film. The fringe pattern generated by the shear plate is reflected from the film and falls on the interferometry grating G, which produces an

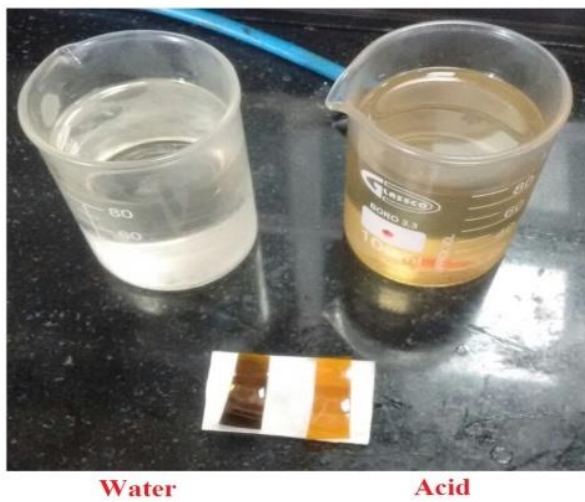


**Figure 7.11: Pictures showing the contamination test results with water and acid**

## 7.4 Shape memory alloy Belt for Energy Harvesting

A significant amount of thermal energy from our ecosystem as well as in industry is not utilised to its potential. Resources of energy include industrial waste heat, geothermal heat, oceanic thermal gradients, and solar radiation. As shown in Fig. 7.12, due to the amount of thermal energy that is produced by artificial structures it is immensely resourceful to convert low-grade energy sources to mechanical work. Even though there are plenty of devices and mechanisms to utilise this thermal energy, the efficiency of such devices makes it insignificant to manufacture in large scale. Past efforts to generate useful forms of power from small temperature difference heat sources were unsuccessful, as standard recovery techniques generally have not approached competitive efficiency.

### Drivers for Industrial Waste Heat Management

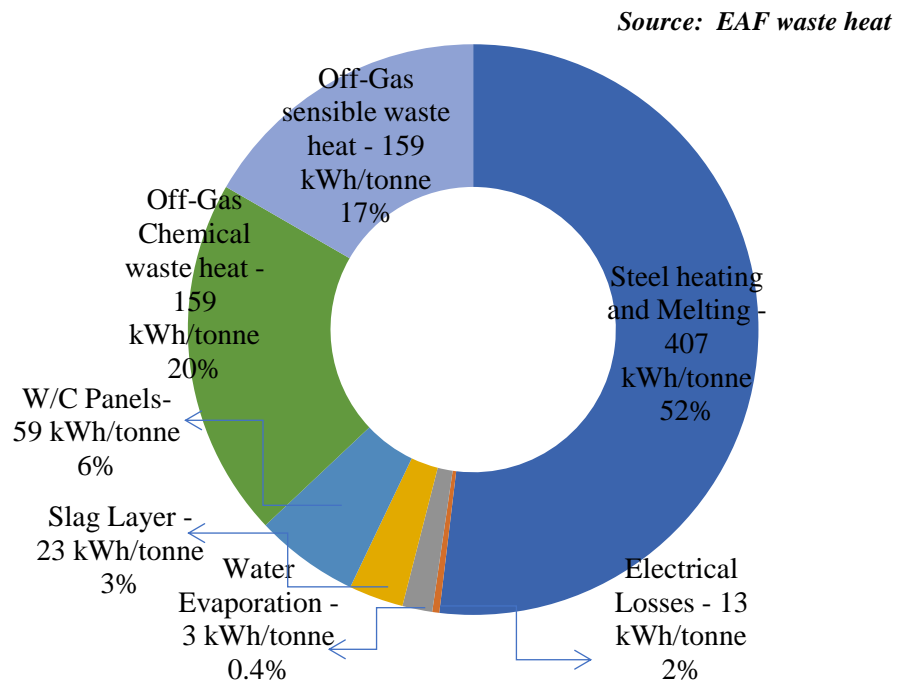


**Figure 7.12: Drivers of Industrial waste heat sources**

Shape memory alloys are attractive material for consuming waste heat from industrial and environmental sources. Among them, shape memory alloy based Nitinol heat engine or the Johnson heat engine was the elite method for converting the low-grade thermal output to useful mechanical work. In most cases, springs and wires are used for energy conversion, and they tend to slip from the driving unit. Several designs have been proposed and patented using Nitinol wires and springs

as shown in Fig. 7.13, for various energy harvesting applications, however, they are not as efficient as compared to solar power systems.

The technology of integrating SMA structures in the form of composites and bimorph has opened up new application towards the development from macro to microdevices. One such technology is of using a flexible polyimide substrate to act along with the SMA film is a novel and cutting-edge phenomenon [12,30,31]. Flexible substrates can be developed as a belt, and it can be deposited with smart materials, and the composite structures can be used for energy harvesting devices. The flexible substrate can act as a bias force during the cooling cycle, and there won't be any concern about slip [22,32,156].

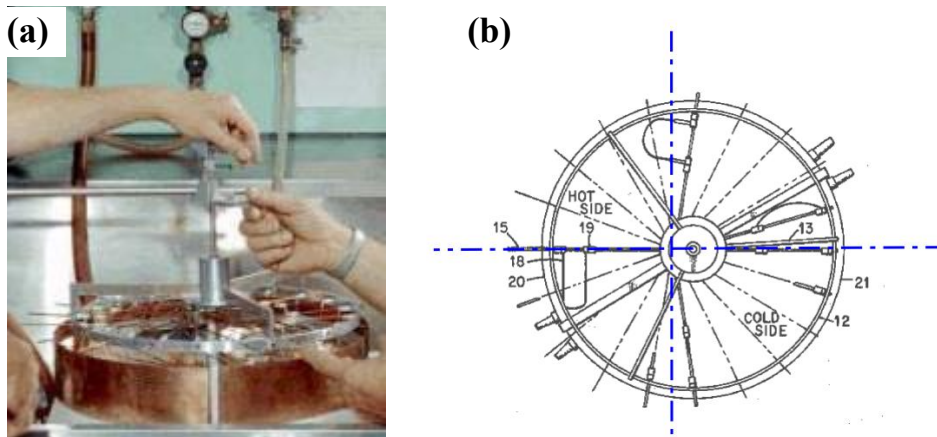
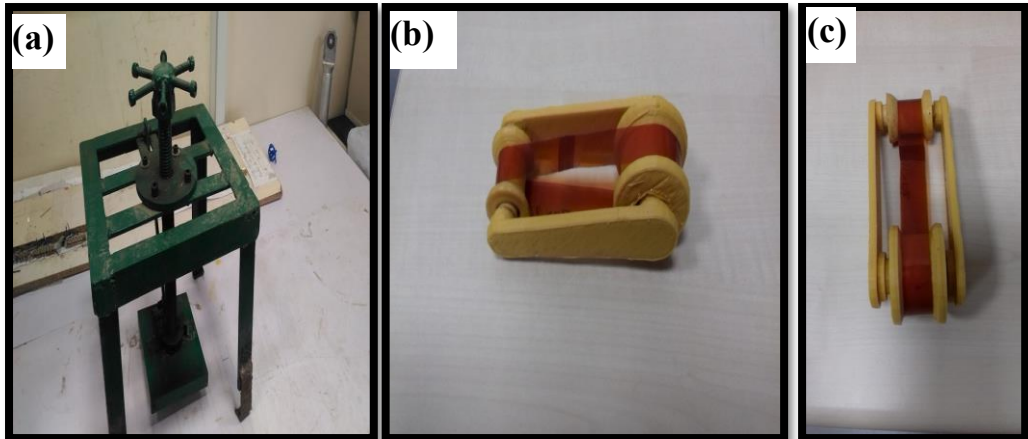


Figure 7.13: First Shape memory alloy heat engine developed by Bank's (a) actual photograph (b) top view of the engine with SMA wires.

#### 7.4.1 Bonding of Polyimide

Seamless polyimide belts were developed by texturing the two ends of the polyimide sheets and bonded using a chemical adhesive. Once the adhesive is applied, manually pressure bonding setup as shown in Fig. 7.14 (a) was used to press the edges. The bonding was checked at high temperature to ensure proper adhesion. Further, mechanical testing will provide the yield point of bonded polyimide belt. A standard diameter was taken for the deposition, and 3D printed pulley arrangement was developed to employ the bimorph belts in different applications. Fig. 7.14 (b) and (c) shows the images of the polyimide belt on the 3D printed pulley setup.



**Figure 7.14: Pictures showing the (a) Pressure bonding setup (b) Polyimide in 3d printed pulley setup (c) Top view of the pulley setup**

#### **7.4.2 Metallic Belt Deposition System**

The bimorph belt was carried out using a customised flash evaporation unit with the feasibility of holding the belt as shown in Fig. 7.15 (a). Flash evaporation was preferred to develop thicker films and the pulley arrangement as shown in Fig. 7.15 (b), has the ability to rotate up to 50 rpm. Further, there is an idler pulley, acting as a load to induce strain to the belt during deposition, thereby two-way shape memory effect. The deposition is carried out at varying rpm, and the effect of strain and feed rate is investigated on the structural and morphological properties of the bimorph belt. The preliminary results exhibited the reproducibility of similar phase as observed from thermal evaporation at 8 rpm, with a feed rate of 0.015 g/min.

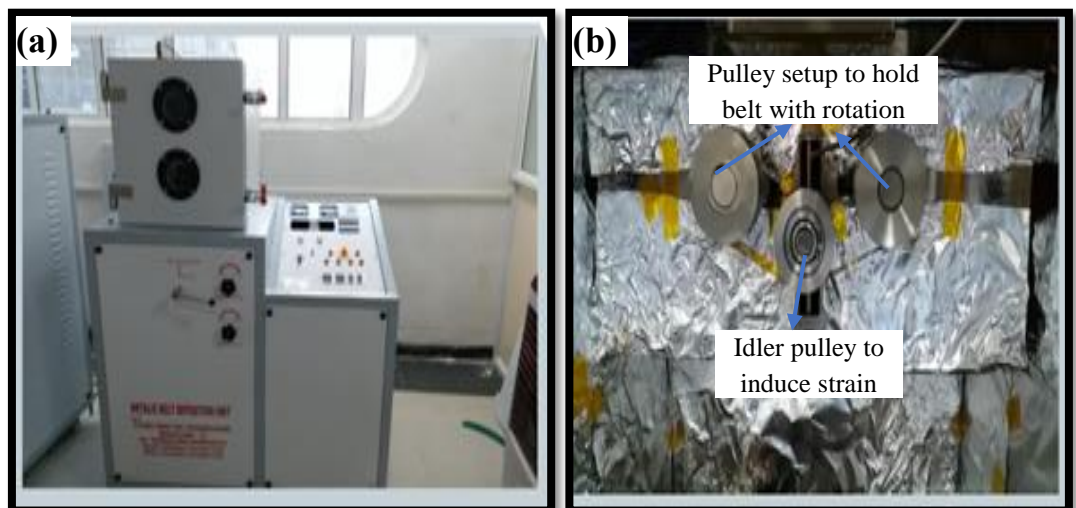


**Figure 7.15: Pictures showing the (a) Metallic Deposition Unit (b) Pulley arrangement for belt deposition**

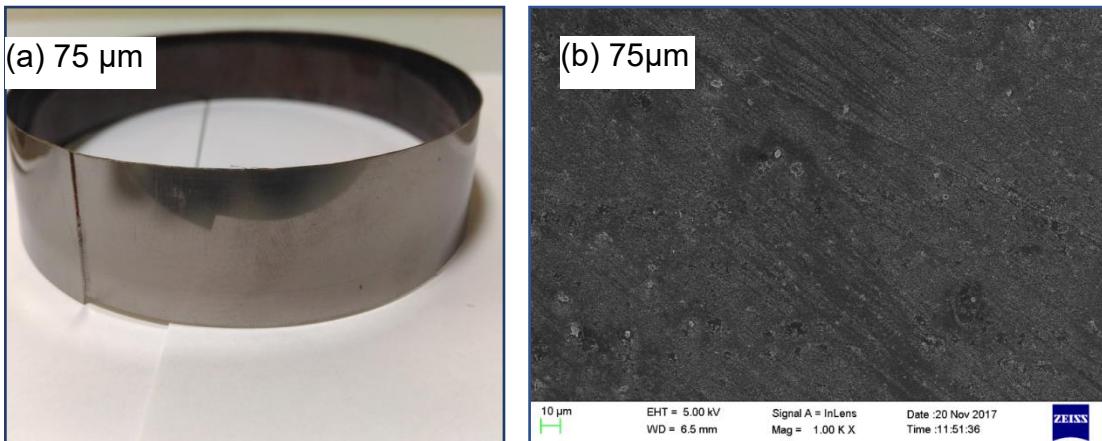


**Figure 7.16: Images of (a) developed belt with 75  $\mu\text{m}$  thickness and (b) SEM image of the bimorph belt.**

The preliminary morphological analysis exhibited the martensite textures in large numbers, and the adhesion was excellent. The bimorphs developed with higher feed rate was having poor adhesion.

### 7.4.3 Proposed Methodology

The analysis was extended with aluminium pulleys which can withstand the high temperature of the exhaust as shown in Fig. 7.16 (a). Further, the bimorph belt could be coupled with SMA springs made out of NiTi to build a more efficient method. The test results displayed the pulley was able to rotate at 84 rpm at a temperature beyond 140 °C. The separate effect of spring and bimorph has to be calculated.

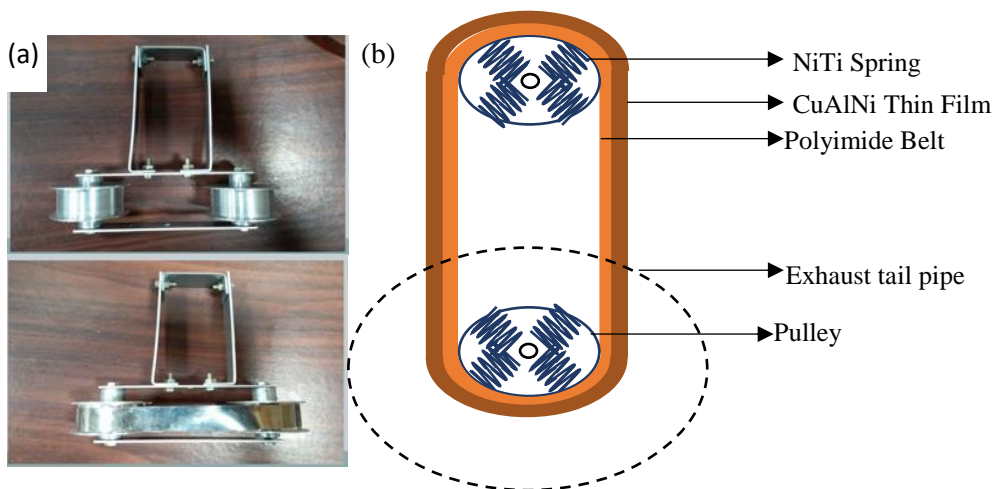


**Figure 7.17: Developed belt with aluminium pulleys for exhaust gas test (b) Proposed block diagram of hybrid energy harvesting system with NiTi springs and CuAlNi bimorphs**

## 7.5 Summary

The suitability of CuAlNiMn bimorphs was explored in functional applications such as microflapper, temperature sensor and energy harvesting belt. The results can be summarised as

- The bimorphs were employed as microflapper which could actuate at frequencies higher than 5 Hz, and the displacement was less than 1mm.
- The force generated from the edge of bimorph was found to be approximately less than  $1.5 \times 10^{-3}$  N. Increasing the thickness of the SMA thin will lead to generating higher force.
- The bimorphs were further controlled with PID control strategies, and the controller parameters were found to be,  $K_p=5.88$   $T_i=2$   $T_d=0.5$ .
- The utilisation of bimorph for temperature sensing in transformer oils was explored. A sensitive of  $0.2 \text{ mm}/^\circ\text{C}$  was observed with the bimorph.
- Higher resolution sensor had to be used for the measurement of displacement in both the cases. An interferometry technique was proposed for measuring the displacement in micron order.
- Further, bimorph belts were made with a customised flash evaporation system for recovering waste heat from vehicle exhaust. Preliminary results exhibited minor results similar to Johnson's heat engine.



# Chapter 8

---

## Conclusions and Future Scope

### 8.1 Conclusions

CuAlNi SMA bimorph was developed through physical vapour deposition, and the material behaviour was studied in detail through various characterization techniques. Further, the thermomechanical and life cycle behaviour of CuAlNi and CuAlNiMn was analysed with various desirable actuator properties. Functional applications were tested with the developed bimorph in suitable areas. The results of the work can be summarized as

- Copper-based shape memory alloys of CuAlNi and CuAlNi was developed through physical vapour deposition.
- The influence of different substrates indicated the incomplete phase formation at glass substrate with poor adhesion. Silicon substrate films were peeled off for actuation analysis with no visible shape change.
- The samples developed on Kapton polyimide substrates actuated without any post-processing.
- The pre-straining of polyimide substrates during deposition aided in two-way shape memory effect.
- The investigations on the influence of polyimide substrate thickness revealed the high recovery ratio with 75  $\mu\text{m}$  bimorphs.
- The curvature of bimorphs developed on 25  $\mu\text{m}$  was high with minor actuation. The adhesion was slightly reduced, and the samples were omitted from thermomechanical analysis.
- The morphology displayed uniform surface with  $\beta$  martensite phase in both 50  $\mu\text{m}$  and 75  $\mu\text{m}$  substrate thickness.
- The bimorph developed on 75  $\mu\text{m}$  polyimide displayed stable life for 500 cycles.
- The growth substrate temperature was varied from 100  $^{\circ}\text{C}$  to 200  $^{\circ}\text{C}$ , and its influence on thermomechanical behaviour was investigated.

- The samples developed at 150 °C substrate temperature displayed stable martensite phase without any precipitates.
- The grain size was found to be less than 150 nm for all the developed samples.
- The adhesion was poor with samples developed at 200 °C substrate temperature.
- Bimorphs developed at 150 °C substrate temperature displayed resolute characters with large displacement and stable life.
- The theoretical simulations on structural analysis of CuAlNi/polyimide composite displayed the stress-strain behaviour with Von mises analysis.
- The results indicated that a maximum deformation of 6.5 mm was induced with 50 mN load applied at free ends of the bimorph
- The thermal analysis indicated that currently, less than 1 amp should be sufficient to actuate the bimorphs.
- The emissivity vs temperature plot revealed the variation at different currents and assuming the current flow to be 1 amp, the emissivity of the film will be in-between  $\epsilon = 0.2 - 0.4$ .
- The addition of Mn resulted in an increase in grain size, which affected the electrical, thermal and mechanical properties.
- The improvement in ductility was evident from the thermomechanical analysis, as the bimorphs developed with Mn addition exhibited improvement in displacement.
- The improvement in ductility after the load bearing capacity, as the bimorphs failed to actuated under 60 mg load.
- The Mn addition improved the life cycle of the bimorph from 14,000 cycles to 23,000 cycles.
- The developed CuAlNiMn bimorphs were incorporated in the functional application as a micro flapper.
- The study indicated the ability of the bimorphs to work with frequencies more than 10 Hz.
- The force generated from the edge of the bimorph was found to be less than  $1.5 \times 10^{-3}$  N, which can be improved by increasing the thickness of SMA film. However the force will be much higher with plate heating results.

- The SMA bimorph was utilised as a thermal sensor in transformer oils, and it had a sensitivity of  $0.2\text{mm}/^\circ\text{C}$ .
- The utilisation of bimorph belt was explored for harvesting waste heat from vehicle exhaust.
- Preliminary results indicated the ability of the belt to actuate on applying heat. Further, the adhesion of the developed belts was excellent.

## 8.2 Scope and Future Work

The research work reported here can be used as a parameter set for developing several MEMS devices such as gripper, pumps and platforms. The work can be extended by improving the load bearing capacity and the force generated by the bimorphs. Further studies on the interface and the mechanical properties will have a substantial effect in developing efficient actuators. The bimorph belt for energy harvesting can be used as a platform to provide electricity with very low cost. Further, some interesting and noteworthy scope of the work are given below.



**Figure 8.1: Samples developed with selective laser melting on Kapton polyimide sheets.**

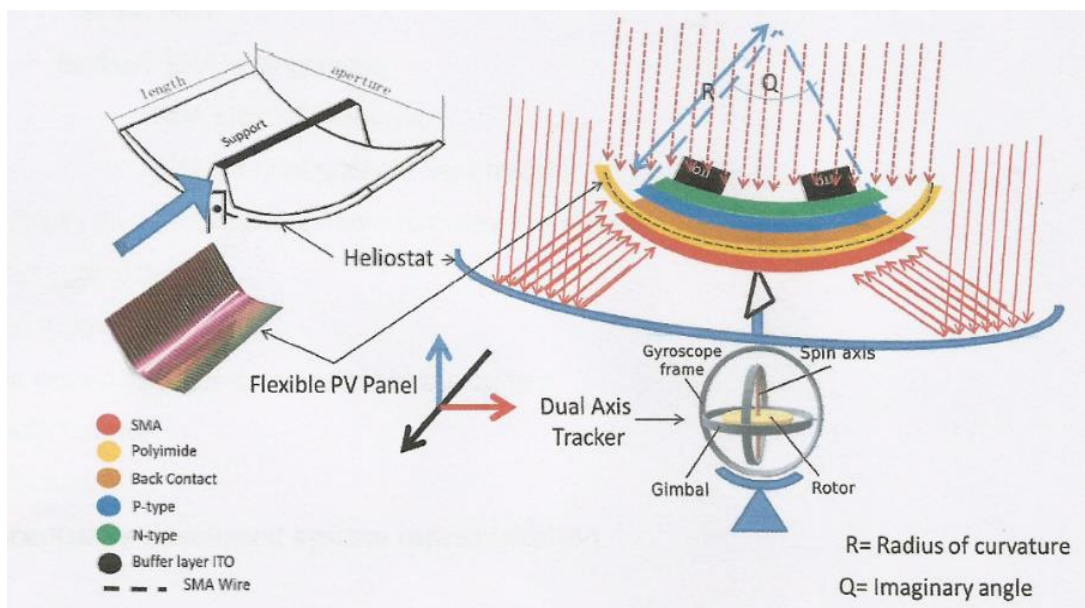


**Figure 8.2: Schematic layout of hybrid SMA/solar tracker self-energized device**

- Utilizing the CuAlNi bimorphs as damper layer for ballistic applications.
- Addition of nanoparticles to precisely tune the transformation temperature.
- Develop different shapes of bimorphs as required by the application.
- The sensor application for robust measuring can be carried out with interferometry techniques for measuring displacement.
- Developing hybrid structures with SMA/Piezo and SMA/solar cell can be utilised in developing self-energised devices.
- Developing complex structures with selective laser melting on polyimide substrates.

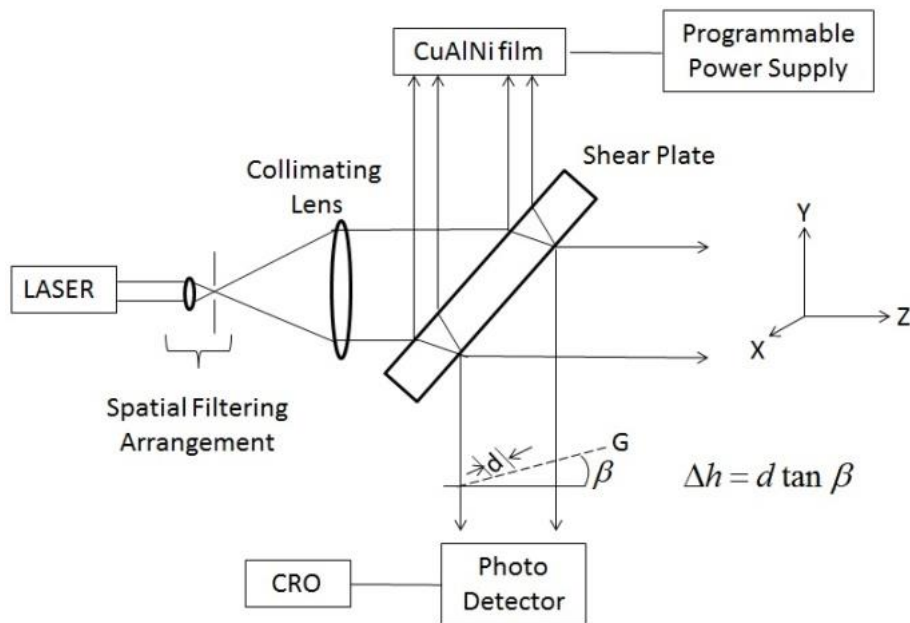


**Figure 8.3: Schematic layout of the interferometry technique proposed for measuring micron deflections**

# References

- [1] Dimitris C. Lagoudas. *Shape Memory Alloys: Modeling and Engineering Applications*. Springer; 2008. doi:10.1007/978-0-387-47685-8.
- [2] Sundarkrishna KL. *Springer Series in Materials Science*. vol. 171. 2012. doi:10.1007/978-3-642-33848-9.
- [3] Menna C, Auricchio F, Asprone D. *Applications of Shape Memory Alloys in Structural Engineering*. 2015. doi:10.1016/B978-0-08-099920-3.00013-9.
- [4] Otsuka K, Wayman C. *Shape Memory Materials*. 1998.
- [5] Duerig T, Melton K, Stockel D, Wayman C. *Engineering aspects of shape memory alloys*. 1990.
- [6] Yamauchi K, Ohkata I, Tsuchiya K, Miyazaki S. *Shape memory and superelastic alloys Technologies and applications*. Woodhead Publishing; 2011.
- [7] Huang WM, Ding Z, Wang CC, Wei J, Zhao Y, Purnawali H. *Shape memory materials*. *Mater Today* 2010;13:54–61. doi:10.1016/S1369-7021(10)70128-0.
- [8] Otsuka K, Ren X. *Recent developments in the research of shape memory alloys*. *Intermetallics* 1999;7:511–28.
- [9] Leppäniemi A. *Shape memory alloys – applications and commercial aspects* 2000:1–16.
- [10] Sun L, Huang WM, Ding Z, Zhao Y, Wang CC, Purnawali H, et al. *Stimulus-responsive shape memory materials: A review*. *Mater Des* 2012;33:577–640. doi:10.1016/j.matdes.2011.04.065.
- [11] Mohd Jani J, Leary M, Subic A, Gibson M a. *A review of shape memory alloy research, applications and opportunities*. *Mater Des* 2014;56:1078–113. doi:10.1016/j.matdes.2013.11.084.
- [12] Wei, Z. G.; Sandström, R.; Miyazaki S. *Review Shape memory materials and hybrid composites for smart systems*. *J Mater Sci* 1998;33:3743–62. doi:10.1023/A:1004692329247.
- [13] Engineers E. *Compliant Modular Shape Memory Alloy Actuators* 2014.
- [14] Lester BT, Baxevanis T, Chemisky Y, Lagoudas DC. *Review and perspectives: shape memory alloy composite systems*. *Acta Mech* 2015;226:3907–60. doi:10.1007/s00707-015-1433-0.
- [15] Leal PBC, Savi MA. *Shape memory alloy-based mechanism for aeronautical application: Theory, optimization and experiment*. *Aerosp Sci Technol* 2018;76:155–63. doi:10.1016/j.ast.2018.02.010.
- [16] Otsuka K, Ren X. *Physical metallurgy of Ti-Ni-based shape memory alloys*. *Prog Mater Sci* 2005;50:511–678. doi:10.1016/j.pmatsci.2004.10.001.
- [17] Gao Y, Casalena L, Bowers ML, Noebe RD, Mills MJ, Wang Y. *An origin of functional fatigue of shape memory alloys*. *Acta Mater* 2017;126:389–400. doi:10.1016/j.actamat.2017.01.001.
- [18] Wang ZG, Zu XT, Fu P, Dai JY, Zhu S, Wang LM. *Two-way shape memory effect of TiNi alloy coil extension springs*. *Mater Sci Eng A* 2003;360:126–31. doi:10.1016/S0921-5093(03)00376-9.
- [19] Kumar PK. *Influence of Inelastic Phenomena on the Actuation Characteristics of High*

Temperature Shape Memory Alloys 2009.

- [20] Tsoi KA, Schrooten J, Zheng Y, Stalmans R. Part II. Thermomechanical characteristics of shape memory alloy composites. *Mater Sci Eng A* 2004;368:299–310. doi:10.1016/j.msea.2003.11.007.
- [21] Vokoun D, Sysel P, Heller L, Kadeřávek L, Svatuška M, Goryczka T, et al. NiTi-Polyimide Composites Prepared Using Thermal Imidization Process. *J Mater Eng Perform* 2016;25:1993–9. doi:10.1007/s11665-016-2019-2.
- [22] Meng Q, Hu J. A review of shape memory polymer composites and blends. *Compos Part A Appl Sci Manuf* 2009;40:1661–72. doi:10.1016/j.compositesa.2009.08.011.
- [23] Saunders WR, Robertshaw HH, Rogers CA. Structural Acoustic Control of a Shape memory Alloy Composite Beam. *J Intell Mater Syst Struct* 1991;2:508–27.
- [24] Ishida A. Ti–Ni–Cu/polyimide composite–film actuator and simulation tool. *Sensors Actuators A Phys* 2015;222:228–36. doi:10.1016/j.sna.2014.12.012.
- [25] Ishida A, Sato M. Ti-Ni-Cu shape-memory alloy thin film formed on polyimide substrate. *Thin Solid Films* 2008;516:7836–9. doi:10.1016/j.tsf.2008.04.091.
- [26] Ishida A, Sato M. Development of Polyimide/SMA Thin-Film Actuator. *Mater Sci Forum* 2010;654–656:2075–8. doi:10.4028/www.scientific.net/MSF.654-656.2075.
- [27] Ishida A, Martynov V. Sputter-Deposited Alloy Thin Films : Properties and Applications. *MRS Bull* 2002:111–4.
- [28] Kotnur VG, Tichelaar FD, Fu WT, De Hosson JTM, Janssen GC. AM. Shape memory NiTi thin films deposited at low temperature. *Surf Coatings Technol* 2014;258:1145–51. doi:10.1016/S0921-5093(99)00403-7.
- [29] Kotnur VG, Tichelaar FD, Janssen GC a M. Sputter deposited Ni-Ti thin films on polyimide substrate. *Surf Coatings Technol* 2013;222:44–7. doi:10.1016/j.surfcoat.2013.01.058.
- [30] Miyazaki S, Fu YQ, Huang WM. Overview of sputter-deposited TiNi based thin films. 2009. doi:https://doi.org/10.1557/mrs2002.43.
- [31] Wei ZG, Sandström R, Miyazaki S. Shape-memory materials and hybrid composites for smart systems: Part I Shape-memory materials. *J Mater Sci* 1998;33:3743–62. doi:10.1023/A:1004692329247.
- [32] Kishi Y, Ikenaga N, Sakudo N, Yajima Z. Shape memory behavior of TiNi alloy films sputter-deposited on polyimide substrate. *J Alloys Compd* 2013;577:S210–4. doi:10.1016/j.jallcom.2012.02.020.
- [33] Lovey FC, Condó a. M, Guimpel J, Yacamán MJ. Shape memory effect in thin films of a Cu–Al–Ni alloy. *Mater Sci Eng A* 2008;481–482:426–30. doi:10.1016/j.msea.2007.01.175.
- [34] Yin H, Yan Y, Huo Y, Sun Q. Rate dependent damping of single crystal CuAlNi shape memory alloy. *Mater Lett* 2013;109:287–90. doi:10.1016/j.matlet.2013.07.062.
- [35] Fu YQ, Luo JK, Flewitt a. J, Huang WM, Zhang S, Du HJ, et al. Thin film shape memory alloys and microactuators. *Int J Comput Mater Sci Surf Eng* 2009;2:208. doi:10.1504/IJCMSSE.2009.027483.
- [36] Araujo VE a., Gastien R, Zelaya E, Beiroa JI, Corro I, Sade M, et al. Effects on the martensitic transformations and the microstructure of CuAlNi single crystals after ageing at 473K. *J Alloys Compd* 2015;641:155–61. doi:10.1016/j.jallcom.2015.04.065.
- [37] Segui C. Characterization of a hot-rolled Cu Al Ni Ti shape memory alloy. *Mater Sci Eng*

A 1999;275:625–9.

- [38] Akash K, Shukla AK, Mani Prabu SS, Narayane DC, Kanmanisubbu S, Palani IA. Parametric investigations to enhance the thermomechanical properties of CuAlNi shape memory alloy Bi-morph. *J Alloys Compd* 2017;720:264–71. doi:10.1016/j.jallcom.2017.05.255.
- [39] Akash K, S S MP, Shukla AK, Nath T, S K, Palani IA. Investigations on the life cycle behavior of Cu-Al-Ni/polyimide shape memory alloy bi-morph at varying substrate thickness and actuation conditions. *Sensors Actuators A Phys* 2017;254:28–35. doi:10.1016/j.sna.2016.12.008.
- [40] Ikenaga N, Kishi Y, Yajima Z, Sakudo N. Low Temperature Crystallization of TiNi Films by Ion Irradiation. *ESOMAT 2009 - 8th Eur Symp Martensitic Transform* 2009;05010:05010. doi:10.1051/esomat/200905010.
- [41] Sakamoto H. Fatigue Behavior of Monocrystalline Cu–Al–Ni Shape Memory Alloys under Various Deformation Mode. *Trans Japan Inst Met* 1983;24:665–73. doi:10.2320/matertrans1960.24.665.
- [42] Portier R a., Ochin P, Pasko A, Monastyrsky GE, Gilchuk A V., Kolomytsev VI, et al. Spark plasma sintering of Cu-Al-Ni shape memory alloy. *J Alloys Compd* 2013;577:S472–7. doi:10.1016/j.jallcom.2012.02.145.
- [43] Volyanski I, Shishkovsky I V., Yadroitsev I, Shcherbakov VI, Morozov YG. Layer-by-layer laser synthesis of Cu–Al–Ni intermetallic compounds and shape memory effect. *Inorg Mater* 2016;52:566–72. doi:10.1134/S0020168516060170.
- [44] Dar RD, Yan H, Chen Y. Grain boundary engineering of Co-Ni-Al, Cu-Zn-Al, and Cu-Al-Ni shape memory alloys by intergranular precipitation of a ductile solid solution phase. *Scr Mater* 2016;115:113–7. doi:10.1016/j.scriptamat.2016.01.014.
- [45] Swann PR, Warlimont H. The electron-metallography and crystallography of copper-aluminum martensites. *Acta Metall* 1963;11:511–27. doi:DOI: 10.1016/0001-6160(63)90086-5.
- [46] Otsuka, K. Shimizu, K. Cornelis, I. Wayman CM. SHAPE RECOVERY TEMPERATURE RANGE IN Cu-Al-Ni AND Cu-Zn MARMEM ALLOYS. *Scr Metallurgica* 1972;6:377–82. doi:10.1017/CBO9781107415324.004.
- [47] Otsuka K, Tokonami M, Shimizu K, Iwata Y, Shibuya I. Structure analysis of stress-induced  $\beta''1$  martensite in a Cu-Al-Ni alloy by neutron diffraction. *Acta Metall* 1979;27:965–72. doi:10.1016/0001-6160(79)90184-6.
- [48] Otsuka K, Sakamoto H, Shimizu K. Successive stress-induced martensitic transformations and associated transformation pseudoelasticity in Cu-Al-Ni alloys. *Acta Metall* 1979;27:585–601. doi:10.1016/0001-6160(79)90011-7.
- [49] Friend CM. The effect of aluminium content on the martensite phase stabilities in metastable CuAlNi alloys. *Scr Metall* 1989;23:1817–20. doi:10.1016/0036-9748(89)90367-0.
- [50] Recarte V, Hurtado I, Herreros J, N6 ML, San Juan J. Precipitation of the stable phases in Cu-Al-Ni shape memory alloys. *Scr Mater* 1996;34:255–60. doi:10.1016/1359-6462(95)00493-9.
- [51] Mazzer EM, Kiminami CS, Bolfarini C, Cava RD, Botta WJ, Gargarella P. Thermodynamic analysis of the effect of annealing on the thermal stability of a Cu–Al–Ni–Mn shape memory alloy. *Thermochim Acta* 2015;608:1–6. doi:10.1016/j.tca.2015.03.024.
- [52] Xiao Z, Li Z, Fang M, Xiong S, Sheng X, Zhou M. Effect of processing of mechanical

alloying and powder metallurgy on microstructure and properties of Cu-Al-Ni-Mn alloy. *Mater Sci Eng A* 2008;488:266–72. doi:10.1016/j.msea.2007.11.037.

- [53] Dutkiewicz J, Czeppe T, Morgiel J. Effect of titanium on structure and martensitic transformation in rapidly solidified Cu–Al–Ni–Mn–Ti alloys. *Mater Sci Eng A* 1999;273–275:703–7. doi:10.1016/S0921-5093(99)00400-1.
- [54] Sapozhnikov K, Golyandin S, Kustov S, Van Humbeeck J, Schaller R, De Batist R. Transient internal friction during thermal cycling of Cu-Al-Ni single crystals in  $\beta'$  martensitic phase. *Scr Mater* 2002;47:459–65. doi:10.1016/S1359-6462(02)00162-8.
- [55] Tatar C, Zengin R. The effects of  $\gamma$ -irradiation on some physical properties of Cu-13.5 wt.%Al-4 wt.%Ni shape memory alloy. *Mater Lett* 2005;59:3304–7. doi:10.1016/j.matlet.2005.04.062.
- [56] Shishkovsky I, Yadroitsev I, Morozov Y. Laser-assisted synthesis in Cu-Al-Ni system and some of its properties. *J Alloys Compd* 2016;658:875–9. doi:10.1016/j.jallcom.2015.10.299.
- [57] Rodriguez-Aseguinolaza J, Ruiz-Larrea I, No ML, Lopez-Echarri A, Bocanegra EH, San Juan J. Thermal history effects of Cu-Al-Ni shape memory alloys powder particles compared with single crystals behaviour. *Intermetallics* 2010;18:2183–90. doi:10.1016/j.intermet.2010.07.002.
- [58] Juan BG and PB and BM and SM and MLN and JS. Elastic properties of Cu?Al?Ni shape memory alloys studied by dynamic mechanical analysis. *Smart Mater Struct* 2010;19:15010. doi:10.1088/0964-1726/19/1/015010.
- [59] Saud SN, Hamzah E, Abubakar T, Bakhsheshi-Rad HR. Correlation of microstructural and corrosion characteristics of quaternary shape memory alloys Cu-Al-Ni-X (X=Mn or Ti). *Trans Nonferrous Met Soc China (English Ed)* 2015;25:1158–70. doi:10.1016/S1003-6326(15)63711-6.
- [60] Recarte V, Pérez-Sáez RB, Nó ML, San Juan J. Evolution of martensitic transformation in Cu – Al – Ni shape memory alloys during low-temperature aging. *J Mater Res* 1999;14:2806–13.
- [61] Recarte V, Lambri OA, Pérez-Sáez RB, Nó ML, San Juan J. Ordering temperatures in Cu-Al-Ni shape memory alloys. *Appl Phys Lett* 1997;70:3513–5. doi:10.1063/1.119217.
- [62] Recarte V, Pérez-Sáez RB, Nó ML, San Juan J. Ordering kinetics in Cu-Al-Ni shape memory alloys. *J Appl Phys* 1999;86:5467–73. doi:10.1063/1.371547.
- [63] Baldwin W. *Metallography and Microstructures* 2004 ASM. *Managing* 2004;9:2733. doi:10.1361/asmhba0003771.
- [64] Recarte V, Lambri OA, Pérez-Sáez RB, Nó ML, San Juan J. Ordering temperatures in Cu-Al-Ni shape memory alloys. *Appl Phys Lett* 1997;70:3513–5. doi:10.1063/1.119217.
- [65] Dagdelen F, Gokhan T, Aydogdu A, Aydogdu Y, Adigu O. Effects of thermal treatments on transformation behaviour in shape memory Cu – Al – Ni alloys. *Mater Lett* 2003;57:1079–85.
- [66] Picornell C, Rapacioli R, Pons J, Cesari E. Two way shape memory effect in Cu–Al–Ni single crystals. *Mater Sci Eng A* 1999;273–275:605–9. doi:10.1016/S0921-5093(99)00438-4.
- [67] Juan JS, López GA, Chengge J, Nó ML, Física D, Condensada M, et al. Nano-scale Superelastic behavior of Shape Memory Alloys for potential MEMS applications 2000:2–3. doi:10.1016/j.jallcom.2011.10.110.
- [68] Soediono B. No Title No Title. *J Chem Inf Model* 1989;53:160.

doi:10.1017/CBO9781107415324.004.

- [69] Alfonso E, Olaya J, Cubillos G. Thin film growth through sputtering technique and its applications. *Cryst - Sci Technol* 2012;397–432. doi:10.5772/35844.
- [70] Boo J-H, Jung MJ, Park HK, Nam KH, Han JG. High-rate deposition of copper thin films using newly designed high-power magnetron sputtering source. *Surf Coatings Technol* 2004;188–189:721–7. doi:10.1016/j.surfcoat.2004.07.005.
- [71] Ishida A, Sato M, Miyazaki S. Mechanical properties of Ti-Ni shape memory thin films formed by sputtering. *Mater Sci Eng a-Structural Mater Prop Microstruct Process* 1999;273:754–7. doi:10.1016/s0921-5093(99)00410-4.
- [72] Dejam L, Elahi SM. Structural and Optical Properties of Al–Zn–Cu Thin Films Prepared by DC-Magnetron Sputtering at Different Sputtering Powers. *Mol Cryst Liq Cryst* 2013;577:59–70. doi:10.1080/15421406.2013.786644.
- [73] Espinoza Torres C, Condó a. M, Haberkorn N, Zelaya E, Schryvers D, Guimpel J, et al. Structures in textured Cu–Al–Ni shape memory thin films grown by sputtering. *Mater Charact* 2014;96:256–62. doi:10.1016/j.matchar.2014.08.005.
- [74] Espinal AE, Zhang L, Chen C-H, Morey A, Nie Y, Espinal L, et al. Nanostructured arrays of semiconducting octahedral molecular sieves by pulsed-laser deposition. *Nat Mater* 2010;9:54–9. doi:10.1038/nmat2567.
- [75] Cha JO, Nam TH, Alghusun M, Ahn JS. Composition and crystalline properties of TiNi thin films prepared by pulsed laser deposition under vacuum and in ambient Ar gas. *Nanoscale Res Lett* 2012;7:37. doi:10.1186/1556-276X-7-37.
- [76] Sato M, Ishida a, Miyazaki S. Two-way shape memory effect of sputter-deposited thin films of Ti 51.3 at% Ni. *Thin Solid Films* 1998;315:305–9. doi:10.1016/s0040-6090(97)00746-3.
- [77] Ishida A, Takei A, Sato M, Miyazaki S. Stress-strain curves of sputtered thin films of Ti-Ni. *Thin Solid Films* 1996;281–282:337–9. doi:10.1016/0040-6090(96)08634-8.
- [78] Sadrnezhaad SK, Yasavol N, Ganjali M, Sanjabi S. Property change during nanosecond pulse laser annealing of amorphous NiTi thin film. *Bull Mater Sci* 2012;35:357–64. doi:10.1007/s12034-012-0293-7.
- [79] Wang X, Bellouard Y, Xue Z, Vlassak JJ. Thermal modeling of laser-annealing-induced crystallization of amorphous NiTi thin films. *Appl Phys A* 2007;90:689–94. doi:10.1007/s00339-007-4331-z.
- [80] Wang X, Bellouard Y, Vlassak JJ. Laser annealing of amorphous NiTi shape memory alloy thin films to locally induce shape memory properties. *Acta Mater* 2005;53:4955–61. doi:10.1016/j.actamat.2005.07.022.
- [81] Nakata Y, Osamu Y, Shimizu K. Effect of Aging in Cu-Zn-Al Shape Memory Alloys. *Mater Trans JIM* 1993;34:429–37.
- [82] Ao YG, Kong H. Microstructure characterization and effect of thermal cycling and ageing on vanadium-doped Cu – Al – Ni – Mn high-temperature shape memory alloy 1998;3:3579–84. doi:10.1023/A:1004647127294.
- [83] Miyazaki S, Ishida a. Martensitic transformation and shape memory behavior in sputter-deposited TiNi-base thin films. *Mater Sci Eng a-Structural Mater Prop Microstruct Process* 1999;273:106–33. doi:10.1016/s0921-5093(99)00292-0.
- [84] Fu YQ, Luo JK, Huang WM, Flewitt a J, Milne WI. Thin film shape memory alloys for optical sensing applications. *J Phys Conf Ser* 2007;76:012032. doi:10.1088/1742-6596/76/1/012032.

- [85] Makino E, Mitsuya T, Shibata T. Micromachining of TiNi shape memory thin film for fabrication of micropump. *Sensors Actuators, A Phys* 2000;79:251–9. doi:10.1016/S0924-4247(99)00290-3.
- [86] Agouram S, Bensalah MO, Ghazali A. A MICROMECHANICAL MODELLING OF THE HYSTERETIC BEHAVIOUR IN THERMALLY INDUCED MARTENSITIC PHASE TRANSITIONS : APPLICATION TO Cu ± Zn ± Al SHAPE MEMORY ALLOYS 1999;47.
- [87] Huang W. On the selection of shape memory alloys for actuators. *Mater Des* 2002;23:11–9.
- [88] Torra V, Isalgue a., Lovey FC, Sade M. Shape memory alloys as an effective tool to damp oscillations. *J Therm Anal Calorim* 2015;119:1475–533. doi:10.1007/s10973-015-4405-7.
- [89] Cabrera S, Harrison N, Lunking D, Tang R. Shape Memory Alloy Latching Microactuator. *MseUmdEdu* 2002.
- [90] Eskil M, Kayali N. X-ray analysis of some shape memory CuZnAl alloys due to the cooling rate effect. *Mater Lett* 2006;60:630–4. doi:10.1016/j.matlet.2005.09.019.
- [91] Haberkorn N, Lovey FC, Condó a. M, Guimpel J. Development and characterization of shape memory Cu–Zn–Al thin films. *Mater Sci Eng B* 2010;170:5–8. doi:10.1016/j.mseb.2010.01.058.
- [92] Studenikin S a., Golego N, Cocivera M. Fabrication of green and orange photoluminescent, undoped ZnO films using spray pyrolysis. *J Appl Phys* 1998;83:2104. doi:10.1063/1.368295.
- [93] Prasada Rao T, Santhosh Kumar MC, Safarulla a., Ganesan V, Barman SR, Sanjeeviraja C. Physical properties of ZnO thin films deposited at various substrate temperatures using spray pyrolysis. *Phys B Condens Matter* 2010;405:2226–31. doi:10.1016/j.physb.2010.02.016.
- [94] Filipovic L, Selberherr S, Mutinati GC, Brunet E, Steinhauer S, Anton K, et al. Modeling Spray Pyrolysis Deposition. *Proc World Congr Eng* 2013;II:6–11.
- [95] Madler L, Kammler HK, Mueller R, Pratsinis SE. Controlled synthesis of nanostructured particles by flame spray pyrolysis. *J Aerosol Sci* 2002;33:369–89. doi:10.1016/s0021-8502(01)00159-8.
- [96] Dhonge BP, Mathews T, Sundari ST, Thinaharan C, Kamruddin M, Dash S, et al. Spray pyrolytic deposition of transparent aluminum oxide (Al<sub>2</sub>O<sub>3</sub>) films. *Appl Surf Sci* 2011;258:1091–6. doi:10.1016/j.apsusc.2011.09.040.
- [97] Guerioune M, Amiour Y, Bounour W, Guellati O, Benaldjia a., Amara a., et al. SHS of shape memory CuZnAl alloys. *Int J Self-Propagating High-Temperature Synth* 2008;17:41–8. doi:10.3103/S1061386208010044.
- [98] Zengin R, Kayal N. Structural and Morphological Investigations on Shape Memory CuZnAl Alloys. *Acta Phys Pol A* 2010;118.
- [99] Ozgen S, Adiguzel O. Molecular dynamics simulation of diffusionless phase transformation in a quenched NiAl alloy model. *J Phys Chem Solids* 2003;64:459–64. doi:10.1016/S0022-3697(02)00335-9.
- [100] Cimpoesu N, Ursanu A. Preliminary Results of Copper Based Shape Memory Alloys Analyze Used for MEMS Applications. *Appl Mech ...* 2013:1–5.
- [101] Sampath V. Studies on the effect of grain refinement and thermal processing on shape memory characteristics of Cu–Al–Ni alloys. *Smart Mater Struct* 2005;14:S253–60.

doi:10.1088/0964-1726/14/5/013.

- [102] Zhang. J X, Liu. Y X, Cai. W ZLC. The mechanisms of two way-shape memory effect in a Cu-Zn-Al alloy. *Mater Lett* 1997;33:211–4.
- [103] Bhuniya a. K, Chattopadhyay PP, Datta S, Banerjee MK. On the degradation of shape memory effect in trace Ti-added Cu–Zn–Al alloy. *Mater Sci Eng A* 2005;393:125–32. doi:10.1016/j.msea.2004.09.068.
- [104] Kim HW. A study of the two-way shape memory effect in Cu–Zn–Al alloys by the thermomechanical cycling method. *J Mater Process Technol* 2004;146:326–9. doi:10.1016/j.jmatprotec.2003.11.018.
- [105] Bujoreanu L-G. On the influence of austenitization on the morphology of  $\alpha$ -phase in tempered Cu–Zn–Al shape memory alloys. *Mater Sci Eng A* 2008;481–482:395–403. doi:10.1016/j.msea.2006.12.223.
- [106] Shiva S, Palani I a., Mishra SK, Paul CP, Kukreja LM. Investigations on the influence of composition in the development of Ni–Ti shape memory alloy using laser based additive manufacturing. *Opt Laser Technol* 2015;69:44–51. doi:10.1016/j.optlastec.2014.12.014.
- [107] Xu JW. Effects of Gd addition on microstructure and shape memory effect of Cu–Zn–Al alloy. *J Alloys Compd* 2008;448:331–5. doi:10.1016/j.jallcom.2006.11.159.
- [108] Aldirmaz E, Celik H, Aksoy I. SEM and X-Ray Diffraction Studies on Microstructures in Cu-26.04%Zn-4.01%Al Alloy. *Acta Phys Pol A* 2013;124:87–9. doi:10.12693/APhysPolA.124.87.
- [109] Natali S, Zorteza L, Cocco V Di, Iacoviello F. Martensitic phase transformation of Cu-Zn-Al alloy, induced by cold rolling deformation. *Convegno Naz. IGF XXII*, 2013, p. 132–9.
- [110] Chentouf SM, Bouabdallah M, Gachon JC, Patoor E, Sari a. Microstructural and thermodynamic study of hypoeutectoidal Cu-Al-Ni shape memory alloys. *J Alloys Compd* 2009;470:507–14. doi:10.1016/j.jallcom.2008.03.009.
- [111] Bhattacharyya A, Lagoudas DC. Shape Memory Alloys. *Smart Mater Struct* 2007;16. doi:10.1088/0964-1726/16/1/E01.
- [112] Picornell C, Pons J, Cesari E. Mechanical stabilisation and anomalous behaviour of the stress-strain loops in Cu-Al-Ni single crystals. *Scr Mater* 2006;54:459–63. doi:10.1016/j.scriptamat.2005.10.002.
- [113] Gastien R, Corbellani CE, Álvarez Villar HN, Sade M, Lovey FC. Pseudoelastic cycling in Cu-14.3Al-4.1Ni (wt%) single crystals. *Mater Sci Eng A* 2003;349:191–6. doi:10.1016/S0921-5093(02)00789-X.
- [114] Zhu JJ, Liang NG, Cai M, Liew KM, Huang WM. Theory of phase transformation and reorientation in single crystalline shape memory alloys. *Smart Mater Struct* 2008;17:015041. doi:10.1088/0964-1726/17/01/015041.
- [115] Nishiyama Z. *Martensitic Transformation*. Academic Press; 1978.
- [116] Bo Z, Lagoudas DC. Thermomechanical modeling of polycrystalline SMA under cyclic loading, Part III: Evolution of plastic strains and two-way shape memory effect. *Int J Eng Sci* 1999;37:1175–203. doi:10.1016/S0020-7225(98)00115-3.
- [117] Creuziger a., Crone WC. Observation and prediction of out-of-plane deformation in CuAlNi. *Scr Mater* 2008;59:95–8. doi:10.1016/j.scriptamat.2008.02.035.
- [118] Gallardo FJM, Paul G, Strittmatter J. Phase Change Behavior of Nitinol Shape Memory Alloys Influence of Heat and Thermomechanical Treatments. *Adv Eng Mater* 2002;4:437–51. doi:10.1002/1527-2648(20020717).

- [119] Vajpai SK, Dube RK, Sangal S. Application of rapid solidification powder metallurgy processing to prepare Cu-Al-Ni high temperature shape memory alloy strips with high strength and high ductility. *Mater Sci Eng A* 2013;570:32–42. doi:10.1016/j.msea.2013.01.063.
- [120] Takhakh AM, Rahim A, Ali KA. Effect of Ta addition on hardness and wear resist of Cu-Al-Ni shape memory alloy fabricated by powder metallurgy. *IEEE Bus. Eng. Ind. Appl. Colloq.*, 2013, p. 327–32.
- [121] Saud SN, Hamzah E, Abubakar T, Bakhsheshi-Rad HR, Farahany S, Abdolahi a., et al. Influence of Silver nanoparticles addition on the phase transformation, mechanical properties and corrosion behaviour of Cu-Al-Ni shape memory alloys. *J Alloys Compd* 2014;612:471–8. doi:10.1016/j.jallcom.2014.05.173.
- [122] Chen C, Liu T. Phase transformations in a Cu-14.2 Al-12.0 Ni alloy. *Scr Mater* 2002;47:515–520.
- [123] Bellouard Y. Shape memory alloys for microsystems: A review from a material research perspective. *Mater Sci Eng A* 2008;481–482:582–9. doi:10.1016/j.msea.2007.02.166.
- [124] Pakhuruddin ZM, Ibrahim K, Abdul, Azlan A. Properties of polyimide substrate for applications in flexible solar cells. *Optoelectron Adv Mater* 2013;7.
- [125] Malarr??a J, Sade M, Lovey F. Microstructural evolution in the pseudoelastic cycling of Cu-Zn-Al single crystals: Behaviour at a transition stage. *Mater Sci Eng A* 2001;308:88–100. doi:10.1016/S0921-5093(00)02023-2.
- [126] Sure GN, Brown LC. The fatigue properties of grain refined ??-Cu Al Ni strain-memory alloys. *Scr Metall* 1985;19:401–4. doi:10.1016/0036-9748(85)90102-4.
- [127] Saud SN, Hamzah E, Abubakar T, Bakhsheshi-Rad HR, Zamri M, Tanemura M. Effects of Mn additions on the structure, mechanical properties, and corrosion behavior of Cu-Al-Ni shape memory alloys. *J Mater Eng Perform* 2014;23:3620–9. doi:10.1007/s11665-014-1134-1.
- [128] Ozgen S, Tatar C. Thermoelastic transition kinetics of a gamma irradiated CuZnAl shape memory alloy. *Met Mater Int* 2012;18:909–16. doi:10.1007/s12540-012-6001-8.
- [129] Duggin M, Rachinger W. The Nature of the Martensite Transformation in ACopper-Nickel-Aluminium Alloy. *Acta Metall* 1964;12.
- [130] Lojen G, Anžel I, Kneissl a., Krizman a., Unterweger E, Kosec B, et al. Microstructure of rapidly solidified Cu-Al-Ni shape memory alloy ribbons. *J Mater Process Technol* 2005;162–163:220–9. doi:10.1016/j.jmatprotec.2005.02.196.
- [131] N6 ML, Ibarra a., Caillard D, San Juan J. Quantitative analysis of stress-induced martensites by in situ transmission electron microscopy superelastic tests in Cu-Al-Ni shape memory alloys. *Acta Mater* 2010;58:6181–93. doi:10.1016/j.actamat.2010.07.038.
- [132] P6rez-Landaz6bal JI, Recarte V, Campo J, N6 ML, Juan JS. Neutron diffraction analysis of the  $\beta$  decomposition process in a texture free Cu-Al-Ni shape memory alloy. *Phys B Condens Matter* 2004;350:1007–9. doi:10.1016/j.physb.2004.03.277.
- [133] Izadinia M, Dehghani K. Structure and properties of nanostructured Cu-13.2Al-5.1Ni shape memory alloy produced by melt spinning. *Trans Nonferrous Met Soc China* 2011;21:2037–43. doi:10.1016/S1003-6326(11)60969-2.
- [134] Kannarpady GK, Bhattacharyya A, Wolverton M, Brown DW, Vogel SC, Pulnev S. Phase quantification during pseudoelastic cycling of Cu-13.1Al-4.0Ni (wt.%) single-crystal shape memory alloys using neutron diffraction. *Acta Mater* 2008;56:4724–38. doi:10.1016/j.actamat.2008.05.028.

- [135] Kaur N, Kaur D. Grain refinement of NiTi shape memory alloy thin films by W addition. *Mater Lett* 2013;91:202–5. doi:10.1016/j.matlet.2012.09.073.
- [136] Pereira EC, Mathlakova LA, da Silva Figueiredo ABH, Lima ES, dos Santos Paula A, Monteiro SN. Grain ejection associated with thermocycling of Cu-Al-Ni shape memory alloy. *Mater Lett* 2018;210:54–7. doi:10.1016/j.matlet.2017.08.123.
- [137] Zhang X, Sui J, Liu Q, Cai W. Effects of Gd addition on the microstructure, mechanical properties and shape memory effect of polycrystalline Cu-Al-Ni shape memory alloy. *Mater Lett* 2016;180:223–7. doi:10.1016/j.matlet.2016.05.149.
- [138] Morán MJ, Condó AM, Soldera F, Sirena M, Haberkorn N. Martensitic transformation in freestanding and supported Cu–Al–Ni thin films obtained at low deposition temperatures. *Mater Lett* 2016;184:177–80. doi:10.1016/j.matlet.2016.08.027.
- [139] Morris MA, Lipe T. Microstructural influence of Mn additions on thermoelastic and pseudoelastic properties of CuAlNi alloys. *Acta Metall Mater* 1994;42:1583–94. doi:10.1016/0956-7151(94)90368-9.
- [140] Izadinia M, Dehghani K. Structure and properties of nanostructured Cu-13.2Al-5.1Ni shape memory alloy produced by melt spinning. *Trans Nonferrous Met Soc China* 2011;21:2037–43. doi:10.1016/S1003-6326(11)60969-2.
- [141] Li Z, Pan ZY, Tang N, Jiang YB, Liu N, Fang M, et al. Cu–Al–Ni–Mn shape memory alloy processed by mechanical alloying and powder metallurgy. *Mater Sci Eng A* 2006;417:225–9. doi:10.1016/j.msea.2005.10.051.
- [142] Jani JM. *Design Optimisation of Shape Memory Alloy Linear Actuator Applications*. 2016.
- [143] Jani JM, Huang S, Leary M, Subic A. Numerical modeling of shape memory alloy linear actuator. *Comput Mech* 2015;56:443–61. doi:10.1007/s00466-015-1180-z.
- [144] Schmidt M, Schütze A, Seelecke S. scientific test setup For investigation of Shape memory alloy based elastocaloric cooling processes. *Int J Refrig* 2015;4:1–10. doi:10.1016/j.ijrefrig.2015.03.001.
- [145] Fornell J, Tuncer N, Schuh CA. Orientation dependence in superelastic Cu-Al-Mn-Ni micropillars. *J Alloys Compd* 2017;693:1205–13. doi:10.1016/j.jallcom.2016.10.090.
- [146] Dutkiewicz J, Morgiel J. The effect of DO3 ordering on the parent martensitic transformation in the CuZnAl shape-memory alloy. *J Mater Sci* 1986;21:429–34. doi:10.1007/BF01145505.
- [147] Bell DJ, Lu TJ, Fleck N a., Spearing SM. MEMS actuators and sensors: observations on their performance and selection for purpose 2005;15:153–64. doi:10.1088/0960-1317/15/7/022.
- [148] Bhuniya a. K, Chattopadhyay PP, Datta S, Banerjee MK. Study on the effect of trace zirconium addition on the microstructural evolution in Cu–Zn–Al shape memory alloy. *Mater Sci Eng A* 2005;391:34–42. doi:10.1016/j.msea.2004.09.063.
- [149] Sedlák P, Seiner H, Landa M, Novák V, Šittner P, Maňosa L. Elastic constants of bcc austenite and 2H orthorhombic martensite in CuAlNi shape memory alloy. *Acta Mater* 2005;53:3643–61. doi:10.1016/j.actamat.2005.04.013.
- [150] Dasgupta R. A look into Cu-based shape memory alloys: Present scenario and future prospects. *J Mater Res* 2014;29:1681–98. doi:10.1557/jmr.2014.189.
- [151] Creuziger a., Crone WC. Initial transformation around a notch tip in CuAlNi: Experiment and modeling. *Acta Mater* 2008;56:518–26. doi:10.1016/j.actamat.2007.09.043.

- [152] Rodríguez-Aseguinolaza J, Ruiz-Larrea I, Nó ML, López-Echarri a., Juan JS. A new quantitative approach to the thermoelastic martensitic transformation: The density of elastic states. *Acta Mater* 2008;56:6283–90. doi:10.1016/j.actamat.2008.08.059.
- [153] Inoue T, Horita Z, Somekawa H, Ogawa K. Effect of initial grain sizes on hardness variation and strain distribution of pure aluminum severely deformed by compression tests. *Acta Mater* 2008;56:6291–303. doi:10.1016/j.actamat.2008.08.042.
- [154] Chung CY, Lam CWH, Tan SS. Effect of parent phase ageing on CuZnAl shape memory alloys with Mn and Zr addition. *Mater Lett* 1998;33:291–6.
- [155] Wang X, Xu S, Zhou S, Xu W, Leary M, Choong P, et al. Topological design and additive manufacturing of porous metals for bone scaffolds and orthopaedic implants: A review. *Biomaterials* 2016;83:127–41. doi:10.1016/j.biomaterials.2016.01.012.
- [156] Lester B, Baxevanis T, Chemisky Y, Lagoudas D, Lester B, Baxevanis T, et al. Review and Perspectives : Shape Memory Alloy Composite Systems To cite this version : Science Arts & Métiers ( SAM ) 2015.